UNIVERSITÀ DELLA CALABRIA

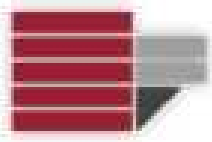

UNIVERSITY OF CALABRIA
DEPARTMENT OF PHYSICS

PHD IN
PHYSICAL, CHEMICAL AND MATERIALS SCIENCES AND TECHNOLOGIES

Cycle
XXXVII

Black Hole Dynamics from Vacuum Spacetime to Surrounding Turbulent Plasmas

Scientific-Disciplinary Sector FIS/05

Coordinator:
Prof. Gabriella Cipparrone

Gabriella Cipparrone
20.03.2025 12:46:30 GMT+01:00

Supervisor:
Prof. Sergio Servidio

SERGIO SERVIDIO
25.04.2025 18:21:39 GMT+02:00

PhD Candidate:
Mario Imbrogno

Mario Imbrogno
18.03.2025 12:28:49 GMT+02:00

Declaration of Authorship

I, Mario IMBROGNO, declare that this thesis titled, "Black Hole Dynamics from Vacuum Spacetime to Surrounding Turbulent Plasmas" and the work presented in it are my own. I confirm that:

- This work was done wholly or mainly while in candidature for a research degree at this University.
- Where any part of this thesis has previously been submitted for a degree or any other qualification at this University or any other institution, this has been clearly stated.
- Where I have consulted the published work of others, this is always clearly attributed.
- Where I have quoted from the work of others, the source is always given. With the exception of such quotations, this thesis is entirely my own work.
- I have acknowledged all main sources of help.
- Where the thesis is based on work done by myself jointly with others, I have made clear exactly what was done by others and what I have contributed myself.

Signed: 

Dedicated to my grandparents and my family

"Every time I talk to a savant, I feel quite sure that happiness is no longer a possibility. Yet, when I talk to my gardener, I'm convinced of the opposite."

Fritz Zwicky

UNIVERSITÀ DELLA CALABRIA

Abstract

Department of Physics

Doctor of Physics

Black Hole Dynamics from Vacuum Spacetime to Surrounding Turbulent Plasmas

by Mario IMBROGNO

The nonlinear behavior of black holes, governed by the Einstein field equations, coupled with the turbulent dynamics of plasma in relativistic regimes, constitutes the cornerstone of both general relativity and high-energy astrophysics. In this thesis, we employ advanced numerical simulations and cutting-edge techniques in numerical relativity and plasma physics to investigate these extreme systems and probe the intricate nonlinear interactions between black holes and relativistic plasmas.

The investigation begins with simulations of black hole systems in vacuum spacetimes, using the 3+1 formalism to explore both binary and multi-body interactions. The three-body problem is examined by transitioning from Newtonian mechanics to general relativity. In the classical framework, the interactions are modeled in a typically chaotic configuration, identifying extreme gravitational interactions (EGIs) as transients characterized by complex and highly energetic dynamics. We concentrate on selecting these EGIs as initial data for the general relativistic case, performing a series of numerical relativity simulations to establish a comprehensive set of cases. The analysis of three-body black hole dynamics reveals intricate gravitational waveforms, which are crucial for interpreting observational data and refining detection strategies. Within the 3+1 framework and in the presence of matter, a novel logarithmic formulation has been developed to enhance numerical stability in scenarios characterized by steep gradients, such as those found in stellar atmospheres. Preliminary applications of this formulation include the propagation of classical sound waves and the study of the Kelvin-Helmholtz instability.

In the second part, we perform simulations using the `BHAC` code within the GRMHD framework to model the accreting plasma flow near black holes. These simulations provide significant insights into the behavior of matter in magnetically dominated regions, such as those surrounding Sgr A* and M87*, bridging theoretical models with observational data and offering new perspectives on high-energy astrophysical processes, including jet formation, accretion mechanisms, and magnetic reconnection. Our results demonstrate the presence of a strong turbulent cascade that transfers energy from large (inhomogeneous) accretion scales down to smaller (homogeneous) lengths. This process, therefore, may continue to kinetic scales, where collisionless, relativistic physics becomes dominant.

Due to the cross-scale cascade, our focus ultimately shifts to local plasma behavior, where we explore fully kinetic plasma turbulence through high-resolution, direct numerical simulations based on the PIC method. These simulations incorporate realistic mass ratios between particle species, allowing for a detailed examination of particle acceleration mechanisms within plasma turbulence. We observe the formation of long-lived vortices with profiles typical of macroscopic, magnetically dominated force-free states. Inspired by the Harris pinch model for inhomogeneous equilibria, we describe these metastable solutions using a self-consistent kinetic model in a cylindrical coordinate system centered on a representative vortex, starting from an explicit form of the particle velocity distribution function. Turbulence is mediated by these long-lived structures, accompanied by transients in which such vortices merge and self-similarly form new metastable equilibria. For future research, we plan to broaden the scope of this investigation by including positrons as a third particle species, enabling a more comprehensive analysis of multi-species plasma behavior and elucidating the dominant processes governing energy transfer, particle energization, and the resulting electromagnetic emissions.

Acknowledgements

I would like to express my deepest gratitude to my supervisor, Prof. S. Servidio, for his invaluable guidance throughout the course of my PhD. His insightful and consistently stimulating direction has been a crucial source of intellectual growth, providing me with the essential tools to navigate and overcome the challenges of this research. I am also sincerely grateful to C. Meringolo, whose constant involvement and close attention to the development of my work have been immensely beneficial, offering constructive feedback, encouragement, and unwavering support. I also wish to express my profound gratitude to B. Cerutti, who generously hosted me during my research stay at the *Institut de Planétologie et d'Astrophysique de Grenoble* (IPAG, University of Grenoble-Alpes). His unwavering support, constant availability, and readiness to assist with any aspect of my work were truly invaluable. Lastly, I extend my heartfelt appreciation to the external referees, Prof. L. Sironi and Prof. C. F. Gammie, for their time, effort, and invaluable suggestions, which have significantly contributed to the success and quality of this dissertation.

Contents

List of Figures

List of Tables

List of Abbreviations

PIC	**P**article-**I**n-**C**ell
BSSN	**B**aumgarte-**S**hapiro-**S**hibata-**N**akamura
HD	**H**ydro**D**ynamics
RHD	**R**elativistic **H**ydro**D**ynamics
MHD	**M**agneto**H**ydro**D**ynamics
GRHD	**G**eneral **R**elativistic **H**ydro**D**ynamics
GRMHD	**G**eneral **R**elativistic **M**agneto**H**ydro**D**ynamics
KHI	**K**elvin-**H**elmholtz **I**nstability
BHAC	**B**lack **H**ole **A**ccretion **C**ode
PDE	**P**artial **D**ifferential **E**quation
ODE	**O**rdinary **D**ifferential **E**quation
FFT	**F**ast **F**ourier **T**ransform
DFT	**D**iscrete **F**ourier **T**ransform
CFL	**C**ourant-**F**riedrichs-**L**ewy
TT	**T**ransverse-**T**raceless
SFINGE	**S**pectral-**FI**ltered **N**umerical **G**ravity cod**E**
AMR	**A**daptive **M**esh **R**efinement
EoS	**E**quation **o**f **S**tate
RMS	**R**oot **M**ean **S**quare

Physical Constants

FUNDAMENTAL CONSTANTS

Speed of Light	$c = 2.997\,924\,58 \times 10^{10}\,\mathrm{cm/s}$
Gravitational Constant	$G = 6.674\,30 \times 10^{-8}\,\mathrm{cm^3/(g\,s^2)}$
Boltzmann Constant	$k_B = 1.380\,649 \times 10^{-16}\,\mathrm{erg/K}$
Electron Mass	$m_e = 9.109\,383\,56 \times 10^{-28}\,\mathrm{g}$
Proton Mass	$m_p = 1.672\,621\,923\,69 \times 10^{-24}\,\mathrm{g}$
Planck's Constant	$h = 6.626\,070\,15 \times 10^{-27}\,\mathrm{erg\,s}$
Reduced Planck's Constant	$\hbar = 1.054\,571\,8 \times 10^{-27}\,\mathrm{erg\,s}$
Elementary Charge	$e = 4.803\,204\,25 \times 10^{-10}\,\mathrm{statC}$
Vacuum Permittivity	$\epsilon_0 = 1/(\mathrm{cm\,statC^2})$
Vacuum Permeability	$\mu_0 = 1\,\mathrm{g}/(\mathrm{cm\,s^2})$

ASTRONOMICAL CONSTANTS

Astronomical Unit	$\mathrm{AU} = 1.495\,978\,707 \times 10^{13}\,\mathrm{cm}$
Light Year	$\mathrm{ly} = 9.4607 \times 10^{17}\,\mathrm{cm}$
Parsec	$\mathrm{pc} = 3.0857 \times 10^{18}\,\mathrm{cm}$

Sun

Solar Mass	$M_\odot = 1.989 \times 10^{33}\,\mathrm{g}$
Solar Radius	$R_\odot = 6.963 \times 10^{10}\,\mathrm{cm}$
Solar Luminosity	$L_\odot = 3.828 \times 10^{33}\,\mathrm{erg/s}$

Earth

Earth Mass	$M_\oplus = 5.972\,19 \times 10^{27}\,\mathrm{g}$
Equatorial Radius	$R_\oplus = 6.378 \times 10^{8}\,\mathrm{cm}$

Sgr A*

Sgr A* Mass	$M_{\mathrm{Sgr\,A^*}} = 4.1 \times 10^{6}\,\mathrm{M_\odot}$
Sgr A* Radius	$R_{\mathrm{Sgr\,A^*}} = 1.3 \times 10^{12}\,\mathrm{cm}$
Mean distance from the Sun	$d_{\odot,\,A*} = 2.5 \times 10^{22}\,\mathrm{cm}$

M87*

M87* Mass	$M_{\mathrm{M87^*}} = 6.6 \times 10^{9}\,\mathrm{M_\odot}$
M87* Radius	$R_{\mathrm{M87^*}} = 1.8 \times 10^{14}\,\mathrm{cm}$
Mean distance from the Sun	$d_{\odot,\,M87*} = 5.2 \times 10^{25}\,\mathrm{cm}$

Notation and Conventions

Throughout this thesis, geometric units are employed, where fundamental constants are normalized to unity: $c = G = k_B = 1$, $\epsilon_0 = (4\pi)^{-1}$, and $\mu_0 = 4\pi$. Here, c denotes the speed of light, G is Newton's gravitational constant, k_B is the Boltzmann constant, and ϵ_0 and μ_0 represent the permittivity and permeability of free space, respectively. In this unit system, all physical quantities are expressed in terms of length. Time is measured in meters, defined as the distance light travels in one meter. Mass is likewise expressed, with one meter of mass corresponding to the mass of a particle in Newtonian theory that has an escape velocity equal to the speed of light at a distance of two meters. One meter of time equates to approximately 3×10^{-9} seconds, while one meter of mass is approximately 1.3×10^{27} kilograms, or about 200 times the mass of Earth. Consequently, in these units, the mass of the Earth is roughly 0.5 centimeters, and the Sun's mass is approximately 1.5 kilometers. Additionally, Einstein's summation convention is applied throughout this work, meaning that repeated indices are implicitly summed unless otherwise specified.

As follows, we provide a schematic summary of the fundamental conventions employed.

Signature

We will use the conventions of Misner, Thorne, and Wheeler [1] for the metric signature together with all the sign conventions. In particular, the signature of the Minkowski 4-metric will be taken as:

$$\eta_{\mu\nu} = \begin{pmatrix} -1 & 0 & 0 & 0 \\ 0 & +1 & 0 & 0 \\ 0 & 0 & +1 & 0 \\ 0 & 0 & 0 & +1 \end{pmatrix}.$$

Objects in four-dimensional spacetime

Greek indices ($\mu, \nu, \rho, \sigma, ...$) refer to four-dimensional spacetime and take values from 0 to 3, with 0 indicating the time variable, while others refer to spatial Cartesian coordinates:

- The 4-metric tensor is $g_{\mu\nu}$, depending on the four-vector $x^\mu = (t, x, y, z)$;
- The proper distance is $ds^2 = \eta_{\mu\nu} dx^\mu dx^\nu = -dt^2 + dx^2 + dy^2 + dz^2$;
- Covariant derivatives along x^μ are defined as D_μ.

Objects in three-dimensional space

Latin indices ($i, j, k, l, ...$) refer to three-dimensional space and take values from 1 to 3:

- The 3-metric tensor is γ_{ij}, the three-vector $x^i = (x, y, z)$;
- The proper distance is $dl^2 = \eta_{ij} dx^i dx^j = dx^2 + dy^2 + dz^2$;
- Covariant spatial derivatives along x^i are defined as D_i;
- Partial derivatives along x^i are defined as $\partial_i = \frac{\partial}{\partial x^i}$.

Indices symmetries

- The symmetric part of a tensor $T_{\mu\nu}$ is defined as $T_{(\mu\nu)} = \frac{1}{2}(T_{\mu\nu} + T_{\nu\mu})$;
- The antisymmetric part of a tensor $T_{\mu\nu}$ is defined as $T_{[\mu\nu]} = \frac{1}{2}(T_{\mu\nu} - T_{\nu\mu})$.

These relations are used to simplify notation, for example:

$$T_{\mu(\nu} T_{\rho)\sigma} = \frac{1}{2} \left(T_{\mu\nu} T_{\rho\sigma} + T_{\mu\rho} T_{\nu\sigma} \right),$$

$$T_{\mu[\nu} T_{\rho]\sigma} = \frac{1}{2} \left(T_{\mu\nu} T_{\rho\sigma} - T_{\mu\rho} T_{\nu\sigma} \right).$$

Relevant plasma parameters

In the context of kinetic plasmas, several key parameters must be defined to accurately characterize a given configuration.

The effective temperature of each plasma species T_α is related to the dimensionless temperature θ_α as follows:

$$T_\alpha = \frac{\theta_\alpha m_\alpha c^2}{k_B}.$$

The effective temperature is directly proportional to the plasma beta of the α-th species and inversely proportional to the square of the magnetic field strength:

$$\beta_\alpha = \frac{8\pi n_\alpha k_B T_\alpha}{B_0^2}.$$

In the kinetic plasma framework, quantities are typically expressed in terms of powers of the electron skin depth. More generally, the skin depth for the α-th species is defined as:

$$d_\alpha = \frac{c}{\sqrt{\frac{4\pi n_\alpha e^2}{m_\alpha}}}.$$

Introduction

Astrophysical phenomena involving black holes and the surrounding relativistic plasmas provide a remarkable opportunity to explore the intricate interactions between matter, spacetime, and extreme gravitational forces. The behavior of black holes, governed by Einstein field equations, combined with the turbulent dynamics of plasmas in relativistic environments, is central to both general relativity and high-energy astrophysics. This thesis focuses on the numerical simulation of these extreme systems, employing cutting-edge techniques in numerical relativity and plasma physics to explore the nonlinear interactions between black holes and relativistic plasmas.

The first part of this thesis investigates the dynamics of black holes in vacuum spacetimes, with particular attention to multi-body systems. By applying the 3+1 formalism and the BSSN formulation, stable numerical evolutions of black hole configurations were achieved, enabling the extraction of different gravitational signals. These waveforms are essential for the interpretation of observational data from gravitational wave detectors such as LIGO and Virgo. The gravitational wave signals emitted during these mergers have yielded critical insights into the nature of black holes and their extreme environments. Through the numerical evolution of binary systems, we have gained a deeper understanding of the emission phases of gravitational waves, from the inspiral and merger to the formation of the final remnant black hole. These simulations are vital for improving detection strategies and refining waveform templates for future gravitational wave observations. Beyond binary systems, this thesis also explores the more complex dynamics of three-body black hole systems. The gravitational interactions between three massive bodies introduce a level of complexity not present in binaries, due to the chaotic and nonlinear nature of these interactions. Simulating three-body systems poses significant numerical challenges, particularly in achieving stability and accuracy when solving the Einstein field equations in such extreme regimes. Special attention was given to the computational techniques necessary for obtaining convergent solutions. The simulations conducted for three-body systems reveal intricate gravitational waveforms that differ from those generated by binary systems, offering potential signatures for the detection of such systems. The chaotic and non-periodic nature of three-body interactions leads to gravitational waveforms with multiple frequency components and non-trivial patterns, creating new possibilities for observational studies in dense stellar environments or galaxy mergers. These simulations represent an important step towards understanding multi-body black hole interactions within the framework of general relativity. Triple black hole mergers are anticipated to be relatively rare phenomena in the Universe, primarily due to the specific and complex conditions required for their occurrence. Nonetheless, they hold significant interest, as they offer valuable insights into the dynamics of black holes themselves and the processes governing galaxy evolution. While precise estimates vary, it is generally accepted that triple black hole mergers occur far less frequently than binary mergers, which are detected by observatories such as LIGO and Virgo at rates of several per year. The occurrence of triple mergers is projected to span timescales ranging

from millions to billions of years within a given galaxy. Consequently, triple black hole mergers are considered exceedingly rare, likely occurring millions or even billions of times less frequently than binary mergers. However, this estimate may differ substantially in the early Universe, where multi-body interactions were likely more prevalent.

The second part of this thesis shifts focus to the dynamics of relativistic plasmas near compact objects, particularly black holes. Using the GRHD formalism, we simulate plasma flows in the strong gravitational fields surrounding black holes, where the interaction between gravity and fluid dynamics leads to complex, often turbulent behavior. To address the numerical challenges posed by steep gradients, such as those encountered in shock formations, we introduce a novel logarithmic method designed to enhance numerical stability. This approach improves the accuracy of the simulations by transforming conserved variables into logarithmic space, reducing numerical errors in extreme environments characterized by large variations in fluid properties. One of the primary focuses of this section is the study of the KHI, which plays a crucial role in the mixing of plasma layers with different velocities. This instability arises when there is a velocity shear between two fluids or between different layers of plasma. In relativistic astrophysical contexts, such as accretion disks around black holes, the KHI significantly influences the overall dynamics of the plasma, contributing to the generation of turbulence and enhancing tenergy dissipation. By simulating this instability in relativistic regimes, we aim to understand its role in the development of turbulence and the subsequent impact on the behavior of plasma in these extreme environments. In addition to the GRHD simulations, we employ the `BHAC` code [2] within the GRMHD framework to model magnetized plasmas in the accretion disks surrounding black holes. These efforts focus on accretion flows and the role of magnetic reconnection in redistributing energy within the disk. Due to the inherent turbulence in accretion flows, magnetic fields play a key role in transferring angular momentum, allowing matter to accrete onto the black hole. Magnetic reconnection can lead to substantial energy release, contributing to the complex dynamics observed in these regions. To better characterize the turbulence, we conduct an in-depth spectral analysis across different regions near black holes, such as the disk, wind, and jet areas. The average power spectrum analysis reveals variations in the scaling laws governing each region and demonstrates the presence of a strong turbulent cascade that transfers energy from large (inhomogeneous) to smaller (homogeneous) scales, eventually reaching kinetic scales where collisionless, relativistic physics becomes dominant. These comprehensive studies on systems such as Sgr A* and M87* provide valuable insights into the role of magnetic fields in shaping the evolution of accretion flows and the mechanisms of energy transfer within magnetically dominated regions. The simulations and spectral analyses may illuminate the conditions that govern the formation of turbulent structures and the efficient transfer of energy in relativistic plasma flows near black holes.

The final part of this thesis centers on kinetic simulations of relativistic plasmas using the PIC method. Unlike fluid-based models, PIC simulations track individual macro-particles, making them well-suited for studying non-collisional plasmas dominated by long-range electromagnetic forces. The `Zeltron` code [3] is employed to model the complex dynamics of a plasma composed of protons and electrons in the vicinity of black holes, in a trans-relativistic regime where the velocities of electrons approach the speed of light, while those of protons remain sub-relativistic. This regime is crucial for understanding the small-scale processes driving particle acceleration, energy dissipation, and electromagnetic emissions near black holes. By resolving these microscopic interactions, the simulations offer insights into the

fundamental mechanisms underlying relativistic plasma behavior, which are essential for understanding high-energy radiation and jet formation. A key focus of these simulations is the identification and characterization of long-lived coherent structures within turbulent plasmas. These persistent structures, resembling macroscopic, magnetically dominated force-free states, emerge from the chaotic turbulent background and play a critical role in driving magnetic reconnection and generating high-energy radiation. Inspired by the Harris pinch model for inhomogeneous equilibria, a self-consistent kinetic model is employed to describe these structures in a cylindrical coordinate system centered on a representative vortex, using an explicit form of the particle velocity distribution function. These equilibria can be simplified to a modified force-free state, analogous to the Gold-Hoyle solution, which describes a twisted magnetic flux tube. The detailed spectral analysis of these structures reveals how these long-lived features play a central role in mediating turbulence, accompanied by transient events where vortices merge and form new metastable equilibria in a self-similar manner. This process is relevant to understanding various astrophysical phenomena, such as the formation of plasmoids and magnetic islands near compact objects. Moreover, these simulations provide valuable insights into the interplay between turbulence, magnetic fields, and relativistic particles, illustrating how magnetic energy is efficiently converted into particle kinetic energy, accelerating particles to ultra-relativistic speeds. The inclusion of additional particle species, particularly positrons, further enhances the realism of the simulations, as positrons are often produced in significant quantities in environments surrounding black holes, especially within jets. This multi-species approach allows for a more comprehensive exploration of how different species interact within turbulent fields, resulting in enhanced particle acceleration and energy dissipation. Furthermore, this investigation may contribute to understanding how energy is redistributed during magnetic reconnection events, where magnetic energy is rapidly converted into kinetic energy and heat, driving particle acceleration.

This thesis aims to bridge the gap between vacuum solutions of Einstein equations and the complex, nonlinear behavior of relativistic plasmas in extreme astrophysical environments. By integrating GRHD, GRMHD, and kinetic PIC simulations, this work provides a comprehensive framework for studying interactions between spacetime curvature, plasma turbulence, and magnetic fields in black hole physics. The results contribute significantly to both numerical relativity and plasma physics, laying the groundwork for future research on the interactions between gravitational forces, plasma turbulence, and magnetic fields in extreme environments near black holes.

The structure of this work is as follows. Chapter 1 delves into the Einstein field equations in vacuum, with a particular emphasis on black hole solutions and multi-body systems, as well as the extraction of gravitational waves from various merging configurations. Chapter 2 introduces the GRHD formalism and presents a logarithmic approach aimed at enhancing numerical stability and handling strong shocks in simulations of relativistic fluids. This Chapter also investigates the dynamics of matter in the vicinity of black holes, focusing on the examination of the KHI in localized regions (assuming flat spacetime) and employing GRMHD simulations using the `BHAC` code for a broader perspective (considering curved spacetime). The study offers a detailed exploration of large-scale turbulence, characterized through spectral analysis across different regions near black holes. Finally, Chapter 3 explores kinetic simulations of a plasma composed of two species (protons and electrons) in the trans-relativistic regime within local turbulent environments using the

Zeltron code, emphasizing the emergence of long-lived structures and characterizing these structures with a self-consistent kinetic model. The inclusion of a third species, positrons, is preliminarily discussed for future research.

Chapter 1

The Einstein Field Equations in Vacuum

The Einstein field equations represent the foundational framework of general relativity, articulating the profound interconnection between the geometry of spacetime and the distribution of matter and energy within it. Rooted in the principle of general covariance, these equations assert that the curvature of spacetime is directly linked to the energy-momentum tensor, which encapsulates the content of matter and energy. The general form of the Einstein field equations is given by [4]:

$$R_{\mu\nu} - \frac{1}{2}Rg_{\mu\nu} + \Lambda g_{\mu\nu} = \frac{8\pi G}{c^4}T_{\mu\nu}, \tag{1.1}$$

where $R_{\mu\nu}$ is the Ricci curvature tensor, R denotes the Ricci scalar, $g_{\mu\nu}$ is the metric tensor, Λ is the cosmological constant, G is the gravitational constant, c is the speed of light, and $T_{\mu\nu}$ is the energy-momentum tensor that represents the distribution of matter and energy in spacetime. The indices $\mu, \nu = 0, 1, 2, 3$ label the four spacetime coordinates, where $\mu, \nu = 0$ corresponds to the time coordinate, and $\mu, \nu = 1, 2, 3$ correspond to the spatial coordinates. The cosmological constant Λ, originally introduced by Einstein, plays a significant role in describing the accelerated expansion of the Universe as observed in modern cosmology. However, for the purposes of our discussion, we will set $\Lambda = 0$, simplifying the equations and focusing on spacetimes without this additional term.

The Ricci curvature tensor $R_{\mu\nu}$ encapsulates the influence of matter and energy on the geometry of spacetime, describing the degree to which spacetime is curved in the presence of mass-energy, particularly in relation to the evolution of geodesic volumes. It plays a crucial role in understanding how the curvature of spacetime responds to distributions of energy and momentum, making it fundamental for predicting gravitational phenomena such as the bending of light and the motion of compact objects. The Ricci tensor, a symmetric tensor, is obtained by contracting the Riemann tensor $R^{\lambda}_{\mu\nu\rho}$, specifically as:

$$R_{\mu\nu} = g^{\rho}_{\lambda}\, g^{\sigma}_{\rho}\, R^{\lambda}_{\mu\sigma\nu} = R^{\rho}_{\mu\rho\nu} = \partial_\rho \Gamma^{\rho}_{\mu\nu} - \partial_\nu \Gamma^{\rho}_{\mu\rho} + \Gamma^{\gamma}_{\mu\nu}\Gamma^{\rho}_{\gamma\rho} - \Gamma^{\gamma}_{\mu\rho}\Gamma^{\rho}_{\gamma\nu}, \tag{1.2}$$

where the Christoffel symbols $\Gamma^{\lambda}_{\mu\nu}$ are defined in terms of the metric tensor $g_{\mu\nu}$ as:

$$\Gamma^{\lambda}_{\mu\nu} = \frac{1}{2}g^{\lambda\rho}(\partial_\mu g_{\nu\rho} + \partial_\nu g_{\rho\mu} - \partial_\rho g_{\mu\nu}). \tag{1.3}$$

The Riemann tensor provides a comprehensive measure of curvature, capturing how mass-energy distorts spacetime in all possible directions. The number of independent components of the Riemann tensor in n dimensions is given by $N =$

$n^2(n^2-1)/12$. In four dimensions, the Riemann tensor has 20 independent components, 10 of which are captured by its trace, the Ricci tensor, while the remaining 10 are represented by its traceless part, the Weyl tensor.

The Ricci scalar R, obtained by further contracting the Riemann tensor, is calculated by taking the trace of the Ricci tensor $R_{\mu\nu}$:

$$R = g^{\mu\nu} R_{\mu\nu}. \tag{1.4}$$

It represents a measure of the scalar curvature of spacetime, providing a single value that characterizes the overall curvature at a given point. In vacuum spacetimes, where the energy-momentum tensor $T_{\mu\nu}$ vanishes, the Ricci scalar R must also vanish, resulting in a simplified form of the Einstein equations. This vanishing condition is crucial for describing the geometry of empty regions of spacetime, such as those far from any mass or energy, where the dynamics are governed solely by the intrinsic curvature of spacetime.

The metric tensor $g_{\mu\nu}$ is the cornerstone of general relativity, defining the infinitesimal distance between two points in spacetime through the line element:

$$ds^2 = g_{\mu\nu} dx^\mu dx^\nu. \tag{1.5}$$

The components of the metric tensor are functions of the spacetime coordinates and encode all the information about the geometry of spacetime, including lengths, angles, and volumes. It also determines how objects move through spacetime and how gravitational fields influence that motion, making it a fundamental object in describing both the structure and dynamics of the Universe.

In the absence of matter or energy, i.e., in a vacuum, the Einstein field equations become significantly simpler. However, they still capture the complex dynamics of spacetime, particularly in regions dominated by strong gravitational fields, such as near black holes or in the propagation of gravitational waves. In these extreme environments, the vacuum Einstein equations describe phenomena like the distortion of spacetime and the emission of gravitational waves, offering profound insights into the Universe's behavior under the most extreme conditions. With no matter to act as a source, the energy-momentum tensor $T_{\mu\nu}$ vanishes, leading to the condition:

$$R_{\mu\nu} = 0. \tag{1.6}$$

The above does not imply that spacetime curvature is zero, as the overall curvature is determined by the full Riemann tensor, not just its trace, the Ricci tensor. The vacuum equations explain how gravitational fields propagate through empty space and, much like Maxwell's equations for electromagnetism, imply the existence of waves—gravitational waves—that travel through spacetime at the speed of light. These waves are ripples in spacetime itself, carrying information about dynamic gravitational interactions across vast distances.

For simplicity, we will henceforth adopt geometric units, in which all fundamental constants are normalized to unity. This unit system streamlines both equations and calculations by eliminating the need to explicitly include these constants in most expressions.

1.1 Black Hole Metric Solutions in General Relativity

In general relativity, the metric describes the geometric structure of spacetime, providing solutions to the Einstein field equations in specific regions, such as those surrounding black holes. According to the no-hair theorem, all stationary black holes can be fully characterized by three independent, externally observable classical parameters: mass M, angular momentum (or intrinsic spin) J, and electric charge Q. These parameters encapsulate all the observable information about the black hole, with no other features, such as shape or internal structure, being detectable from outside the event horizon. This theorem underscores the simplicity and profound nature of black hole solutions within the framework of general relativity.

Solutions to the vacuum Einstein equations are of significant interest in general relativity, particularly for understanding the geometry and dynamics of spacetime around black holes. A prominent application of general relativity is the description of the exterior gravitational field of a static, spherically symmetric object. In early 1916, Karl Schwarzschild [5] discovered the first non-trivial exact solution to the Einstein field equations in vacuum, for a spherical, non-rotating ($J = 0$), and non-electrically charged ($Q = 0$) mass distribution ($M \neq 0$). This solution is the Schwarzschild metric, which is expressed as:

$$ds^2 = -\left(1 - \frac{2M}{r}\right) dt^2 + \left(1 - \frac{2M}{r}\right)^{-1} dr^2 + r^2 \left(d\theta^2 + \sin^2\theta \, d\phi^2\right). \tag{1.7}$$

This metric describes spacetime curvature due to the presence of mass, leading to well-known relativistic effects such as gravitational lensing and the precession of planetary orbits, exemplified by Mercury's perihelion shift. The solution holds in the vacuum region of any spherical spacetime, including those containing matter. The parameter M represents the mass as measured by a distant static observer in the vacuum exterior. When the vacuum extends down to $r = 2M$, the solution corresponds to a black hole with mass M, with the event horizon located at $r = 2M$, commonly referred to as the Schwarzschild radius. This surface is also known as the "surface of infinite redshift," as photons emitted from just outside $r = 2M$ will appear infinitely redshifted to an observer at infinity. While the Schwarzschild metric seems to have two singularities at $r = 0$ and $r = 2M$, only the former represents a physical singularity. The apparent singularity at $r = 2M$ is a coordinate singularity, which can be resolved by employing alternative coordinate systems, such as *Kruskal coordinates* [6].

Another solution for a spherical black hole with electric charge ($M, Q \neq 0$) was independently discovered by Reissner and Nordström shortly after Schwarzschild's work [7]. However, a non-spherical black hole solution was not found until 1963, when Kerr derived the spacetime metric for a rotating black hole ($M, J \neq 0$) [8]. Unlike the Schwarzschild solution, the Kerr metric introduces the concept of the ergosphere (see Fig. 1.1), a region outside the event horizon where spacetime dragging becomes significant due to the black hole's rotation. This metric elegantly captures

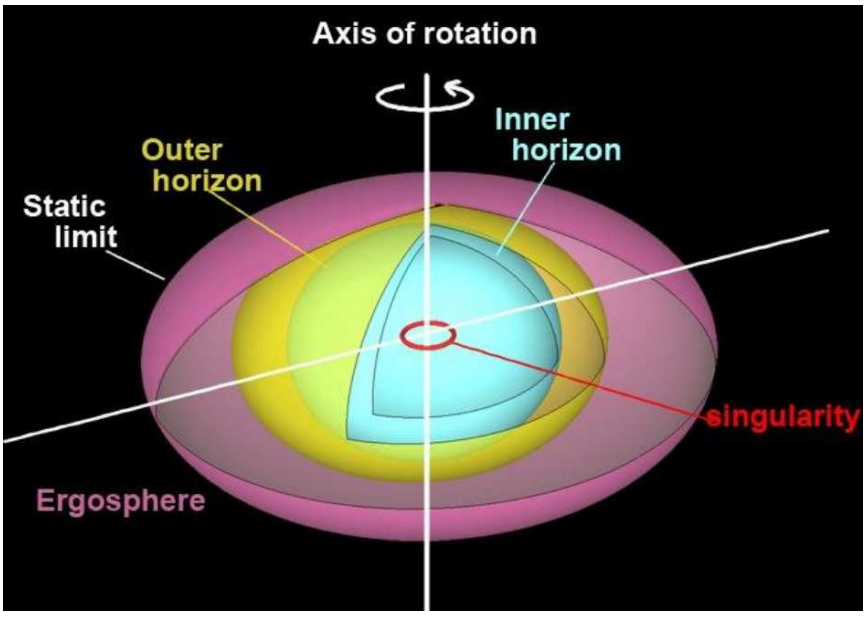

FIGURE 1.1: Rotating black hole: the outer region represents the ergosphere, where spacetime is dragged by the black hole's rotation; the innermost region represents the outer event horizon, which encloses the singularity.

the rotational effects and is given by:

$$\begin{aligned} ds^2 &= -\left(1-\frac{2GMr}{\rho^2}\right)c^2\,dt^2 - \frac{4GMar\sin^2\theta}{\rho^2}\,dt\,d\phi \\ &\quad + \frac{\rho^2}{\Delta}\,dr^2 + \rho^2\,d\theta^2 \\ &\quad + \left(r^2+a^2+\frac{2GMa^2r\sin^2\theta}{\rho^2}\right)\sin^2\theta\,d\phi^2, \end{aligned} \tag{1.8}$$

where $\Delta = r^2 - 2GMr + a^2$ is the radial lapse function, $\rho^2 = r^2 + a^2\cos^2\theta$ defines the radial-angular function, and $a = J/M$ represents the dimensionless spin parameter, with J being the angular momentum and M the mass of the black hole. The Kerr metric encapsulates the effects of rotation, including frame-dragging and the presence of the ergosphere, phenomena that are essential for understanding astrophysical black holes. Still today, it is not clear how Kerr obtained this solution, and is not that easy to obtain it starting from first principles [9].

These solutions not only illustrate the complexity and richness of the Einstein field equations but also highlight their significance in describing real astrophysical phenomena, such as black holes and gravitational waves. It is noteworthy that the resulting singularities are merely apparent and can be resolved through an appropriate change of coordinates, thereby preserving the continuity of spacetime. The introduction of Boyer–Lindquist coordinates proves particularly useful in simplifying the Kerr metric, as they generalize the coordinates used in the Schwarzschild solution to more effectively capture the rotating nature of Kerr black holes [10]. These coordinates are essential because they reduce the off-diagonal components of the metric, especially the cross-term involving $d\phi\,dt$, thereby rendering the metric more

interpretable and manageable. The transformation from Boyer–Lindquist coordinates (r, θ, ϕ) to Cartesian coordinates (x, y, z) is expressed as:

$$x = \sqrt{r^2 + a^2} \sin\theta \cos\phi, \tag{1.9}$$
$$y = \sqrt{r^2 + a^2} \sin\theta \sin\phi, \tag{1.10}$$
$$z = r \cos\theta. \tag{1.11}$$

Boyer–Lindquist coordinates allow a clearer geometrical interpretation of the Kerr spacetime (Eq. (1.8) represents a solution in these coordinates) and facilitate the study of black hole properties, such as the structure of the ergosphere and the dynamics of particles orbiting the black hole. However, standard coordinate systems attached to physical observers, while regular at the horizon, may lack stationarity. To overcome this, horizon-adapted coordinates are introduced, providing a stationary metric and a spacelike foliation, better suited for examining the near-horizon geometry [11]. A comprehensive family of horizon-adapted coordinates for the Kerr spacetime can be constructed through a transformation from the standard Boyer–Lindquist coordinates to new coordinates $\tilde{t}$ and $\tilde{\phi}$. The line element in these adapted coordinates is given by:

$$ds^2 = -(1 - Z)\, d\tilde{t}^2 - 2aZ \sin^2\theta\, d\tilde{t}\, d\tilde{\phi} + 2Z\, d\tilde{t}\, dr \tag{1.12}$$
$$+(1 + Z)\, dr^2 - 2a(1 + Z) \sin^2\theta\, dr\, d\tilde{\phi} \tag{1.13}$$
$$+\rho^2\, d\theta^2 + \sin^2\theta \left[\rho^2 + a^2(1 + Z) \sin^2\theta\right] d\tilde{\phi}^2, \tag{1.14}$$

where

$$d\tilde{\phi} = d\phi + \frac{a}{\Delta}\, dr, \tag{1.15}$$
$$d\tilde{t} = dt + \left(\frac{1 + Y}{1 + Y - Z} - \frac{1 - Z^k}{1 - Z}\right) dr \tag{1.16}$$
$$\overset{k=1}{=} dt + \frac{2Mr}{\Delta}\, dr, \tag{1.17}$$

with $Y = a^2 \sin^2\theta/\rho^2$ and $Z = 2Mr/\rho^2$. These adapted coordinates are especially useful for numerical simulations and for analyzing the structure of the Kerr black hole near its event horizon, where traditional coordinate systems might encounter singularities (such as the ring singularity depicted in Fig. 1.1) or other complications.

The most general solution for a spherical, rotating ($J \neq 0$) and electrically charged ($Q \neq 0$) mass distribution ($M \neq 0$) is the Kerr–Newman metric [12], whose line element in spherical coordinates reads:

$$\begin{aligned} ds^2 &= -\frac{\Delta}{\rho^2}\left(dt - a \sin^2\theta\, d\phi\right)^2 + \frac{\sin^2\theta}{\rho^2}\left((r^2 + a^2)\, d\phi - a\, dt\right)^2 \\ &\quad +\rho^2\, d\theta^2 + \frac{\rho^2}{\Delta}\, dr^2 \\ &= -\left(\frac{\Delta - a^2 \sin^2\theta}{\rho^2}\right) dt^2 + \frac{\rho^2}{\Delta}\, dr^2 \\ &\quad + \frac{(r^2 + a^2)^2 \sin^2\theta - \Delta a^2 \sin^4\theta}{\rho^2}\, d\phi^2 \\ &\quad +\rho^2\, d\theta^2 + \frac{2a \sin^2\theta}{\rho^2}\left(\Delta - (r^2 + a^2)\right) dt\, d\phi, \end{aligned} \tag{1.18}$$

where the radial lapse function $\Delta = r^2 - 2Mr + a^2 + Q^2$ accounts for the total charge of the black hole.

The Kerr–Newman metric, typically expressed in spherical coordinates, can also be reformulated in a more versatile form known as the Kerr–Schild metric. This alternative representation, introduced by Kerr and Schild (1965) [13], uses a specific set of Cartesian coordinates that offer significant advantages for various calculations in general relativity. The line element in the Kerr–Schild form is given by:

$$\begin{aligned} ds^2 &= dx^2 + dy^2 + dz^2 - dt^2 + \\ &\quad f\left(dt + \frac{z}{r}\,dz + \frac{r}{r^2+a^2}(x\,dx + y\,dy) - \frac{a}{r^2+a^2}(x\,dy - y\,dx)\right)^2 \end{aligned} \tag{1.19}$$

where

$$f = \frac{r^2(2Mr - Q^2)}{r^4 + a^2 z^2}, \tag{1.20}$$

$$k_\mu = \left(1, \frac{rx + ay}{r^2 + a^2}, \frac{ry - ax}{r^2 + a^2}, \frac{z}{r}\right), \tag{1.21}$$

$$r = \frac{x^2 + y^2}{r^2 + a^2} + \frac{z^2}{r^2} = 1. \tag{1.22}$$

The Kerr–Schild form is particularly useful because it expresses the metric as a perturbation of the flat Minkowski metric, simplifying many calculations in general relativity. This is especially advantageous when dealing with asymptotic properties or linearized gravity. In this form, the gravitational field is encapsulated in the term involving f and the null vector k_μ, making it easier to analyze the propagation of gravitational waves or study the behavior of black holes in the weak-field limit. Moreover, this coordinate system proves advantageous in numerical relativity, as it alleviates certain complexities associated with singularities and horizon crossing.

Boyer-Lindquist and Kerr-Schild coordinates are two of the coordinate systems available within the `BHAC` code for numerically modeling black hole accretion in arbitrary metric theories of gravity [2], as we will discuss in Chapter 3. These coordinate systems, along with flexible metric data structures, are designed to provide maximum adaptability.

1.2 The 3+1 Formalism in Numerical Relativity

To facilitate numerical simulations, particularly in scenarios such as black hole mergers or gravitational wave propagation, the Einstein field equations are reformulated using the 3+1 formalism [14]. This method foliates spacetime into a series of three-dimensional spatial slices Σ, each labeled by a time coordinate, effectively decoupling "space" from "time." In this framework, spatial variables evolve over time, allowing the complex dynamics of spacetime to be expressed in a form amenable to numerical integration. The resulting system consists of constraint equations, which must be satisfied on each spatial slice, and evolution equations, which govern how these slices progress in time. This decomposition is fundamental for studying dynamical spacetimes, as it enables a systematic description of the system's evolution by integrating both geometric and matter variables over time. Widely employed in numerical relativity, this method allows for detailed simulations of highly non-linear

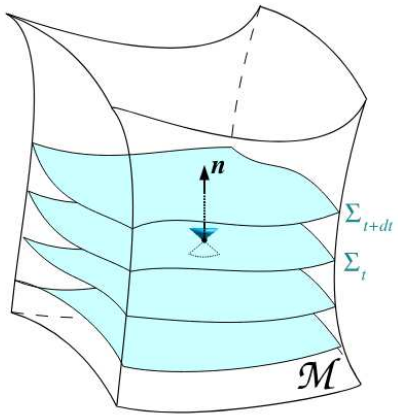

FIGURE 1.2: Slicing of spacetime: the hypersurfaces Σ_i represent level surfaces of the coordinate time t. Figure adapted from Gourgoulhon [17].

gravitational systems, such as black hole coalescence and neutron star mergers. Additionally, it is crucial for predicting gravitational waveforms, which are currently detected by observatories such as LIGO, Virgo, and KAGRA [15].

The ADM formalism [14] is a Hamiltonian formulation of general relativity, in which spacetime is foliated into a family of space-like surfaces Σ, labeled by a time coordinate t, with spatial coordinates on each slice denoted by x^i. The dynamical variables in this framework are the three-dimensional spatial metric γ_{ij} and its conjugate momentum π^{ij}. These variables allow the definition of a Hamiltonian, enabling the equations of motion for general relativity to be expressed in the form of Hamilton's equations. The original purpose of the ADM formalism was to establish a Hamiltonian structure for general relativity that could serve as a foundation for quantum gravity, rather than simply providing a system of evolution equations. In numerical relativity, however, a significant reformulation introduced by York [16] is commonly used, where the primary variables are the 3-metric γ_{ij} and the extrinsic curvature K_{ij}, instead of the canonical conjugate momentum π^{ij}.

If we denote by $\mathcal{M}$ the 4-dimensional spacetime manifold, we can assume it can be foliated into a family of non-intersecting spacelike 3-surfaces Σ, as illustrated in Fig. 1.2. Each hypersurface arises, at least locally, as the level surface of a scalar function t, which can be interpreted as a global time function [18]. This construction allows for the definition of a time direction through the vector field $\Omega_\mu = D_\mu t$, with the normalization condition:

$$||\Omega_\mu||^2 = g^{\mu\nu} D_\mu t D_\nu t = -\frac{1}{\alpha^2}, \tag{1.23}$$

where D_μ represents the covariant derivative with respect to the 4-metric $g_{\mu\nu}$. Here, α, referred to as the lapse function, plays a central role in general relativity, as it quantifies the proper time elapsing between neighboring time slices along the normal vector Ω_μ to the hypersurface Σ. The unit normal vector n^μ to the slices is defined by:

$$n^\mu = -\alpha g^{\mu\nu} \Omega_\nu = -\alpha g^{\mu\nu} D_\nu t, \tag{1.24}$$

where the negative sign ensures that n_μ points in the direction of increasing t. The proper time interval $d\tau$ between two hypersurfaces Σ, as measured by an observer

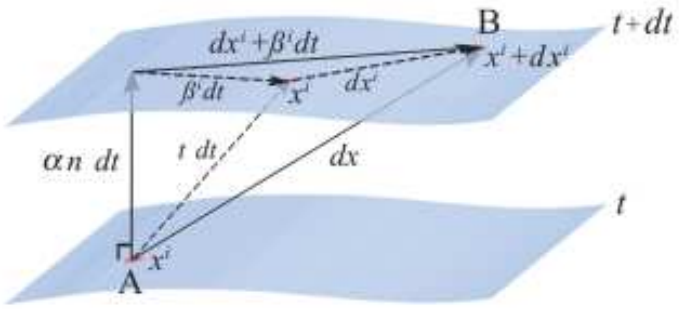

FIGURE 1.3: Schematic representation of the 3+1 decomposition of spacetime: the four-vector t^μ represents the direction of evolution of the time coordinate t and is decomposed into a timelike component αn^μ, where n^μ is the timelike unit normal to the hypersurface, and a spacelike component, represented by the shift vector β^i. Figure adapted from Baumgarte and Shapiro [18].

moving along the normal direction n^μ, is given by:

$$d\tau = \alpha(t, x^i)\, dt. \tag{1.25}$$

By contracting two unit normal vectors, we find:

$$n_\mu n^\mu = \alpha^2 g^{\mu\nu}(D_\mu t)(D_\nu t) = \begin{cases} -1 & \text{if } n_\mu \text{ is time-like,} \\ +1 & \text{if } n_\mu \text{ is space-like.} \end{cases} \tag{1.26}$$

The lapse function α is assumed to be non-negative, ensuring that Ω_μ is timelike, and the hypersurface Σ remains spacelike.

We now consider the vector

$$t^\mu = \alpha n^\mu + \beta^\mu, \tag{1.27}$$

where α is the lapse function and β^μ is the spatial shift vector. It is useful to choose t^μ as the vector field that propagates the spatial coordinate grid from one time slice to the next. In other words, t^μ connects points with the same spatial coordinates on neighboring time slices. The shift vector β^μ measures the displacement of spatial coordinates within a slice relative to the normal vector, encapsulating the effect of frame-dragging, where the rotation of massive objects, such as black holes, induces a dragging of spacetime, necessitating the adjustment of spatial coordinates over time. Solving Eq. (1.27) for the normal vector yields:

$$n^\mu = \frac{1}{\alpha}(t^\mu - \beta^\mu) = \frac{1}{\alpha}(1, -\beta^i). \tag{1.28}$$

By normalizing n^μ, one obtains the following for the normal vector:

$$n_\mu = (\alpha, 0, 0, 0)\,, \qquad n_\mu n^\mu = n_0 n^0 = \frac{n_0}{\alpha} = -1. \tag{1.29}$$

In this 3+1 formalism, as one transitions from one time slice to the next, a generic event moves from point A, with coordinates x^i, to point B, with coordinates $x^i + dx^i$, as illustrated in Fig. 1.3. The position change of B, relative to the normal projection

of A, is determined not only by the displacement dx^i, but also by the shift between the two slices, $\beta^i dt$. Thus, the total displacement is given by $\delta^i = \beta^i dt + dx^i$.

The line element in this formalism is expressed as:

$$ds^2 = -\alpha^2 dt^2 + \gamma_{ij}(dx^i + \beta^i dt)(dx^j + \beta^j dt), \tag{1.30}$$

where γ_{ij} represents the spatial metric, with $i, j = 1, 2, 3$, and the other quantities have been previously introduced.

The extrinsic curvature K_{ij} measures how the three-dimensional slice is embedded within the four-dimensional spacetime and can be determined by projecting the gradients of the normal vector into the slice Σ. More formally, within the framework of the 3+1 formalism, this tensor is defined as:

$$K_{\mu\nu} = \gamma^{\rho}_{\mu}\gamma^{\sigma}_{\nu} D_{\rho} n_{\sigma}. \tag{1.31}$$

The evolution equations for γ_{ij} and K_{ij}, derived from the Einstein field equations, are highly non-linear and require careful treatment to ensure numerical stability during simulations. To express the Einstein equations within the framework of the 3+1 formalism, a number of differential geometry identities due to Gauss, Codazzi, and Ricci are employed [1]. The ADM equations consist of two constraint equations (a scalar Hamiltonian constraint and three scalar momentum constraints) and two evolution equations. The constraint equations are given by:

$$R + K^2 - K_{ij}K^{ij} = 16\pi\rho, \tag{1.32}$$

$$D_j(K^{ij} - \gamma^{ij}K) = 8\pi S^i, \tag{1.33}$$

while the evolution equations are:

$$\partial_t \gamma_{ij} = -2\alpha K_{ij} + D_i\beta_j + D_j\beta_i, \tag{1.34}$$

$$\begin{aligned}\partial_t K_{ij} = {} & \alpha\left(R_{ij} - 2K_{ik}K^k_j + KK_{ij}\right) - D_iD_j\alpha \\ & + \beta^k\partial_k K_{ij} + K_{ik}\partial_j\beta^k + K_{kj}\partial_i\beta^k \\ & - 8\pi\alpha\left(S_{ij} - \frac{1}{2}\gamma_{ij}(S - \rho)\right),\end{aligned} \tag{1.35}$$

where the mass-energy density ρ, the momentum density S^i, the fully spatial projection of the energy-momentum tensor S_{ij}, and its trace S are zero in a vacuum spacetime. It is important to note that while the Einstein field equations consist of ten second-order PDEs, the ADM formulation leads to twenty first-order PDEs: twelve evolution equations (six for the 3-metric γ_{ij} and six for the extrinsic curvature K_{ij}), four constraint equations (one Hamiltonian constraint and three momentum constraints), and four additional equations that govern the evolution of the gauge variables α and β^i (one for the lapse function and three for the shift vector).

Since researchers began working with full three-dimensional evolution codes in numerical relativity, it became apparent that the ADM equations lacked the necessary stability properties for long-term numerical simulations. This issue, now understood to be related to the fact that these equations are only weakly hyperbolic, posed significant challenges for accurate and stable computations. In mathematics, a hyperbolic PDE of order n is one that has a well-posed initial value problem for the first $n-1$ derivatives. More precisely, the Cauchy problem can be locally solved for arbitrary initial data along any non-characteristic hypersurface. The same holds

for a system of partial differential equations, where the property of well-posedness implies that its solutions depend continuously on the initial data. In other words, small changes in the initial data result in small changes in the solution. More formally, if the solution of a system of PDEs is given by a function $f(\boldsymbol{x}, t)$, the system is called "well-posed" if one can define a norm $||\cdot||$ such that:

$$||f(\boldsymbol{x}, t)|| \leq Ce^{kt}||f(\boldsymbol{x}, 0)||, \qquad C, k \in \mathbb{R}, \tag{1.36}$$

where C and k are constants independent of the initial data. This indicates that the norm of the solution at time t increases at most exponentially in relation to its norm at the initial time $t = 0$, thereby ensuring that, for a hyperbolic system, the solution will not exhibit uncontrollably growth over time unless an instability is introduced.

To address the stability issues of the ADM equations, Baumgarte, Shibata, Shapiro, Nakamura, Oohara, and Kojima introduced a reformulation of the ADM evolution equations in 1987, based on a conformal transformation that improved stability compared to ADM [19]. Although this formulation evolved over the following years, it remained relatively unnoticed by the numerical relativity community until Baumgarte and Shapiro systematically compared it to ADM for various spacetimes. They demonstrated that the new formulation exhibited significantly better stability properties in all cases considered [20]. Since then, this reformulation has gained widespread adoption and is now used, in one form or another, by most large-scale three-dimensional codes in numerical relativity. The most effective approach to achieving stability is known as the BSSN formulation [6, 18]. This formulation has also been referred to as the "conformal ADM," though this name does not emphasize the most significant difference between the BSSN and ADM formulations, which is the introduction of auxiliary variables, such as the conformal Christoffel symbols $\tilde{\Gamma}^i$. In the BSSN formulation, a conformal transformation of the spatial metric is performed, and the extrinsic curvature is decomposed into its trace and trace-free parts.

The spatial metric γ_{ij} is conformally rescaled as:

$$\tilde{\gamma}_{ij} = \psi^{-4}\gamma_{ij}, \tag{1.37}$$

where ψ is the conformal factor. In the BSSN formulation, ψ is chosen such that the conformal metric $\tilde{\gamma}_{ij}$ has a unit determinant, i.e., $\det[\tilde{\gamma}_{ij}] = \tilde{\gamma} = 1$. This condition is written as:

$$\psi^4 = \gamma^{1/3} \implies \psi = \gamma^{1/12}, \tag{1.38}$$

where γ represents the determinant of the physical spatial metric γ_{ij}. The use of conformal transformation in the BSSN formulation is vital for improving numerical stability, particularly in black hole spacetimes, as it efficiently controls the behavior of the metric near singularities. Typically, the conformal factor is expressed as $\phi = \ln\psi = \frac{1}{12}\ln\gamma$, resulting in:

$$\tilde{\gamma}_{ij} = e^{-4\phi}\gamma_{ij}. \tag{1.39}$$

This method provides a logarithmic variation of the metric in the vicinity of singular regions. However, Campanelli et al. [21] suggested that evolving the variable

$$\chi = \psi^{-4} = e^{-4\phi} \tag{1.40}$$

offers a more robust alternative, particularly in black hole spacetimes, as it improves stability and accuracy in numerical simulations. The advantage is that ψ typically displays a $1/r$ singularity near black holes, leading to a logarithmic singularity in ϕ, whereas χ remains a smooth C^4 function at $r = 0$.

Within the current formalism, the extrinsic curvature K_{ij} is decomposed into its trace K and its trace-free part A_{ij} as follows:

$$A_{ij} = K_{ij} - \frac{1}{3}\gamma_{ij}K. \tag{1.41}$$

The conformally rescaled traceless extrinsic curvature is then expressed as:

$$\tilde{A}_{ij} = \psi^{-4}A_{ij} = \chi A_{ij}. \tag{1.42}$$

The BSSN formulation introduces three auxiliary variables, referred to as the *conformal connection functions*, defined by the following relation:

$$\tilde{\Gamma}^i = \tilde{\gamma}^{jk}\tilde{\Gamma}^i_{jk} = -\partial_j\tilde{\gamma}^{ij}, \tag{1.43}$$

where $\tilde{\Gamma}^i_{jk}$ are the Christoffel symbols associated with the conformal metric $\tilde{\gamma}_{ij}$, expressed analogously to Eq. (1.3). The introduction of the conformal connection functions $\tilde{\Gamma}^i$ is essential in the BSSN formalism, as they are directly involved in the evolution equations for the metric and curvature. These functions enhance the stability of numerical simulations by improving the control over the evolution of the conformal metric and its derivatives.

Incorporating these variables, the BSSN formulation encompasses 17 evolution variables, namely χ, K, $\tilde{\gamma}_{ij}$, $\tilde{A}_{ij}$, and $\tilde{\Gamma}^i$. The corresponding evolution equations for these variables are given by:

$$\partial_t\widetilde{\gamma}_{ij} = -2\alpha\widetilde{A}_{ij} + \beta^k\partial_k\widetilde{\gamma}_{ij} + \widetilde{\gamma}_{ik}\partial_j\beta^k + \widetilde{\gamma}_{kj}\partial_i\beta^k - \frac{2}{3}\widetilde{\gamma}_{ij}\partial_k\beta^k, \tag{1.44}$$

$$\partial_t\chi = \frac{2}{3}\chi\left(\alpha K - \partial_i\beta^i\right) + \beta^i\partial_i\chi, \tag{1.45}$$

$$\partial_t K = -D^2\alpha + \alpha\left(\widetilde{A}_{lm}\widetilde{A}^{lm} + \frac{1}{3}K^2\right) + \beta^i\partial_i K, \tag{1.46}$$

$$\begin{aligned}\partial_t\widetilde{A}_{ij} = {} & \alpha\left(K\widetilde{A}_{ij} - 2\widetilde{A}_{ik}\widetilde{\gamma}^{mk}\widetilde{A}_{mj}\right) + \chi\left[-D_iD_j\alpha + \alpha R_{ij}\right]^{TF} \\ & + \beta^k\partial_k\widetilde{A}_{ij} + \widetilde{A}_{ik}\partial_j\beta^k + \widetilde{A}_{kj}\partial_i\beta^k - \frac{2}{3}\widetilde{A}_{ij}\partial_k\beta^k,\end{aligned} \tag{1.47}$$

$$\begin{aligned}\partial_t\widetilde{\Gamma}^i = {} & \widetilde{\gamma}^{lm}\partial_l\partial_m\beta^i + \frac{1}{3}\widetilde{\gamma}^{il}\partial_l\partial_m\beta^m + \beta^k\partial_k\widetilde{\Gamma}^i - \widetilde{\Gamma}^k\partial_k\beta^i + \frac{2}{3}\widetilde{\Gamma}^i\partial_k\beta^k \\ & -2\widetilde{A}^{ik}\partial_k\alpha + \alpha\left(2\widetilde{\Gamma}^i_{lm}\widetilde{A}^{lm} - \frac{3}{\chi}\widetilde{A}^{ik}\partial_k\chi - \frac{4}{3}\widetilde{\gamma}^{ik}\partial_k K\right),\end{aligned} \tag{1.48}$$

where D_i represents the covariant derivative with respect to the 3-metric tensor γ_{ij}, and "TF" stands for the trace-free part of a tensor. The Ricci tensor R_{ij}, as explicitly given in Eq. (1.2), can be decomposed in terms of the conformal metric $\tilde{\gamma}_{ij}$ into two components: $R_{ij} = \tilde{R}_{ij} + \tilde{R}^{\chi}_{ij}$. In this decomposition, $\tilde{R}_{ij}$ denotes the Ricci tensor computed from the conformal metric $\tilde{\gamma}_{ij}$, while $\tilde{R}^{\chi}_{ij}$ represents the contribution

arising from the conformal factor χ. These components are given by:

$$\begin{aligned}\tilde{R}_{ij} &= -\frac{1}{2}\tilde{\gamma}^{lm}\partial_l\partial_m\tilde{\gamma}_{ij} + \tilde{\gamma}_{k(i}\partial_{j)}\tilde{\Gamma}^k + \tilde{\Gamma}^k\tilde{\Gamma}_{(ij)k} \\ &\quad +\tilde{\gamma}^{lm}\left(2\tilde{\Gamma}^k_{l(i}\tilde{\Gamma}_{j)km} + \tilde{\Gamma}^k_{im}\tilde{\Gamma}_{klj}\right), \qquad (1.49)\\ \tilde{R}^{\chi}_{ij} &= \frac{1}{2\chi}\left\{\left[\partial_i\partial_j\chi - \frac{1}{2\chi}(\partial_i\chi)(\partial_j\chi) - \tilde{\Gamma}^k_{ij}\partial_k\chi\right]\right. \\ &\quad \left.+\tilde{\gamma}_{ij}\tilde{\gamma}^{lm}\left[\partial_l\partial_m\chi - \frac{3}{2\chi}(\partial_l\chi)(\partial_m\chi) - \tilde{\Gamma}^k_{lm}\partial_k\chi\right]\right\}, \qquad (1.50)\end{aligned}$$

where the subscripts $(i\ j)$ denote symmetrization of the indices. For improved numerical stability, whenever $\widetilde{\Gamma}^i$ is not being differentiated, it is replaced by $-\partial_j\widetilde{\gamma}^{ij}$ [21]. Additionally, imposing the traceless condition on $\tilde{A}_{ij}$ and ensuring that $\tilde{\gamma}_{ij}$ maintains a unit determinant are key factors that contribute to the overall stability of numerical simulations [22]. The formalism adopted closely aligns with the approach outlined by Campanelli et al. [21].

The evolution of the lapse function α and the shift vector β^i is governed by slicing conditions such as the Bona-Massó family of conditions [23, 24]. These conditions introduce a family of lapse functions parametrized by $f(\alpha)$, offering a tunable framework adaptable to various scenarios. This flexibility helps control the evolution of the spacetime geometry and prevents the development of pathological behaviors that could lead to numerical instabilities. In many simulations, the lapse is evolved using the widely adopted "1 + log" slicing condition:

$$\partial_t\alpha = -\alpha^2 K + \beta^i\partial_i\alpha, \qquad (1.51)$$

and the shift vector β^i is evolved according to the Gamma-driver condition. The Gamma-driver condition introduces an auxiliary vector field B^i, which is used to evolve the shift vector β^i to prevent excessive distortion in the coordinate system:

$$\begin{aligned}\partial_t\beta^i &= \frac{3}{4}B^i, \qquad (1.52)\\ \partial_t B^i &= \partial_t\tilde{\Gamma}^i - \beta^j\partial_j\tilde{\Gamma}^i - \eta B^i. \qquad (1.53)\end{aligned}$$

Here, η is a damping parameter introduced to control the growth of the auxiliary field B^i and stabilize the evolution of the shift vector. As noted in the literature [21, 25], η is a positive constant that influences the system's dynamics (with typical values such as $\eta = 2.8$ resulting in stable simulations) and the factor $3/4$ is an arbitrary coefficient chosen for its ability to produce stable numerical results.

The Hamiltonian and momentum constraints play a crucial role in ensuring the consistency and accuracy of the solutions in numerical relativity [19, 16, 6]. These constraints are derived from the Einstein field equations and must be satisfied at every time step during the evolution of the system to maintain the physical validity of the simulation. The Hamiltonian constraint arises from the time-time component of the Einstein equations and ensures that the total energy density, as measured in a given spatial slice, is consistent with the geometry of that slice. In the context of the BSSN formulation, this constraint is expressed as:

$$\mathcal{H} = R - \tilde{A}_{ij}\tilde{A}^{ij} + \frac{2}{3}K^2 = 0, \qquad (1.54)$$

where R is the Ricci scalar associated with the three-dimensional spatial metric γ_{ij}.

This equation essentially provides a relationship between the curvature of the spatial slice and the distribution of energy (or mass) within that slice. For a vacuum spacetime, as considered here, the Hamiltonian constraint ensures that the curvature balances the contributions from the extrinsic curvature. The momentum constraints, on the other hand, arise from the time-space components of the Einstein equations. They ensure that the momentum density in the spatial slice is consistent with both the curvature and the extrinsic curvature. The momentum constraint equations in the BSSN formulation are written as:

$$\mathcal{M}^i = \partial_j \tilde{A}^{ij} + \tilde{\Gamma}^i_{jk}\tilde{A}^{jk} - \frac{3}{2\chi}\tilde{A}^{ij}\partial_j\chi - \frac{2}{3}\tilde{\gamma}^{ij}\partial_j K = 0. \tag{1.55}$$

This equation enforces the consistency of the extrinsic curvature with the spatial distribution of matter and energy within each slice. The term $\partial_j \tilde{A}^{ij}$ represents the divergence of the trace-free part of the extrinsic curvature, while the terms involving $\tilde{\Gamma}^i_{jk}$ and χ account for the geometric properties of the spatial slice, including the effects of the conformal transformation. During numerical evolution, these constraints must be continuously monitored to ensure that the solution remains physically accurate. Violations of the Hamiltonian or momentum constraints can indicate instabilities or inaccuracies in the numerical simulation.

These adjustments are crucial for evolving black hole spacetimes in a stable and accurate manner. The introduction of auxiliary variables such as $\tilde{\Gamma}^i$, the conformal metric $\tilde{\gamma}_{ij}$, and the trace-free part of the extrinsic curvature $\tilde{A}_{ij}$ significantly enhances the stability and accuracy of numerical simulations, particularly in the challenging context of black hole spacetimes, where singularities can complicate the evolution of the system [19, 21, 26].

1.3 Multiple Black Holes Initial Data

After introducing the 3+1 formalism, which serves as the foundation for numerical simulations of dynamical spacetimes, we now turn our attention to the initial data problem, particularly for multiple black holes. This step is crucial because the correct choice of initial data ensures that the system's evolution adheres to the Einstein field equations and remains physically consistent. These equations impose strict conditions not only on the evolution of spacetime but also on the initial data used to describe it. Specifically, any initial data selected for numerical simulations of spacetime must satisfy the Hamiltonian (1.54) and momentum (1.55) constraints to maintain physical consistency. While the evolution equations govern the geometry's progression over time, the constraint equations must be satisfied continuously, including at the simulation's outset. Therefore, the initial values of the twelve dynamical variables, $\{\gamma_{ij}, K_{ij}\}$, cannot be chosen arbitrarily but must be carefully selected to satisfy these constraints from the beginning. The constraint equations in this context are analogous to the Poisson equation in Newtonian gravity, though their nonlinear nature and coupling make them significantly more complex. In practice, solving these equations to obtain physically meaningful initial data is a nontrivial task, and various approaches have been developed to address this challenge in specific scenarios.

One approach to simplifying the problem of obtaining initial data for black hole spacetimes is to consider time-symmetric, conformally flat initial data [27]. This scenario reflects a state in which the black holes are temporarily at rest relative to each other, analogous to a Schwarzschild-type black hole configuration [16, 28]. Although this assumption of staticity does not fully capture the dynamic nature of black holes

in astrophysical systems—where they are typically in orbital motion—it provides a valuable simplification for exploring the fundamental aspects of the initial data problem [29]. In time-symmetric configurations, the extrinsic curvature vanishes, i.e., $K_{ij} = 0$. This vanishing occurs because, in a time-symmetric scenario, the initial slice of spacetime is chosen such that the time derivative of the spatial metric γ_{ij} is zero, implying that the geometry of the slice remains unchanged as one moves forward or backward in time from this moment [30, 31]. In vacuum spacetimes, the condition $K_{ij} = 0$ ensures that the momentum constraints are automatically satisfied since they involve the divergence of K_{ij}. However, the Hamiltonian constraint remains, and it now depends on the Ricci scalar of the physical metric. Solving the Hamiltonian constraint in this context remains challenging, as it requires determining a metric that satisfies the nonlinear differential equation resulting from the constraint. To address this, we consider the conformal factor ψ, as defined in Eq. (1.38), which is related to the conformal factor χ used in the evolution equations through Eq. (1.40). The Ricci scalar R can then be reformulated in terms of the conformal quantities:

$$R = \psi^{-4}\tilde{R} - 8\psi^{-5}\tilde{D}^2\psi, \tag{1.56}$$

where $\tilde{R}$ and $\tilde{D}^2$ refer to the Ricci scalar and the Laplacian of the conformally related metric, respectively. Substituting this expression into the Hamiltonian constraint yields:

$$H = 8\tilde{D}^2\psi - \psi\tilde{R} - \psi^5(K^2 - K_{ij}K^{ij}) = 0. \tag{1.57}$$

Since in the time-symmetric case we have $K_{ij} = 0$, the Hamiltonian constraint simplifies to:

$$\tilde{D}^2\psi = \frac{1}{8}\psi\tilde{R}. \tag{1.58}$$

To further simplify the problem, we assume that the conformally related metric is flat, meaning $\tilde{\gamma}_{ij} = \eta_{ij} = diag(1,1,1)$, and that the physical spatial metric is *conformally flat*. This assumption is particularly useful because it aligns with the approximate spherical symmetry often present in isolated or binary black hole systems. Conformal flatness not only simplifies the mathematical formulation but also reduces the Hamiltonian constraint to a Laplace equation, thereby making the problem more tractable both analytically and numerically. Conformal flatness implies that any spherically symmetric spatial metric can be expressed as:

$$\gamma_{ij} = \psi^4\tilde{\gamma}_{ij} = \psi^4\eta_{ij}. \tag{1.59}$$

Under this assumption, the Ricci tensor and the scalar curvature of the conformally related metric vanish, reducing the Hamiltonian constraint to a Laplace equation for the conformal factor ψ:

$$\tilde{D}^2\psi = 0. \tag{1.60}$$

The solutions to this Laplace equation, assuming spherical symmetry, take the form:

$$\psi = A + \frac{B}{r}, \tag{1.61}$$

where A and B are constants determined by boundary conditions. For asymptotically flat solutions, we impose that the metric approaches flat spacetime at infinity, which sets $A = 1$. The constant B is related to the mass of the black hole; in isotropic coordinates [1], $B = M/2$ ensures that the conformal factor ψ correctly reproduces the Schwarzschild metric. Consequently, the conformal factor for a single, static,

spherically symmetric Schwarzschild black hole is given by:

$$\psi = 1 + \frac{M}{2r}, \tag{1.62}$$

where M represents the black hole's mass and r is the radial coordinate. While this scenario is highly idealized, it serves as a fundamental basis for analyzing more complex configurations, including those involving multiple black holes with initial linear and/or angular momenta, which will be explored further.

The initial data for a single Schwarzschild black hole, initially at rest in a vacuum, can then be described using a conformally flat metric. By applying Eq. (1.62), the spatial metric γ_{ij} is expressed in terms of the conformal metric $\tilde{\gamma}_{ij}$ through the conformal factor as follows:

$$\gamma_{ij} \;=\; \psi^4 \tilde{\gamma}_{ij} = \left(1 + \frac{M}{2r}\right)^4 \eta_{ij}, \tag{1.63}$$

where $\tilde{\gamma}_{ij} = \eta_{ij}$ represents the flat conformal metric, and the extrinsic curvature is zero:

$$K_{ij} = 0 \implies K = 0. \tag{1.64}$$

Since Eq. (1.60) is linear, the solution for multiple black holes can be obtained by superposing the individual contributions of each i-th black hole:

$$\psi = \psi_{BL} = 1 + \sum_{i=1}^{N} \frac{M_i}{2r_i}. \tag{1.65}$$

This solution, referred to as the *Brill–Lindquist initial data*, describes N black holes that are initially at rest, with zero spin and linear momentum, in a vacuum [32, 33].

Time-symmetric initial configurations of multiple black holes can serve as valuable test cases for numerical codes, even though their physical relevance is limited, as black holes are generally expected to have both linear and angular momenta. In such scenarios, the momentum constraints do not trivially vanish, and the conformal factor can no longer be expressed as a simple superposition of individual contributions from each black hole. The constraint equations, in fact, take on the following, more complicated form:

$$\mathcal{H} \;=\; \tilde{D}^2\psi - \frac{1}{8}\psi\tilde{R} + \frac{1}{8}\psi^5 \tilde{A}_{ij}\tilde{A}^{ij} - \frac{1}{12}\psi^5 K^2 = 0, \tag{1.66}$$

$$\mathcal{M}^i \;=\; \partial_j \tilde{A}^{ij} + \tilde{\Gamma}^i_{lm}\tilde{A}^{lm} + 6\psi^{-1}\tilde{A}^{ij}\partial_j\psi - \frac{2}{3}\tilde{\gamma}^{ij}\partial_j K = 0, \tag{1.67}$$

The increased complexity of the problem can be addressed by applying a conformal transformation to the traceless part of the extrinsic curvature A_{ij} (see Chapter 3.1 of *Baumgarte and Shapiro* [18]), leading to the following definitions:

$$\bar{A}_{ij} \;=\; \psi^2 A_{ij} = \psi^6 \tilde{A}_{ij}, \tag{1.68}$$

$$\bar{A}^{ij} \;=\; \psi^{10} A^{ij} = \psi^6 \tilde{A}^{ij}. \tag{1.69}$$

This transformation is crucial as it simplifies the constraint equations, making them more tractable under various gauge conditions, as further illustrated within this Section.

One such important gauge condition in numerical relativity is the *maximal slicing*, which imposes that the trace of the extrinsic curvature is zero ($K = 0$). This condition is particularly advantageous as it minimizes the growth of the volume element over time, thereby preventing the formation of singularities and enhancing the stability of simulations. Imposing maximal slicing simplifies the constraint equations, making them more manageable in numerical calculations. When maximal slicing is not applied ($K \neq 0$) and assuming vacuum conditions (i.e., no source terms), by substituting Eq.s (1.56, 1.69) into Eq. (1.54) and expressing Eq. (1.55) in terms of the conformal factor ψ, the constraint equations take the following form:

$$\mathcal{H} = \bar{D}^2\psi - \frac{1}{8}\psi\bar{R} + \frac{1}{8}\psi^{-7}\bar{A}_{ij}\bar{A}^{ij} - \frac{1}{12}\psi^5 K^2 = 0, \tag{1.70}$$

$$\mathcal{M}^i = \partial_j\bar{A}^{ij} + \bar{\Gamma}^i_{lm}\bar{A}^{lm} - \frac{2}{3}\psi^6\bar{\gamma}^{ij}\partial_j K = 0, \tag{1.71}$$

where $\bar{D}_i$ denotes the covariant derivative with respect to $\bar{\gamma}_{ij} = \tilde{\gamma}_{ij}$ and $\bar{R} = \tilde{R}$. Conversely, when maximal slicing is imposed ($K = 0$) [34] and under vacuum conditions, the constraint equations reduce to:

$$\mathcal{H} = \bar{D}^2\psi - \frac{1}{8}\psi\bar{R} + \frac{1}{8}\psi^{-7}\bar{A}_{ij}\bar{A}^{ij} = 0, \tag{1.72}$$

$$\mathcal{M}^i = \bar{D}_j\tilde{A}^{ij} = \partial_j\bar{A}^{ij} + \bar{\Gamma}^i_{lm}\bar{A}^{lm} = 0. \tag{1.73}$$

In this scenario, the momentum constraints become linear and decouple from the Hamiltonian constraint. This simplified form of the constraints is referred to as the *Bowen-York solutions* [32], which can be derived using methods such as the *conformal transverse decomposition* or the *conformal thin-sandwich approach*. The *conformal transverse decomposition* simplifies the momentum constraint by decomposing the extrinsic curvature into a transverse-traceless part, which is particularly effective for finding initial data for multiple black holes. The *conformal thin-sandwich approach*, on the other hand, accounts for the evolution of both the spatial metric and the extrinsic curvature, making it well-suited for generating initial data in dynamic scenarios, such as inspiraling black holes. Both methods are critical for determining initial data that satisfy the Hamiltonian and momentum constraints, thereby ensuring the accurate evolution of black hole spacetimes in numerical relativity.

In general relativity, no information can propagate from inside the event horizon of a black hole to the outside, meaning that the external spacetime cannot be influenced by the black hole's interior. This leads to the idea that, in numerical simulations, it suffices to evolve only the exterior spacetime, excluding the region inside the event horizon. This method is known as *black hole excision*. However, special numerical treatment is often required at the excision boundary to ensure stability and accuracy in simulations. A different approach to avoid dealing directly with singularities is the so-called *puncture method*. The central idea of the puncture method is to decompose the metric into two parts: one that contains the singularity but is analytically manageable, and another that is regular and must be evolved numerically. Initial attempts at implementing this method used a fixed puncture approach. In this setup, the singular part of the metric remains static, while only the regular correction evolves. This approach has the disadvantage of keeping the black holes at fixed coordinate positions, making it less suited for configurations where the black holes have significant momentum. As a result, fixed puncture methods have not yielded long-term stable evolutions, particularly for binary black hole systems where orbital motion is expected. In such cases, the singularities are forced to remain stationary

in the chosen coordinates, which limits the flexibility of the simulation. The breakthrough came with the development of the *moving puncture method*. In this approach, the singular part of the metric is not kept static; instead, the entire metric evolves dynamically. The puncture is free to move according to the chosen gauge conditions, ensuring that the singularity never directly coincides with a grid point. The choice of gauge conditions is crucial for the stability of the moving puncture method. Typically, a *1+log slicing condition* is employed for the lapse function, while the shift vector is evolved using a condition from the *Gamma-driver family*. These gauge conditions help ensure that the punctures move smoothly across the grid during the evolution.

The moving puncture method can be considered as a perturbative approach, where the conformal factor takes the following form [27]:

$$\psi = \psi_{BL} + u, \tag{1.74}$$

where ψ_{BL} is the Brill-Lindquist conformal factor as defined in Eq. (1.65), and the function u represents a regular correction term that must be determined numerically.

Enforcing the conditions $K = 0$ and a conformally flat spatial metric, such that $\bar{R} = 0$, the Hamiltonian constraint for the correction term u can be expressed as:

$$\tilde{D}^2 u = -\frac{1}{8}\psi_0^{-7}\bar{A}_{ij}\bar{A}^{ij}\left(1+\psi_0^{-1}(1+u)\right)^{-7}, \tag{1.75}$$

where $\psi_0 = \sum_{i=1}^{N} m_i/2r_i$, and $\bar{A}_{ij} = \psi^2 A_{ij} = \psi^6 \tilde{A}_{ij}$, as defined in Eq.s (1.69) [6]. The term $\bar{A}_{ij}\bar{A}^{ij}$ appears with a sufficiently high power to suppress divergences, thereby regularizing the source term. This regularity enables the correction term u to be solved using standard methods for nonlinear elliptic equations. For a system of multiple black holes (N), when the linear momentum $P_i = (P_x, P_y, P_z)$ and spin momentum $S_i = (S_x, S_y, S_z)$ are small, the correction term u can be approximated as:

$$\begin{aligned} u &= \sum_{k=1}^{N}\left[\frac{\boldsymbol{P}_{(k)}^2}{m_{(k)}^2}\left(a_{1(k)} + a_{2(k)}\left(3\mu_{p(k)}^2 - 1\right)\right) + 6\frac{a_{3(k)}}{m_{(k)}^4}S_{(k)}^2\left(1+\mu_{s(k)}^2\right)\right. \\ &\quad \left. + \frac{a_{4(k)}}{m_{(k)}^3}\boldsymbol{P}_{(k)} \times \boldsymbol{S}_{(k)} \cdot \boldsymbol{n}_{(k)}\right], \end{aligned} \tag{1.76}$$

where the constants $a_{1(k)}$, $a_{2(k)}$, $a_{3(k)}$, and $a_{4(k)}$ are functions of the parameters specific to each black hole and their relative distances:

$$a_{1(k)} = \frac{5l_{(k)}}{8}\left(1 - 2l_{(k)} + 2l_{(k)}^2 - l_{(k)}^3 + \frac{l_{(k)}^4}{5}\right), \tag{1.77a}$$

$$a_{2(k)} = \frac{1}{40b_{(k)}^2}\left(15 + 117l_{(k)} - 79l_{(k)}^2 + 43l_{(k)}^3 - 14l_{(k)}^4 + 2l_{(k)}^5\right), \tag{1.77b}$$

$$a_{3(k)} = \frac{l_{(k)}}{20}\left(1 + l_{(k)} + l_{(k)}^2 - 4l_{(k)}^3 + 2l_{(k)}^4\right), \tag{1.77c}$$

$$a_{4(k)} = \frac{l_{(k)}^2}{10}\left(10 - 25l_{(k)} + 21l_{(k)}^2 - 64l_{(k)}^3\right), \tag{1.77d}$$

with $b_{(k)} = 2r_{(k)}/m_{(k)}$, $l_{(k)} = 1/(1+b_{(k)})$, $\mu_{p(k)} = \boldsymbol{P}_{(k)} \cdot \boldsymbol{n}_{(k)}/|\boldsymbol{P}_{(k)}|$, and $\mu_{s(k)} = \boldsymbol{S}_{(k)} \cdot \boldsymbol{n}_{(k)}/|\boldsymbol{S}_{(k)}|$ serving as parameters that characterize the k-th black hole.

The momentum constraints require solving for the components of the conformal

extrinsic curvature tensor $\bar{A}_{ij}$, which are influenced by the linear and angular momenta of the black holes. This procedure is commonly known as the *Bowen-York method* [35]. The trace-free part of the extrinsic curvature, often referred to as the *Bowen-York extrinsic curvature* [32], is expressed as [36]:

$$\begin{aligned}\bar{A}_{ij}^{(k)} &= \frac{3}{2(r^{(k)})^2}\Big[P_i^{(k)}n_j^{(k)} + P_j^{(k)}n_i^{(k)} - \left(\delta_{ij} - n_i^{(k)}n_j^{(k)}\right)P^{l(k)}n_l^{(k)} \\ &\quad + \frac{2}{r^{(k)}}\left(\epsilon_{ilm}S^{l(k)}n^{m(k)}n_j^{(k)} + \epsilon_{jlm}S^{l(k)}n^{m(k)}n_i^{(k)}\right)\Big], \end{aligned} \tag{1.78}$$

where $n_i^{(k)}$ denotes component of the unit vector pointing from the center of the k-th black hole, $P_i^{(k)}$ and $S_i^{(k)}$ represent the linear and angular momenta, respectively, and ϵ_{ijk} is the three-dimensional Levi-Civita symbol.

The process of generating initial data for multiple black holes is computationally demanding, particularly when the black holes are in motion. To mitigate the computational cost, a numerical elliptic solver based on an iterative *Gauss-Seidel algorithm* [37] is employed, using the initial guess provided by the solution for u in Eq. (1.76). This solver incorporates an iterative grid-refinement technique, which begins with low-resolution grids and then interpolates the solution onto higher-resolution grids using Fourier transforms, as outlined by *Cao et al.* [38].

1.4 The Spectral FIltered Numerical Gravity codE (SFINGE)

In numerical relativity, accurately solving the Einstein field equations in highly dynamic and non-linear scenarios, such as black hole collisions and mergers, necessitates the use of advanced numerical techniques. Spectral methods, which express the solution of differential equations as a series of basis functions—typically trigonometric polynomials or Fourier modes—are particularly effective in achieving high precision and stability in such complex simulations. These methods are especially advantageous for problems with smooth solutions due to their exponential convergence rates, where the accuracy of the solution improves rapidly as more terms are included in the series. Unlike finite difference methods, such as Runge-Kutta or Euler schemes, which operate locally, spectral methods span the entire computational grid, thus increasing their computational complexity. However, their primary advantage lies in their exceptional accuracy: errors are typically limited by machine precision, and phase errors are entirely eliminated. The exponential convergence of spectral methods makes them highly efficient for a wide range of applications, though their effectiveness is closely linked to the specific characteristics of the problem being solved.

In this Section, we outline the main features of the SFINGE code [39], a computational algorithm developed at the University of Calabria. The code implements a filtered pseudo-spectral scheme to integrate the BSSN equations and extract gravitational wave signals from coalescing black holes. Pseudo-spectral methods alternate between physical (real) and Fourier (complex) space. The principle is straightforward: derivatives are computed in spectral space, while products are computed in physical space to avoid computationally expensive convolutions. The key advantage of this approach is that each field and its derivatives are accurately represented at the collocation points, ensuring highly precise solutions. Errors in the computation of derivatives are on the order of machine truncation error, delivering reliable results in demanding numerical simulations.

1.4.1 Fast Fourier Transform

The algorithm extensively makes use of Fourier spectral techniques to efficiently solve PDEs in the context of general relativity. By expanding functions into Fourier modes, spectral methods provide highly accurate numerical solutions in a variety of scenarios.

For simplicity, we consider a 1D compact domain, e.g., $\mathcal{D} = [-1, 1]$, and a PDE of the form:

$$\mathcal{L}f(x) = g(x), \qquad x \in \mathcal{D}, \tag{1.79}$$

where $f(x)$ is the solution that satisfies specific boundary conditions at $x = \pm 1$, depending on the operator $\mathcal{L} = \mathcal{L}(\partial_t, \partial_x, \partial_{xx}, \ldots)$, and $g(x)$ is a source term independent of $f(x)$.

In spectral methods, the solution $f(x,t)$ is approximated by a finite sum of N modes:

$$f(x,t) \simeq f_N(x,t) = \sum_{k=-N/2}^{N/2} a_k(t)\phi_k(x), \tag{1.80}$$

where the coefficients $a_k(t) \in \mathbb{C}$ are complex, and $\phi_k(x)$ represents a set of basis functions. An appropriate selection of basis functions should ensure that the approximation converges as the number of modes increases, such that as $N \to \infty$, the approximated solution $f_N(x,t)$ approaches the true solution $f(x,t)$. Furthermore, the computation of derivatives $\partial_x f_N$ should be efficient, allowing for the straightforward determination of a new set of complex coefficients $a'_k(t)$, which characterize the derivative of f_N:

$$\partial_x f_N(x,t) = \sum_{k=-N/2}^{N/2} a_k(t)\,\frac{d\phi_k(x)}{dx} = \sum_{k=-N/2}^{N/2} a'_k(t)\,\phi_k(x). \tag{1.81}$$

Finally, it is crucial that the reconstruction of the coefficients $a_k(t)$ from a given function $f(x,t)$ remains computationally feasible.

For periodic functions $f(x,t)$, a suitable choice of basis functions is the Fourier basis $\phi_k(x) = e^{ikx}$, where $k = 0, \pm 1, \pm 2, \ldots, \pm N_k$, with $N_k = N/2$ representing the Nyquist mode, and $x \in (-\pi, \pi)$. This transforms the series into:

$$f_N(x,t) = \sum_{k=-N/2}^{N/2} a_k(t)e^{ikx}. \tag{1.82}$$

With this choice, both convergence and differentiation properties are satisfied, while computational efficiency is ensured through the use of the FFT algorithm [40].

The term "spectral methods" refers to the expansion of the solution $f(x,t)$ into a series of orthogonal eigenfunctions of an operator $\mathcal{L}$. For instance, considering the Laplace operator $\mathcal{L} = \nabla^2 = \partial_j^2$ on a periodic domain, the spectrum consists of Fourier modes, and the operator acts on them as:

$$-\nabla^2 e^{-ikx} \quad = \quad |k|^2 e^{-ikx}. \tag{1.83}$$

The coefficients $a_k(t)$ of the Fourier expansion can be computed using the inverse discrete Fourier transform, which is expressed as:

$$a_k(t) = \frac{1}{N}\sum_{j=0}^{N-1} f(x_j)e^{-ikx_j}, \quad x_j = j\Delta x = j\frac{2\pi}{N}, \tag{1.84}$$

where x_j are the collocation points on the grid. Consequently, the function $f(x_j)$ at each grid point is written as:

$$f(x_j) = \sum_{k=0}^{N-1} a_k(t)\, e^{ikx_j}. \tag{1.85}$$

One significant property of the FFT is that the first coefficient a_0 represents the average value of the function across all the grid points:

$$a_0 = \frac{1}{N} \sum_{j=0}^{N-1} f(x_j) = \langle f \rangle. \tag{1.86}$$

For real-valued functions $f(x)$, the Fourier coefficients satisfy $a_k = a^*_{(N-k)}$, and the coefficient $a_{\frac{N}{2}}$ is real. While this coefficient represents a numerical artifact and lacks physical significance, it becomes negligible as N increases.

To compute the first derivative of the function $f(x) = \sum_{k=0}^{N} a_k(t) e^{ikx}$, the Fourier coefficients are transformed as follows:

$$f'(x) = \sum_{k=0}^{N-1} ika_k\, e^{ikx} = \sum_{k=0}^{N-1} a'_k\, e^{ikx}, \tag{1.87}$$

where $a'_k = ika_k$. Specifically, the first coefficient $a'_0 = 0$, since the derivative of a constant (the average) is zero. For the remaining modes, $a'_k = ika_k$ for $1 \leq k < \frac{N}{2}$, while $a'_{\frac{N}{2}} = i\frac{N}{2} a_{\frac{N}{2}}$ is purely imaginary. Since this term should not contribute to the real derivative of the function, we impose $a'_{\frac{N}{2}} = 0$ to ensure that $f'(x) \in \mathbb{R}$.

Similarly, for the second derivative of the function, we have:

$$f''(x) = \sum_{k=0}^{N-1} -k^2 a_k\, e^{ikx} = \sum_{k=0}^{N-1} a''_k\, e^{ikx}, \tag{1.88}$$

where $a''_k = -k^2 a_k$. As expected, the first coefficient $a''_0 = 0$, since the derivative of a constant is zero. For the higher-order modes, $a''_k = -k^2 a_k$ for $1 \leq k < N/2$, and for $k = N/2$, the second derivative becomes $a''_{\frac{N}{2}} = -\frac{N^2}{4} a_{\frac{N}{2}}$, which is real and thus not set to zero.

1.4.2 Aliasing effect

Although pseudo-spectral methods are among the most accurate numerical techniques, particularly well-suited for solving complex small-scale problems such as wave dynamics and turbulence, careful attention must be given to the treatment of nonlinear terms. Nonlinearity is a fundamental characteristic not only in gravitation but also in hydrodynamics and plasma dynamics, though the degree of nonlinearity is typically less pronounced in the latter fields. In spectral methods, nonlinear terms manifest as convolutions, and several transform-based techniques have been developed to evaluate them efficiently [41, 42, 40]. Nevertheless, a significant numerical challenge arises from aliasing instabilities [43], which are caused by spectral leakage. When products between fields are computed, new wavenumber components are generated that may lie outside the range of the sampled Fourier modes. In discrete Fourier transforms, aliasing occurs when the number of sampled Fourier modes N_k is insufficient to represent the system adequately. Due to the periodic nature of the

discrete Fourier transform, wavenumbers exceeding the sampled range are aliased back into the domain, effectively folding high-frequency components onto lower frequencies. In time-evolving systems, this aliasing can introduce numerical instabilities, significantly compromising the accuracy and stability of the simulations. The elimination of aliasing errors, or dealiasing, has been a crucial area of study since the seminal work by Orszag [44], and continues to be a key consideration in the application of pseudo-spectral methods.

To illustrate this, consider the simplest form of nonlinearity, namely the product of two functions $f(x)$ and $g(x)$, each represented by their truncated Fourier series with N modes [45]:

$$f_N(x) = \sum_{p=-m}^{m} \tilde{f}_p e^{ipx}, \quad g_N(x) = \sum_{q=-m}^{m} \tilde{g}_q e^{iqx}, \tag{1.89}$$

where $\tilde{f}_p$ and $\tilde{g}_q$ are the corresponding Fourier coefficients. On a periodic domain, it is easy to show that the above series are simply truncated at $m = N/2$. The product of two functions in physical space, defined on a finite, periodic grid (where $m = N/2$), becomes a convolution product in Fourier space:

$$f(x) * g(x) = \left(\sum_{p=-m}^{m} \tilde{f}_p e^{ipx} \right) \left(\sum_{q=-m}^{m} \tilde{g}_q e^{iqx} \right) = \sum_{p=-m}^{m} \sum_{q=-m}^{m} \tilde{f}_p \, \tilde{g}_q \, e^{i(p+q)x}. \tag{1.90}$$

The product contains high-order harmonics beyond the truncated Fourier series of the individual functions, leading to aliasing. The Fourier transform of this product is given by:

$$\tilde{Q}_k = \int f(x) g(x) e^{-ikx} \, dx \approx \sum_{p+q=k} \tilde{f}_p \, \tilde{g}_q, \tag{1.91}$$

where we define a single sum over selected couplings, $\sum_{p+q=k}\{...\} \equiv \sum_p \sum_q \{...\} \delta_{p+q,k}$. This aliasing error can lead to numerical instabilities. To prevent this, we define a cutoff k^* such that all coefficients p, q corresponding to $k\,(= p + q), > k^*$ are set to zero. For quadratic nonlinearity, it has been shown that filtering out modes with $k > k^* = 2N/3$ is sufficient to eliminate aliasing instability [41, 46].

We adopt the FFT to compute spatial derivatives, while filtering out high harmonics:

$$f_N(x) = \sum_{k=-N/2}^{N/2} \tilde{f}_k e^{ikx} \Phi_{k^*}(k), \tag{1.92}$$

where $\Phi_{k^*}(k)$ is the *filter function*, often defined as a *Heaviside step function*:

$$\Phi_{k^*}(k) = \begin{cases} 1, \text{ if } |k| \leq k^*, \\ 0, \text{ if } |k| > k^*. \end{cases} \tag{1.93}$$

Alternatively, for smoother filtering, we use a Gaussian function:

$$\Phi_k(k) = e^{-a\left(\frac{|k|}{k^*}\right)^a}, \tag{1.94}$$

where a is a free parameter that controls the smoothness of the filter around the cutoff k^*, often set to 20 in our simulations. In this way, when $|k| \ll k^*$, then $\Phi_{k^*}(k) \simeq 1$; when $|k| \lesssim k^*$, then $\Phi_{k^*}(k)$ approaches zero quickly but smoothly; when $|k| > k^*$,

then $\Phi_{k^*}(k) \simeq 0$ [39]. Throughout, we set $k^* = N/2.5$, where N is the number of grid points in each spatial direction.

1.4.3 The Running Stability Check

The CFL condition ensures convergence in time integration schemes [47]. Suppose we describe the motion of a wave traveling through a discrete spatial grid with speed v. The length interval Δx of the spatial grid and the time step Δt are not independent quantities. In order to achieve stable and accurate results, the CFL condition dictates that Δt must be proportional to Δx. In simple terms, the condition states that if a wave is propagating across a discrete spatial grid, the time step must be smaller than the time it takes for the wave to travel between adjacent grid points. This establishes a tight relationship between the time step and the spatial step (i.e., the grid point separation), where reducing one typically necessitates reducing the other. For a simple one-dimension propagating fluctuation with speed v, the CFL condition imposes:

$$\Delta t < C\frac{\Delta x}{v}, \tag{1.95}$$

where C is the Courant number, typically chosen as $1/2$. To ensure stability in solving the BSSN equations, we continuously calculate the time step for each variable using the *Running Stability Check*. For any variable U_{ij}, the time step is estimated as $\mathcal{T}(U_{ij}) \stackrel{d}{=} U_{ij}/\partial_t U_{ij}$. We then apply:

$$\Delta t < C \min\{\mathcal{T}_j\}, \tag{1.96}$$

where j runs over all BSSN variables. The time step Δt adjusts dynamically based on the smallest characteristic timescale.

1.4.4 The Implicit Hyperviscous Boundary method

To manage boundary conditions in pseudo-spectral codes, we employ the *Implicit Hyperviscous Boundary* (IHB) method [44]. The primary advantage of pseudo-spectral codes lies in their relative speed and high precision. At a given resolution, these methods generally surpass the accuracy achievable by finite difference or finite volume techniques [39]. However, when employing Fourier basis functions, a significant limitation of this method is the requirement for periodic boundary conditions, which may not be suitable for all scenarios in general relativity, particularly those involving the mergers of compact objects. The IHB algorithm mitigates this limitation by using dissipating boundaries, combined with implicit time integration. This method has been successfully tested in simulations involving gravitational waves and the dynamics of compact objects, where ripples and numerical artifacts have been effectively suppressed in regions near corners and boundaries. It is relatively easy to implement and efficient.

For each BSSN variable, we evolve an ideal field $f^{\{ideal\}}(\boldsymbol{x}, t)$ using the second-order Runge-Kutta method [48, 49], and a hyperviscous field $f^{\{H\}}(\boldsymbol{x}, t)$ subject to hyperviscous dissipation. The evolution equation for $f^{\{H\}}$ is:

$$\frac{\partial f^{\{H\}}(\boldsymbol{x}, t)}{\partial t} = N(\boldsymbol{x}, t) - \nu_4 \nabla^4 f^{\{H\}}(\boldsymbol{x}, t), \tag{1.97}$$

where $N(\boldsymbol{x}, t)$ stands for the BSSN evolution equations, and ν_4 is the hyperviscous coefficient. The use of the Crank-Nicolson method ensures stability for the hyperviscous fields. Using the Fourier transform, the Crank-Nicolson scheme for hyperviscous fields at a give time t^* becomes:

$$\tilde{f}_{\boldsymbol{k}}^{\{H\}}(t^* + \Delta t) = \left[\frac{1 - \frac{\nu_4 k^4}{2}\Delta t}{1 + \frac{\nu_4 k^4}{2}\Delta t}\right] \tilde{f}_{\boldsymbol{k}}^{\{H\}}(t^*) + \left[\frac{\Delta t}{1 + \frac{\nu_4 k^4}{2}\Delta t}\right] \tilde{N}_{\boldsymbol{k}}\left(t^* + \frac{\Delta t}{2}\right). \tag{1.98}$$

To handle the boundary conditions, we interpolate between the ideal and hyperviscous solutions near the boundaries. At the end of each time step, we apply the following matching condition:

$$f(\boldsymbol{x}, t) = \begin{cases} f^{\{ideal\}}(\boldsymbol{x}, t) & \text{if } |\boldsymbol{x} - \boldsymbol{x_0}| \leq \lambda, \\ f^{\{ideal\}}(\boldsymbol{x}, t)\left[2 - \frac{|\boldsymbol{x}-\boldsymbol{x_0}|}{\lambda}\right] + f^{\{H\}}(\boldsymbol{x}, t)\left[\frac{|\boldsymbol{x}-\boldsymbol{x_0}|}{\lambda} - 1\right] & \text{otherwise.} \end{cases} \tag{1.99}$$

Here, λ is typically chosen as $L_0/4$, where L_0 is the size of the computational domain. This technique preserves the ideal dynamics in the central region while dissipating unwanted boundary effects. This method stabilizes the solution while ensuring that the core dynamics of the computational domain remain unaffected [39].

1.5 Gravitational Wave Extraction and Analysis

We aim to analyze gravitational signals arising from multi-body interactions within the dynamical evolution of the Einstein field equations. Gravitational waves, which are perturbations of spacetime propagating at the speed of light, constitute one of the most profound predictions of general relativity. These waves emerge from the acceleration of massive objects and are inherently tied to regions with strong, dynamic gravitational fields. In the context of numerical relativity, the study and prediction of gravitational waves are of paramount importance, as they convey detailed information about their sources, including binary black hole mergers, neutron star collisions, and other astrophysical phenomena. Gravitational radiation not only carries energy and momentum away from isolated systems, but it also encodes information regarding the intrinsic properties of these systems, such as mass, spin, and orbital dynamics. Accurate predictions of gravitational waveforms are essential, as they provide templates for detectors like LIGO and Virgo, significantly enhancing the likelihood of detection and enabling precise source characterization. These efforts are at the heart of gravitational wave astronomy, offering unprecedented insights into some of the most energetic and enigmatic events in the Universe.

Gravitational wave information is extracted using the components of the Weyl curvature tensor in a null tetrad frame, as formulated in the *Newman–Penrose formalism* [50]. In an n-dimensional space, the Riemann tensor $R^{\alpha}_{\beta\mu\nu}$ can be decomposed into its trace—the Ricci tensor $R_{\mu\nu} = R^{\alpha}_{\mu\alpha\nu}$, given in Eq. (1.2)—and its traceless part, known as the Weyl tensor $C_{\alpha\beta\mu\nu}$. The latter, which encodes the free gravitational field and is central to the study of gravitational waves, is defined as:

$$\begin{aligned} C_{\alpha\beta\mu\nu} &= R_{\alpha\beta\mu\nu} - \frac{1}{n-2}\left(g_{\alpha\mu}R_{\nu\beta} - g_{\alpha\nu}R_{\mu\beta} - g_{\beta\mu}R_{\nu\alpha} + g_{\beta\nu}R_{\mu\alpha}\right) \\ &+ \frac{1}{(n-1)(n-2)}\left(g_{\alpha\mu}g_{\nu\beta} - g_{\alpha\nu}g_{\mu\beta}\right)R, \end{aligned} \tag{1.100}$$

The Weyl tensor shares the symmetries of the Riemann tensor and is traceless:

$$C^{\alpha}_{\mu\alpha\nu} = 0. \tag{1.101}$$

In n dimensions, the Weyl tensor has $\frac{n(n+1)(n+2)(n-3)}{12}$ independent components (e.g., 10 components in a 4-dimensional spacetime) and vanishes identically for $n \leq 3$. Importantly, the Weyl tensor remains invariant under conformal transformations:

$$\tilde{C}^{\alpha}_{\beta\mu\nu} = C^{\alpha}_{\beta\mu\nu}, \tag{1.102}$$

which is why it is often referred to as the *conformal curvature tensor*.

The basic concept behind the Newman-Penrose formalism is to introduce a null tetrad of vectors, starting from an orthonormal tetrad $\{\boldsymbol{e}_{(a)}\}$, which satisfies:

$$g_{\mu\nu} = -e_{(0)\mu}e_{(0)\nu} + e_{(1)\mu}e_{(1)\nu} + e_{(2)\mu}e_{(2)\nu} + e_{(3)\mu}e_{(3)\nu}. \tag{1.103}$$

Following the conventional approach in numerical relativity, we construct the tetrad from the time-like unit normal vector, $e^{\mu}_{t} = n^{\mu} = \left(1/\alpha, -\beta^{i}/\alpha\right)$, as well as applying the Gram-Schmidt orthonormalization procedure to the three-dimensional vectors:

$$\begin{aligned} e^{\mu}_{r} &= (0, u^{i}) = (0, x, y, z)\,, && (1.104)\\ e^{\mu}_{\varphi} &= (0, v^{i}) = (0, -y, x, 0)\,, && (1.105)\\ e^{\mu}_{\theta} &= (0, w^{i}) = \epsilon^{i}_{jk}v^{j}u^{k} = \left(0, xz, yz, -x^{2} - y^{2}\right), && (1.106) \end{aligned}$$

where x, y, z are the Cartesian coordinates of the computational grid. Using this orthonormal basis $\{e^{\mu}_{t}, e^{\mu}_{r}, e^{\mu}_{\varphi}, e^{\mu}_{\theta}\}$, two null vectors can be constructed as follows:

$$\begin{aligned} l^{\mu} &= \frac{1}{\sqrt{2}}\left(e^{\mu}_{t} + e^{\mu}_{r}\right) = \frac{1}{\sqrt{2}}\left(\frac{1}{\alpha}, -\frac{\beta^{i}}{\alpha} + u^{i}\right), && (1.107)\\ k^{\mu} &= \frac{1}{\sqrt{2}}\left(e^{\mu}_{t} - e^{\mu}_{r}\right) = \frac{1}{\sqrt{2}}\left(\frac{1}{\alpha}, -\frac{\beta^{i}}{\alpha} - u^{i}\right), && (1.108) \end{aligned}$$

where l^{μ} is outgoing and k^{μ} is ingoing. The other two null vectors m^{μ} and $\bar{m}^{\mu}$ are defined as complex combinations of angular unit vectors:

$$\begin{aligned} m^{\mu} &= \frac{1}{\sqrt{2}}(e^{\mu}_{\theta} + ie^{\mu}_{\varphi}) = \frac{1}{\sqrt{2}}\left(0, w^{i} + iv^{i}\right), && (1.109)\\ \bar{m}^{\mu} &= \frac{1}{\sqrt{2}}(e^{\mu}_{\theta} - ie^{\mu}_{\varphi}) = \frac{1}{\sqrt{2}}\left(0, w^{i} - iv^{i}\right). && (1.110) \end{aligned}$$

This set of four null vectors forms the *null tetrad*, satisfying the following orthonormalization conditions:

$$\begin{aligned} l_{\mu}l^{\mu} &= k_{\mu}k^{\mu} = m_{\mu}m^{\mu} = \bar{m}_{\mu}\bar{m}^{\mu} = 0,\\ l_{\mu}k^{\mu} &= -1, \quad m_{\mu}\bar{m}^{\mu} = 1. && (1.111) \end{aligned}$$

These properties are crucial in general relativity for describing the paths of light rays and the structure of spacetime in regions of strong gravitational fields. The use of null vectors within a tetrad provides a more natural framework for describing the propagation of light and gravitational waves in curved spacetime. With this null

tetrad, the spacetime metric is expressed as:

$$g_{\mu\nu} = -l_\mu k_\nu - k_\mu l_\nu + m_\mu \bar{m}_\nu + \bar{m}_\mu m_\nu. \tag{1.112}$$

In the Newman-Penrose formalism, the components of the Weyl tensor are represented by five complex scalar quantities, known as the *Weyl scalars*, defined as:

$$\begin{aligned}
\Psi_0 &= C_{\alpha\beta\mu\nu} l^\alpha m^\beta l^\mu m^\nu, && (1.113)\\
\Psi_1 &= C_{\alpha\beta\mu\nu} l^\alpha k^\beta l^\mu m^\nu, && (1.114)\\
\Psi_2 &= C_{\alpha\beta\mu\nu} l^\alpha m^\beta \bar{m}^\mu k^\nu, && (1.115)\\
\Psi_3 &= C_{\alpha\beta\mu\nu} l^\alpha k^\beta \bar{m}^\mu k^\nu, && (1.116)\\
\Psi_4 &= C_{\alpha\beta\mu\nu} k^\alpha \bar{m}^\beta k^\mu \bar{m}^\nu. && (1.117)
\end{aligned}$$

As is the case for all Newman-Penrose quantities, the Ψ_a are scalars with respect to coordinate transformations, but their values depend on the choice of the null tetrad. These five complex scalars are sufficient to fully characterize all 10 independent components of the Weyl tensor. The symmetries of the Weyl tensor imply that any other contractions of $C_{\alpha\beta\mu\nu}$ with tetrad vectors either vanish or can be expressed as combinations of the Ψ_a. It is possible to identify a class of tetrads, called *transverse frames* [51, 52], where the "odd" scalars Ψ_1 and Ψ_3 vanish. A further subset of these, known as *quasi-Kinnersley frames* [53], allows for an interpretation where Ψ_0 and Ψ_4 represent ingoing and outgoing gravitational radiation, respectively, while Ψ_2 corresponds to the longitudinal, or "Coulombic," part of the gravitational field, associated with the mass and angular momentum of the spacetime.

Of the five scalars defined above, Ψ_4 is of particular importance because it encodes the outgoing gravitational radiation in an asymptotically flat system. It can be interpreted as the relativistic analogue of the Poynting vector, representing the energy flux of the gravitational waves. In the asymptotic limit, Ψ_4 is directly related to the metric perturbation in the TT gauge:

$$\Psi_4 = \partial_t^2 (h_+ - i h_\times), \tag{1.118}$$

where h_+ and $h_\times$ represent the two independent polarization modes of the gravitational wave.

The calculation of Ψ_4 from the ADM variables can be carried out by reconstructing the spacetime metric from the spatial metric, lapse, and shift vector. Alternatively, one can use the electric E_{ij} and magnetic B_{ij} components of the Weyl tensor, defined as:

$$\begin{aligned}
E_{ij} &= R_{ij} + \gamma^{mn}(K_{ij}K_{mn} - K_{im}K_{jn}), && (1.119)\\
B_{ij} &= \gamma_{ik}\epsilon^{kmn} D_m K_{nj}, && (1.120)
\end{aligned}$$

where, for the Levi-Civita symbol, we have $\epsilon^{kmn} = \epsilon_{kmn}$. The final expression for Ψ_4 is given by [6]:

$$\Psi_4 = Q_{ij}\bar{m}^i\bar{m}^j = (E_{ij} - iB_{ij})\bar{m}^i\bar{m}^j. \tag{1.121}$$

or equivalently [54, 55, 56, 57]:

$$\begin{aligned}
\Psi_4 = \frac{1}{2}\left[E_{ij}(w^i w^j - v^i v^j) - B_{ij}(w^i v^j + v^i w^j)\right] \\
- \frac{i}{2}\left[E_{ij}(w^i v^j + v^i w^j) + B_{ij}(w^i w^j - v^i v^j)\right].
\end{aligned} \tag{1.122}$$

It is convenient to project Ψ_4 onto the sphere and describe its angular dependence in terms of the *spin-weighted spherical harmonics* ${}^{(-2)}Y_{lm}(\theta,\varphi)$ [58]. These harmonics are a generalization of the standard spherical harmonics that account for the spin weight of the fields, which for gravitational waves is $s=-2$. The reason for this specific spin weight is rooted in the nature of gravitational waves, which are perturbations in spacetime described by a spin-2 field. Spin-weighted spherical harmonics are used to correctly represent the angular dependence of such fields. They include the effects of spin by applying differential operators to the standard spherical harmonics, thereby adapting them to describe fields that transform non-trivially under rotations. By projecting Ψ_4 onto these harmonics, we can decompose the waveform into contributions from individual modes characterized by l and m. This method allows for a clearer analysis of the angular structure and polarization states of the gravitational wave signal [59]. To better understand the role of these harmonics, consider the Laplace operator in spherical coordinates, expressed as:

$$\nabla^2 f = \frac{1}{r^2}\partial_r^2(r^2 f) + \frac{1}{r^2}\hat{L}^2 f, \tag{1.123}$$

where $\hat{L}^2$ is the angular operator:

$$\hat{L}^2 f = \frac{1}{\sin\theta}\partial_\theta(\sin\theta\partial_\theta f) + \frac{1}{\sin^2\theta}\partial_\varphi^2 f. \tag{1.124}$$

By separating variables, we can show that f solves the Laplace equation $\nabla^2 f = 0$ if it can be written as:

$$f(r,\theta,\varphi) = r^l g_1(\theta,\varphi) + \frac{1}{r^{l+1}} g_2(\theta,\varphi), \tag{1.125}$$

where $g_{1,2}(\theta,\varphi)$ are eigenfunctions of the angular operator $\hat{L}^2$, such that:

$$\hat{L}^2 g = -l(l+1)g. \tag{1.126}$$

The solutions to this equation are the spherical harmonics $Y_{lm}(\theta,\varphi)$, which are expressed as:

$$Y_{lm}(\theta,\varphi) = \left[\frac{(2l+1)}{4\pi}\frac{(l-m)!}{(l+m)!}\right]^{1/2} P_{lm}(\cos\theta)e^{im\varphi}, \tag{1.127}$$

where $P_{lm}(\cos\theta)$ are the associated Legendre polynomials, and the orthonormality condition of these harmonics reads:

$$\int d\Omega\, \bar{Y}_{lm}(\theta,\varphi)Y_{l'm'}(\theta,\varphi) = \delta_{ll'}\delta_{mm'}. \tag{1.128}$$

When dealing with spin-weighted functions like Ψ_4, which has spin weight $s=-2$, the standard spherical harmonics must be generalized. The *spin-weighted spherical harmonics* ${}^{(s)}Y_{lm}(\theta,\varphi)$ are constructed by acting with differential operators on the ordinary spherical harmonics and are explicitly given by:

$${}^{(s)}Y_{lm}(\theta,\varphi) = (-1)^s\sqrt{\frac{2l+1}{4\pi}}d^l_{m(-s)}(\theta)e^{im\varphi}, \tag{1.129}$$

where $d^l_{m(-s)}(\theta)$ are the real Wigner d-functions. These harmonics satisfy a similar orthonormality relation:

$$\int d\Omega\, \bar{Y}^{(s)}_{lm}(\theta,\varphi) Y^{(s)}_{l'm'}(\theta,\varphi) \quad = \quad \delta_{ll'}\delta_{mm'}. \tag{1.130}$$

The projection of Ψ_4 onto these spin-weighted spherical harmonics is given by the scalar product:

$$A_{lm} = \int_0^{2\pi}\int_0^{\pi} \Psi_4 \bar{Y}^{(-2)}_{lm} \sin\theta\, d\theta\, d\varphi, \tag{1.131}$$

which, in practice, is evaluated at a finite extraction radius r_{ext}. The spin-weighted spherical harmonics $Y^{(-2)}_{lm}$ can be defined in terms of the Wigner d-functions (e.g., [58]) as:

$$Y^{(s)}_{lm}(\theta,\varphi) = (-1)^s \sqrt{\frac{2l+1}{4\pi}}\, d^l_{m(-s)}(\theta) e^{im\varphi}, \tag{1.132}$$

where the Wigner d-functions are given by:

$$\begin{aligned} d^l_{ms}(\theta) = \sum_{t=C_1}^{C_2} & \frac{(-1)^t \sqrt{(l+m)!(l-m)!(l+s)!(l-s)!}}{(l+m-t)!(l-s-t)!t!(t+s-m)!} \\ & \times (\cos\theta/2)^{2l+m-s-2t} (\sin\theta/2)^{2t+s-m} \end{aligned} \tag{1.133}$$

with $C_1 = \max(0, m-s)$ and $C_2 = \min(l+m, l-s)$.

In practice, more than 98% of the energy is radiated in the dominant $l = 2$, $m = \pm 2$ modes [58]. This dominance arises because gravitational waves are primarily emitted due to changes in the quadrupole moment of the source, corresponding to the $l = 2$ mode. The $m = \pm 2$ values represent the most symmetric and energetically favorable configurations, commonly observed in binary systems during inspiral and merger phases. These modes effectively capture the dominant contributions to gravitational radiation, reflecting the inherent symmetries of the source. Consequently, the final waveform is obtained by projecting Ψ_4 onto the spin-weighted spherical harmonic $Y^{(-2)}_{22}(\theta,\varphi)$:

$$A_{22} = \langle Y^{(-2)}_{22}, \Psi_4 \rangle = \int_0^{2\pi}\int_0^{\pi} \Psi_4 \bar{Y}^{(-2)}_{22} \sin\theta\, d\theta\, d\varphi. \tag{1.134}$$

This decomposition enables the gravitational wave signal to be broken down into modes, with the quadrupole mode ($l = 2$, $m = 2$) typically being the most significant. Higher-order modes may also be present, especially in systems with asymmetries or high spins.

The projection of Ψ_4 onto spin-weighted spherical harmonics reveals the detailed structure of the gravitational wave signal. In the context of binary black hole mergers, the waveform typically consists of three distinct phases: inspiral, merger, and ringdown. During the inspiral phase, as the black holes spiral closer together, the gravitational wave amplitude and frequency increase, reflecting the emission of energy and angular momentum. The merger phase is characterized by a sharp peak in the waveform, representing the moment when the two black holes coalesce. Following the merger, the ringdown phase begins, where the final black hole emits a series of decaying quasi-normal modes as it settles into a stable Kerr solution.

The spherical harmonic projection of Ψ_4 also provides valuable information about the recoil velocity, or "kick," imparted to the final black hole. This kick results from

the asymmetric emission of gravitational waves during the merger, which imparts momentum to the remnant black hole. Accurate predictions of the kick velocity are critical for understanding the dynamics of black hole mergers, particularly whether the resultant black hole remains within its host galaxy or is ejected.

Projecting Ψ_4 onto spherical harmonics not only aids in decomposing the waveform components but also offers valuable insights into the angular distribution of the emitted gravitational radiation. This approach is particularly crucial for analyzing the dynamics of the system, such as determining the spin and mass of the remnant black hole, as well as identifying any higher-order modes present in the signal. To this end, we implemented a module within the `SFINGE` code for gravitational wave extraction, as detailed in Imbrogno, Meringolo, and Servidio [60].

In summary, the Newman-Penrose formalism, when combined with the projection of Ψ_4 onto spin-weighted spherical harmonics, provides a robust framework for extracting and analyzing gravitational wave signals from numerical simulations. This methodology not only enhances the study of black hole mergers but also aids in comparing theoretical predictions with observational data, thereby deepening our understanding of gravitational wave physics and astrophysical processes.

1.6 Direct Numerical Simulations of Binary Black Holes in Vacuum

In this Section, we focus on the problem of two black holes, specifically a black-hole binary. Our goal is to accurately reproduce the gravitational waveforms generated by such a binary system, comparing the waves detected by the interferometers *LIGO* and *Virgo* [61, 62] with those extrapolated from numerical simulations. The objective is to validate our simulation by matching it with the experimental data, thereby establishing a robust foundation for extending the code to simulate more complex systems, such as three-body mergers of compact objects. By doing so, we aim to develop a predictive tool that could eventually be confirmed by future astronomical observations. For the evolution of black-hole binaries, we follow the approach outlined by *Campanelli et al.* [21], who employed the *Finite Difference Method* to simulate the final waveform. In contrast, our algorithm leverages the high accuracy offered by spectral methods, which are particularly well-suited for capturing the subtle features of gravitational waveforms in such dynamic systems.

The simulation we conducted describes the evolution of two black holes of equal mass, with zero total angular momentum and zero intrinsic spin, resulting in a system constrained to evolve within the two-dimensional xy-plane. Initially, the black holes are symmetrically positioned along the x-axis, with equal but opposite velocities along the y-axis. Specifically, they are moving along the Innermost Stable Circular Orbit (ISCO), which occurs immediately before the merger and ring-down phases. To generate the initial data for the black holes, we apply the method outlined in Sec. 1.3. In particular, we employ the approach developed by *Brandt and Brügmann* [27], allowing for a small violation of the condition that the black holes are initially placed at a sufficiently large separation. In this context, we verified that the iterative scheme converges and that the initial constraint violations are minimal, with values on the order of 10^{-8}. The computational grid used for the simulation is a cube with 512 points in each direction, covering a physical space of 50 M along each axis, where M denotes the total mass of the system. The initial time step is set to $\Delta t = 8 \times 10^{-3}$, but this value is dynamically adjusted to ensure compliance with the *CFL conditions* for the evolving variables (see Sec. 1.4.3). This adaptive time-stepping

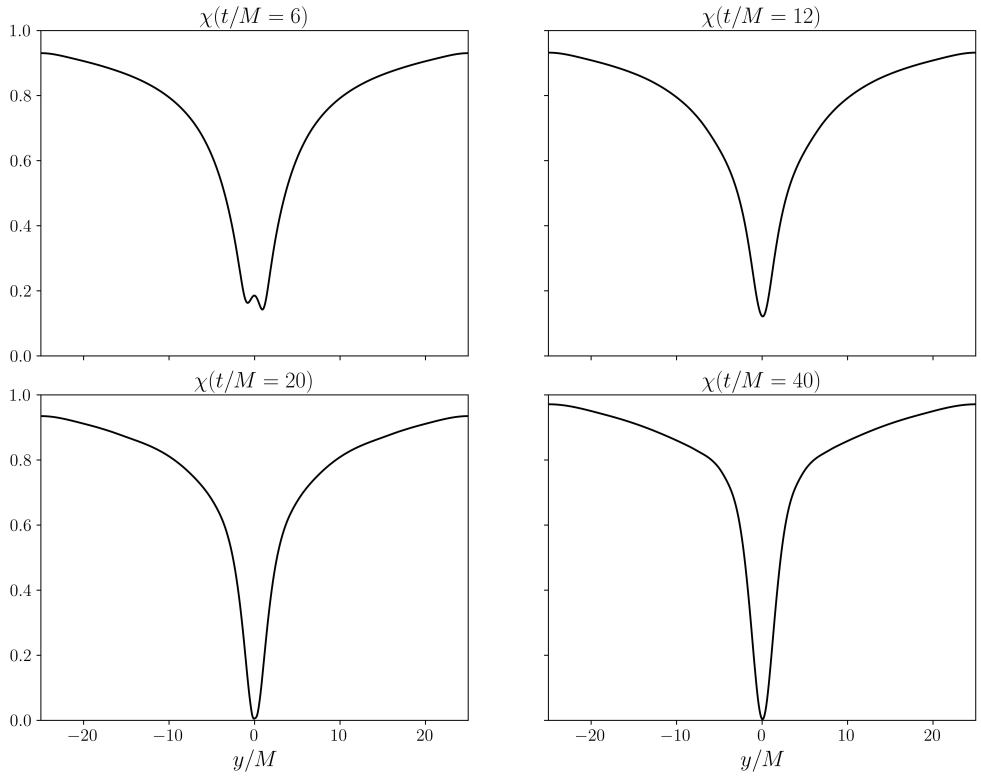

FIGURE 1.4: One-dimensional cuts of the conformal factor $\chi = \psi^{-4}$ along the y-direction at various time instants during the evolution of the binary black hole system.

is essential for maintaining both numerical stability and accuracy throughout the simulation. Furthermore, we rigorously enforce the Hamiltonian and momentum constraints not only at the initial time but continuously throughout the evolution, ensuring that the simulated dynamics remain physically realistic (see Appendix A). For the system's evolution, we employ the "1 + log *lapse*" and "*Gamma-driver shift*" gauge conditions, which are standard choices in numerical relativity for maintaining the stability and accuracy of the evolution. These gauge conditions are particularly effective in controlling the coordinate movement of the black holes, preventing coordinate singularities. To minimize the impact of boundary effects, which could otherwise introduce spurious reflections or distortions in the simulation, we apply the *IHB* methods as detailed in Sec. 1.4.4. This technique allows us to smoothly dampen outgoing waves at the grid boundaries, thus preserving the integrity of the gravitational wave signals generated during the simulation.

We now turn to the results of the simulation. The conformal factor χ, depicted in Fig. 1.4 (one-dimensional representation) and Fig. 1.5 (two-dimensional representation), plays a key role in general relativity, analogous to the gravitational potential ϕ in classical physics. Both χ and ϕ describe how mass warps the surrounding space. In Newtonian mechanics, ϕ governs gravitational effects, determining the acceleration of a freely falling object via $\boldsymbol{a} = -\boldsymbol{\nabla}\phi$, and is related to the mass density through $\nabla^2\phi = 4\pi\rho$. In general relativity, the information about spacetime curvature is encoded in the metric tensor $g_{\mu\nu}$. The conformal factor χ, associated with the determinant of the spatial metric γ, thus plays the role of the gravitational potential, describing how the geometry of space evolves under the influence of mass and energy. As such, the evolution of χ reveals the dynamics of spacetime curvature as the

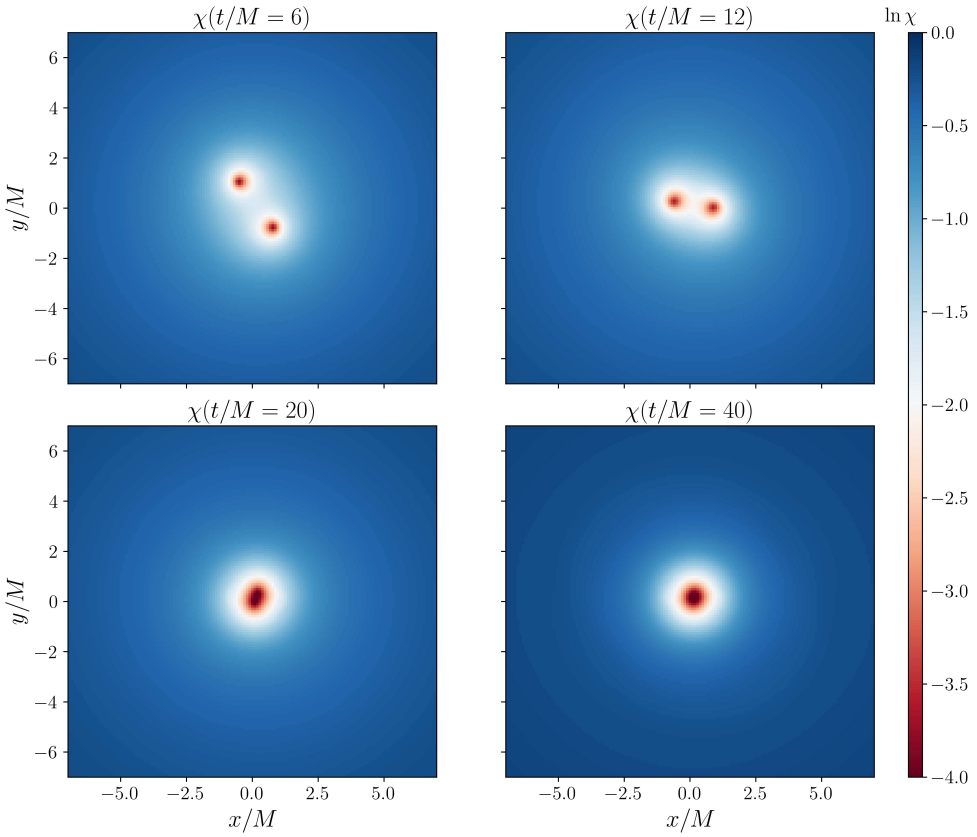

FIGURE 1.5: Two-dimensional surfaces showing the evolution of the conformal factor $\chi = \psi^{-4}$ in the xy-plane at various time steps during the binary system's evolution. The colors, displayed on a logarithmic scale for improved comprehension, represent the potential: cool colors indicate weaker potential values, while warm colors indicate regions where the potential is stronger.

black holes draw closer and eventually merge.

As illustrated in Fig. 1.4, the initial phase of the evolution reveals two distinct minima in χ, corresponding to the exact locations of the two black holes. These minima gradually merge as the black holes coalesce, eventually forming a single black hole with spin, characteristic of a Kerr black hole. In non-vacuum environments, Kerr black holes are notable for their ergoregion, where the dragging of spacetime caused by the rotating mass creates gravitational vortices, influencing the motion of nearby matter. Over time, as the system stabilizes after the merger, the gravitational potential smoothly approaches unity, indicating the relaxation of the system and the formation of a stable, stationary black hole. This behavior shows that the system has settled into a final state that closely resembles a Kerr black hole. It is important to note that in the early stages of evolution, the potential does not reach unity at the boundaries of the computational domain, as it ideally should only approach this value at infinity. This discrepancy arises due to the finite size of the simulation box, which is a necessary constraint in numerical simulations. However, these boundary effects are confined to the hyperviscous region and do not influence the genuine dynamics occurring in the central region of the system.

Fig. 1.5 provides a comprehensive view of the black holes' positions over time through the bidimensional map of the conformal factor χ. Light colors represent regions of spacetime near the singularity, while dark colors indicate areas farther away, where the metric can be approximated as flat. Initially, the two black holes are

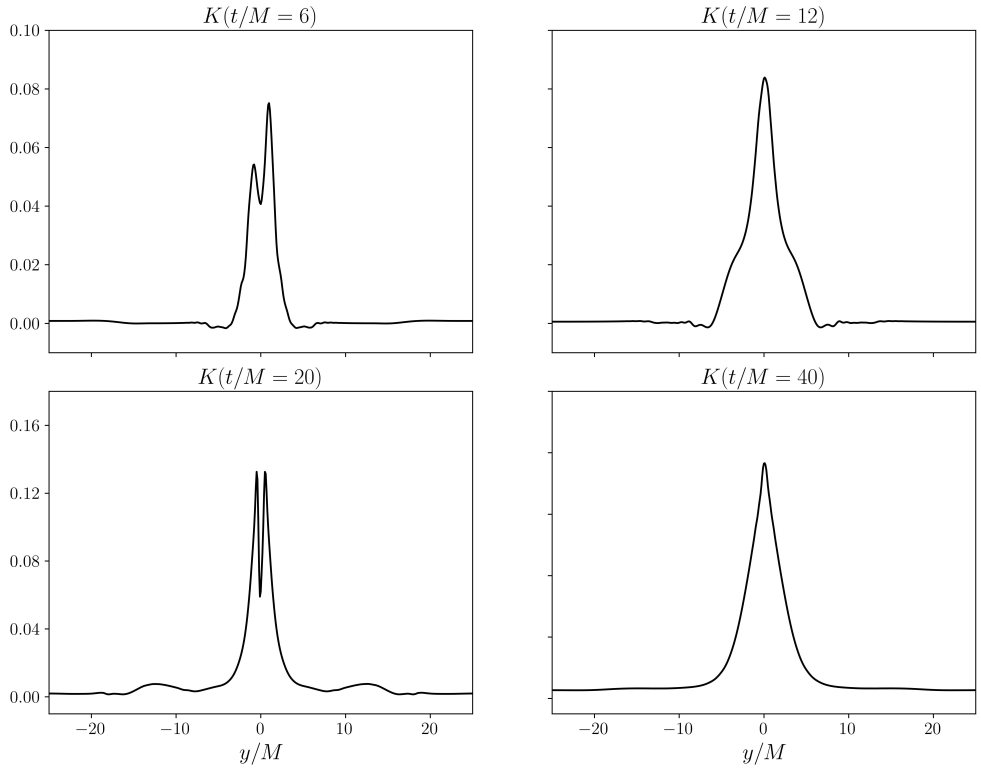

FIGURE 1.6: One-dimensional cuts of the trace of the extrinsic curvature K along the y-direction at different time instants during the binary system's evolution.

distinct and separate, but they gradually approach each other while orbiting until they merge, forming a single, stationary black hole.

One way to identify the emergence of gravitational waves from merging black holes is to analyze the trace of the extrinsic curvature tensor K at various time instants, as shown in Fig. 1.6 for a one-dimensional view. The extrinsic curvature K_{ij} represents the relativistic analogue of classical conjugate momenta, offering insights into the dynamics of spacetime as black holes evolve and merge.

In Fig. 1.6, the increasing orbital frequency of the black holes as they approach each other leads to a corresponding rise in the scalar extrinsic curvature K in their vicinity, indicating the intense gravitational interactions that shape the surrounding spacetime. This behavior may suggest the system's progression towards a final Kerr black hole. However, to confirm this, it would be necessary to analyze the evolution of the shift vector $\boldsymbol{\beta}$ over time, since in the Schwarzschild metric, the mixed terms involving the shift vector are expected to vanish. It is worth noting that the black holes were initially given a boost, causing them to rotate around each other and immediately acquire intrinsic momentum. In contrast, a Schwarzschild-type black hole, which is the simplest form, exhibits spherical symmetry and remains at rest, with a metric depending solely on the radial coordinate. As time progresses, the second panel illustrates the propagation of waves in both directions, coinciding with the merger of the event horizons. Subsequently, smaller waves are emitted until the system "relaxes" into a single black hole with intrinsic momentum, as indicated by the persistent non-zero extrinsic curvature near the object for extended periods. The detailed investigation of this specific feature lies beyond the scope of this work, so we did not pursue this point further.

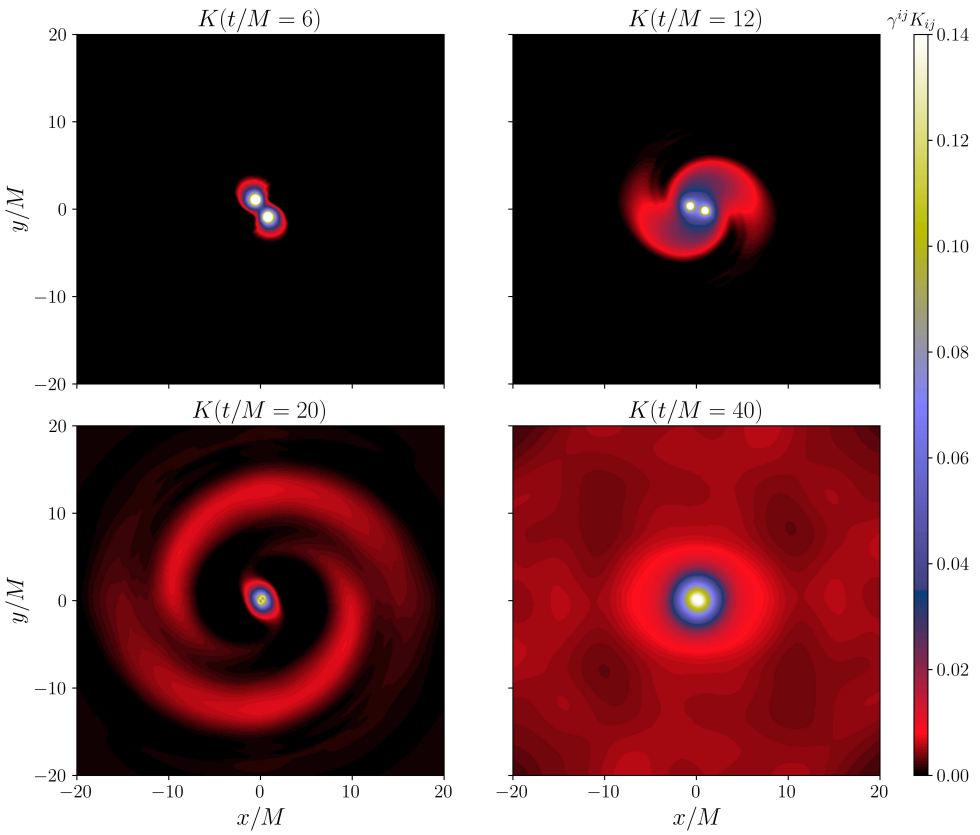

FIGURE 1.7: Two-dimensional surfaces illustrating the evolution of the extrinsic curvature $K = \gamma^{ij}K_{ij}$ in the xy-plane at various time steps during the binary system's evolution. The colors represent K values: white denotes zero extrinsic curvature, while yellow, blue, and red indicate non-zero values.

A detailed examination of gravitational wave propagation can be achieved through the analysis of two-dimensional surfaces that illustrate the scalar values of the extrinsic curvature at each point. As depicted in Fig. 1.7, small-amplitude waves are observed to propagate even before the black holes merge, as their substantial masses in motion perturb the surrounding spacetime. Following the contact of the event horizons, larger waves are emitted, and the system eventually "relaxes," leading to the formation of a single Kerr black hole. The blue region in the final panel signifies the ergoregion, where spacetime is dragged due to the rotation of the resultant black hole.

Subsequently, the waveform generated by the binary system can be analyzed by projecting the Newman-Penrose scalar Ψ_4, which quantifies the outgoing radiation from the gravitational wave source, as outlined in Sec. 1.5. This scalar, interpreted as the relativistic analogue of the *Poynting vector* (which represents the energy flux emanating from a surface enclosing a given volume), is projected onto the spin-weighted spherical harmonic ${}^{(-2)}Y_{22}(\theta, \varphi)$, as shown in Fig. 1.8, where we display both its real and imaginary components.

The x-axis of the waveform represents the temporal coordinate during signal acquisition. It is worth noting that, in geometric units, both distances and time are expressed in terms of mass. This system of units simplifies numerical relativity calculations, as the mass of the system becomes the fundamental scale, eliminating the need to differentiate between spatial and temporal units. Observing the waveform,

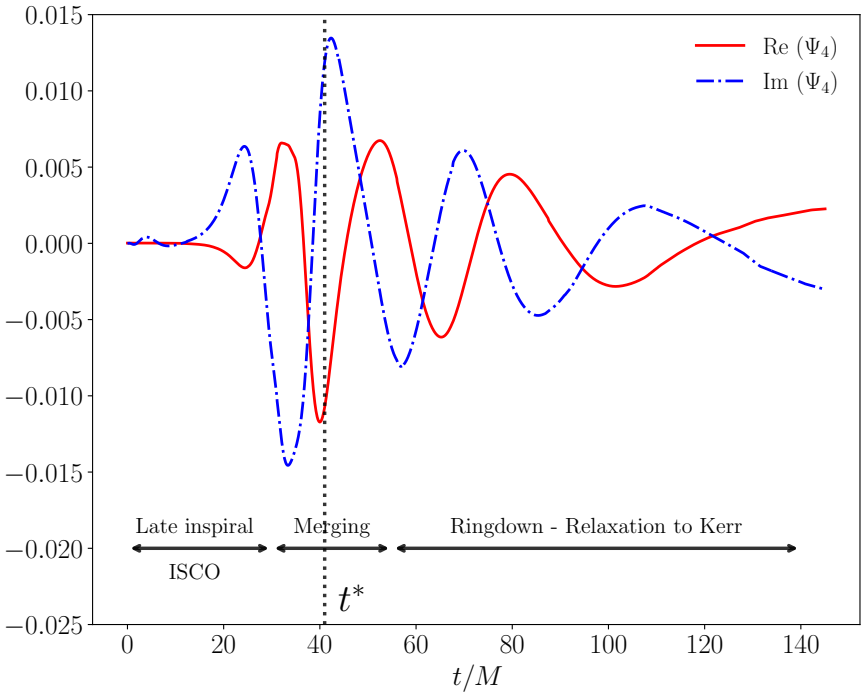

FIGURE 1.8: Waveform from the binary black hole system. The graph depicts the real and imaginary components of the Newman-Penrose scalar Ψ_4, projected onto the spin-weighted spherical harmonic $Y_{22}^{(-2)}(\theta, \varphi)$ and multiplied by the radial coordinate r. The x-axis represents both the time and radial coordinates normalized to the system's total mass, as the wave propagates at the speed of light c. The y-axis shows the amplitude $A_{22} = \langle Y_{22}^{(-2)}, \Psi_4 \rangle$. The specific time t^* corresponds to the moment of the binary merger, while the double arrows indicate the three distinct stages of the binary dynamics: late inspiral, merger, and ringdown.

one can see that the peaks of the real and imaginary components are offset by $\pi/2$. This phase difference suggests a close relationship between these components and the two independent polarization states, h_+ and $h_\times$, in the Transverse-Traceless (TT) gauge.

In the context of weak gravitational fields, gravitational waves are treated as small perturbations to the flat spacetime described by the Minkowski metric. In this approximation, the metric tensor can be expressed as $g_{\mu\nu} = \eta_{\mu\nu} + h_{\mu\nu}$, where $h_{\mu\nu}$ represents the small perturbation. The TT gauge is characterized by the conditions $\partial_\mu h^\mu_\nu = 0$, $h_{0\mu} = 0$, and $h = h^\mu_\mu = 0$. These conditions yield the wave equation $\Box h_{\mu\nu} = 0$, indicating that gravitational waves propagate at the speed of light. The two polarization states, h_+ and $h_\times$, describe how spacetime is stretched and compressed in perpendicular directions by the passing wave. This approximation holds true when observed from large distances, as in our simulations. Consequently, the numerical results align well with experimental data. As time progresses, the peaks of the real and imaginary components of the waveform converge, reflecting the decreasing orbital period and increasing frequency of the black holes as they merge. Even after the event horizons have merged, the black holes continue to rotate until their singularities fully merge, as depicted in Fig. 1.5. It is precisely this phenomenon that is responsible for the formation of a Kerr-type black hole.

The waveform is multiplied by the radial coordinate r to account for the fact that the wave's amplitude decreases with distance. By doing so, we preserve the

waveform's shape, allowing for consistent comparison of various harmonics at large distances.

1.7 Direct Numerical Simulations of Three Black Holes in Vacuum

The gravitational three-body problem represented the non-linear problem *par excellence* [63]. This problem has applications spanning from microphysical phenomena to large-scale astrophysical systems. Despite extensive study, the problem remains enigmatic due to the chaotic behavior exhibited by the bodies involved (see [64] for a review). In classical celestial mechanics, for instance, the three-body problem typically involves a binary system interacting with a third body. The binary system can be treated as a single entity with specific internal properties, analogous to a molecule. This coupled system interacts with the third body, either in isolated encounters or repeatedly, resulting in changes to the binary's internal properties. Throughout these interactions, the system conserves total energy, mass, momentum, and angular momentum, despite the unpredictable nature of the individual trajectories [65, 63]. During such complex dynamics, the system effectively redistributes energy and angular momentum, leading to an increase in the overall kinetic energy—a process often referred to as 'heating' the system. This has significant implications for the structure and evolution of stellar clusters. Consequently, three-body or many-body interactions are expected to be prevalent in clusters and galactic cores [66]. Multiple black holes may also form in galactic nuclei experiencing sequential mergers [67, 64], as well as in triple quasar systems [68], globular clusters, and galactic disks [69, 70, 71].

At some point during the interaction, it is highly probable that the three bodies become strongly influenced by their mutual gravitational attraction. In this regime, especially when the masses are large, the complex dynamics of the three-body system must be addressed using general relativistic models. Moreover, when distances approach the scale of gravitational radii, merging events are likely to occur [72, 73]. In globular clusters, for instance, N-body interactions play a crucial role in the formation of massive black holes [69, 74, 75]. In such systems, the conservation laws of classical mechanics require revision in the context of general relativity [76, 77]. It is noteworthy that the dynamics exhibit chaotic behavior only for specific combinations of mass and orbital parameters, while triple systems are relatively frequently organized as hierarchical systems.

The mergers of compact massive objects represent some of the most remarkable and extraordinary events in nature. According to general relativity, these systems are powerful sources of gravitational waves. However, gravitational radiation detected by modern experimental facilities cannot unambiguously characterize the processes occurring near the merging region, necessitating complementary studies in numerical relativity [78, 79, 80, 81, 82]. Therefore, it is crucial to guide future observational campaigns by exploring a wide range of three-body configurations, varying parameters such as initial distributions, total angular momentum, spin, and masses. Understanding these extreme, nonlinear interactions poses a significant challenge for cosmological studies and needs to be tackled using appropriate models, in line with Einstein's theory of gravitation [83, 84].

Hereafter, we explore the intrinsic dynamics of the three-body problem, as reported in Imbrogno, Meringolo, and Servidio [60], starting with a classical mechanics framework and progressively extending the analysis to incorporate the principles of general relativity. Initially, we examine the motion of three point-like bodies governed by Newton's classical laws. Utilizing a Lagrangian numerical model, we adopt a geometric configuration known as the *Burrau problem* [77]. Following this, we investigate variations in global momentum and mass distribution to establish a framework for understanding analogous dynamics in systems involving highly massive objects. In the second part of our research, we perform direct numerical simulations within the context of general relativity, employing initial conditions derived from the preceding Newtonian analysis. Finally, we analyze the waveform of gravitational radiation emitted by the system, comparing it with that of a binary inspiral. These investigations may contribute to a deeper understanding of gravitational signals and have potential applications in the detection and interpretation of such signals [85, 86, 87].

1.7.1 Three-bodies problem in the Newtonian case

Despite the significant progress in understanding simplified (reduced) cases [63, 88], the solution to the general three-body problem remained elusive for nearly 200 years following the publication of Newton's *Principia*. In the general three-body problem, all three masses are comparable, and their initial positions and velocities are not arranged in any particular manner. The complexity of the problem arises from the absence of coordinate transformations that could simplify the system. This is in contrast with the two-body problem, where solutions are most easily found in the center-of-mass coordinate system. In the three-body case, such transformations do not alleviate the problem, leaving the system analytically intractable until the advent of modern computational methods. Numerical simulations, in fact, have demonstrated that the resulting orbits are prime examples of chaotic behavior in nature [89, 90, 91].

Various numerical methods can be applied to solve the three-body problem, although our focus was not on classical integration. The problem has been approached using several methods [92], including arbitrary precision regularization [93]. The literature on this subject is extensive, with many other intriguing approaches being explored [94, 95], but the detailed investigation of the classical case falls outside the scope of this discussion. In what follows, we go through the main numerical results of the classical three-body problem. The system of equations describing the multi-body system of N point-like masses M_i, influenced solely by their mutual gravitational forces, is given by:

$$\dot{\boldsymbol{x}}_i = \boldsymbol{v}_i, \tag{1.135}$$

$$M_i \dot{\boldsymbol{v}}_i = -\sum_{j\neq i}^{N} \frac{M_i M_j}{(\boldsymbol{r}_i - \boldsymbol{r}_j)^2} \hat{\boldsymbol{r}}_{ij} = -\sum_{j\neq i}^{N} M_i M_j \frac{\boldsymbol{r}_i - \boldsymbol{r}_j}{|\boldsymbol{r}_i - \boldsymbol{r}_j|^3}, \tag{1.136}$$

where $\boldsymbol{r}_i$ is the position of the i^{th} body, $\boldsymbol{v}_i$ is its velocity, and $N = 3$ represents the number of bodies. We numerically solved the above equations using a fourth-order Runge-Kutta technique with quadruple precision. We began with a specific initial configuration of the three-body problem that leads directly to chaotic motion, namely the so-called *Pythagorean problem* proposed by Burrau in the early 1900s [96]. The point-like bodies, with masses $M_1 = 3$, $M_2 = 4$, and $M_3 = 5$, are initially

TABLE 1.1: Initial parameters for the classical simulations in the four cases investigated. The values are presented in geometrized units, where the initial positions and velocities are normalized with respect to the system's total mass M.

Run	a	b	c	d
Name	Classical Burrau	Equal masses	Normalized masses	Spinning Burrau
M_1	3.0	0.33	0.25	0.25
M_2	4.0	0.33	0.33	0.33
M_3	5.0	0.33	0.42	0.42
$\boldsymbol{r}_1/M$	(1, 3, 0)	(1, 3, 0)	(1, 3, 0)	(1, 3, 0)
$\boldsymbol{r}_2/M$	(-2, -1, 0)	(-2, -1, 0)	(-2, -1, 0)	(-2, -1, 0)
$\boldsymbol{r}_3/M$	(1, -1, 0)	(1, -1, 0)	(1, -1, 0)	(1, -1, 0)
$\boldsymbol{v}_1/M$	(0, 0, 0)	(0, 0, 0)	(0, 0, 0)	(-0.299, 0.050, 0)
$\boldsymbol{v}_2/M$	(0, 0, 0)	(0, 0, 0)	(0, 0, 0)	(0.149, -0.100, 0)
$\boldsymbol{v}_3/M$	(0, 0, 0)	(0, 0, 0)	(0, 0, 0)	(0.059, 0.050, 0)

positioned at the corners of a Pythagorean triangle. These bodies are primarily located on the xy-plane ($z = 0$), as illustrated in Fig. 1.9(a), with (colored) bullets sized proportionally to their masses.

In the beginning, the bodies are all at rest. Burrau's calculation revealed the typical behavior of a three-body system: two bodies approach each other, have a close encounter, and then recede again. Subsequently, Burrau calculated other two-body encounters until he exhausted his computational capacity. Later works showed that the solution to this problem is quite typical of initially bound three-body systems. After many close two-body approaches, a configuration arises in which one body escapes, leaving the other two to form a binary system [63], as represented in Fig. 1.9 (a), where the trajectories of the three bodies are shown up to $t = 70$ for the chosen configuration.

We measured the kinetic energy T, potential energy U, and total energy E of the system as functions of time, up until one of the bodies separated from the remaining binary, which occurs at approximately $t \approx 60$. The potential energy, indicative of the gravitational interaction, is shown in Fig. 1.9 (b). These interactions are extraordinarily intermittent. We refer to these bursts as Extreme Gravitational Interactions (EGIs), following the terminology in Imbrogno, Meringolo, and Servidio [60], which occur when two (or all) of the three bodies come into close proximity, resulting in a system with very high potential (and kinetic) energy. At later times, for $t \gtrsim 60$, small, periodic energy spikes can be observed. This transition marks the point at which the system evolves into a stable binary configuration with one escaping body, losing the stochastic behavior typical of three-body systems. The phenomenon of the "escaper" has been widely explored in the literature [63]. To characterize the system's configuration, especially during the most energetic periods, we measured the moment of inertia $I = \sum_i M_i r_i^2$ and its acceleration

$$\ddot{I} = \frac{d^2 I}{dt^2} = 2M_1\left(v_1^2 + \mathbf{r}_1 \cdot \ddot{\mathbf{r}}_1\right) + 2M_2\left(v_2^2 + \mathbf{r}_2 \cdot \ddot{\mathbf{r}}_2\right) + 2M_3\left(v_3^2 + \mathbf{r}_3 \cdot \ddot{\mathbf{r}}_3\right). \quad (1.137)$$

As shown in Fig. 1.9 (c), $\ddot{I}$ peaks precisely at the EGIs, as expected. Additionally, by differentiating the moment of inertia twice with respect to time, one obtains the Lagrange-Jacobi identity $\ddot{I} = 4T + 2U = 4E_0 + 2|U|$ (E_0 is the total energy of the system), providing a measure of the compactness of the three-body system: in coalescence events, $\ddot{I} \sim 2|U|$, leading to a very large value.

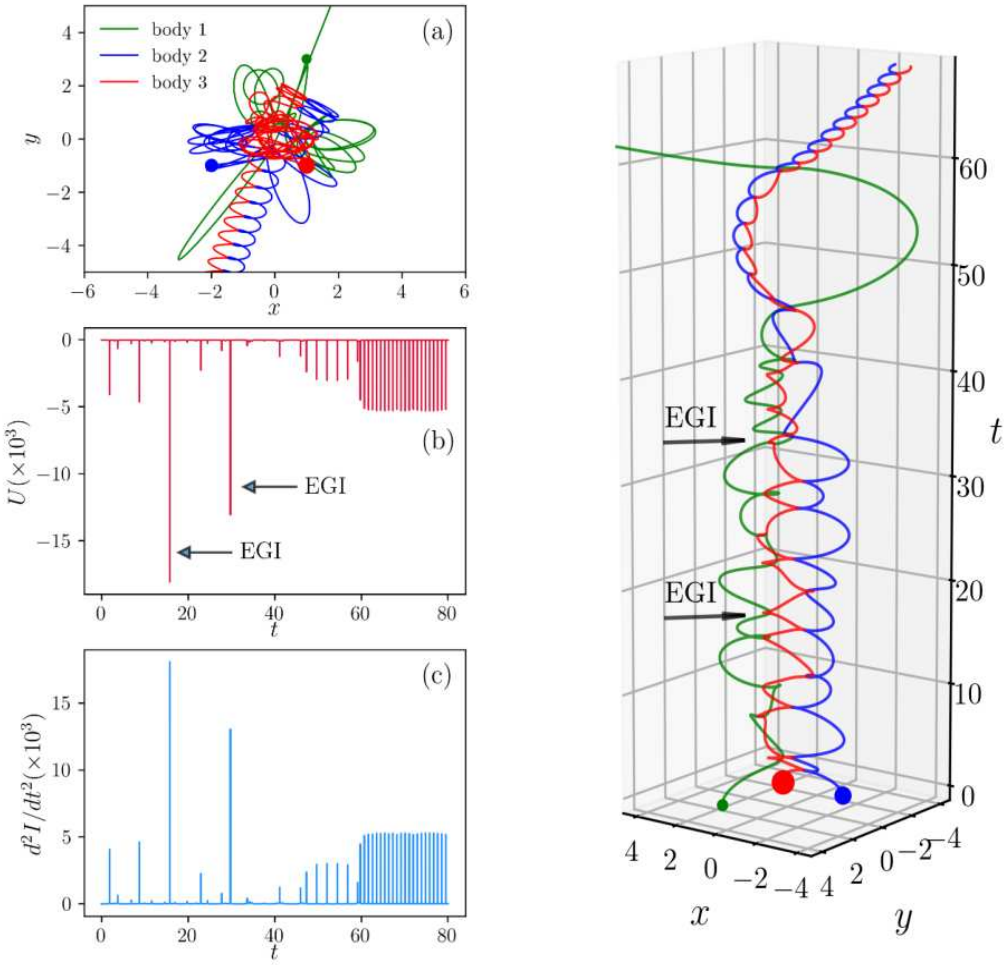

FIGURE 1.9: Overview of the Burrau three-body problem in the classical case. Left: (a) Trajectories originating from the Burrau configuration, with the initial positions of the bodies emphasized by colored spheres, extending up to $t = 70$. (b) Time history of the potential energy. (c) Second time derivative of the moment of inertia for the system. The spikes observed in (b) and (c) correspond to typical Extreme Gravitational Interactions (EGIs). Right: Temporal evolution of the trajectories of the three bodies from the Burrau configuration. One can easily distinguish the moments at which the objects are very close to each other and interact strongly, i.e., the EGIs.

To explore the parameter space, we conducted a series of simulations, varying the masses and the overall angular momentum (and hence the velocities of the individual bodies) relative to the Burrau case (Run a). The different cases are summarized in Table 1.1. In the case of equal masses, Run b, we essentially retained the Burrau configuration as in Run a, but with the total mass set to unity. Similarly, in Run c, we maintained the same conditions as in Run a but re-scaled the individual masses so that the total mass of the system remained equal to one. Finally, in the "Spinning Burrau" case (Run d), we selected non-zero initial velocities to ensure the conservation of total angular momentum. In this scenario, the entire system possessed a global spin, which confined the masses to interact within a limited region of space. This case may be of particular interest for modeling the coalescence of galactic-scale systems.

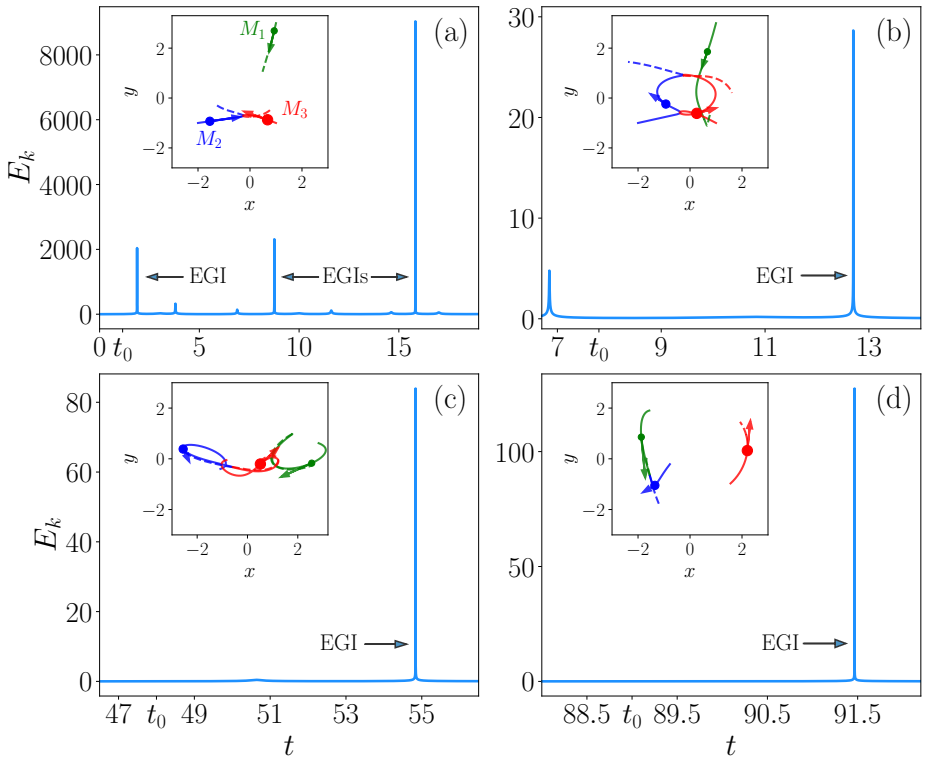

FIGURE 1.10: Overview of the kinetic energy time history for each of the classical cases, namely, Runs a–d in Table 1.1 (with each label corresponding to a specific configuration). The insets depict the positions of the bodies, represented by mass-proportional spheres, along with the direction of the velocity vectors at the pre-EGI time t_0. This particular time point is highlighted with an arrow.

In Fig. 1.10, we present an overview of all the Newtonian simulations summarized in Table 1.1. Each panel depicts the total kinetic energy of the system, with a focus on time windows surrounding extreme nonlinear interaction events. In the inset of each panel, we illustrate the positions of the three bodies at a time just preceding an EGI, labeled as t_0, which will be of practical relevance for our general relativistic experiments (discussed later). Besides, we include mass-proportional spheres, with corresponding velocity arrows, to provide a comprehensive view of each EGI event. The systems are all long-living and exhibit long-term chaotic behavior.

These numerical simulations may hold relevance for systems with small-mass celestial bodies, but they become unrealistic when applied to massive objects. Specifically, one might naturally question what occurs when three large compact objects collide during an EGI. To address this, it is necessary to approach the problem from a completely different perspective, invoking general relativity. We used the Newtonian configurations at the quiet times preceding the EGIs, specifically at t_0, as initial data for numerical relativity, thereby exploring the spacetime dynamics of Runs a–d.

1.7.2 The "Three-black-hole problem" in general relativity

In the previous Section, we began by performing Newtonian integration of a three-body configuration using a variety of general initial conditions, primarily to gather insights pertinent to the general relativistic case. Our objective is to understand how Newtonian EGIs manifest in the dynamical evolution of such systems and to explore the potential for detecting observable gravitational wave signals. The loss of energy

TABLE 1.2: Parameters of the BSSN simulations, based on the Newtonian cases listed in Table 1.1, evaluated at a specific time t_0 before the occurrence of EGIs. The values are reported in geometric units. The final row indicates the initial ADM mass, calculated according to the method suggested by Baumgarte [97].

RUN	I	II	III	IV	V	VI
Name	2 BHs	Classical Burrau	Equal masses	Normalized masses	Spinning Burrau	Intrinsic Momentum
M_1	0.450	0.250	0.333	0.250	0.250	0.250
M_2	0.450	0.333	0.333	0.333	0.333	0.333
M_3	//	0.417	0.333	0.417	0.417	0.417
r_1/M	(0, 1.151, 0)	(0.931, 2.695, 0)	(0.671, 1.857, 0)	(2.554, -0.172, 0)	(-1.874, 0.856, 0)	(-1.874, 0.856, 0)
r_2/M	(0, -1.151, 0.0)	(-1.544, -0.931, 0)	(-0.929, -0.242 , 0)	(-2.557, 0.385, 0)	(-1.352, -1.048, 0)	(-1.352, -1.048, 0)
r_3/M	//	(0.676, -0.872, 0)	(0.259, -0.615, 0)	(0.513, -0.205, 0)	(2.206, 0.325, 0)	(2.206, 0.325, 0)
v_1/M	(0.335, 0, 0)	(-0.037, -0.039, 0)	(-0.119, -0.358, 0)	(-0.296, -0.132, 0)	(0.036, -0.382, 0)	(0.036, -0.382, 0)
v_2/M	(-0.335, 0, 0)	(0.251, 0.037, 0)	(-0.336, 0.229, 0)	(0.034, -0.070, 0)	(-0.059, -0.035, 0)	(-0.059, -0.035, 0)
v_3/M	//	(-0.179, 0.066, 0)	(0.455, 0.129, 0)	(0.150, 0.135, 0)	(0.025, 0.258, 0)	(0.025, 0.258, 0)
J_1/M^2	(0, 0, 0)	(0, 0, 0)	(0, 0, 0)	(0, 0, 0)	(0, 0, 0)	(0, 0, 0.100)
J_2/M^2	(0, 0, 0)	(0, 0, 0)	(0, 0, 0)	(0, 0, 0)	(0, 0, 0)	(0, 0, -0.050)
J_3/M^2	(0, 0, 0)	(0, 0, 0)	(0, 0, 0)	(0, 0, 0)	(0, 0, 0)	(0, 0, -0.050)
M_{ADM}	0.904	1.001	1.003	1.004	1.008	1.007

and angular momentum from the system via gravitational radiation modifies the key parameters governing the three-body problem, necessitating the inclusion of general relativistic effects. This radiation causes the decay of binary orbits, ultimately leading to the collapse of the black-hole binary system into a single black hole. The final stages of this decay are extremely rapid, potentially inducing dramatic changes in the evolution of the three-body problem within the framework of singular spacetimes. When three black holes interact strongly, the possible outcomes include the escape of one black hole with the binary recoiling in the opposite direction, or the eventual merger of all three massive objects [77, 83, 84].

In this Section, we focus on the interaction of the three black holes, varying the initial configurations as outlined in Table 1.1, to explore different scenarios. To better understand these emissions, we will compare the gravitational waveforms from a two-body inspiral with those from the three-body case.

The three-body problem in general relativity, involving three interacting black holes, is significantly more complex due to the chaotic nature of the system. Unlike binary black hole systems, where the evolution is relatively predictable, the dynamics of three black holes can lead to a wide range of scenarios. In classical mechanics, the three-body problem is notorious for its chaotic solutions, where small differences in initial conditions can produce vastly different results. In general relativity, this complexity is further amplified by the nonlinear nature of Einstein's equations. The gravitational radiation emitted during the interaction of three black holes is highly sensitive to the initial conditions, including the masses, spins, and initial velocities of the black holes. Possible outcomes include the formation of a single black hole with the other two being ejected, the creation of a temporary binary with the third black hole being expelled, or a more intricate interaction where all three black holes merge into a single, highly spinning black hole.

The initial data for multiple black holes involve more conditions and require a longer convergence time for the iterative algorithm. Specifically, these calculations may require several CPU hours when employing the Gauss-Seidel method introduced at the end of Sec 1.3. To accelerate convergence, we begin with a low-resolution initial cube (using a 64^3 mesh), which allows the Hamiltonian constraint to be solved relatively quickly. Then, to interpolate onto a finer grid (i.e., reducing the grid spacing), we first transform to Fourier space, increase the number of

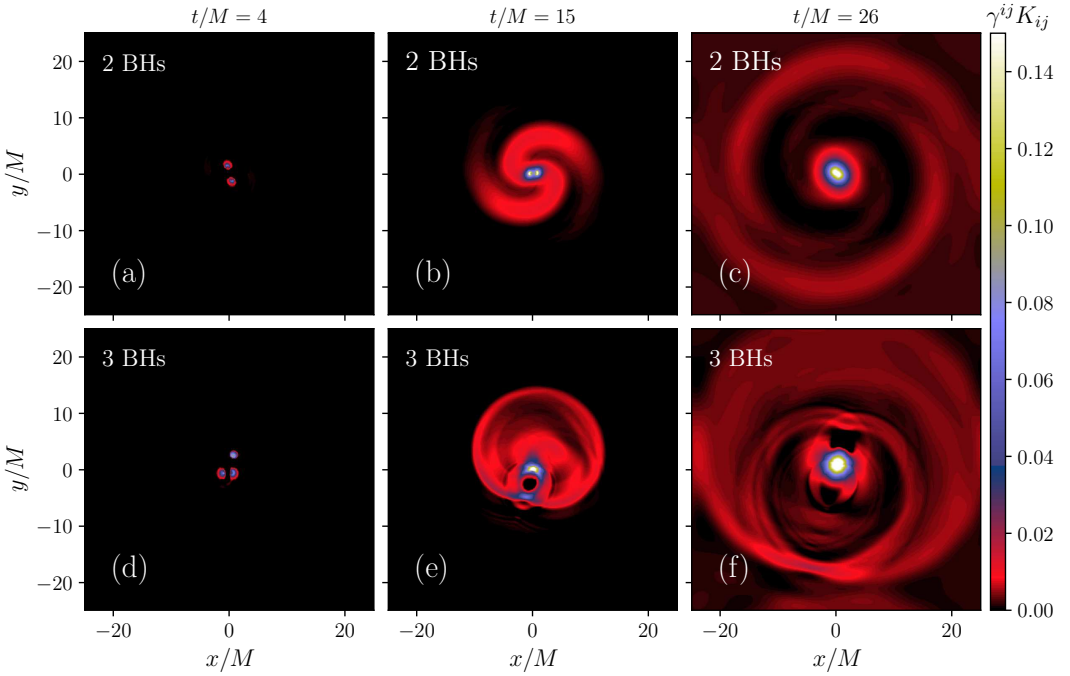

FIGURE 1.11: Shaded contours of the extrinsic curvature K for the two black holes (RUN I, top row) and the 'Classical Burrau' three-body interaction (RUN II, bottom row) at three distinct stages of evolution: before, during, and after the merger.

k-vectors via zero-padding, and subsequently recover the physical fields by performing an inverse FFT. This approach provides a better initial guess on the higher-resolution grid, leading to a much faster convergence rate. By iteratively applying this technique and recursively refining the solution through interpolation to finer grids, we ultimately acquire the initial data.

When dealing with multiple black holes (BHs), accurately estimating their apparent horizons (AHs) is crucial [98, 99, 100, 101, 102]. The apparent horizon is a locally defined surface that represents the boundary beyond which light cannot escape, effectively marking the presence of a black hole. Unlike the event horizon, which is a global feature that requires the entire evolution of spacetime to be fully determined, the apparent horizon is based on local properties at a specific moment in time and can be identified using only the current configuration. This makes the apparent horizon particularly valuable in numerical relativity, where simulations often require a real-time, local criterion to identify black holes during dynamical processes. Our initial data for the 2-BH case are consistent with those in *Campanelli et al.* [21], where each black hole is shown to be a well-separated body with a distinct AH (and no common initial AH). For our 3-BH cases, given that the masses, linear momenta, and separations are comparable to those in Campanelli's work, it is reasonable to expect similar AH configurations. Additionally, we estimated the ellipsoidal AH shapes, typical of boosted (and spinning) black holes, as the initial guesses described in *Huq et al.* [103]. These surfaces remain safely separated at the onset of the EGIs.

Concerning the simulation parameters, for all the BSSN simulations, the domain is represented by a cube of side $L_0 = 50M$, with 512^3 mesh points. The time step is initially chosen to be $\Delta t = 8 \times 10^{-3}$. Furthermore, we ensure that the Hamiltonian and momentum constraints are well satisfied for each case. The parameters

of the BSSN simulations are summarized in Table 1.2, where they are labeled with Roman numbers. Specifically, we focus on the fully relativistic evolution of the classical system as it approaches an EGI, verifying that, at the initial time t_0, the black holes (BHs) are sufficiently far apart. On the other hand, we avoid excessively large distances that would result in an excessive numerical cost.

Before addressing the complex three-body problem, we first calibrate our numerical experiments using the two-body inspiral, which provides us with the classical waveform [104, 105, 106]. As explained in Sec. 1.6, our objective is to compare the properties of the gravitational waves generated by both binary and three-body systems. The parameters for this "2 BHs" configuration are summarized in Table 1.2 as RUN I. As expected, the black holes spiral around each other, completing a single orbital period before merging, as shown in Fig. 1.11. A straightforward and efficient way to identify a gravitational disturbance is to examine a scalar measure of the extrinsic curvature, particularly in the ecliptic plane. Panels (a)–(c) show that small amplitude waves propagate outward during the merger. Subsequently, a large amplitude modulation propagates away once the two Marginally Outer Trapped Surfaces (MOTSs)—which locally indicate the presence of a black hole by marking the boundary inside which light rays converge—come into contact [107, 108, 109, 110, 111]. At this point, several smaller disturbances propagate until the system ultimately settles into a Kerr-type black hole.

In the second campaign of general relativistic simulations, we focus on the evolution of three black holes (3-BHs), inspired by Runs a–d. In particular, we use the initial data from these cases at t_0, as described in Fig. 1.10. This strategy allows us, using spectral methods, to concentrate on events that are energetically significant and therefore potentially detectable in experiments. As summarized in Table 1.2, RUN II corresponds to the "Classical Burrau" case from Run *a*, but with masses normalized so that the total system mass is unity. RUN III ("Equal masses") describes a similar system where the black holes' masses are equal, as in Run *b*. RUN IV describes a case similar to RUN II, but with different initial configurations (i.e., positions and momenta of the BHs). All these configurations assume that the three bodies are initially at rest, so no global inspiral is expected. The "Spinning Burrau" (RUN V) explores a scenario where the initial configuration possesses non-zero angular momentum, as in Run *d*. The final simulation, labeled "Intrinsic spin" (RUN VI), shares the same initial setup as RUN V, but with the BHs having intrinsic spin.

Focusing on the overview of K depicted in Fig. 1.11 (d)–(f), it is evident that, compared to the 2-BH case, the patterns are more distorted and exhibit finer scales. In the post-merger phase, after the system has been allowed to "relax," a different pattern in the extrinsic curvature emerges, suggesting a distinct asymptotic solution for the final black hole. Fig. 1.12 presents a three-dimensional rendering of this RUN II, illustrating the gravitational radiation following the successive merger events. The shaded (red and blue) contours represent isosurfaces of constant K at two different values, highlighting how the outgoing waves are irregular and skewed. The region near the final event horizon is represented with a (black) sphere.

To gain deeper insights into the dynamics of multiple black holes, we analyze the waveform by computing the projection of the Newman-Penrose scalar Ψ_4. After calculating this quantity following the procedure outlined in Sec. 1.5, we interpolate Ψ_4 from a Cartesian grid to a spherical grid using trilinear interpolation, which enables the calculation of outgoing gravitational radiation using the spin-weighted spherical harmonic $Y_{22}^{(-2)}(\theta, \varphi)$. This projection isolates the dominant contribution to the emitted waves, which primarily arises from the quadrupole mode ($l = 2$,

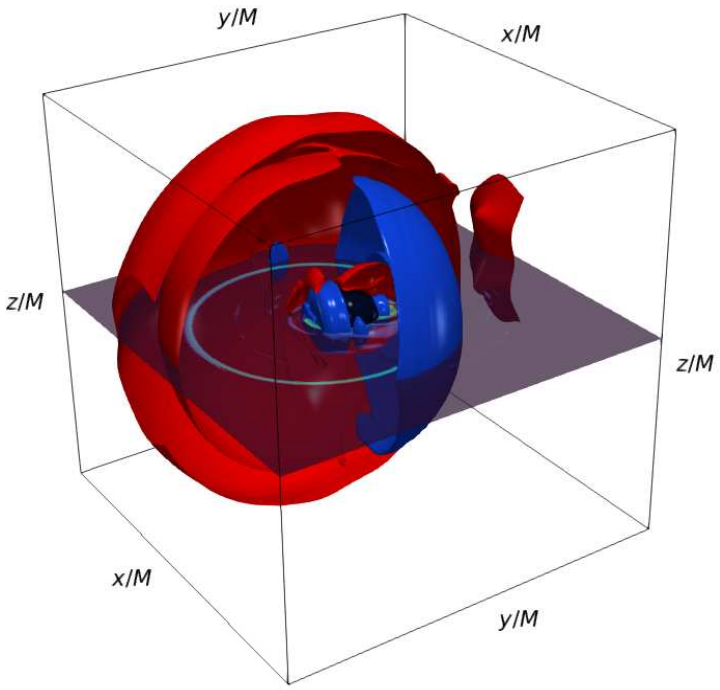

FIGURE 1.12: 3D representation of the three-black hole interaction, at time $t/M = 26$ for RUN II ("Classical Burrau" in Table 1.2). The (red and blue) isosurfaces represent constant values of the extrinsic curvature K, outside from the final black hole (central black-shaded region). The 2D transparent plane represents a color contour of the Newman-Penrose scalar Ψ_4, with maxima in light-green color.

$m = 2$). In Fig. 1.12, we present a color contour plot of Ψ_4 in the equatorial xy-plane (at $z/M = 25$), for the three-body case (RUN II), where the outgoing gravitational radiation is clearly visible.

We compared all the signals resulting from these multiple black hole interactions by examining the outgoing radiation as measured at a distance from the sources. Specifically, we evaluated the projection described above at a fixed distance from the center of the computational domain, namely at $r^\star = 20M$, as a function of time while the disturbances pass through the virtual detector. We defined the merging time t^* as the moment when a single connected isosurface of the lapse $\alpha = 0.3$ forms around the two approaching black holes [57, 112, 106]. These times are indicated in Fig. 1.13 using vertical dotted black lines. It is important to note that, since our focus is on EGIs, we do not describe the long-duration "chirped" signal occurring before the merger.

The signals are depicted in Fig. 1.13, revealing clear differences among the cases. First, unlike the binary case [panel (a)], the real and imaginary parts of the waveform

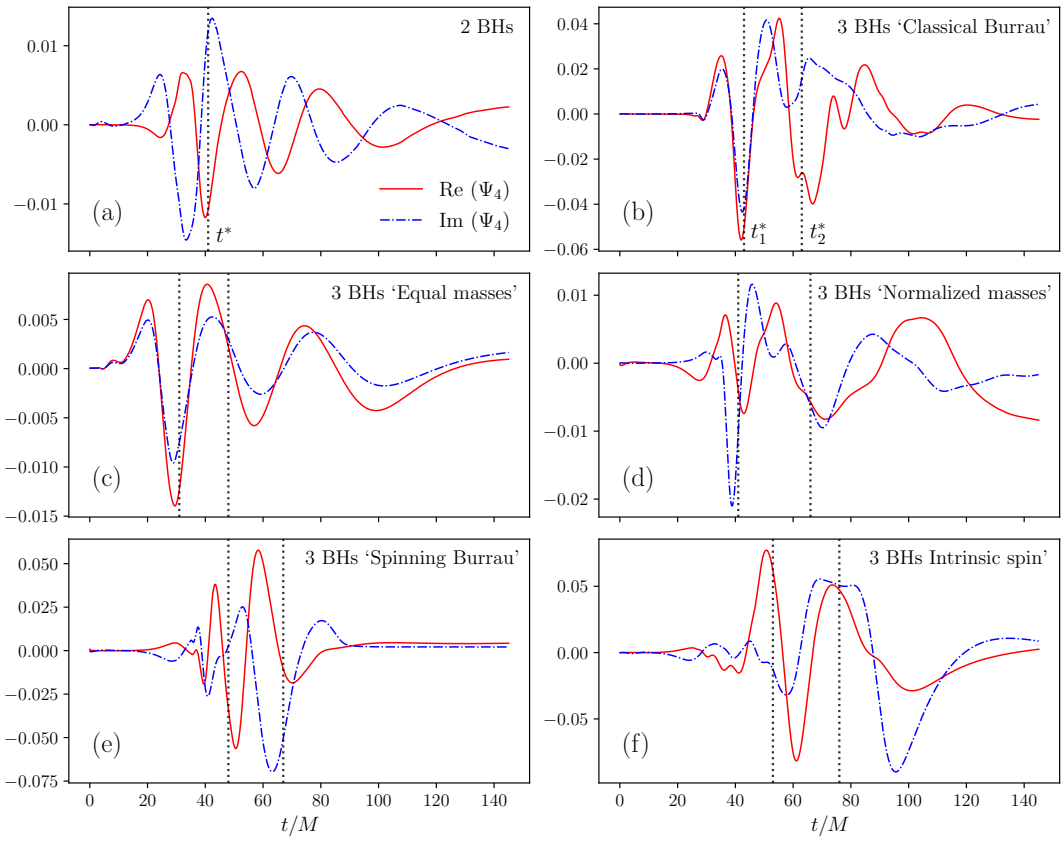

FIGURE 1.13: Reconstruction of the gravitational wave signal for (a) the binary black hole system and (b)–(f) the three-black hole systems. Figures (a)–(f) correspond respectively to RUNs I–VI listed in Table 1.2. The solid (dash-dotted) lines represent the real (imaginary) part of the spherical projection of Ψ_4; the vertical dotted black lines indicate the merging time(s) of the black holes (t^* corresponds to the 2-BH merger, while t_1^* and t_2^* correspond to the 3-BH mergers), as defined in [57, 112, 106]. All simulations are carried out up to $t/M = 145$. The three-black hole cases reveal a more complex and nonlinear behavior.

in some of the 3-BH cases are almost in phase. Second, while the 2-BH system exhibits a single peak corresponding to the merger, the other cases show multiple-scale disturbances due to subsequent collapses. Third, the signal from the three-body system is significantly more irregular and unpredictable, indicating the presence of higher-order nonlinearities [108, 113, 26, 21, 77, 83, 84]. These more structured signals necessitate a more in-depth statistical investigation, which is conducted as follows.

To further highlight the differences among the configurations and identify possible peculiarities in the 3-BH interactions, we performed a spectral analysis of the metric disturbances shown in Fig. 1.13. First, we smoothed the boundaries using a *generalized normal window*, then computed the Fourier transform to obtain the power spectrum. This spectrum was cross-validated using the Blackman-Tukey method [114], which involves transforming the windowed auto-correlation function of the signal. The spectrum was calculated for both the real and imaginary parts of the projection shown in Fig. 1.13. To reduce statistical uncertainties, we averaged the power spectra. As shown in the averaged power spectra in Fig. 1.14, the 3-BH cases generally produce a broader frequency distribution. The excess of high frequencies

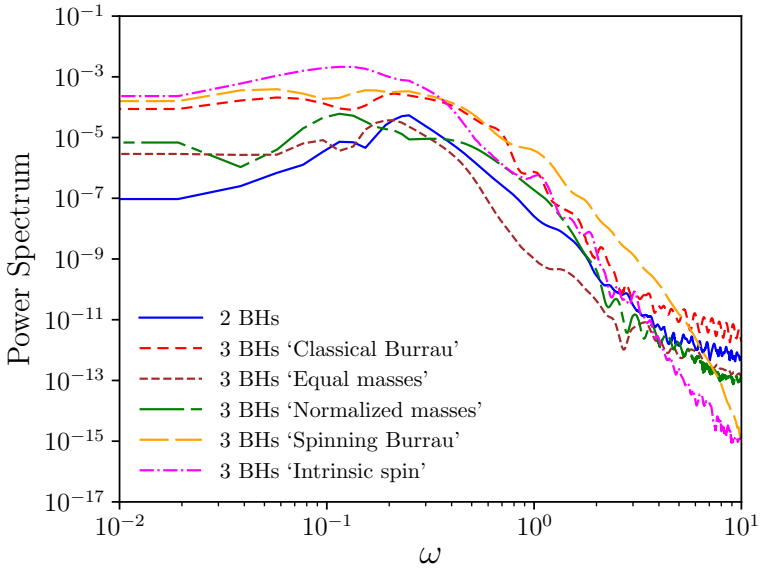

FIGURE 1.14: Power spectrum of the waveforms in Fig. 1.13. The spectrum represents an average of the power spectra of both the real and imaginary components of the Newman-Penrose scalar Ψ_4 projection.

reflects the small-scale features observed near the three-body system, as previously noted in Fig.s 1.11 and 1.12. The narrowest spectrum is observed in the binary system and in RUN III, where the head-on collision of the smallest black holes did not produce significant nonlinearity. On the other hand, the "Spinning Burrau" case exhibits the smallest scales of our simulation campaign. Notably, in the three-body case, the spectrum shows a power-law behavior for $0.6 < \omega < 3$, raising intriguing possibilities regarding a *gravitational turbulent cascade*. However, the classical one-dimensional Fourier spectrum alone is insufficient to fully characterize the dynamics, as these processes are highly non-stationary. Therefore, we proceed with a more refined analysis, detailed below.

Due to the non-stationary nature of the signal, we apply wavelet decomposition to the wavefront. Wavelet transforms offer a time-frequency representation of the gravitational wave signal, providing a complementary analysis particularly suited for complex systems like three-body black hole interactions, where the signal may exhibit multiple close encounters or successive mergers. By decomposing the waveform into localized frequency components, wavelet analysis enables the identification of distinct features within the chaotic dynamics of multi-black hole systems. A key advantage of wavelets lies in their ability to naturally split fluctuations into different scale components according to multi-scale resolution analysis [115], making them a powerful tool for studying multi-body coalescence events. Among the various options, all of which provide qualitatively consistent results, the clearest findings are obtained here using the Shannon generating function [116]. This reconstruction uses the "sinc function", which is highly localized and rapidly decays to zero—ideal for capturing discrete frequencies, though less effective for time localization [117, 118]. A typical wavelet spectrogram is presented in Fig. 1.15, where we consider three characteristic cases: RUN I, II, and V. The 2-BH case exhibits a distinct single peak in frequency, corresponding to the merger event. A frequency increase is observable for $5 < t < 40$, characteristic of the inspiral phase [21, 108]. The real and imaginary components of the scalar exhibit very similar behavior. At later times,

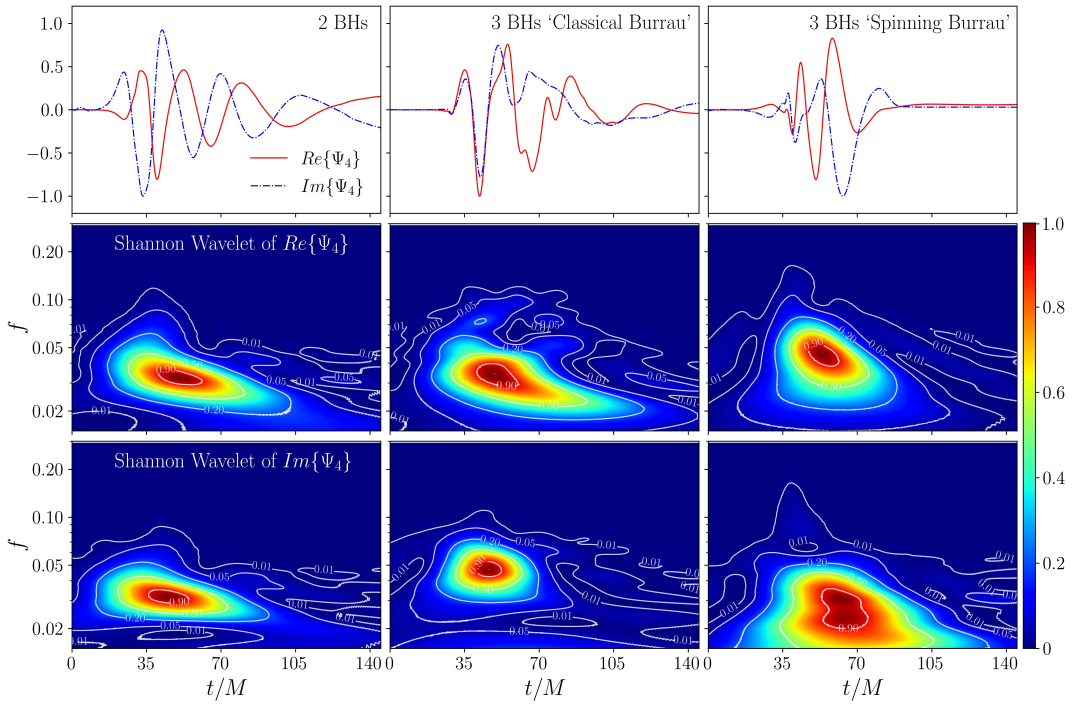

FIGURE 1.15: Spectrogram of the Shannon wavelet (second and third row) for three different waveforms (first row), corresponding to RUN I (left), RUN II (center), and RUN V (right). The middle and bottom rows present the wavelet analysis for the real and imaginary parts of Ψ_4, respectively. The signals and spectra have been normalized to one for ease of comparison.

the system shows the typical low-frequency modulation of the resultant perturbed black hole. In contrast, the behavior of the 3-BH cases is markedly different. In the 'Classical Burrau' scenario, focusing on $Re\{\Psi_4\}$, aside from the main frequency similar to that of the 2-BH case due to the initial head-on merger, secondary peaks are evident. A secondary peak occurs at $t \sim 70$ and $f \sim 0.08$, resulting from the subsequent disturbance propagating from the secondary EGI, when the larger BH *eats* the remaining one. This corresponds to a disturbance arising from the coalescence of a large mass ratio system. Finally, we performed the same analysis for the case with the broadest Fourier spectrum in Fig. 1.14, namely RUN V. In the Spinning Burrau case, the BHs are confined by the large global angular momentum. This constraint forces the two mergers to occur nearly simultaneously, with multiple nonlinear effects. This highly nonlinear interaction is evident as a noticeable broadening of the wavelet spectrum. In this scenario, the outgoing gravitational waves carry away from the final event horizon the remnants of this extreme interaction.

In Fig. 1.15, we present the spectrograms from our numerical simulations to assess their potential for comparison with future observational data, with the expectation that future measurements may capture signals similar to those simulated, thereby enhancing our understanding of merger dynamics and the associated spectral features. The prospects for measuring spectrograms of merging black holes depend on the sensitivity and frequency range of current and upcoming gravitational wave detectors, such as LIGO, Virgo, and the planned LISA mission. These detectors are capable of capturing gravitational wave signals from black hole mergers, which can then be analyzed to obtain corresponding spectrograms (e.g., [61]). Advances in detector sensitivity and the extension of their frequency coverage will significantly

improve the accuracy and resolution of these spectrograms, enabling more detailed studies of such astrophysical events.

1.8 Discussions and Future Directions

The three-body problem serves as a classical example of complex dynamics, where the interactions between three massive objects can lead to chaotic behavior. In this study, we focused on two distinct approaches: (1) the Newtonian approach and (2) Einstein's theory of general relativity. In the first part, we reviewed classical results and developed a highly accurate Lagrangian code to solve the trajectories of the bodies, beginning with the Pythagorean configuration. This configuration rapidly evolves into a nonlinear regime. Throughout the evolution, the system experiences quiet transients interspersed with highly intermittent, burst-like behaviors, characteristic of chaotic dynamics [119]. We precisely calculated the trajectories and identified these intense spikes, known as EGIs. For future research, it would be of great interest to compare these findings with models that incorporate post-Newtonian corrections [120].

In the second, and more challenging, part, we built a gravitational model to investigate the dynamics of EGIs within the framework of general relativity. Through a sequence of conformal transformations, we briefly introduced the BSSN equations, which were subsequently integrated using the `SFINGE` code, described in Sec 1.4. As a preliminary step for our general relativistic experiments, we examined the binary black hole problem during the final stage of coalescence within the ISCO. To measure the emitted gravitational waves, we addressed the issue of wave extraction. Employing spherical interpolation and following the Newman-Penrose prescription, we quantified the outgoing gravitational waves, as is traditionally done in simulations involving compact objects. After conducting two-body simulations, we extended our analysis to the interaction of three black holes. We derived initial data preceding a strong EGI from Newtonian simulations, ensuring that the bodies were sufficiently far apart. We monitored several key quantities, such as the metric tensor and the extrinsic curvature of the system, which indicated intense emission during the multiple-coalescence events. Analogous to the 2-BH case, we employed numerical extraction techniques to reconstruct the emitted waveform, which proved to be highly irregular and nonlinear. Finally, we compared the binary merger with the extreme three-body interaction by computing the power spectra of the signals for all cases. We observed significant differences, particularly at high frequencies, where the 3-BH system exhibited a broader power distribution. The spectrum appeared consistent with a power-law distribution, suggesting that gravitation, similar to hydrodynamics, may be subject to a turbulent cascade.

To further investigate the outcome of multi-black-hole radiation, we performed a refined analysis of the signals. Specifically, to detect the main differences among the cases, we employed a Shannon wavelet analysis. This analysis reveals distinct differences between the 2-BH and 3-BH cases. In the former, the projection shows a single dominant frequency, whereas in the 3-BH case the wavelets indicate the presence of multiple frequencies during the evolution, attributable to the multiple EGIs. Finally, in scenarios where there is a global angular momentum confining the black holes, a significant broadening of the wavelet power spectrum is observed, characteristic of nonlinear phenomena.

While the 2-BHs inspiral has been extensively investigated in the literature [110, 38, 121, 122, 123, 124, 125, 126, 106], much less documentation exists regarding the

initial data for 3-BHs EGIs [77, 76], and currently, no observational evidence has been found. These results may hold considerable significance for future observational campaigns, as advancements in modern technologies are expected to enhance signal-to-noise sensitivity, enabling the exploration of whether such extraordinary events might indeed occur in the Universe.

Numerical simulations of both binary and multiple black hole systems have provided valuable insights, particularly in the context of gravitational waveforms. The comparison between the relativistic and Newtonian dynamics of the three-body problem, alongside the extraction of gravitational waves, reveals discrepancies that become pronounced in highly relativistic regimes. As observed in the waveforms, deviations from the expected Newtonian trajectories increase as the system approaches the relativistic regime, consistent with the predictions of General Relativity. These findings corroborate previous studies [21, 78], further validating the robustness of the BSSN formalism in 3+1 relativity.

A particularly novel aspect of this study is the comprehensive analysis of waveforms generated by the interaction of three black holes in vacuum, an area that has received limited attention so far. The incorporation of higher harmonic modes in the waveform analysis has provided new insights, particularly when compared to the results from binary black hole systems. The complex gravitational interactions among the three black holes produce unique waveform signatures, which could potentially be detected by next-generation observatories such as LISA [86, 85]. This presents an exciting opportunity for future research, offering the potential to observe and analyze such rare events. Moreover, these findings raise new questions about the stability of triple black hole systems and their relevance in astrophysical scenarios, including hierarchical systems in dense stellar environments. Future work could expand these simulations to encompass more intricate initial conditions, such as non-vacuum spacetimes or charged black holes, and examine the long-term stability of such systems. In conclusion, this study contributes to the expanding body of research on black hole mergers by exploring novel dynamical configurations and extracting gravitational wave signals that have yet to be observed, thereby advancing our understanding of black hole dynamics and laying the groundwork for future observational discoveries.

Chapter 2

Einstein Field Equations in the Presence of Matter

In the previous Chapter, we focused on the Einstein field equations in vacuum, which describe the dynamics of spacetime in the absence of matter. These vacuum solutions provide valuable insights into the geometric structure of spacetime, particularly in regions dominated by gravitational effects, such as near black holes or during gravitational wave propagation. Nevertheless, a comprehensive understanding of many astrophysical phenomena, especially those involving compact objects like neutron stars, black holes, and their accretion disks, or the dynamics of the early Universe, requires considering the interaction between matter and spacetime. To accurately model such systems, it is necessary to extend the vacuum framework to include matter, typically treated as a fluid interacting with spacetime curvature. In this context, the fluid approximation conceptualizes matter as a continuum, considering an infinitesimal fluid element that is small relative to the system but large enough to contain a significant number of particles. For plasmas, this means that the mean distance between particles and the mean free path between collisions must be much smaller than the system's microscopic characteristic length. Thus, GRHD becomes indispensable, providing a robust framework for describing the behavior and evolution of matter under strong gravitational fields, while neglecting the influence of electromagnetic forces. This approach is particularly crucial for simulating highly energetic astrophysical phenomena, such as neutron star or black hole mergers and supernovae, where both gravitational forces and fluid dynamics play significant roles. Furthermore, modeling accretion disks around black holes adds another layer of complexity. These disks, composed of plasma—a highly conductive, quasi-neutral state of matter consisting of charged particles—must be carefully treated to capture fluid dynamics accurately in such extreme environments, even though the electromagnetic backreaction on spacetime is not considered in this framework. Plasma dynamics introduce essential processes for understanding mass and energy transport within the disk. This Chapter, therefore, establishes the foundation for investigating GRHD and plasma dynamics in astrophysical contexts, where the interaction between matter and spacetime is intricately coupled.

Firstly, we extend the $3+1$ formalism by incorporating the stress-energy tensor of a perfect fluid into the Einstein field equations, thereby enabling the modeling of interactions between matter and spacetime curvature. This extension allows for the simultaneous evolution of both spacetime geometry and the physical properties of matter, such as density, pressure, and velocity, within the strong gravitational fields produced by compact objects [6]. All these features are appropriately integrated into the `SFINGE` code, illustrated in the previous Chapter, to facilitate simulations of matter in an evolving curved spacetime using pseudo-spectral methods, which provide

high precision in the calculation of derivatives. Introducing matter into the equations significantly increases the complexity of the system, especially when dealing with phenomena involving steep gradients, discontinuities, and shock waves, which present challenges for both the mathematical formulation and numerical stability. Therefore, we aim to examine the fundamental equations governing GRHD and provide the necessary tools for understanding the evolution of matter and spacetime in numerical relativity. In this regard, we present a "logarithmic" formalism designed to handle discontinuities, with the objective of ensuring numerical stability in simulations, as detailed in Imbrogno et al. [127] (submitted). By expanding beyond vacuum solutions to those involving matter, we can simulate more realistic astrophysical scenarios, offering deeper insights into the behavior of matter in extreme gravitational environments.

Following this, we present preliminary tests performed using the `SFINGE` code in a flat metric to systematically verify the effectiveness of the strategy adopted to incorporate matter into the system's dynamics. To this end, a concise introduction to special relativistic hydrodynamics is provided, focusing on the Kelvin-Helmholtz Instability (KHI) within the framework of Minkowski spacetime. Specifically, we analyze the KHI in the absence of electromagnetic fields, deriving its dispersion relation and growth rate, and performing numerical simulations of unstable layers to study the evolution of the instability.

Finally, we investigate the interplay between gravitational and magnetic forces in shaping the dynamics of accretion disks and driving the formation of relativistic jets, using the well-established `BHAC` code [2]. Among the available coordinate systems, we select Kerr-Schild coordinates and simulate a magnetized plasma surrounding a Kerr-type black hole. The processes examined are critical for understanding key astrophysical phenomena such as X-ray emissions, gamma-ray bursts, and gravitational waves. Indeed, the interaction between gravitational, hydrodynamic, and electromagnetic forces in systems involving compact objects gives rise to some of the most energetic events in the Universe. In particular, magnetic fields play a fundamental role in these environments, necessitating the extension of the GRHD framework to GRMHD to accurately model the evolution of matter and magnetic fields in the intense gravitational environments surrounding black holes, as well as for investigating the mechanisms driving accretion and jet formation. The GRMHD framework allows for the investigation of energy extraction mechanisms from rotating black holes, such as the Blandford-Znajek process [128], which is widely believed to power astrophysical jets.

Black holes, with their extreme gravitational influence and event horizons, exert a profound effect on the surrounding matter. Accretion disks, composed of gas and plasma spiraling inward, are key structures in these systems. The dynamics of accretion disks are governed by a delicate balance of gravitational forces, pressure gradients, and angular momentum transport. Introducing magnetic fields adds further complexity through MHD processes, which significantly influence the behavior of accretion disks. These fields can channel plasma into relativistic jets that eject matter at nearly the speed of light. Such jets are associated with observable phenomena, including gamma-ray bursts and radio emissions from active galactic nuclei, all intricately linked to the magnetic fields near the black hole (see Fig. 2.1 for a comprehensive illustration of the black hole environment). Due to the inherent turbulence in accretion flows, magnetic fields play a key role in transferring angular momentum, allowing matter to accrete onto the black hole. Magnetic reconnection can lead to substantial energy release, contributing to the complex dynamics observed

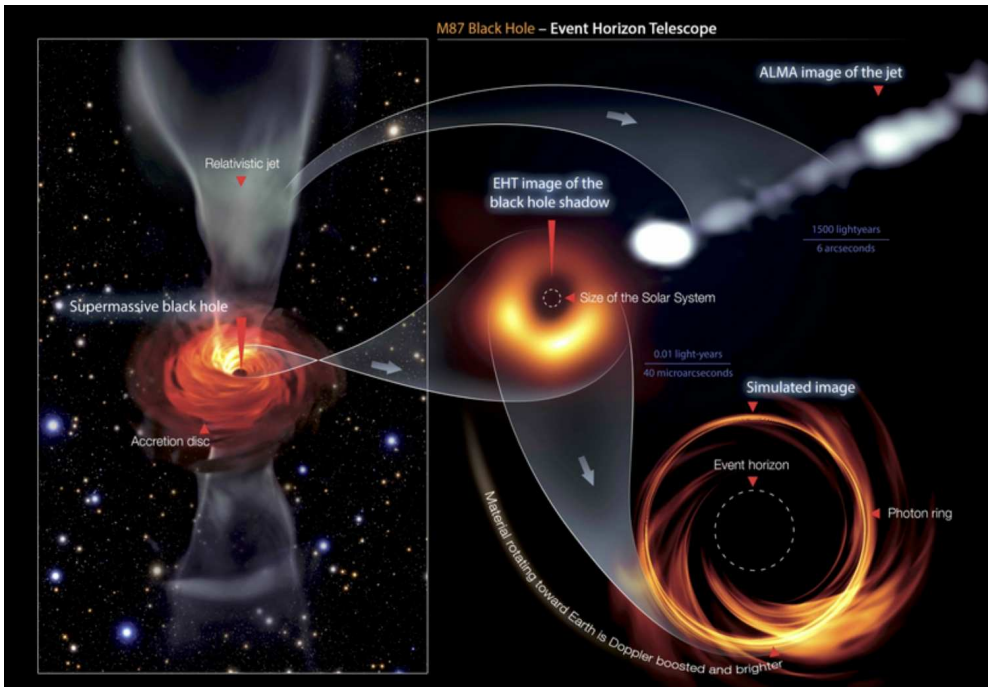

FIGURE 2.1: Illustration of M87*, with emphasis on its accretion disk and relativistic jets. Image courtesy of the Event Horizon Telescope Collaboration.

in these regions. To better characterize the turbulence, we conduct an in-depth spectral analysis across different regions near black holes, such as the disk, wind, and jet areas. The average power spectrum analysis reveals variations in the scaling laws governing each region and demonstrates the presence of a strong turbulent cascade that transfers energy from large (inhomogeneous) to smaller (homogeneous) scales, eventually reaching kinetic scales where collisionless, relativistic physics becomes dominant. These comprehensive studies on systems such as Sgr A* and M87* provide valuable insights into the role of magnetic fields in shaping the evolution of accretion flows and the mechanisms of energy transfer within magnetically dominated regions. The simulations and spectral analyses illuminate the conditions that govern the formation of turbulent structures and the efficient transfer of energy in relativistic plasma flows near black holes.

Numerous astrophysical phenomena, such as accretion disks around black holes, neutron star mergers, and core-collapse supernovae, are best understood within the framework of RHD in curved spacetime. These events take place in regions dominated by extreme gravitational fields, making it essential to describe matter-spacetime interactions in the context of general relativity. In such extreme environments, fluid dynamics cannot be studied in isolation, as the strong gravitational field significantly influences the fluid's motion and behavior, requiring a precise integration of RHD with Einstein field equations. RHD, and its extension to GRHD, play a central role in investigating these high-energy events. Commonly, scenarios such as accretion onto compact objects, neutron star mergers, and supernova explosions are modeled using these equations, offering valuable insights into the gravitational wave emissions and electromagnetic signals observed from these phenomena. However, a comprehensive understanding often requires the inclusion of magnetic fields, extending the framework to GRMHD. While incorporating magnetic fields introduces additional complexity, the first part of this Chapter focuses on the purely

hydrodynamic regime, initially excluding magnetic fields from the discussion. In such cases, the dynamics of matter are primarily dictated by the curvature of spacetime, necessitating advanced techniques to couple the fluid's equations of motion with the evolving geometry described by Einstein field equations.

Over the years, significant advancements have been made in the numerical methods used to solve the GRHD equations. Wilson's pioneering work [129] laid the foundational framework that later became the standard in RHD simulations. This approach has been refined and enhanced over the decades by various researchers. Notably, Font [130] made substantial contributions to improving the resolution and stability of numerical schemes for GRHD, while Shibata and Sekiguchi [131] expanded these techniques to tackle more complex scenarios involving dynamic spacetimes, such as binary neutron star mergers and stellar collapses. Additionally, Gammie, McKinney, and Tóth [132] introduced innovative methodologies for modeling magnetized disks and their role in angular momentum transport within accretion flows, pushing forward the connection between GRHD and GRMHD frameworks. In this context, Komissarov's work [133] is a pioneering contribution to GRMHD, advancing understanding of magnetospheres and relativistic plasma around black holes. In recent years, Sironi, Petropoulou, and Giannios [134] has made key advancements in the study of relativistic plasma dynamics and magnetic reconnection, offering new insights into particle acceleration mechanisms in turbulent environments.

Modern numerical methods for GRHD often rely on the 3+1 decomposition of spacetime, as discussed in the previous chapter, especially when combined with the BSSN formalism. This reformulation of the Einstein equations enhances stability and reduces numerical errors in simulations of strongly gravitating systems. A critical aspect of GRHD simulations is the accurate modeling of shock formation and propagation, which is prevalent in many high-energy astrophysical scenarios. For instance, during the collision of two neutron stars, strong shock waves propagate through the surrounding material, generating intense radiation and gravitational waves. Accurately simulating these shock fronts requires specialized numerical techniques, such as High-Resolution Shock-Capturing (HRSC) methods. Martí and Müller [135] introduced a suite of HRSC techniques specifically designed for relativistic flows, which have since become the gold standard for simulations of systems with shocks and discontinuities. These methods have been further refined by various researchers, including Del Zanna and Bucciantini [136], who improved the accuracy of HRSC techniques in relativistic hydrodynamic flows, Shibata [137], who applied these methods to highly dynamic spacetimes, and Mignone, Plewa, and Bodo [138], who made significant advances in ensuring the stability and precision of simulations involving relativistic shocks. Building on these developments, significant efforts in recent years have focused on modeling plasma dynamics around supermassive black holes and neutron stars [139], leading to the development of numerous GRMHD codes worldwide. Notable examples include `BHAC` (Porth et al. [2]), which is extensively used in this Chapter, `HARM` (Gammie, McKinney, and Tóth [132]), which employs HRSC schemes tailored for relativistic MHD in accretion flows, `H-AMR` (Liska et al. [140]), `IllinoisGRMHD` (Etienne et al. [141]), `WhiskyMHD` (Giacomazzo and Rezzolla [142]), `SpEC` (Szilágyi [143]), `GRHydro` (Mösta et al. [144]), `Athena++` (Stone et al. [145]), and `ECHO` (Londrillo and Del Zanna [146]), among others. With modern computational resources and the enormous physical scales involved, global fluid approaches are now capable of capturing the dynamics of entire systems.

Despite recent advancements, accurately modeling environments characterized

by steep gradients and discontinuities remains a significant challenge, particularly in the context of stellar atmospheres. This difficulty is further exacerbated by the extreme conditions surrounding neutron stars, where high-density regions are juxtaposed with low-density areas. Traditional shock-capturing methods often face difficulties in maintaining physical consistency, frequently resulting in negative densities or unphysical states, while excessively dampening the nonlinearity of underlying processes. In these environments, adopting a logarithmic approach may be crucial, as it inherently ensures the preservation of the positivity of conserved fluid variables. Spectral methods, known for their very high precision, can be employed to capture the intricate details of the system. However, achieving a balance between accuracy and stability—particularly in the presence of strong shocks—requires the careful integration of filtering techniques and controlled dissipation mechanisms to mitigate numerical instabilities.

2.1 The Logarithmic Formalism of GRHD

In this study, we aim to address some of the challenges outlined in the introductory part of this Chapter by proposing a novel logarithmic formalism for solving the GRHD equations. This approach builds on existing numerical techniques while introducing new strategies to improve the stability and accuracy of simulations, particularly in scenarios involving steep gradients, shocks, and stellar atmospheres. The logarithmic formulation offers several advantages over traditional methods, especially when employing pseudo-spectral techniques. This is particularly beneficial when dealing with strongly curved spacetimes and extreme astrophysical events. By leveraging advanced numerical methods within the 3+1 framework, this new formalism is well-suited for simulating systems where fluid dynamics and gravitational interactions are deeply intertwined, such as neutron star mergers or the formation of black hole accretion disks.

Moreover, the proposed logarithmic formalism is particularly advantageous for studying high-energy astrophysical phenomena characterized by large density contrasts and steep gradients. Such conditions often present numerical challenges, as the significant variations in fluid properties can cause standard numerical methods to break down. The present logarithmic formulation addresses these issues by transforming the conserved variables into a logarithmic space, which smooths out extreme variations and enhances numerical stability. This feature may prove especially valuable for investigating gravitational wave signals and electromagnetic counterparts from binary mergers, where accurately modeling fluid behavior is important for understanding the dynamics of these events and their observational signatures.

This study aims to present the logarithmic GRHD formalism as a method for improving numerical stability and accuracy. By integrating this approach with the well-established 3+1 decomposition, we provide a useful tool for investigating a wide range of astrophysical phenomena, from the dynamics of accretion disks to the complex interactions in neutron star mergers. As will be discussed, the logarithmic approach addresses several of the persistent challenges in relativistic hydrodynamics simulations, establishing a more robust framework for examining the intricate dynamics of matter in strong gravitational fields.

The conservation laws governing relativistic hydrodynamics are derived from the stress-energy tensor $T^{\mu\nu}$ and the continuity equation. In curved spacetime, these conservation laws are expressed using the 3+1 decomposition, which separates spacetime into three spatial dimensions and one temporal dimension, thereby simplifying

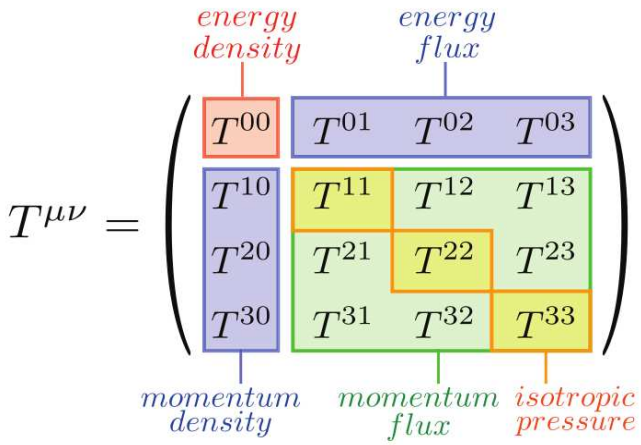

FIGURE 2.2: Schematic diagram illustrating the components of the energy-momentum tensor for a perfect fluid in the local rest frame of a co-moving observer. The mass-energy density T^{00} is highlighted in red, the energy flux T^{0i} and momentum density T^{i0} in violet, the momentum flux T^{ij} in green, and the isotropic pressure in yellow. Adapted from Rezzolla and Zanotti [147].

the numerical analysis of both Einstein field equations and the fluid dynamics. The stress-energy tensor, which encodes the distribution and flow of energy and momentum within spacetime, for a perfect fluid is given by:

$$T^{\mu\nu} = (\rho + P)u^\mu u^\nu + P g^{\mu\nu}, \tag{2.1}$$

where ρ is the total mass-energy density as measured by a Lagrangian observer (co-moving with the fluid), P is the pressure, u^μ is the four-velocity of the fluid element, and $g^{\mu\nu}$ is the contravariant spacetime metric. Typically, the total mass-energy density is decomposed into contributions from the rest mass-energy density and the internal energy density, i.e., $\rho = \rho_0(1+\varepsilon)$, where ε denotes the specific internal energy density. A schematic representation of $T^{\mu\nu}$ in the local rest frame of a co-moving observer is depicted in Fig. 2.2. In our framework, the stress-energy tensor is symmetric, a property that arises from the conservation of angular momentum and derives directly from the underlying principles of general relativity and field theory.

The evolution of the fluid can be described starting from five conservation laws (one for the conservation of rest mass, three for the conservation of energy-momentum) and one EoS for the pressure:

$$D_\mu(\rho_0 u^\mu) = 0, \tag{2.2}$$
$$D_\mu T^{\mu\nu} = 0, \tag{2.3}$$
$$P = P(\rho_0, h), \tag{2.4}$$

where D_μ denotes the covariant derivative with respect to the 4-metric $g_{\mu\nu}$, ρ_0 is the rest-mass energy density as measured by an Eulerian observer (normal to the slice Σ), and h is the specific enthalpy, namely the enthalpy per unit mass.

Within the 3+1 formalism, the stress-energy tensor can be decomposed into its constituent components using the contravariant spatial metric γ^{ij} and the time-like

unit normal vector n^μ, which is orthogonal to the hypersurface Σ, as follows:

$$T^{\mu\nu} = \left(\begin{array}{c|c} S^0 = n^\mu n^\nu T_{\mu\nu} & S^i = -\gamma^{\mu i} n^\nu T_{\mu\nu} \\ \hline S^i = -\gamma^{i\mu} n^\nu T_{\mu\nu} & S^{ij} = \gamma^{i\mu}\gamma^{j\nu} T_{\mu\nu} \end{array}\right), \tag{2.5}$$

where the components are defined as:

$$S^0 = \rho_0 h W^2 - P = \tau + D, \tag{2.6}$$
$$S^i = \rho_0 h W^2 v^i, \tag{2.7}$$
$$S^{ij} = (\tau + D + P)\, v^i v^j = S^i v^j + \gamma^{ij} P. \tag{2.8}$$

Here, S^0, S^i, and S^{ij} represent, respectively, the total mass-energy density, momentum density, and stress tensor as measured by a normal observer. Here, D is the rest-mass energy density, and τ is the difference between the total energy density and the rest-mass energy density as measured by an Eulerian observer. The three-velocity of the fluid, v^i, is related to the four-velocity by:

$$v_i = \frac{u_i}{W}, \tag{2.9}$$
$$v^i = \frac{u^i}{W} + \frac{\beta^i}{\alpha}, \tag{2.10}$$

where $W = \alpha u^0 = (1 - v_i v^i)^{-1/2}$ is the Lorentz factor, and, as usual, α and β^i denote the lapse function and the shift vector, as derived in Sec. 1.2.

The state of the fluid at any given time is characterized by the variables (ρ_0, P, and v^i), which will henceforth be referred to as the *primitive variables*. These variables are fundamental because the *conserved variables* can be expressed in terms of them as follows:

$$D = \rho_0 W, \tag{2.11}$$
$$S^i = \rho_0 h W^2 v^i, \tag{2.12}$$
$$\tau = \rho_0 h W^2 - P - D, \tag{2.13}$$

where the specific enthalpy h is defined as:

$$h = 1 + \frac{\Gamma}{\Gamma - 1}\frac{P}{\rho_0}, \tag{2.14}$$

with Γ being the adiabatic index. These quantities are referred to as *conserved variables* because they satisfy conservation laws, enabling their direct evolution in numerical simulations. It is important to note that while the energy density equation can be derived in different ways, we opt to use τ as the conserved variable to evolve rather than, for instance, the internal energy density $E = \rho_0 \varepsilon W$. This choice is motivated by the fact that the conservation equation for E would involve the time derivative of the Lorentz factor W, complicating its formulation as a balance law. However, since these conserved variables are derived from the primitive variables, recovering the primitive variables from the conserved quantities is a non-trivial task—a challenge that will be addressed in detail in the next Section.

The evolution of fluid in curved spacetime is governed by the conservation laws for mass, momentum, and energy. These laws, when expressed within the "3+1"

GRHD framework, are written as follows:

$$\partial_t D = \alpha K D + \beta^i \partial_i D - \partial_i \left(\alpha D v^i\right), \tag{2.15}$$

$$\partial_t S^i = -\left(\tau + D\right)\partial^i \alpha + \alpha K S^i + \beta^j D_j S^i - S^j D_j \beta^i - \partial_j \left[\alpha \left(S^i v^j + \gamma^{ij} p\right)\right], \tag{2.16}$$

$$\partial_t \tau = \left(\tau + p + D\right)\left(\alpha v^j v^l K_{jl} - v^j \partial_j \alpha\right) + \alpha K\left(\tau + p\right) - \partial_i \left[\alpha v^i \left(\tau + p\right)\right] + \beta^i \partial_i \tau. \tag{2.17}$$

We now manipulate the above equations as follows. A logarithmic transformation is applied specifically to the rest-mass density D and the energy density τ, as these scalar quantities are particularly prone to discontinuities and are inherently well-suited for logarithmic representation—unlike quantities such as the 3-velocity v^i, which can assume negative values. In this way, the evolution equations (2.15)–(2.17) become less sensitive to large variations in these quantities, thereby enhancing numerical stability, particularly when using pseudo-spectral methods. This approach is especially crucial in simulations of phenomena such as neutron star mergers, supernovae, and accretion onto black holes, where sharp transitions in fluid properties are common.

For the mass conservation equation, we introduce the logarithmic rest-mass density δ, defined as:

$$\delta = \ln D, \tag{2.18}$$

so that, from Eq. (2.15), the evolution of δ follows:

$$e^{\delta}\partial_t \delta = \alpha K e^{\delta} - e^{\delta}\partial_i \left(\alpha v^i\right) - \alpha v^i \partial_i e^{\delta} + \beta^i \partial_i e^{\delta}. \tag{2.19}$$

This expression simplifies to:

$$\partial_t \delta = \alpha K - \left(\alpha v^i - \beta^i\right)\partial_i \delta - \partial_i \left(\alpha v^i\right), \tag{2.20}$$

where all relevant variables have been previously introduced.

For the momentum density equation, we define the new variable $\sigma^i = h u^i = hWv^i$, where h is the specific enthalpy, W is the Lorentz factor, and v^i represents the fluid's three-velocity. This allows us to express the momentum density as:

$$S^i = \rho_0 h W^2 v^i = (\rho_0 W)(hWv^i) = D\sigma^i = e^{\delta}\sigma^i, \tag{2.21}$$

where ρ_0 denotes the rest-mass density, $D = \rho_0 W$ is the conserved density, and δ is the logarithmic scaling factor introduced in Eq. (2.18). Starting from Eq. (2.16), the evolution equation for σ^i becomes:

$$\partial_t \sigma^i = -\left(\alpha v^j - \beta^j\right) D_j \sigma^i - \left(1 + e^{-(\delta - \varepsilon)}\right)\gamma^{ij}\partial_j \alpha - \sigma^j D_j \beta^i - e^{-\delta} D_j \left(\alpha \gamma^{ij} P\right), \tag{2.22}$$

where γ^{ij} is the inverse spatial metric, and P denotes the pressure. This equation incorporates the pressure gradient and accounts for spacetime curvature effects, represented by the extrinsic curvature, as well as the lapse and shift functions.

Finally, for the energy density τ, we introduce the logarithmic variable ε, defined as:

$$\varepsilon = \ln \tau, \tag{2.23}$$

so that the evolution equation (2.17), in its logarithmic form, reads:

$$\begin{aligned} \partial_t \varepsilon &= -\left(\alpha v^i - \beta^i\right) \partial_i \varepsilon + \left[\Pi + \alpha K - D_i\left(\alpha v^i\right)\right]\left(1 + P e^{-\varepsilon}\right) \\ &\quad + \Pi\, e^{\delta - \varepsilon} - e^{-\varepsilon} \alpha v^i \partial_i P, \end{aligned} \tag{2.24}$$

where $\Pi = \alpha v^i v^j K_{ij} - v^j \partial_j \alpha$. This equation governs the evolution of the energy density, ensuring that the effects of both the fluid's motion and the curvature of spacetime are appropriately accounted for.

The complete set of GRHD evolution equations (BSSN + HD) in logarithmic form, compatible with the $3+1$ formalism, is given by:

$$\begin{aligned} \partial_t \tilde{\gamma}_{ij} &= -2\alpha \tilde{A}_{ij} + \tilde{\gamma}_{ik} \partial_j \beta^k + \tilde{\gamma}_{kj} \partial_i \beta^k - \frac{2}{3} \tilde{\gamma}_{ij} \partial_k \beta^k \\ &\quad + \beta^k \partial_k \tilde{\gamma}_{ij}, \end{aligned} \tag{2.25}$$

$$\begin{aligned} \partial_t \tilde{A}_{ij} &= \chi \left[\alpha \left(\tilde{R}_{ij} + \tilde{R}^{\chi}_{ij} - \frac{1}{3} \tilde{\gamma}_{ij} R\right) - \left(D_i D_j \alpha - \frac{1}{3} \tilde{\gamma}_{ij} D^k D_k \alpha\right)\right] \\ &\quad + \alpha \left(K \tilde{A}_{ij} - 2 \tilde{A}_{ik} \tilde{\gamma}^{kl} \tilde{A}_{lj}\right) \\ &\quad + \tilde{A}_{ik} \partial_j \beta^k + \tilde{A}_{kj} \partial_i \beta^k - \frac{2}{3} \tilde{A}_{ij} \partial_k \beta^k \\ &\quad + \beta^k \partial_k \tilde{A}_{ij} + 4\pi\alpha \left(\tilde{\gamma}_{ij} S - 2 S_{ij}\right), \end{aligned} \tag{2.26}$$

$$\partial_t \chi = \frac{2}{3} \chi \left(\alpha K - \partial_k \beta^k\right) + \beta^k \partial_k \chi, \tag{2.27}$$

$$\begin{aligned} \partial_t K &= -\tilde{\gamma}^{ij} D_i D_j \alpha + \alpha \left(\tilde{A}_{ij} \tilde{A}^{ij} + \frac{1}{3} K^2\right) + \beta^k \partial_k K \\ &\quad + 4\pi\alpha (e^{\delta} + e^{\varepsilon} + S), \end{aligned} \tag{2.28}$$

$$\begin{aligned} \partial_t \tilde{\Gamma}^i &= \tilde{\gamma}^{jk} \partial_j \partial_k \beta^i + \frac{1}{3} \tilde{\gamma}^{ij} \partial_j \partial_k \beta^k + \beta^j \partial_j \tilde{\Gamma}^i - \tilde{\Gamma}^j \partial_j \beta^i + \frac{2}{3} \tilde{\Gamma}^i \partial_j \beta^j \\ &\quad - 2 \tilde{A}^{ij} \partial_j \alpha + \alpha \left(2 \tilde{\Gamma}^i_{jk} \tilde{A}^{jk} - \frac{3}{\chi} \tilde{A}^{ij} \partial_j \chi\right. \\ &\quad \left. - \frac{4}{3} \tilde{\gamma}^{ij} \partial_j K - 16\pi e^{\delta} \sigma^i\right), \end{aligned} \tag{2.29}$$

$$\partial_t \delta = \alpha K - \left(\alpha v^i - \beta^i\right) \partial_i \delta - D_i\left(\alpha v^i\right), \tag{2.30}$$

$$\begin{aligned} \partial_t \sigma^i &= -\left(\alpha v^j - \beta^j\right) D_j \sigma^i - \left(1 + e^{-(\delta - \varepsilon)}\right) \gamma^{ij} \partial_j \alpha \\ &\quad - \sigma^j D_j \beta^i - e^{-\delta} D_j\left(\alpha \gamma^{ij} P\right), \end{aligned} \tag{2.31}$$

$$\begin{aligned} \partial_t \varepsilon &= -\left(\alpha v^i - \beta^i\right) \partial_i \varepsilon + \left[\Pi + \alpha K - D_i\left(\alpha v^i\right)\right]\left(1 + P e^{-\varepsilon}\right) \\ &\quad + \Pi\, e^{\delta - \varepsilon} - e^{-\varepsilon} \alpha v^i \partial_i P, \end{aligned} \tag{2.32}$$

where we have defined $\Pi = \alpha v^i v^j K_{ij} - v^j \partial_j \alpha$, $S_{ij} = (e^{\varepsilon} + e^{\delta} + P) v_i v_j + \chi^{-1} \tilde{\gamma}_{ij} P$, $S = \chi \tilde{\gamma}^{ij} S_{ij}$, and we have substituted $\rho = e^{\varepsilon} + e^{\delta}$ and $S^i = e^{\delta} \sigma^i$. These transformed equations establish a robust framework for simulating relativistic hydrodynamics in strongly curved evolving spacetimes. By converting key fluid quantities into logarithmic form, greater numerical stability may be achieved, particularly in

high-energy astrophysical contexts where shocks and strong gravitational fields are prevalent.

2.2 Recovery of Primitive Variables and Numerical Implementation

An essential step in solving the GRHD equations is the recovery of the primitive variables—pressure P, Lagrangian rest-mass density ρ_0, and three-velocity v^i—from the conserved variables—Eulerian rest-mass density D, momentum density S_i, and energy density τ. This process is crucial for accurately representing fluid dynamics within a simulation. The transition from conserved to primitive variables is non-trivial, particularly in the context of highly relativistic flows in curved spacetimes. In the context of GRHD, the conserved quantities are evolved in time as prescribed by the logarithmic formalism. However, these quantities do not directly represent the physical state of the fluid; rather, they are derived from the primitive variables, which are essential for defining the pressure, rest-mass density, and velocity of the fluid. Consequently, to close the system of equations, it is necessary to invert the conserved quantities to recover the primitive variables at each time step. Recovering primitive variables from conserved quantities presents a non-linear challenge. A commonly employed solution is the Newton-Raphson method [148, 149], an iterative algorithm used for root-finding. This method is particularly well-suited for obtaining precise approximations to the roots of non-linear equations, making it ideal for the recovery of primitive variables in numerical simulations of relativistic fluids.

In numerical analysis, the Newton-Raphson scheme is a root-finding algorithm that provides good approximations to the zeroes of a real-valued function. Consider a real function $f : (a, b) \to \mathbb{R}$ and an initial guess x_0 for the root, assuming the regime where $f(x)$ behaves approximately linearly. The basic idea is to approximate the function by its tangent line at x_0 and to assume that the approximate root is the x-intercept of this tangent line. Specifically, consider $f \in \mathcal{C}^2(a, b)$, which, according to the Weierstrass theorem, admits a minimum or maximum within the interval. By computing the first-order Taylor series approximation, we have:

$$f(x) \simeq f(x_0) + (x - x_0) f^{'}(x_0), \tag{2.33}$$

provided that $|x - x_0|$ is sufficiently small. This leads to the iterative formula:

$$x_{n+1} = x_n - \frac{f(x_n)}{f'(x_n)}, \tag{2.34}$$

where $f'(x_n)$ is the derivative of the function $f(x)$ evaluated at x_n. This process is repeated until convergence, that is, when the change in x_n between iterations becomes sufficiently small.

In the context of GRHD, the function $f(Q)$ that we aim to solve corresponds to the residual function, which quantifies the discrepancy between the total energy density $E = S^0$ (derived from the conserved quantities as in Eq. (2.6)) and the energy predicted by the EoS. Specifically, we define:

$$r(Q) = E(P(Q), D(Q)) - E = Q - P(Q) - E, \tag{2.35}$$

where $Q = \rho_0 h W^2$, and $E = \tau + D$ represents the total energy density. The function $r(Q)$ essentially measures how well the current estimate of the primitive variables

aligns with the conserved quantities. The goal of the Newton-Raphson method is to iteratively adjust Q (and consequently the primitive variables) to minimize $r(Q)$, ultimately driving it to zero.

In the specific case of relativistic hydrodynamics, the primitive variables are intricately related to the conserved quantities through the Lorentz factor W, the specific enthalpy h, and the pressure P. The pressure, which plays a critical role in determining the state of the fluid, is obtained from the EoS. For an ideal gas, the EoS is expressed as:

$$P = \frac{\Gamma - 1}{\Gamma} \left(\rho_0 h - \rho_0 \right). \tag{2.36}$$

The initial step in the recovery procedure involves expressing the conserved variables in terms of these primitive variables. Specifically, for the rest-mass density D, the momentum density S_i, and the total energy density τ, these relationships are given by:

$$\begin{aligned} D &= \rho_0 W, & (2.37)\\ S_i &= \rho_0 h W^2 v_i, & (2.38)\\ \tau &= \rho_0 h W^2 - P - D. & (2.39) \end{aligned}$$

These expressions are essential for accurately evolving the fluid's state in a relativistic context, as they form the bridge between the conserved and primitive variables, enabling the application of numerical methods to solve the GRHD equations.

Given the relationships between the conserved and primitive variables, the next step involves applying the Newton-Raphson method to solve for the primitive variables. To do this, we require the derivative of the residual function $r(Q)$ with respect to Q. The total energy density E depends on the pressure $P(Q)$, which in turn is a function of Q through the EoS. Consequently, the derivative of $r(Q)$ is given by:

$$r'(Q) = 1 - \frac{dP(Q)}{dQ}. \tag{2.40}$$

The derivative of the pressure with respect to Q is computed from the EoS. For an ideal gas, the pressure $P(Q)$ is related to Q by:

$$P(Q) = \frac{\Gamma - 1}{\Gamma} \frac{Q - DW}{W^2}. \tag{2.41}$$

Given that:

$$\begin{aligned} \frac{dv^2}{dQ} &= -2\frac{S^2}{Q^3}, & (2.42)\\ \frac{dW}{dQ} &= \frac{W^3}{2}\frac{dv^2}{dQ}, & (2.43)\\ \frac{d\rho_0}{dQ} &= -\frac{DW}{2}\frac{dv^2}{dQ}, & (2.44)\\ \frac{dD}{dQ} &= 0, & (2.45) \end{aligned}$$

where $v^2 = S^2/Q^2$, the derivative of $P(Q)$ with respect to Q is then:

$$\frac{dP(Q)}{dQ} = \frac{\Gamma - 1}{\Gamma} \left(\frac{1}{W^2} - \frac{W\left(D + 2(Q - DW)(1 - v^2)W\right)}{2} \frac{dv^2}{dQ} \right). \tag{2.46}$$

By substituting this expression into the Newton-Raphson iteration formula, we obtain an updated estimate for Q at each iteration:

$$Q_{n+1} = Q_n - \frac{r(Q_n)}{r'(Q_n)} = Q_n - \frac{Q_n - P(Q_n) - \tau - D}{1 - \frac{dP}{dQ}\Big|_{Q_n}}. \tag{2.47}$$

To ensure that the Newton-Raphson method converges efficiently, it is crucial to have a good initial guess for Q. One effective approach is to approximate Q by solving a quadratic equation derived from the momentum density S_i and the total energy density E. Specifically, the quadratic equation is:

$$f(Q) = S^2 - Q^2 + 2Q(2Q - 2E), \tag{2.48}$$

where $S^2 = S_i S^i$ represents the magnitude of the momentum density. The positive root of this equation provides an initial estimate for Q:

$$Q_+ = \frac{2E + \sqrt{4E^2 - 3S^2}}{3}. \tag{2.49}$$

This initial guess ensures that the Newton-Raphson iterations begin close to the true solution [150], thereby enhancing the efficiency and stability of the recovery procedure.

The Newton-Raphson method is pivotal for recovering primitive variables in high-energy astrophysical simulations dominated by relativistic effects and strong gravitational fields. Accurate recovery of these variables is essential for capturing the dynamics of relativistic shocks, accretion processes around compact objects, and neutron star mergers. The stability and efficiency of this method are critical for ensuring the accuracy of numerical simulations over long timescales. Recent advancements have confirmed the robustness of the Newton-Raphson scheme in relativistic hydrodynamics, both in flat and curved spacetimes [151, 152]. This approach remains reliable under extreme conditions, such as those near black holes or during supernovae. Numerical relativity codes, such as `GRHydro` [144] and `Whisky` [142, 153], extensively utilize this method in simulations of gravitational wave sources and compact object mergers [151, 154, 155]. As gravitational wave observatories like LIGO and Virgo continue to detect events involving neutron star mergers and black hole collisions, accurate GRHD simulations will be increasingly vital for interpreting observational data. The Newton-Raphson method, by providing a reliable initial guess, enhances the efficiency and stability of the solution process without the need to store primitive variables from previous steps. Its ability to consistently recover primitive variables from conserved quantities ensures the precision and robustness of relativistic hydrodynamics simulations across both flat and curved spacetimes.

2.3 Kelvin-Helmholtz Instability in Special Relativistic Hydrodynamics

To effectively investigate key astrophysical phenomena—such as gravitational collapse leading to black hole formation, neutron star mergers with binary companions, black hole accretion disks, and supernova explosions—it is imperative to develop a rigorous and self-consistent framework for describing the dynamics of matter [156]. In such extreme environments, various hydrodynamic instabilities can emerge, significantly impacting the transport of energy and angular momentum. Among these,

the KHI plays a fundamental role. This instability arises at the interface of shearing layers of fluid with differing velocities, leading to the formation of vortices and enhanced mixing. The KHI is particularly relevant in the study of relativistic flows, where velocity shears and steep density gradients are prevalent, such as in accretion disks, relativistic jets, and stellar atmospheres.

In this Section, we analyze the KHI within the framework of relativistic hydrodynamics, utilizing a flat Minkowskian metric. We derive the governing equations and linearize them to obtain the dispersion relation, exploring the key conditions for instability. Additionally, we compare numerical simulations to theoretical predictions to elucidate the implications of KHI on turbulence and mixing processes in astrophysical systems.

Typically, the state of a fluid is characterized by its velocity u^i, mass-energy density ρ, and pressure P. The foundation of special relativistic hydrodynamics is rooted in the stress-energy tensor for a perfect fluid, which assumes the absence of viscosity and heat conduction. Within the context of special relativity, employing a flat Minkowski metric, the stress-energy tensor is analogous to Eq. (2.1), presented in Sec. 2.1, and is expressed as:

$$T_{\mu\nu} = (\rho + P)u_\mu u_\nu + P\eta_{\mu\nu}, \tag{2.50}$$

where the metric is given by $g_{\mu\nu} = \eta_{\mu\nu} = \text{diag}(-1, 1, 1, 1)$.

Following a similar derivation as in Sec. 2.1, the set of GRHD equations, namely Eq.s (2.15–2.17), simplify for a special relativistic fluid to:

$$\partial_t D + \partial_i(Dv^i) = 0, \tag{2.51}$$

$$\partial_t S_i + \partial_j(S_i v^j) + \partial_i P = 0, \tag{2.52}$$

$$\partial_t \tau + \partial_i[(\tau + P)v^i] = 0, \tag{2.53}$$

where the various quantities, all measured in an Eulerian frame, have been thoroughly defined in the previous Chapter. The adoption of a flat metric is justified by our focus on examining instabilities and dynamics locally within accretion disks and relativistic jets, thereby allowing the approximation of spacetime as Minkowskian.

KHI represents a fundamental hydrodynamic instability that arises when a perturbation is introduced into a flow exhibiting transverse velocity shear, which may manifest as either a continuous or discontinuous variation [157]. This instability was independently identified by Helmholtz [158] and by Lord Kelvin [159]. Helmholtz's initial contribution provided a qualitative framework for understanding the interaction between two vertically stratified fluids of differing densities, whereas Kelvin extended the analysis to geophysical phenomena, with a particular focus on the interaction between wind and water or, more generally, between fluids and air currents in relative motion. The KHI leads to the dissipation of ordered kinetic energy into turbulent forms, thereby inducing turbulence, heating, and particle acceleration. This instability is frequently observed in natural systems, such as vertical stratification within air currents [160, 161], as depicted in Fig. 2.3, and within Earth's atmosphere [162, 163, 164, 165, 166]. The KHI has also been extensively investigated in various astrophysical contexts, including the study of astrophysical jets, interactions within Earth's magnetosphere, the dynamics of interstellar clouds, clumping in supernova remnants, high-energy plasmas, and even in quantized vortices within quantum fluids [167, 168, 169, 170].

When a denser fluid is situated above a less dense fluid, the ensuing instability is known as the Rayleigh-Taylor Instability (RTI) [171, 172], predominantly driven by

FIGURE 2.3: The so-called Kelvin-Helmholtz clouds arise due to the interaction of two superposed air currents moving at different velocities. This shear flow leads to the formation of vortices, which, in turn, trigger turbulence.

gravitational forces. Another significant fluid instability is the Richtmyer-Meshkov Instability (RMI) [173, 174], which arises due to shock interactions and plays a crucial role in processes such as supernova explosions and the generation of non-uniform turbulence. Each of these instabilities—KHI, RTI, and RMI—exhibits distinct growth characteristics: both KHI and RTI display exponential growth rates, whereas RMI is characterized by linear growth proportional to time. However, in complex interfacial flows where rolling and mixing of layers occur, these instabilities often become intertwined and are collectively referred to as KHI.

To investigate the Kelvin-Helmholtz Instability (KHI) within the framework of relativistic hydrodynamics, Bodo *et al.* [175] analyzed two adjacent flows of a relativistic unmagnetized fluid, with the xz-plane acting as the interface. The system is considered in a reference frame where the two flows move with equal and opposite velocities, described by:

$$\boldsymbol{u} = \begin{cases} (+U,0,0) & \text{for } y \geq 0, \\ (-U,0,0) & \text{for } y < 0, \end{cases} \tag{2.54}$$

where U denotes a positive velocity, as depicted in Fig. 2.4. Both flows consist of the same fluid, thus possessing identical uniform unperturbed mass-energy density ρ and pressure P.

The theoretical foundation of this analysis is grounded in the equations of relativistic hydrodynamics for a perfect fluid in flat Minkowskian geometry [176]. A perfect fluid is characterized by having a velocity $\boldsymbol{u}$ at each point, such that an observer co-moving with this velocity perceives the fluid as isotropic. In the laboratory reference frame, where the fluid is observed to move with velocity $\boldsymbol{u}$ at a given spacetime point, the energy-momentum tensor can be expressed in its boosted form as:

$$T^{\alpha\beta} = \Lambda^{\alpha}_{\gamma}(\boldsymbol{u})\Lambda^{\beta}_{\delta}(\boldsymbol{u})\tilde{T}^{\gamma\delta}, \tag{2.55}$$

where $\tilde{T}^{\gamma\delta}$ denotes the energy-momentum tensor in the fluid's rest frame, and $\Lambda^{\alpha}_{\gamma}(\boldsymbol{u})$ represents the transformation operators that map quantities from the fluid's co-moving frame to the laboratory rest frame. Decomposing the energy-momentum

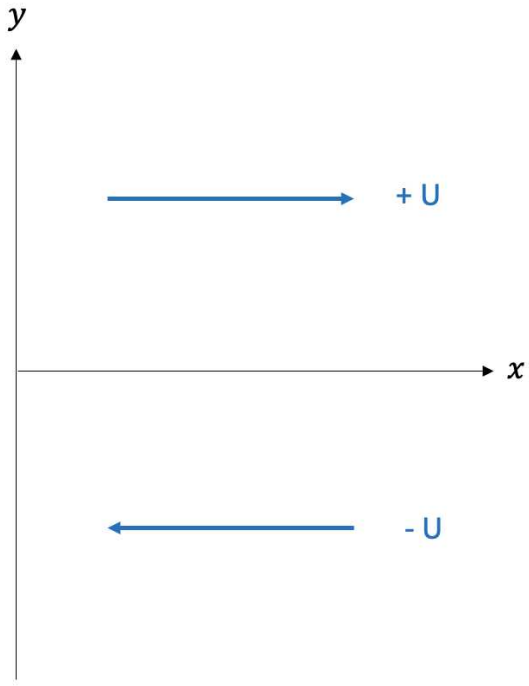

FIGURE 2.4: Sketch of fluid flows in the xy-plane: the two streams move with equal magnitude but in opposite directions within the positive and negative y-half planes, respectively.

tensor into its spatial, mixed, and temporal components, the expression can be written as:

$$\begin{aligned} T^{ij} &= P\delta^{ij} + (P+\rho)\frac{u^i u^j}{1-u^2}, \\ T^{i0} &= T^{0i} = (P+\rho)\frac{u^i}{1-u^2}, \\ T^{00} &= \frac{(\rho + Pu^2)}{1-u^2}, \end{aligned} \tag{2.56}$$

where the four-velocity components are given by:

$$\begin{aligned} \frac{dx^i}{d\tau} &= \frac{u^i}{\sqrt{1-u^2}} \equiv U^i, \\ \frac{dt}{d\tau} &= \frac{1}{\sqrt{1-u^2}} \equiv U^0. \end{aligned} \tag{2.57}$$

We note that in this context, τ represents the proper time, which is the time interval measured by an observer co-moving with the fluid element, corresponding to the time experienced along the fluid's worldline.

The motion of the fluid is governed by the conservation equations for rest-mass density, momentum, and energy, as given in Eq.s (2.51)–(2.53). These equations are closed by an EoS, which is typically expressed as:

$$h = h(P, \rho_0), \tag{2.58}$$

from which the sound speed is defined as:

$$c_s = \sqrt{\frac{1}{h}\frac{\partial P}{\partial \rho_0}\bigg|_s}, \tag{2.59}$$

where the derivative is taken at constant entropy s. For a relativistic non-degenerate perfect gas, the sound speed must satisfy the condition $c_s < 1/\sqrt{3}$. This can be demonstrated by considering a fluid composed of structureless point particles interacting through localized collisions. The energy-momentum tensor for a collection of such particles, which describes the distribution and flow of energy and momentum through spacetime, is given by:

$$T^{\alpha\beta} = \sum_N \frac{p_N^\alpha p_N^\beta}{E_N}\delta^3(\boldsymbol{x} - \boldsymbol{x}_N), \tag{2.60}$$

where p_N^α and E_N are the momentum and energy of the N-th particle, respectively, and δ^3 is the three-dimensional Dirac delta function. In a co-moving Lorentz frame, the energy-momentum tensor $T^{\alpha\beta}$ assumes the isotropic form (2.56), with the pressure P and mass-energy density ρ expressed as:

$$P = \frac{1}{3}\sum_{i=1}^{3} T^{ii} = \frac{1}{3}\sum_N \frac{p_N^2}{E_N}\delta^3(\boldsymbol{x} - \boldsymbol{x}_N), \tag{2.61}$$

$$\rho = T^{00} = \sum_N E_N \delta^3(\boldsymbol{x} - \boldsymbol{x}_N), \tag{2.62}$$

where the particle number density n is defined as:

$$n = \sum_N \delta^3(\boldsymbol{x} - \boldsymbol{x}_N). \tag{2.63}$$

From these relations, we deduce that, in the general case where $E_N \geq |\boldsymbol{p}_N|$, the pressure P and energy density ρ must satisfy the inequality $0 \leq P \leq \rho/3$. This inequality arises because the energy density ρ includes both rest mass energy and kinetic energy contributions, whereas the pressure P is related to the kinetic energy alone. In the case of an extremely relativistic gas, where the particle energies are dominated by their kinetic contributions, i.e., $E_N \simeq |\boldsymbol{p}_N| \gg m$, the pressure and energy density become closely related, leading to the simplified relation $\rho \simeq 3P \gg nm$. This indicates that the fluid's behavior approaches that of a radiation-dominated system, where the pressure is approximately one-third of the energy density. Consequently, the sound speed c_s in such a gas is constrained to be less than $1/\sqrt{3}$, as higher sound speeds would imply superluminal signal propagation, which is physically forbidden.

Our objective now is to derive the dispersion relation for the KHI. To accomplish this, we first obtain the perturbative solutions to the linearized form of the RHD equations (2.51)–(2.53). We begin by considering the reference frame in which the fluid flows are stationary. In this frame, sound wave solutions naturally arise. Denoting a generic three-dimensional perturbation of the flow variables by δq (where q represents either the mass-energy density ρ, the pressure P, or the 4-velocity u^i), we express this perturbation as:

$$\delta\tilde{q}_\pm \propto \exp\left[i\left(\tilde{k}_\pm\tilde{x} + \tilde{l}_\pm\tilde{y} + \tilde{m}_\pm\tilde{z} - \tilde{\omega}_\pm\tilde{t}\right)\right], \tag{2.64}$$

where the tilde denotes quantities in the rest frame, $\tilde{k}$, $\tilde{l}$, and $\tilde{m}$ are the components of the spatial wave vector in the x-, y-, and z-directions, respectively, $\tilde{\omega}$ is the frequency, and the $\pm$ subscripts correspond to the fluid regions in $y > 0$ (positive velocity) and $y < 0$ (negative velocity), respectively. Consequently, the dispersion relation for sound waves in the rest frame is given by:

$$\tilde{\omega}_{\pm}^2 = (\tilde{k}_{\pm}^2 + \tilde{l}_{\pm}^2 + \tilde{m}_{\pm}^2)c_s^2. \tag{2.65}$$

In the laboratory frame, where the flows move with equal and opposite velocities as described by Eq. (2.54), a generic three-dimensional perturbation takes the form:

$$\delta q_{\pm} \propto \exp[i(kx + l_{\pm}y + mz - \omega t)], \tag{2.66}$$

where only the component of the wave vector in the y-direction, $l_{\pm}$, varies across the interface between the two flows. The dispersion relation (2.65) in the laboratory frame can be obtained by applying a Lorentz transformation to the wave 4-vector $K_{\pm}^{\mu} = (k, l_{\pm}, m, \omega)$, translating it into the rest frame quantities $\tilde{k}_{\pm}$, $\tilde{l}_{\pm}$, $\tilde{m}_{\pm}$, and $\tilde{\omega}_{\pm}$. Specifically:

$$\begin{aligned} \tilde{\omega}_{\pm} &= W(\omega \mp kU), \\ \tilde{k}_{\pm} &= W(k \mp \omega U), \\ \tilde{l}_{\pm} &= l_{\pm}, \\ \tilde{m}_{\pm} &= m. \end{aligned} \tag{2.67}$$

Substituting these into the dispersion relation, the expression in the laboratory frame becomes:

$$W^2(\omega \mp kU)^2 = [W^2(k \mp \omega U)^2 + l_{\pm}^2 + m^2]c_s^2. \tag{2.68}$$

If we consider the Lagrangian (or material) derivative of the fluid displacements $\delta\xi_{\pm}(t, x)$ at the interface, we obtain:

$$\frac{d\delta\xi_{\pm}(t,x)}{dt} = \frac{\partial\delta\xi_{\pm}(t,x)}{\partial t} + \boldsymbol{v} \cdot \nabla\delta\xi_{\pm}(t,x), \tag{2.69}$$

where the Lagrangian derivative $\dfrac{d\delta\xi_{\pm}(t,x)}{dt}$ represents the rate of change of displacement as experienced by a fluid element, with $\boldsymbol{v}$ denoting the velocity field of the fluid. It is important to note that $\dfrac{d\delta\xi_{\pm}(t,x)}{dt}$ corresponds to the transverse velocity δv_y of the fluid element. Consequently, ensuring the continuity of displacements across the interface leads to the following condition:

$$\frac{\delta v_{y+}}{\omega - kU} = \frac{\delta v_{y-}}{\omega + kU}. \tag{2.70}$$

This equation arises from the requirement that the displacement of fluid elements on either side of the interface remains continuous. It implies that the ratio of the transverse velocity δv_y to the effective frequency, adjusted for the Doppler shift due to the flow velocity U, must be equal on both sides of the interface. Such continuity is essential for accurately describing the behavior of perturbations at the boundary between the two flows.

To determine the tangential velocity δv_y, we linearize the transverse component of Euler's equation (2.52), which yields the following linearized equation:

$$-i\omega\delta v_{y\pm} + iv_x k\delta v_{y\pm} = -\frac{1}{\rho h W^2}(il_\pm \delta p) + \frac{i\omega v_y \delta p}{\rho h W^2}. \tag{2.71}$$

Simplifying by cancelling the imaginary unit and multiplying by -1, and noting that v_x takes the values $\pm U$ while v_y is zero, we obtain:

$$\delta v_{y\pm} = \frac{l_\pm \delta p}{(\omega \mp kU)\rho h W^2}. \tag{2.72}$$

Next, we introduce the dimensionless particle velocity $\phi = \omega/c_s k$, the classical Mach number $M = U/c_s$, and $\beta = U/c = U$ (considering that we are using natural units where $c = 1$). With these definitions, the dispersion relation (2.68) can be solved to express $l_\pm$ as a function of ϕ, k, m, M, and β. After step-by-step simplification, we find:

$$l_\pm = Wk\sqrt{\left(\phi \mp M\right)^2 - \left(1 \mp \frac{\phi\beta^2}{M}\right)^2 - \frac{m^2}{W^2k^2}}. \tag{2.73}$$

In this expression, $l_\pm$ may generally be complex. For physical consistency, the imaginary part of l_+ must be positive for $y > 0$, while the imaginary part of l_- must be negative for $y < 0$. A revised version of the dispersion relation can be obtained by substituting Eq. (2.72) into Eq. (2.70), yielding:

$$\frac{l_+ \delta p}{(\omega - kU)^2 \rho h W^2} = \frac{l_- \delta p}{(\omega + kU)^2 \rho h W^2}. \tag{2.74}$$

Given that $l_\pm$ is defined by the final form of Eq. (2.73), the expression above becomes:

$$\frac{Wk\sqrt{\left(\phi + M\right)^2 - \left(1 + \frac{\phi\beta^2}{M}\right)^2 - \frac{m^2}{W^2k^2}}}{(\omega + kU)^2}. \tag{2.75}$$

By introducing the parameter $\alpha = m/k$ and explicitly expressing the Lorentz factor as $W = (1-\beta^2)^{-1/2}$, after some algebraic manipulation, Eq. (2.75) can be rewritten as a biquadratic equation:

$$\begin{aligned} &\phi\left\{\left(\frac{\phi}{M}\right)^4 [M^2 + \beta^2 - 2\beta^4] \right. \\ &-2\left(\frac{\phi}{M}\right)^2 \left[M^2 + 1 + \alpha^2 - \alpha^2\beta^2 - 3\beta^2 + \beta^4\right] \\ &\left. + M^2 - 2 - 2\alpha^2 + 2\alpha^2\beta^2 + \beta^2 \right\} = 0. \end{aligned} \tag{2.76}$$

As we will discuss later, the above equation can be reformulated in various ways to ultimately derive the expression for the growth rate of the KHI. At this point, it is useful to introduce the relativistic Mach number, defined as $\mathcal{M} = MW/W_s$, where $W_s = (1 - c_s^2)^{-1/2}$ represents the Lorentz factor associated with the sound speed c_s. Furthermore, we define the effective relativistic Mach number as $\mathcal{M}_e = \mathcal{M}\cos\theta$, where θ denotes the angle between the fluid velocity and the wave vector projection

in the xz-plane. Consequently, $\cos\theta$ is given by $\cos\theta = (1+\alpha^2)^{-1/2}$, with $\alpha = m/k$ as introduced earlier. With all these preconditions, we can derive a new expression for the Mach number as follows:

$$M = \frac{W_s \mathcal{M}}{W} = \sqrt{\frac{1-\beta^2}{M^2-\beta^2}}\frac{\mathcal{M}_e}{\cos\theta}\, M, \tag{2.77}$$

Dividing by M and then squaring, we obtain:

$$M^2 = \beta^2 + \mathcal{M}^2(1-\beta^2). \tag{2.78}$$

Returning to Eq. (2.76), we substitute the final form of M^2 from Eq. (2.78). By simplifying the factor $(1-\beta^2)$, common to all terms, and then dividing by $(1+\alpha^2)$ (which corresponds to $\cos^2\theta$), and recalling the definitions of the effective relativistic Mach number $\mathcal{M}_e$ and the effective fluid velocity $\beta_e = \beta\cos\theta$, we obtain:

$$\phi\left\{\left(\frac{\phi}{M}\right)^4(\mathcal{M}_e^2+2\beta_e^2) - 2\left(\frac{\phi}{M}\right)^2(\mathcal{M}_e^2+1-\beta_e^2) + (\mathcal{M}_e^2-2)\right\} = 0. \tag{2.79}$$

The non-trivial solution to the biquadratic equation is given by:

$$\frac{\phi^2}{M^2} = \frac{(\mathcal{M}_e^2+1-\beta_e^2) \pm \sqrt{4\mathcal{M}_e^2(1-\beta_e^2)+(1+\beta_e^2)^2}}{\mathcal{M}_e^2+2\beta_e^2}. \tag{2.80}$$

It is important to note that if ϕ, and consequently ω, are purely imaginary, we can express ω as $\omega = i\tilde{\omega}$, where $\tilde{\omega} \in \mathbb{R}$. This leads to:

$$\delta q_\pm \propto \exp[i(-i\tilde{\omega}t)] = \exp(\tilde{\omega}t). \tag{2.81}$$

This equation represents the classical exponential growth of the perturbation. Therefore, from Eq. (2.80), to obtain an unstable mode, we must consider only the solution with the negative sign, as this ensures that ϕ, and thus ω, are purely imaginary. Given that the denominator is always positive, we must analyze the conditions under which the numerator becomes negative:

$$\mathcal{M}_e^2 + 1 - \beta_e^2 - \sqrt{4\mathcal{M}_e^2(1-\beta_e^2)+(1+\beta_e^2)^2} < 0. \tag{2.82}$$

After performing the necessary calculations, we arrive at the following condition for instability:

$$\mathcal{M}_e < \sqrt{2}. \tag{2.83}$$

This implies that when $\mathcal{M}_e < \sqrt{2}$, the solution in Eq. (2.80) with the negative sign is unstable, whereas for $\mathcal{M}_e > \sqrt{2}$, the solution becomes stable. Using the instability condition in Eq. (2.83), we can derive a criterion for the velocity. Applying the definitions of $\mathcal{M}_e$, $\mathcal{M}$, M, W, and W_s, we obtain:

$$\frac{U\cos\theta}{c_s} < \sqrt{2}\sqrt{\frac{1-U^2}{1-c_s^2}}. \tag{2.84}$$

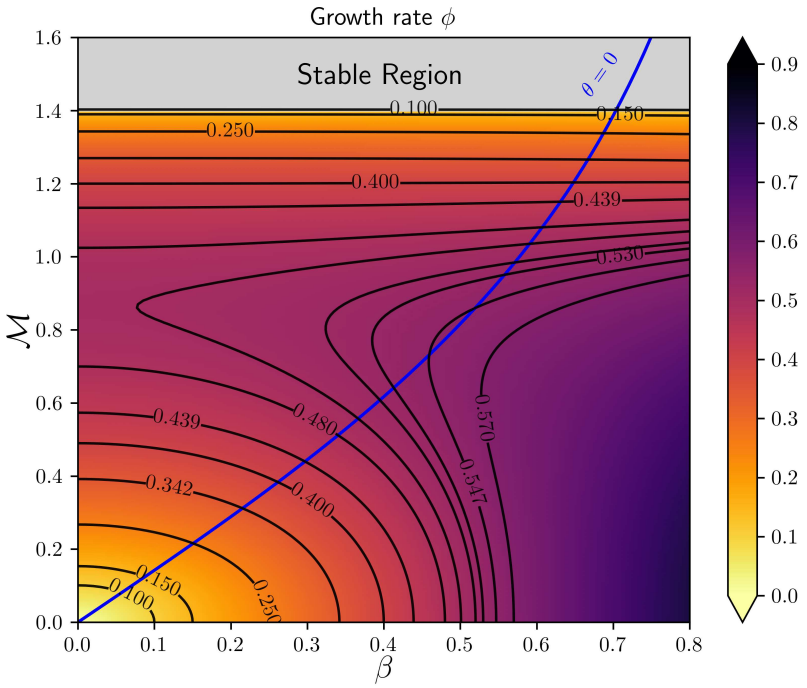

FIGURE 2.5: 2D shaded contour plot of the growth rate for the most unstable mode. The range of $\mathcal{M}$ and β is constrained by the unphysical region where c_s exceeds $1/\sqrt{3}$. The blue curve delineates the upper boundary of this unphysical region for $\theta = 0$. The gray area indicates the region in which this mode becomes stable, specifically for $\mathcal{M}_e > \sqrt{2}$.

Isolating U, we derive the instability condition for the velocity:

$$|U| < \frac{1}{\cos\theta}\sqrt{\frac{2c_s^2}{1+c_s^2}}. \tag{2.85}$$

It is also possible to define a physically accessible region by considering the restriction $c_s < 1/\sqrt{3}$. Given the definitions of β and M, it follows that $c_s = \beta/M$. Therefore, we can express this as:

$$\frac{\beta}{M} < \frac{1}{\sqrt{3}} \;\Rightarrow\; M > \sqrt{3}\beta. \tag{2.86}$$

A corresponding condition can be established for the relativistic Mach number $\mathcal{M}$ to define the physical region. By multiplying all terms of Eq. (2.86) by W/W_s, we obtain:

$$\mathcal{M} > \sqrt{3}\beta W\sqrt{1-c_s^2}. \tag{2.87}$$

Given the upper limit of c_s^2 as $1/3$, the physically accessible region is defined by the following condition:

$$\mathcal{M} > \sqrt{2}\beta W. \tag{2.88}$$

At this stage, we introduce a graphical algorithm to represent the growth rate of the instability by solving for the roots of Eq. (2.80). For simplicity, we focus on a two-dimensional scenario, neglecting the spatial wave number in the z-direction, m. Consequently, $\alpha = 0$ as $m = 0$, and thus $\cos\theta = 1$, allowing us to consider the case where $\theta = 0$. In Fig. 2.5, ϕ is plotted as a function of $\mathcal{M}$ and β for $\cos\theta = 1$.

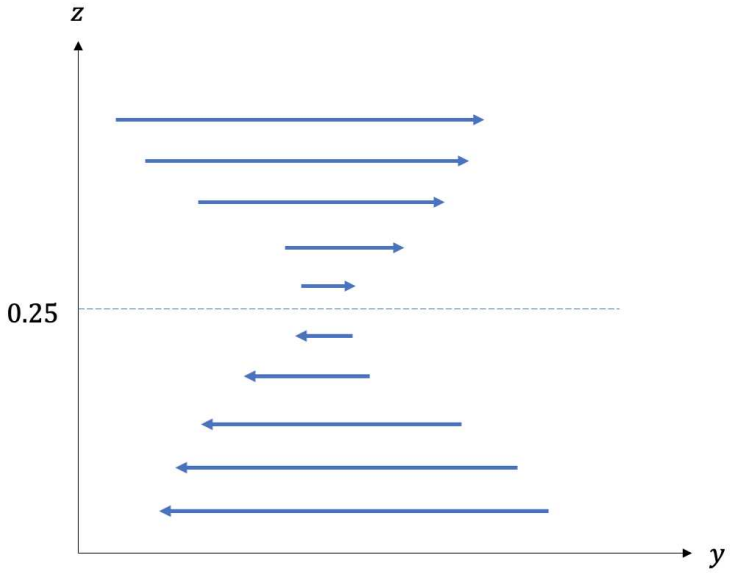

FIGURE 2.6: Sketch of the fluid velocity in the yz-plane as implemented in our code. The figure illustrates the profile of a single hyperbolic tangent, with a change in direction at $z = 0.25$.

The growth rate of the unstable mode is depicted, with the condition in Eq. (2.88) satisfied only above the blue curve.

2.3.1 Numerical Simulations of the KHI in Special Relativity

In the following, we conduct a numerical investigation of the KHI within the framework of special relativity, utilizing a configuration that qualitatively reflects the shear layer conditions described by Bodo *et al.* [175]. To this end, we employ the logarithmic extension of the `SFINGE` code, implemented in accordance with the prescriptions outlined in Sec.s 2.1–2.2. Our objective is to compute the specific growth rate ϕ for given values of the effective Mach number $\mathcal{M}$ and β. We construct an unstable flow in special relativity by perturbing a smooth shear layer of finite thickness. `SFINGE` is implemented in Fortran and leverages parallel computing, with parallelization along the z-direction. Accordingly, our reference frame is the yz-plane, as illustrated in Fig. 2.6. As is typical in numerical methods, we employ hyperbolic tangent profiles. Specifically, we apply periodic boundary conditions in all directions, using a double-hyperbolic-tangent profile to satisfy these conditions, as detailed below.

We now delve into the initial conditions of our KHI simulations. In this case, the 2D spatial domain is defined as $y, z \in [0, L]$, with $L = 1$, and the computational grid consists of $N_y \times N_z = 1024^2$ points. The velocity shear profile is implemented as follows:

$$v_y(z) = v_s \left[\tanh\left(\frac{z - z_1}{a_0}\right) - \tanh\left(\frac{z - z_2}{a_0}\right) - 1 \right], \tag{2.89}$$

where $z_1 = 0.25$, $z_2 = 0.75$, and $a_0 = 0.01$. Fig. 2.7 illustrates this shear profile for a velocity amplitude $v_s = 0.5$. The imposed velocity perturbation is expressed as:

$$v_z(y, z) = A \left\{ \exp\left[-0.5 \left(\frac{z - z_1}{\sigma_0}\right)^2 \right] - \exp\left[-0.5 \left(\frac{z - z_2}{\sigma_0}\right)^2 \right] \right\} \Delta_n, \tag{2.90}$$

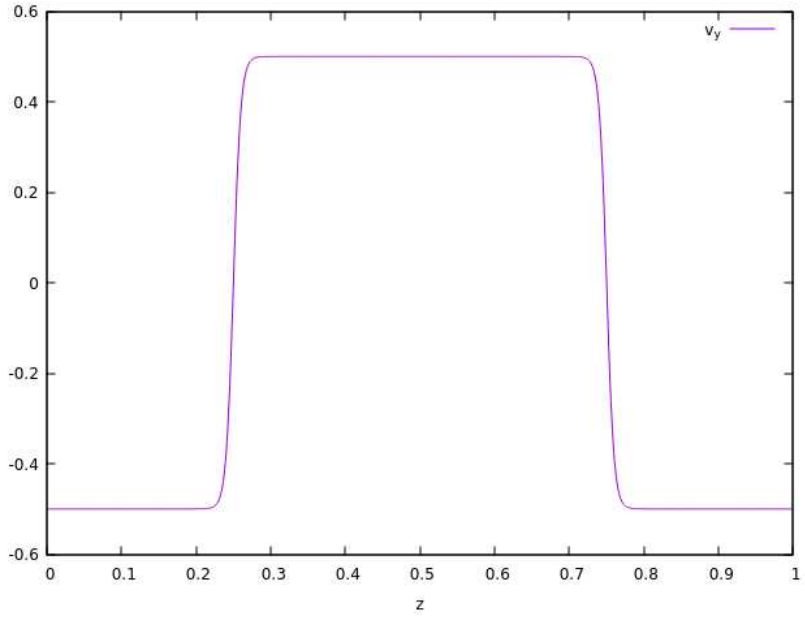

FIGURE 2.7: Profile of the shear velocity $v_y(z)$ for a shear layer thickness $a_0 = 0.01$ and a shear velocity amplitude $v_s = 0.5$.

where the amplitude factor is set to $A = 10^{-8} v_s$, and $\sigma_0 = 0.1$. The term Δ_n is defined as:

$$\Delta_n = \sum_{i=1}^{n} \cos\left(\frac{2\pi y}{L} i + \phi_r\right), \tag{2.91}$$

with $n = 10$, and ϕ_r representing randomly chosen phases.

The equilibrium rest-mass density $\tilde{\rho}_0$ is assumed to be constant, while the enthalpy is derived from the EoS as follows:

$$h = 1 + \frac{\Gamma}{\Gamma - 1} \frac{\tilde{P}_0}{\tilde{\rho}_0}, \tag{2.92}$$

where $\tilde{P}_0$ represents the equilibrium pressure, and the adiabatic index is given as $\Gamma = 4/3$. From the expression for the sound speed:

$$c_s = \sqrt{\frac{\Gamma \tilde{P}_0}{\tilde{\rho}_0 h}}, \tag{2.93}$$

substituting the expression for enthalpy h from Eq. (2.92), and given the values of c_s, Γ, and $\tilde{\rho}_0 = 1$, we find:

$$\tilde{P}_0 = \frac{c_s^2}{\Gamma(1 - 3c_s^2)}. \tag{2.94}$$

This expression for $\tilde{P}_0$ can then be substituted back into Eq. (2.92) to yield:

$$h = 1 + \frac{3c_s^2}{1 - 3c_s^2}. \tag{2.95}$$

It is important to note that both $\tilde{P}_0$ and h are functions of the sound speed c_s. Additionally, it should be clarified that $\tilde{\rho}_0$ and $\tilde{P}_0$ refer to the equilibrium rest-mass energy density and equilibrium pressure, respectively, and should not be confused

with the rest-mass energy density and pressure introduced earlier. For clarity, these equilibrium quantities are denoted with a tilde.

For a relativistic non-degenerate perfect gas, the sound speed must satisfy $c_s < 1/\sqrt{3}$. In our analysis of the growth rate, we determined that for an unstable solution, the relativistic Mach number $\mathcal{M}$ (with $\mathcal{M} \equiv \mathcal{M}_e$ since $\theta = 0$) must satisfy the condition given in Eq. (2.83). Additionally, the velocity shear v_s is constrained by the condition provided in Eq. (2.85), where $\cos\theta = 1$. With these clarifications, we are now prepared to simulate the KHI in special relativistic flows, as described in the following Section. Before proceeding, we will discuss the procedure for measuring the growth rate from our numerical simulations.

For each simulation run, we extract the velocity perturbation $v_z(y, z, t)$ from the data corresponding to each time frame t. A 1D FFT is then applied along the y-direction. At any given time t, the perturbation is projected into Fourier space to obtain the complex coefficients:

$$\tilde{v}_z(k_y, z, t) = \int v_z(y, z, t) e^{-ik_y y}\, dy, \tag{2.96}$$

which are numerically derived via an inverse FFT. To analyze the power spectrum of the fluctuations, we compute the modal energy:

$$E(k_y, z, t) = |\tilde{v}_z|^2. \tag{2.97}$$

The spectra are then averaged along the z-direction through a simple summation:

$$\langle E \rangle (k_y, t) = \frac{1}{N^*} \sum_{i=1}^{N^*} |\tilde{v}_z|^2 (k_y, z, t), \tag{2.98}$$

where the sum extends over a set of N^* points in the z-direction. In practice, this averaging is conducted at the locations corresponding to the maxima of the shear layers (approximately at $z \sim 0.25$ and $z \sim 0.75$). From this, the temporal evolution of the modes is determined as $\langle v \rangle (k_y, t) = \sqrt{\langle E \rangle}$.

If the KHI is accurately modeled, the perturbation modes will exhibit exponential growth over time. This growth can be mathematically expressed as:

$$\langle v \rangle (k_y, t) = A e^{\omega t}, \tag{2.99}$$

from which the exponent ω can be determined. To extract this value, we apply a logarithmic transformation followed by linear regression:

$$\log \langle v \rangle = \log A + \omega t. \tag{2.100}$$

This methodology enables the determination of the experimental growth rate, which can subsequently be compared to the theoretical prediction, given that the growth rate is defined as $\phi = \omega / c_s k$. It is noteworthy that the finite thickness of the shear layers in our simulations may give rise to multiple unstable modes k_y, where $k_y = 2\pi m / L$. The focus of our analysis is on identifying the most unstable mode, namely the k-vector that demonstrates the most rapid growth over time.

In addition to the initial conditions, it is essential to discuss several other numerical parameters. For the first test introduced here, we select a filtering mode of $k^* = N/2.5$, where N represents the number of mesh points along either the z- or y-direction, and an initial integration time step of $\Delta t = 10^{-4}$. The sound speed is

chosen as:

$$c_s = 0.4 < \frac{1}{\sqrt{3}} \approx 0.577, \tag{2.101}$$

which yields the equilibrium pressure as $\tilde{P}_0 = 0.2308$. For the velocity shear, we select:

$$v_s = 0.5 < \sqrt{\frac{2c_s^2}{1+c_s^2}} \approx 0.525. \tag{2.102}$$

Using the values of c_s and v_s, we compute the relativistic Mach number $\mathcal{M}$ as:

$$\mathcal{M} = \frac{\sqrt{1-c_s^2}}{\sqrt{1-v_s^2}} \frac{v_s}{c_s} \approx 1.3228 < \sqrt{2} \approx 1.4142. \tag{2.103}$$

All the relevant parameters are summarized in Table 2.1.

Parameter	*Symbol*	*Value*
Filtering mode	k^*	$N/2.5$
Time step	Δt	10^{-4} M
Sound speed	c_s	0.4
Equilibrium pressure	$\tilde{P}_0$	0.2308
Velocity shear	v_s	0.5
Relativistic Mach number	$\mathcal{M}$	1.3238

TABLE 2.1: Initial conditions of the first KHI simulation.

In Fig. 2.8, we present the time evolution of different modes. The data fitting is restricted to the interval $t \in [0.8, 1.4]$, as the modes undergo stabilization in the early stages, leading to deviations from the expected linear behavior. Among the most unstable modes, the second mode $m = 2$ exhibits the most consistent growth. The growth rate for this mode is given by:

$$\phi = \frac{\omega}{c_s\left(\frac{2\pi m}{L}\right)} = \frac{0.8955}{0.4(4\pi)} = 0.18. \tag{2.104}$$

This value shows good agreement with the theoretical prediction:

$$\phi_{\text{th}} = 0.27. \tag{2.105}$$

Better agreement could be achieved with larger simulations and higher resolution.

For the second test, we modify the values of c_s and $\beta = \mathcal{U}$, and to ensure numerical stability, we introduce a dissipation coefficient. The filtering mode is set to $k^* = N/2.5$, with an initial integration time step of $\Delta t = 6.0 \times 10^{-5}$ and a hyperviscous coefficient $\nu_4 = 10^{-12}$. For the sound speed, we select:

$$c_s = 0.5633 < \frac{1}{\sqrt{3}} \approx 0.577, \tag{2.106}$$

which yields an equilibrium pressure of $\tilde{P}_0 = 4.9497$. For the velocity shear, we set:

$$v_s = 0.6 < \sqrt{\frac{2c_s^2}{1+c_s^2}} \approx 0.694. \tag{2.107}$$

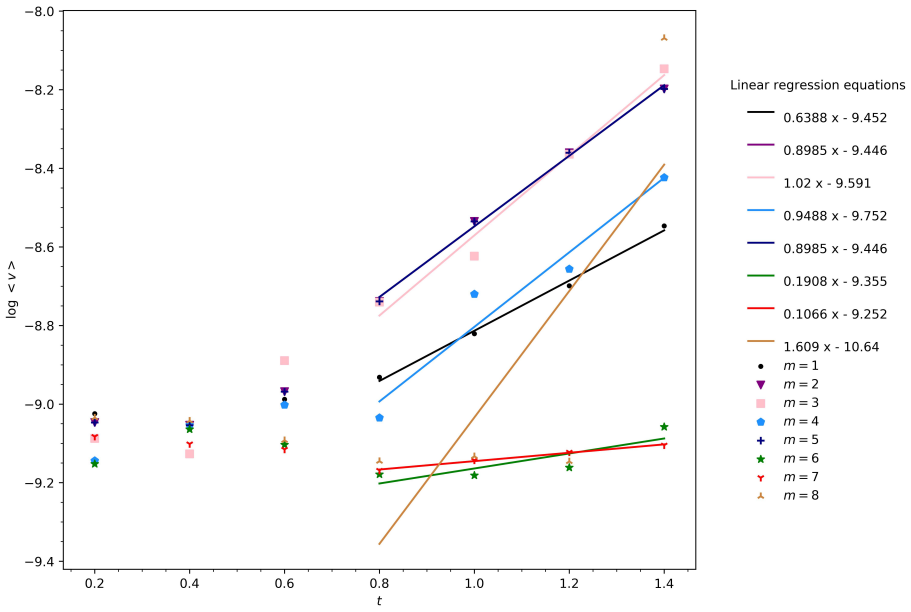

FIGURE 2.8: Natural logarithm of the growth of the perturbation modes $\langle v \rangle$ as a function of t, for the most unstable modes m. The linear regression is performed from $t = 0.8$ to $t = 1.4$. Different colors represent different modes.

Consequently, the relativistic Mach number $\mathcal{M}$ is given by:

$$\mathcal{M} = \frac{\sqrt{1-c_s^2}}{\sqrt{1-v_s^2}} \frac{v_s}{c_s} = 1.1 < \sqrt{2}. \tag{2.108}$$

All the parameters are summarized in Table 2.2.

Parameter	*Symbol*	*Value*
Filtering mode	k^*	$N/2.5$
Time step	Δt	6.0×10^{-5}
Hyperviscous coefficient	ν_4	10^{-12}
Sound speed	c_s	0.5633
Equilibrium pressure	$\tilde{P}_0$	4.9632
Velocity shear	v_s	0.6
Relativistic Mach number	$\mathcal{M}$	1.1

TABLE 2.2: Initial conditions of the second KHI simulation.

In Fig. 2.9, the time history of each mode is shown. We focus on the linear regime, restricting the analysis to $t \leq 2.4$. It can be observed that the most unstable mode corresponds to $m = 4$. The growth rate for this configuration is given by:

$$\phi = \frac{\omega}{c_s \left(\frac{2\pi m}{L}\right)} = \frac{2.269}{0.5633(8\pi)} = 0.16, \tag{2.109}$$

while the theoretical prediction, assuming a sharp boundary, is:

$$\phi_{\text{th}} = 0.46. \tag{2.110}$$

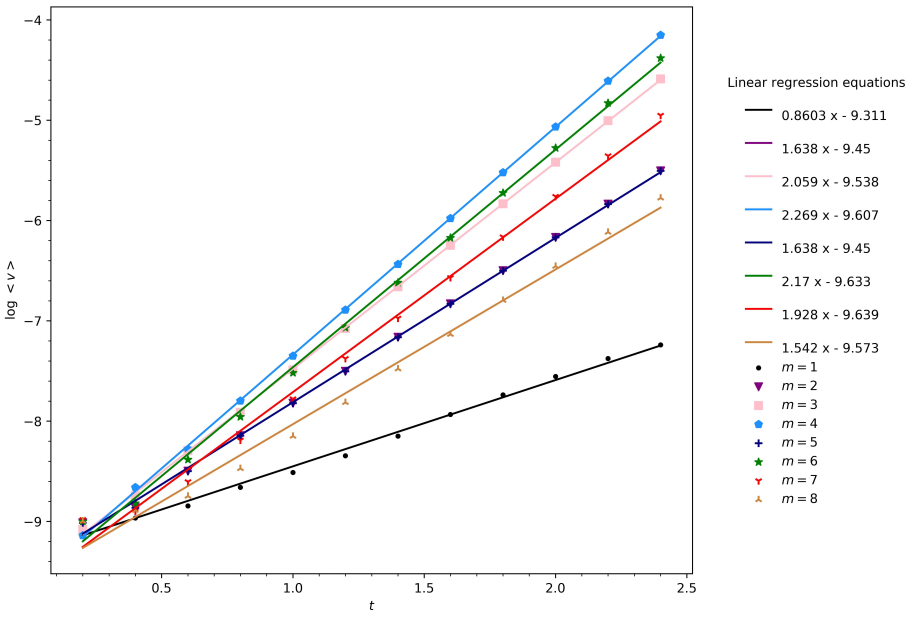

FIGURE 2.9: Natural logarithm of the growth of the perturbation modes $\langle v \rangle$ as a function of t, for the most unstable modes m. Only the linear regime is considered, with the analysis focused on the time interval $t \leq 2.4$. Different colors represent different modes.

Although the agreement between the numerical and theoretical growth rates is primarily qualitative (with the observed numerical growth rates being of the same order as the theoretical predictions), these preliminary tests offer promising insights, particularly in light of the limited literature on this subject under such extreme relativistic conditions. Minor discrepancies between the observed and theoretical values may be attributed to the fact that our simulations account for a shear layer of finite thickness, whereas G. Bodo [175] assumes an infinitesimally thin layer, characterized by a sharp gradient. These simulations are numerically demanding, requiring high resolution and extremely small time steps to maintain accuracy. Improved outcomes may be achieved by employing sufficiently long wavelengths, allowing the shear layer to be perceived as sharp. This approach, which is intended to be explored for future investigation, should still adhere to the theoretical limit.

2.4 Discussion on the Logarithmic Method and Preliminary Numerical Applications

The logarithmic method within the BSSN formalism, detailed in Eq.s (2.25)–(2.32), may represent a significant advancement in the numerical modeling of GRHD in curved spacetimes. This approach effectively overcomes many challenges that traditionally limit the precision and stability of simulations involving strong gravitational fields. Its relevance is particularly evident in systems characterized by sharp gradients, shocks, and discontinuities, such as neutron star mergers or black hole accretion disks.

A key advantage of the logarithmic method lies in its transformation of conserved fluid variables, such as rest-mass density and energy density, into logarithmic space. This transformation inherently ensures the positivity of these variables throughout their evolution, thereby preventing numerical instabilities that can arise

in conventional approaches. Such stability is particularly beneficial for modeling stellar atmospheres, where steep gradients between high-density and low-density regions are prevalent. By effectively handling these sharp transitions, the logarithmic formalism can significantly enhance both the accuracy and stability of simulations, especially in scenarios dominated by intense gravitational forces. This capability is indispensable for simulating high-energy astrophysical events, where abrupt changes in density and pressure frequently occur, such as in the environments surrounding compact objects like neutron stars and black holes.

One of the most notable applications of this method is in the simulation of binary neutron star mergers. During these events, the interaction of relativistic fluid flows with intense gravitational fields generates both gravitational waves and electromagnetic radiation. Accurate simulations of such mergers are crucial for predicting observable phenomena, including gravitational waveforms and their electromagnetic counterparts.

As a preliminary validation of the logarithmic approach, we now proceed to perform tests within a flat metric framework. This choice of a flat Minkowskian metric allows for a controlled examination of two key scenarios: the propagation of sound waves in a relativistic fluid and the nonlinear evolution of the KHI. Focusing on a flat metric simplifies the problem by removing the complexity introduced by curved spacetimes, thereby enabling a more precise evaluation of the numerical methods and their stability. It is important to note that, while the linearized KHI was previously addressed, the current section explores its fully nonlinear development. These tests serve to validate the robustness of the logarithmic approach and provide further insights into the behavior of relativistic fluids in diverse astrophysical contexts.

2.4.1 Propagation of a classical sound wave in the nonlinear regime

To numerically tackle these challenges, we have integrated a dedicated module into the `SFINGE` code, following the prescriptions outlined in Sec.s 2.1 and 2.2. This extension enables the code to solve the system of evolution equations (2.25)–(2.32) using the numerical architecture described in Sec. 1.4. As a preliminary test of the effectiveness of the logarithmic method, we focus on the propagation of a classical 1D sound wave in the nonlinear regime, within a fixed flat Minkowski spacetime. This scenario provides a straightforward but rigorous benchmark for assessing the method's ability to maintain stability and accuracy in the presence of sharp transitions and discontinuities. For this purpose, we initialize the x-component of the 3-velocity in the form of a monochromatic sound wave:

$$v_x(x,t) = Ac_s \sin(kx - \omega t), \tag{2.111}$$

where $A = 0.5$ is the amplitude, $k = 2\pi/L_x$ is the wavenumber, and $L_x = 1$ is the size of the simulation box. Here, c_s represents the phase velocity, equivalent to the classical sound speed ($c_s \ll c$), and is defined as:

$$c_s = \frac{\omega}{k} = \sqrt{\frac{\Gamma \tilde{P}_0}{\tilde{\rho}_0}} = 10^{-2}, \tag{2.112}$$

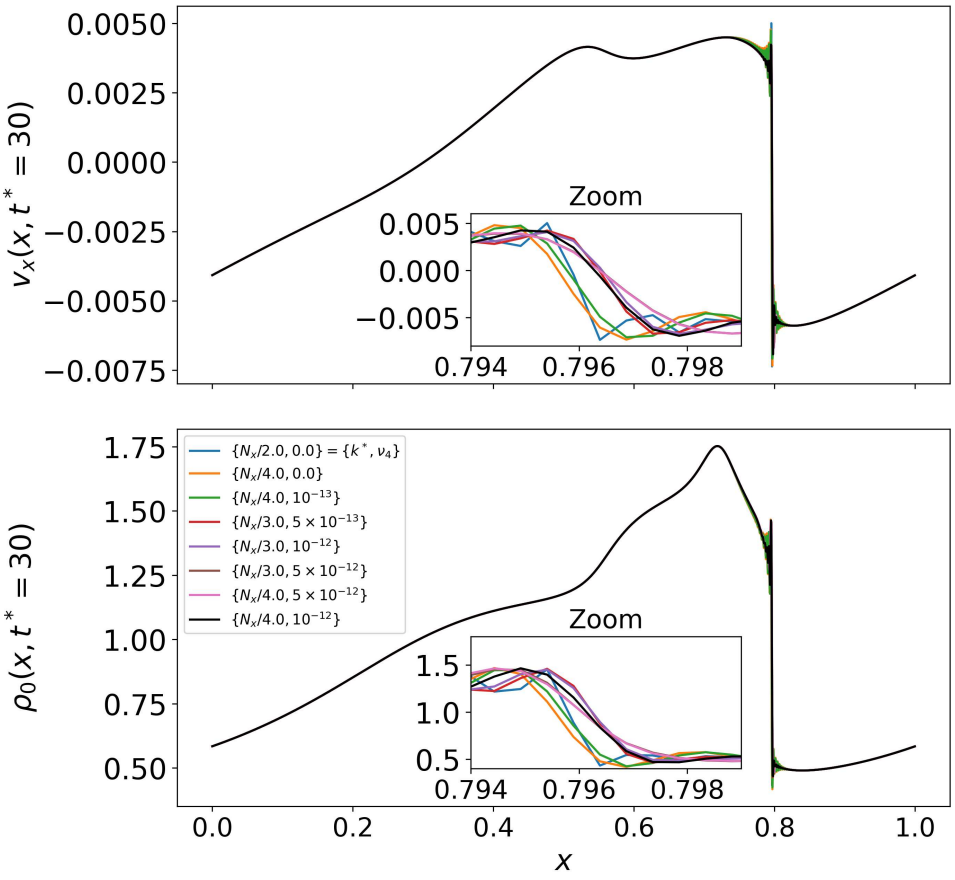

FIGURE 2.10: High-amplitude shock wave profiles for the x-component of the velocity (top) and the rest-mass density (bottom) at $t^* = 30$, displayed for different spectral filters k^* and dissipative coefficients ν_4. The inset provides a magnified view of the shock region, centered around $x \simeq 0.8$, for both fields.

with unperturbed quantities $\tilde{\rho}_0 = 1$ and $\tilde{P}_0 = 10^{-4}/\Gamma$, where $\Gamma = 4/3$ denotes the adiabatic index. The rest-mass density and pressure are initialized as follows:

$$\rho_0(x,t) = \tilde{\rho}_0 \left[1 + Ac_s \sin\left(kx - \omega t\right)\right], \tag{2.113}$$

$$P(x,t) = \tilde{P}_0 \left[1 + Ac_s \sin\left(kx - \omega t\right)\right]. \tag{2.114}$$

The objective is to evolve a clean shock wave, free of spurious oscillations, while ensuring that the simulation remains numerically stable. To this end, we aim to identify the optimal values for the anti-aliasing filter k^* and the dissipative coefficient ν_4, both of which were introduced in Sec. 1.4. It is important to emphasize that, when evolving logarithmic variables $(\delta, \sigma^i, \varepsilon)$, the hyperviscous method is applied exclusively to the equation for σ^i, as this variable is not logarithmic. Throughout all simulated configurations, the spatial and temporal resolutions are kept constant, with $N_x = 2048$ and $\Delta t = 10^{-3}$, while the parameters being adjusted are the values of k^* for the filter and ν_4 for the hyperviscous scheme. Each simulation runs until the shock formation stage, at which point the results are analyzed and compared.

Fig. 2.10 presents the profiles of the numerically simulated wave velocity $v_x(x, t^*)$ (top) and the rest-mass density $\rho_0(x, t^*)$ (bottom) at $t^* = 30$. The grid resolution is fixed at $N_x = 2048$ mesh points, while the dissipation coefficient is varied from $\nu_4 = 10^{-13}$ to $\nu_4 = 5 \times 10^{-12}$, passing through intermediate values of $\nu_4 = 5 \times 10^{-13}$ and

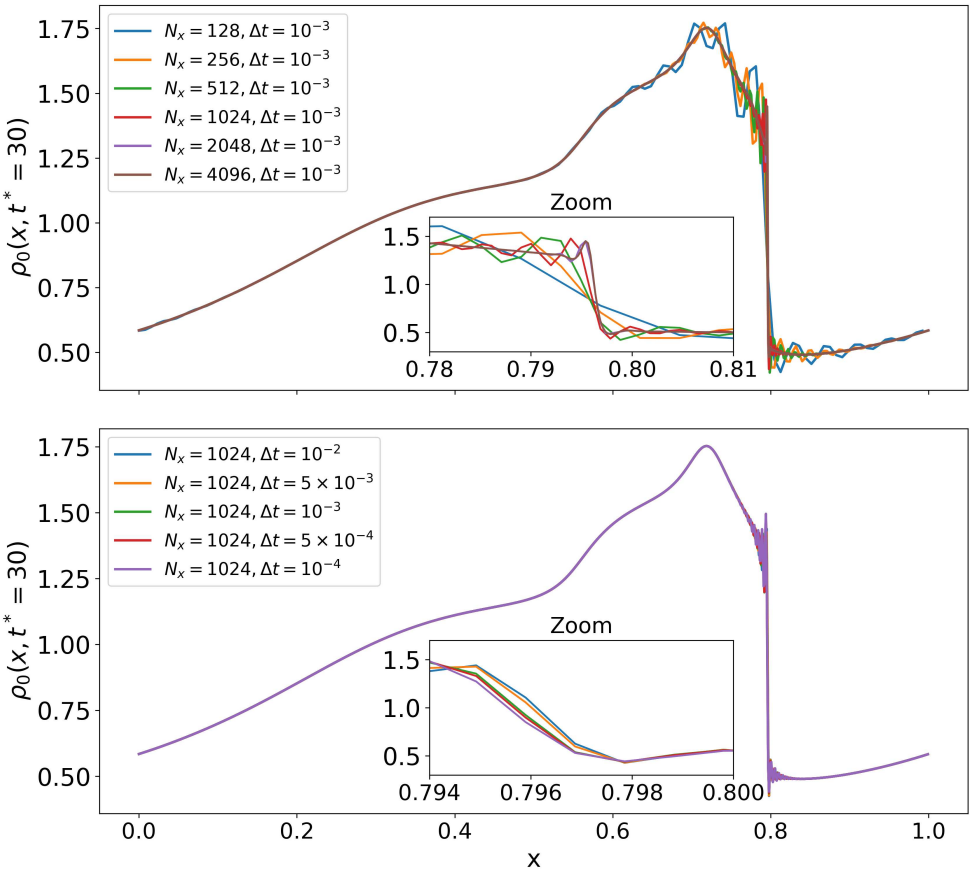

FIGURE 2.11: Spatial (top) and temporal (bottom) convergence tests for shock wave profiles of the rest-mass density ρ_0 at $t^* = 30$, presented for $k^* = 3.0$ and $\nu_4 = 10^{-12}$. The inset shows a magnified view of the shock region, centered around $x \simeq 0.8$, for both tests.

$\nu_4 = 10^{-12}$. The filter is simultaneously adjusted from $k^* = N_x/2.0$ to $k^* = N_x/4.0$, with $k^* = N_x/3.0$ as an intermediate value. Additionally, the 'basic' case (blue line) is included, where the hyperviscous scheme is not applied ($\nu_4 = 0.0$) and the filter acts on as few Fourier modes as possible, specifically at $k^* = N_x/2.0$, corresponding to the Nyquist mode, which is dependent on the discretization. The figure also includes a magnified view of the shock region along the x-axis, which highlights the differences between configurations. For higher values of the dissipation coefficient, the wave is excessively damped, while for lower values, ripples are not fully eliminated. The choice of filter appears to have minimal influence on the smoothness and cleanliness of the wave, particularly as the hyperviscous coefficient increases (the pink line perfectly overlaps with the brown line). Based on this analysis, the optimal parameters are $k^* = N_x/3.0$ and $\nu_4 = 10^{-12}$ (represented by the purple line).

Selecting the optimal filter and dissipation coefficient, we intend to perform a convergence test for the new code formulation. This involves evolving nonlinear classical sound waves while enhancing spatial and temporal resolution to assess the accuracy of the computed solutions. As depicted in Fig. 2.11, the convergence behavior of the rest-mass density ρ_0 has been analyzed. The results indicate that the solution exhibits clear convergence for spatial resolutions greater than $N_x = 1024$. In this regime, the purple and brown lines in the top panel become nearly indistinguishable, signifying that further refinement of the spatial grid yields negligible

differences in the numerical solution. Similarly, for temporal resolutions, convergence is observed for time step sizes smaller than $\Delta t = 5 \times 10^{-3}$. This is evidenced by the green, red, and purple lines in the bottom panel, which demonstrate a consistent and closely aligned trend, indicating that the temporal discretization errors are sufficiently minimized at these finer resolutions.

2.4.2 Kelvin-Helmholtz instability in a flat spacetime

As a second test, we aim to trigger the KHI within the special relativistic framework, adhering to the setup delineated by Beckwith and Stone [177] and Radice and Rezzolla [178], as previously detailed in Subsec. 2.3.1. In this instance, the 2D computational domain is defined by $x, y \in [0, L_x] \times [0, L_y]$, with $L_x = 1$ and $L_y = 2$, and the grid consists of $N_x \times N_y = 1024 \times 2048$ points. The velocity shear profile $v_x(y)$ is initialized using a hyperbolic tangent function as expressed in Eq. (2.89), where $a_0 = 0.01$ denotes the thickness of the shear layer, $v_s = 0.5$ represents the shear velocity amplitude, and the positions $y_1 = 1.5$ and $y_2 = 0.5$ define the shear layer. A velocity perturbation $v_y(x, y)$ is introduced as specified in Eq. (2.90), with a perturbation amplitude of $A = 10^{-1} v_s$, a perturbation mode given by $\Delta_n = \Delta_1 = \sin(kx)$ where the wavenumber is $k = 2\pi / L_x$, and $\sigma_0 = 0.1$. The rest-mass density is initialized as:

$$\rho_0(y) = 1 + 0.45 \left[\tanh\left(\frac{y - 1.5}{a_0} \right) - \tanh\left(\frac{y - 0.5}{a_0} \right) \right]. \tag{2.115}$$

The simulation is performed up to $t = 10$, allowing the characteristic KHI rolls to fully develop and become distinctly visible. The evolved fields are illustrated in Fig.s 2.12–2.14, where the onset of the Kelvin-Helmholtz rolls in the rest-mass density becomes evident around $t = 2.5$. The evolution of the instability is consistent with the numerical findings of Beckwith and Stone [177] and Radice and Rezzolla [178] for a single perturbation mode. Notably, we were able to capture the full evolution of the KHI using the logarithmic approach to GRHD introduced in the previous Sections. This formulation allowed for a stable numerical treatment of the strong gradients characteristic of KHI and provided an efficient means to simulate its complex, non-linear dynamics.

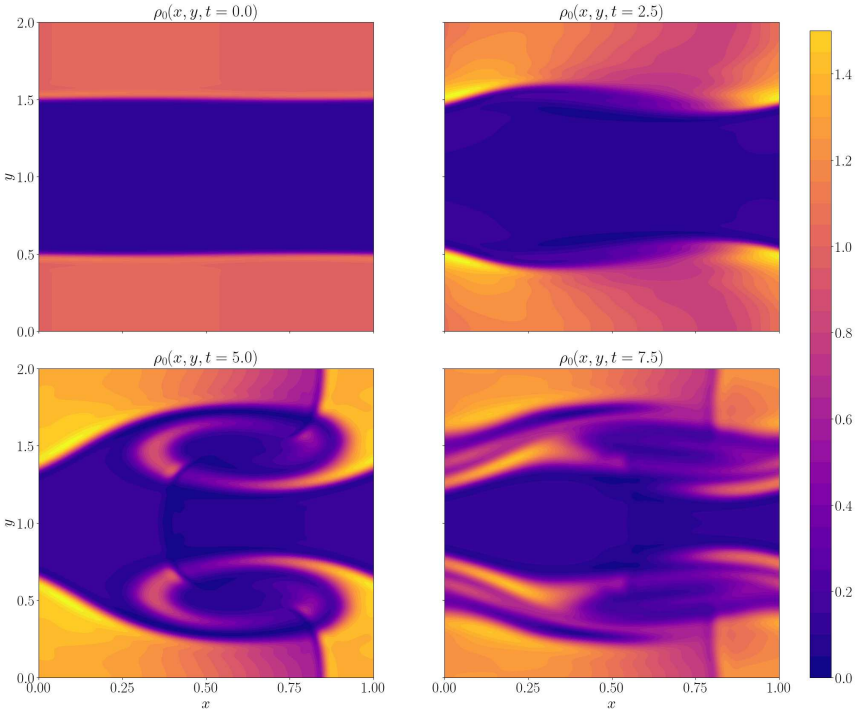

FIGURE 2.12: Two-dimensional evolution of the rest-mass density field.

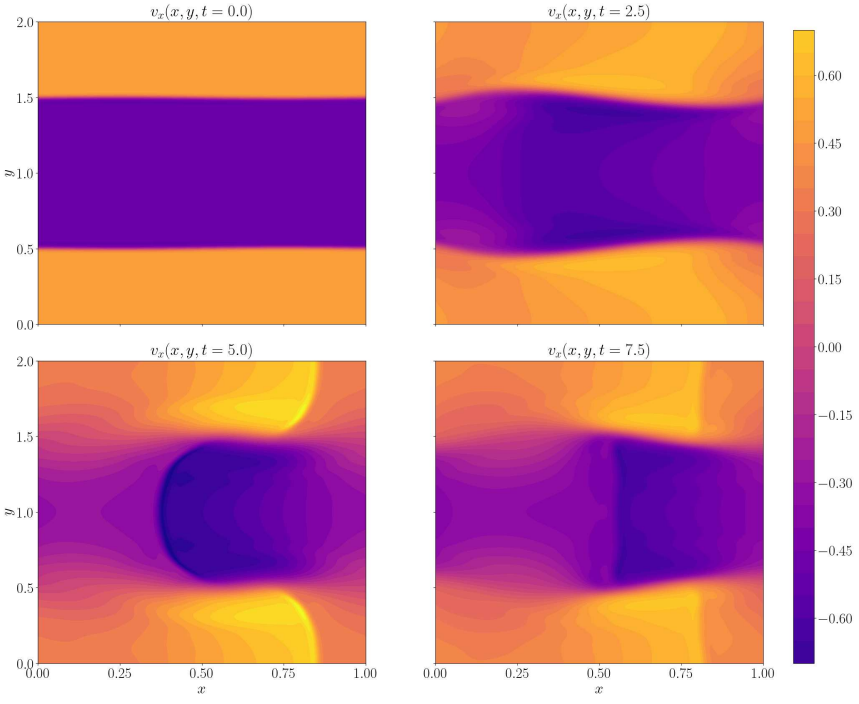

FIGURE 2.13: Two-dimensional evolution of the x-component of the three-velocity field.

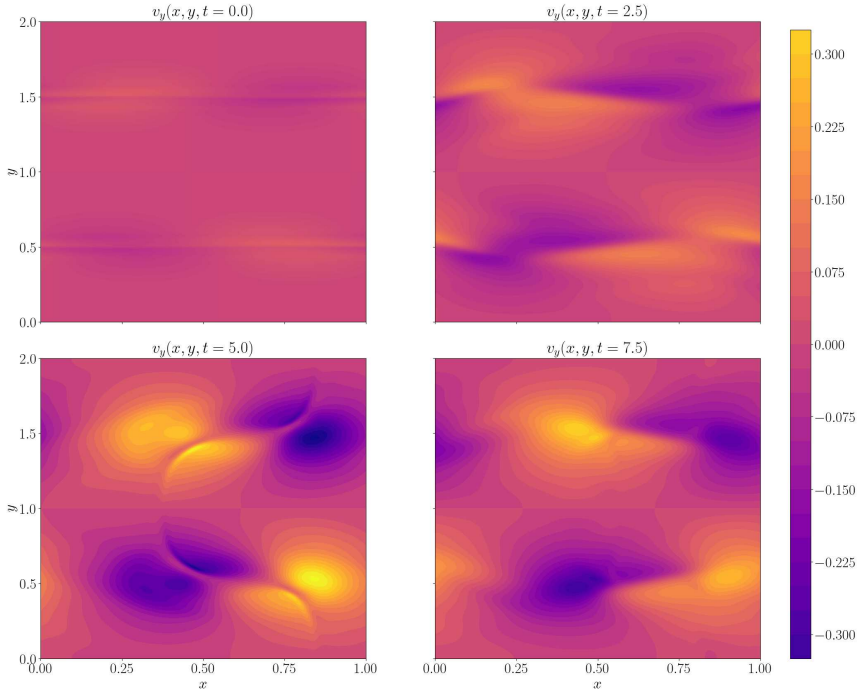

FIGURE 2.14: Two-dimensional evolution of the y-component of the three-velocity field.

Future tests will incorporate the dynamic evolution of spacetime curvature to evaluate the performance of the code when curvature and matter are fully coupled. In this scenario, the complete set of equations, Eq.s (2.25)–(2.32), governing the interaction between matter and spacetime geometry, will be solved while allowing the metric to evolve. This extension aims to provide a comprehensive assessment of the robustness and accuracy of the numerical methods under more physically realistic conditions.

Another promising avenue for future research lies in integrating the logarithmic method with GRMHD, enabling a more in-depth investigation of how magnetic fields influence astrophysical phenomena such as magnetar flares, gamma-ray bursts, and relativistic jet formation. Expanding this framework to include MHD simulations would provide a more comprehensive toolset for studying a wide range of astrophysical systems where magnetic fields play a crucial role. Indeed, many astrophysical environments, particularly those involving compact objects like black holes and neutron stars, cannot be fully understood without considering the interplay between matter and magnetic fields. The incorporation of magnetic fields, as in GRMHD, allows for a more thorough exploration of systems where gravitational and electromagnetic forces are intricately intertwined.

Thus far, throughout this Chapter, we have gained significant insights into fluid dynamics in extreme relativistic regimes. However, at this stage, one may naturally ask: *What happens to the matter surrounding a black hole when both gravitational and electromagnetic fields are present?* This is the natural question we must now address as we transition from studying fluid dynamics and vacuum solutions to examining the intricate interactions between matter, magnetic fields, and gravity. While the behavior of matter in the presence of strong gravitational fields alone has yielded profound insights, the introduction of electromagnetic fields adds a new layer of

complexity. Magnetic fields are believed to play a crucial role in shaping the dynamics of accretion disks, powering relativistic jets, and influencing the overall structure of the plasma surrounding black holes. The coupling of gravity and electromagnetism in such extreme environments may lead to unexpected phenomena, pushing the boundaries of our current understanding of relativistic fluid dynamics.

2.5 Dynamics of Matter in the Vicinity of Black Holes: BHAC Simulations

In this Section, we present the numerical algorithms utilized to explore the dynamics of matter under the influence of gravitational and electromagnetic fields in the vicinity of compact objects. We utilize the Black Hole Accretion Code (BHAC)—a multidimensional GRMHD code based on the MPI-AMRVAC framework—to study large-scale phenomena near black holes and explore the potential for vortical pattern formation. BHAC solves the equations of ideal GRMHD in arbitrary spacetimes, leveraging AMR techniques through an efficient block-based approach [2]. The AMR process operates as follows: the computational domain is initially divided into blocks, each containing an equal number of cells. Each block can subsequently be refined into two (1D), four (2D), or eight (3D) child blocks, each with the same fixed number of cells. This refinement can be repeated *ad libitum*, resulting in a hierarchical data structure akin to a forest (a collection of trees). During our numerical simulations using the surface grid, we observe this refinement process, as illustrated in Fig. 2.15: regions requiring higher precision are refined with a denser mesh, while other areas of the multidimensional grid maintain lower levels of precision and resolution.

The code implements the standard set of MHD equations in covariant form:

$$\begin{aligned} D_\mu(\rho u^\mu) &= 0, \\ D_\mu T^{\mu\nu} &= 0, \\ D_\mu {}^*F^{\mu\nu} &= 0, \end{aligned} \tag{2.116}$$

which correspond to the conservation of mass, conservation of energy-momentum, and the homogeneous form of Faraday's law, respectively. Here, ρ represents the rest-mass density. The dual Faraday tensor ${}^*F^{\mu\nu}$ is expressed in terms of the electric and magnetic fields in the fluid frame, as we focus on the ideal MHD limit, where the electric field vanishes in the fluid frame defined by the four-velocity u^μ. Additionally, the total pressure P and the total specific enthalpy h are included, with an EoS linking these variables, which is required to close the system. Common choices for the EoS include the ideal gas, Synge gas, or isentropic flow models.

Additionally, in BHAC, spacetime is decomposed into its $3+1$ components by introducing a foliation of spacelike hypersurfaces, as discussed in previous Chapters. Unlike SFINGE, BHAC assumes a fixed background metric, which remains static in time. Various coordinate systems can be selected, including Boyer-Lindquist coordinates, Kerr-Schild coordinates, Rezzolla-Zhidenko [179] coordinates, and Hartle-Thorn coordinates [180]. Consequently, an external numerical code is required to evolve the metric dynamically. From this perspective, BHAC is not fully self-contained, as it relies on other codes, such as the Einstein Toolkit [181], to handle the evolution of the spacetime geometry.

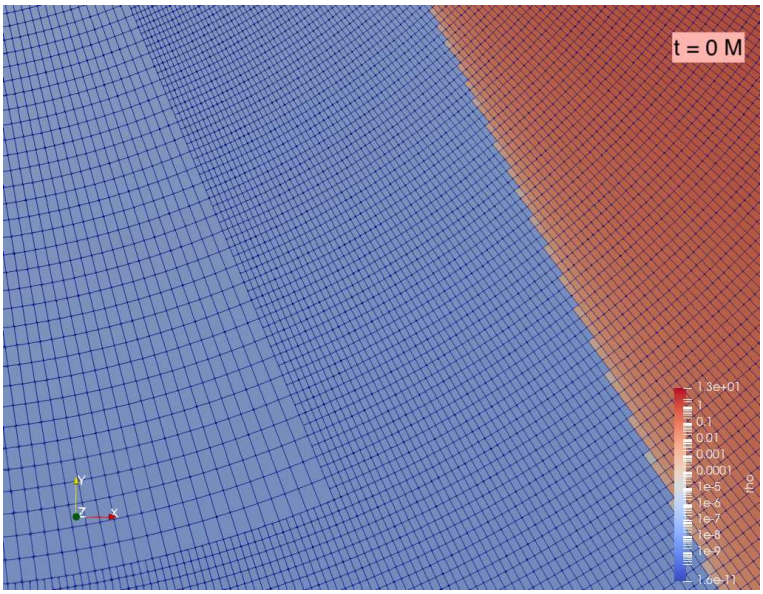

FIGURE 2.15: AMR observed in the numerical simulation.

The GRMHD equations can be decomposed into their spatial and temporal components, resulting in the final form of the conservation laws:

$$\partial_t(\sqrt{\gamma}\mathbf{U}) + \partial_i(\sqrt{\gamma}\mathbf{F}^i) = \sqrt{\gamma}\mathbf{S}, \tag{2.117}$$

where $\mathbf{U}$ represents the conserved variables, $\mathbf{F}^i$ the fluxes, $\mathbf{S}$ the source terms, and γ is the determinant of the spatial metric. Since `BHAC` solves these equations using a finite volume formulation, integrating Eq. (2.117) and applying the divergence theorem to the fluxes yields a semi-discrete equation for the cell-averaged state in the cell (i,j,k) as:

$$\begin{aligned}\frac{d\bar{\mathbf{U}}_{i,j,k}}{dt} = & -\frac{1}{\Delta V_{i,j,k}}\Big[\mathbf{F}^1\Delta S^1\Big|_{i+1/2,j,k} - \mathbf{F}^1\Delta S^1\Big|_{i-1/2,j,k} \\ & +\mathbf{F}^2\Delta S^2\Big|_{i,j+1/2,k} - \mathbf{F}^2\Delta S^2\Big|_{i,j-1/2,k} \\ & +\mathbf{F}^3\Delta S^3\Big|_{i,j,k+1/2} - \mathbf{F}^3\Delta S^3\Big|_{i,j,k-1/2}\Big] \\ & +\mathbf{S}_{i,j,k},\end{aligned} \tag{2.118}$$

where $\bar{\mathbf{U}}_{i,j,k}$ is the volume average of $\mathbf{U}$ in the cell, and ΔS^i are the surface-averaged fluxes. The terms inside the brackets represent the values of the fluxes at the cell midpoints. For computational efficiency, all static integrals, including cell volumes ΔV, surfaces ΔS^i, and barycenter coordinates, are precomputed during the initialization phase using Simpson's rule with fourth-order accuracy.

For the temporal update, the semi-discrete form is treated as an ordinary differential equation in time for each cell, utilizing a multi-step Runge-Kutta scheme to evolve the cell-averaged state, $\bar{\mathbf{U}}_{i,j,k}$. This approach is commonly referred to as the *method of lines*. At each substep, the pointwise interface fluxes, $\mathbf{F}^i$, are computed by performing a limited reconstruction of the cell-averaged state, $\bar{\mathbf{U}}$, at the interfaces, followed by the application of approximate Riemann solvers.

The second-order finite volume algorithm implemented requires the numerical

fluxes to be centered at the interface midpoints. Thus, for higher than first-order accuracy, the fluid variables must be reconstructed at the interface using an appropriate spatial interpolation. The reconstruction process follows these steps:

(1) Compute the primitive variables, $\bar{\mathbf{P}}$, from the averages of the conserved variables, $\bar{\mathbf{U}}$, located at the cell barycenter;

(2) Apply the reconstruction formulae to obtain two distinct representations of the state at the interface, $\bar{\mathbf{P}}^L$ and $\bar{\mathbf{P}}^R$;

(3) Convert the newly obtained pointwise values back into their conserved states, $\bar{\mathbf{U}}^L$ and $\bar{\mathbf{U}}^R$, which serve as input for the approximate Riemann solver.

At each Runge-Kutta substep, the fluxes at the interfaces are computed based on the previous substep, allowing the state to advance to the next substep using the combined fluxes across the cell. To compute these fluxes from the reconstructed conserved variables at the interface, $\bar{\mathbf{U}}^L$ and $\bar{\mathbf{U}}^R$, two approximate Riemann solvers are employed: the total variation diminishing Lax-Friedrichs (TVDLF) scheme and the HLL solver. The Rusanov flux, also known as TVDLF, is based on the largest absolute value of the characteristic wave speeds normal to the interface, while the HLL solver uses the leftmost (high-frequency) and rightmost (low-frequency) wave speeds of the characteristic fan relative to the interface. The calculation of fluxes and source terms requires knowledge of the primitive variables, $\mathbf{P}$. While the transformation from $\mathbf{P}$ to $\mathbf{U}$ is straightforward, the inversion from $\mathbf{U}$ to $\mathbf{P}$ is non-trivial. The primitive variables are determined by solving a single nonlinear equation, which can be approached in various ways, such as by utilizing the entropy. A Newton-Raphson iterative scheme is commonly used to find the root of this equation. Upon completion of the iteration, the primitive variables, $\mathbf{P}$, are recovered.

We now introduce the constrained transport (CT) method, a divergence-control technique that, rather than eliminating magnetic field divergence after it is created, modifies the evolution of the magnetic field transport to prevent the formation of divergence in the first place [182]. The central concept of CT is to assign specific spatial locations to the electromagnetic variables, as illustrated in Fig. 2.16. Specifically, a magnetic flux, Φ, is associated with each face of the cell, while a line integral of the electric field, $\mathcal{E}$, is assigned to each edge. The magnetic flux at each face is updated by the circulation of the electric field, following the integral form of Faraday's law. Since each line integral of the electric field is shared by two adjacent faces but appears with an opposite sign in the time update formula for each, the average value of the magnetic field divergence, $(\overline{\nabla \cdot \mathbf{B}}_{\text{cell}})$, remains zero up to machine precision.

A more advanced method of constrained transport is the Upwind Constrained Transport (UCT) scheme. UCT is used to evolve the magnetic field while, like other constrained transport methods, maintaining the divergence of the magnetic field at machine precision. However, UCT further improves accuracy in reproducing the continuity and transport properties of the magnetic field through the use of limited reconstructions. Two variants of UCT are implemented in BHAC, as detailed in [183, 184], and will be referred to as UCT1 and UCT2, respectively. In this Section, we focus on the calculation of $\mathcal{E}_z$, noting that the other components can be obtained by cyclically rotating $x \to y$, $y \to z$, and $z \to x$. The implementation of UCT2 proceeds as follows:

(1) During the computation of the numerical fluxes, the characteristic wave speeds, $c_i^{\min}$ and $c_i^{\max}$, obtained from the Riemann solver, are stored alongside the

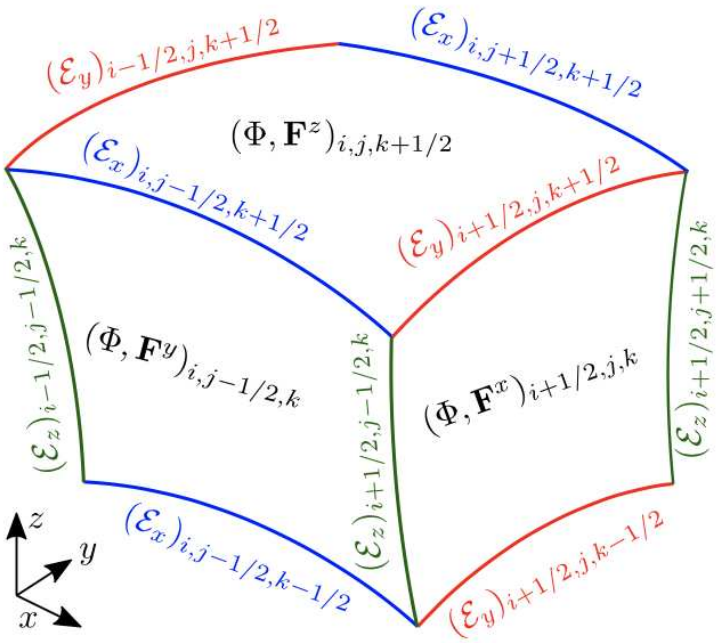

FIGURE 2.16: The constrained transport scheme: line integrals of the electric field, $\mathcal{E}$, are located along the edges of the grid cells, while magnetic fluxes, Φ, and numerical fluxes, $\mathbf{F}^i$, are placed on the faces of each cell. The spatial arrangement of variables corresponds to a cell with indices (i, j, k) along the (x, y, z) directions, respectively. Figure adapted from Olivares et al. [182].

transverse transport velocities at the left and right states. For example, for the x-interface, these velocities are $\mathcal{V}_L^y$, $\mathcal{V}_L^z$, $\mathcal{V}_R^y$, and $\mathcal{V}_R^z$;

(2) A new transverse transport velocity is computed by weighting the velocities of the left and right states by the characteristic speeds [184]. For the x-interface, this is given by

$$\bar{\mathcal{V}}^{y,z} = \frac{c_x^{\max}\mathcal{V}_L^{y,z} + c_x^{\min}\mathcal{V}_R^{y,z}}{c_x^{\max} + c_x^{\min}}; \tag{2.119}$$

(3) The magnetic fields and transport velocities are then reconstructed at the edge where $\mathcal{E}_z$ is to be calculated, yielding $B_{L,R}^{x,y}$ and $\bar{\mathcal{V}}_{R,L}^{x,y}$;

(4) The maximum characteristic speeds in each direction are subsequently computed;

(5) Finally, the electric field is approximated as a weighted average of the maximum characteristic speeds, corrected by the transport of the magnetic field, as follows [184]:

$$\begin{aligned} E_z = \sqrt{\gamma}\Bigg[&- \frac{c_x^+\bar{\mathcal{V}}_L^x B_L^y + c_x^-\bar{\mathcal{V}}_R^x B_R^y - c_x^- c_x^+ (B_R^y - B_L^y)}{c_x^+ + c_x^-} \\ &+ \frac{c_y^+\bar{\mathcal{V}}_L^y B_L^x + c_x^-\bar{\mathcal{V}}_R^y B_R^x - c_y^- c_y^+ (B_R^x - B_L^x)}{c_y^+ + c_y^-}\Bigg]. \end{aligned} \tag{2.120}$$

Parameter	*Symbol*	*Value*
Dimensionless spin	a	0.9375
Inner radius	$r_{\rm in}$	6 M
Radius maximum	$r_{\rm max}$	12 M
(Gas) Adiabatic index	Γ	5/3
(Electron) Adiabatic index	$\Gamma_{\rm e^-}$	4/3
(Proton) Adiabatic index	$\Gamma_{\rm p}$	5/3
Beta of the plasma	$\beta_{\rm plasma}$	10^2
Initial entropy	S	10^{-3}
Minimum density scale	$\rho_{0\,\rm min}$	10^{-5}
Minimum pressure parameter	$P_{\rm min}$	$1/3 \times 10^{-7}$

TABLE 2.3: Initial conditions for the black hole torus simulation.

At this stage, we approximate $\mathcal{E}_z = E_z \Delta z$ and use this value to calculate the circulation needed to evolve the magnetic fluxes. Due to its symmetry, UCT2 is preferred over UCT1. While CT schemes ensure that no magnetic field divergence is created during evolution, they do not eliminate any divergence that may already exist. To fully exploit the benefits of constrained transport in an AMR code, it is necessary to use prolongation and restriction operators that preserve the constraint $\nabla \cdot \mathbf{B} = 0$ to machine precision. Additionally, care must be taken to synchronize the different representations of the electric and magnetic field components across fine-coarse interfaces.

As previously outlined, our primary focus pertains to the large-scale behavior in the vicinity of black holes, which serves as a foundation for conducting a detailed and high-precision analysis of the ensuing dynamics observed within the large-scale framework. The specific solution examined in this context is that of an equilibrium torus with constant specific angular momentum, initially formulated by Fishbone and Moncrief [185]. This solution is expressed in Kerr-Schild coordinates, and we hereby present the initial conditions for the *two-dimensional axisymmetric Fishbone-Moncrief torus*.

2.5.1 GRMHD Simulations: 2D Fishbone-Moncrief Torus

We consider a hydrodynamically stable equilibrium torus permeated by a weak magnetic field loop. The surrounding spacetime corresponds to that of a Kerr black hole with a dimensionless spin parameter $a = 0.9375$. The inner radius of the torus is located at $r_{\rm in} = 6$ M, while the position of the maximum rest-mass density is at $r_{\rm max} = 12$ M. Both the radial and azimuthal coordinates are defined in Boyer-Lindquist coordinates, where M denotes the mass of the black hole. The EoS for the fluid is modeled as an ideal gas, characterized by an adiabatic index $\Gamma = 5/3$. The particles emitted stochastically from the vicinity of the black hole follow a specific heat ratio of $\Gamma_{\rm e^-} = 4/3$ for electrons and $\Gamma_{\rm p} = 5/3$ for protons. The plasma beta, defined as the ratio of plasma pressure to magnetic pressure, is set to $\beta_{\rm plasma} = 10^2$, while the initial entropy is fixed at $S = 10^{-3}$. The minimum rest-mass density is $\rho_{0\,\rm min} = 10^{-5}$, and the minimum pressure is specified as $P_{\rm min} = 1/3 \times 10^{-7}$. A summary of these parameters is provided in Table 2.3. For the 2D simulation, the resolution is dynamically adjusted by the AMR technique, with the following resolutions employed: $N_r \times N_\theta \in \{256 \times 128, 512 \times 256, 1024 \times 512\}$.

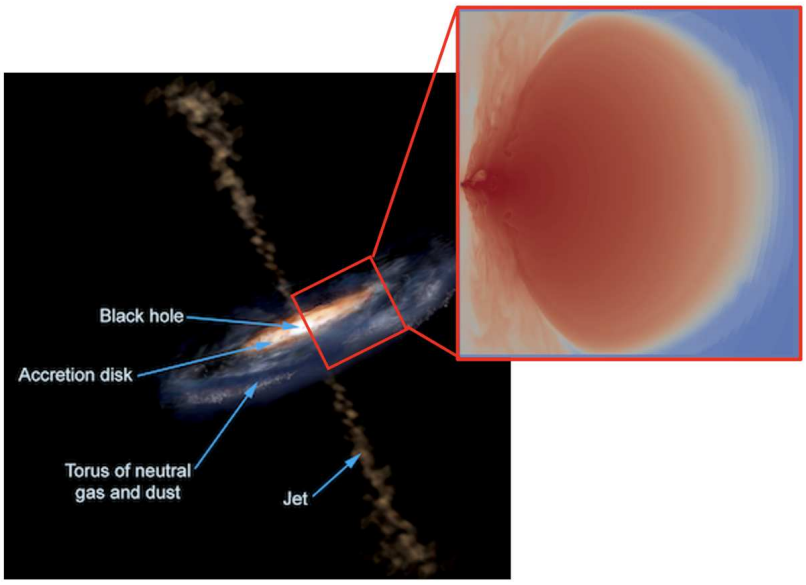

FIGURE 2.17: Schematic representation of the inner region of the black hole torus as modeled in GRMHD simulations. The black hole is encircled by an accretion disk, which rotates about the vertical axis. Surrounding this system is a torus composed of neutral gas and dust. The black hole and the accretion disk generate narrow jets of energetic particles that are ejected in opposite directions away from the disk. The right panel provides a zoomed-in view of the region analyzed in our BHAC simulations.

In the following, we present a series of 2D visualizations illustrating key quantities from the numerical simulations. All the figures share the same fundamental characteristics:

- The computational grid is spherical, and only half of the accretion disk with the torus is depicted, as the other half is symmetrically equivalent.
- The plots represent 2D sections of a fully axially symmetric accretion torus, with x along the horizontal axis, y (the axis of black hole rotation) along the vertical axis, and z directed orthogonally outward from the xy-plane.
- Time is expressed in geometric units, specifically in terms of M (as discussed earlier for radial units), and is indicated in the upper-right corner of each figure.
- The quantity plotted in color scale is indicated in the lower-left corner of each figure, with the color scale representing values in logarithmic units.

To facilitate the understanding of the region under analysis in our simulations, a schematic is provided in Fig. 2.17. Models of black holes often include a region composed of cold gas and dust, typically shaped as a torus, with the black hole and accretion disk located in the central cavity. Along the rotational axis, on opposite sides of the disk, jets of relativistic plasma may be ejected. The right-hand side of the figure offers a magnified view of the region explored in our BHAC numerical simulations.

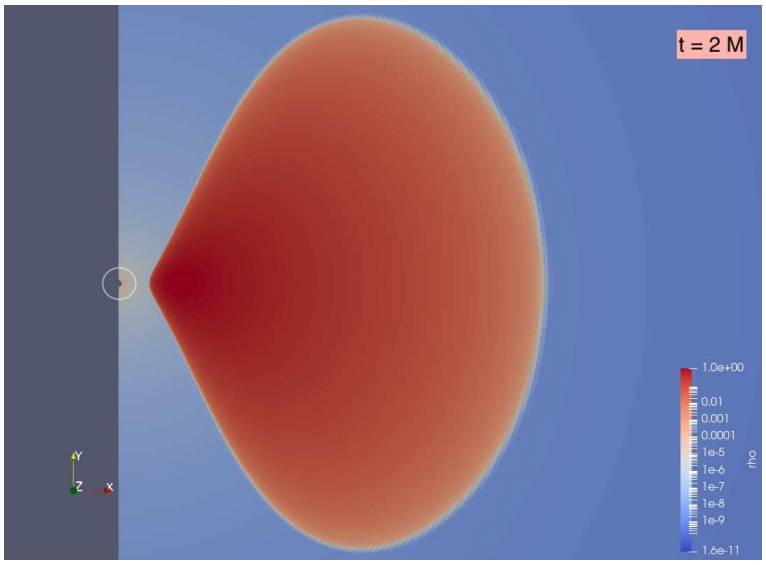

FIGURE 2.18: Initial configuration of the rest-mass density, ρ, at time $t = 2$ for the numerical black hole torus test. The colors represent the logarithmic density of the matter in the accretion torus. The region containing 99% of the maximum density corresponds to the accretion torus, while the density decreases in the surrounding region, which represents the wind around the torus. The black hole is denoted by an open circle on the left.

The initial configuration of the rest-mass density in the black hole torus is illustrated in Fig. 2.18. The small black dot at the cusp of the torus (denoted by an open circle) represents the inner region of the black hole, while the torus extends outward into the surrounding space. The region encompassing 99% of the maximum density corresponds to the accretion disk, with the density gradually decreasing as one moves away from the torus. In the zoomed view of the inner region of the accretion disk, distinct isodensity contours can be observed, as shown in Fig. 2.19.

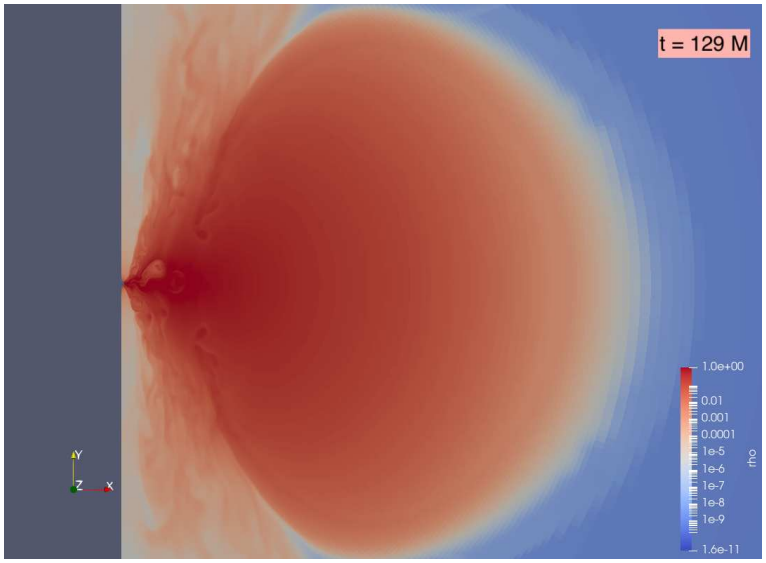

FIGURE 2.20: Rest-mass density distribution, as depicted in Fig. 2.18, at time $t = 129$, clearly showing the development of the jet along the y-axis.

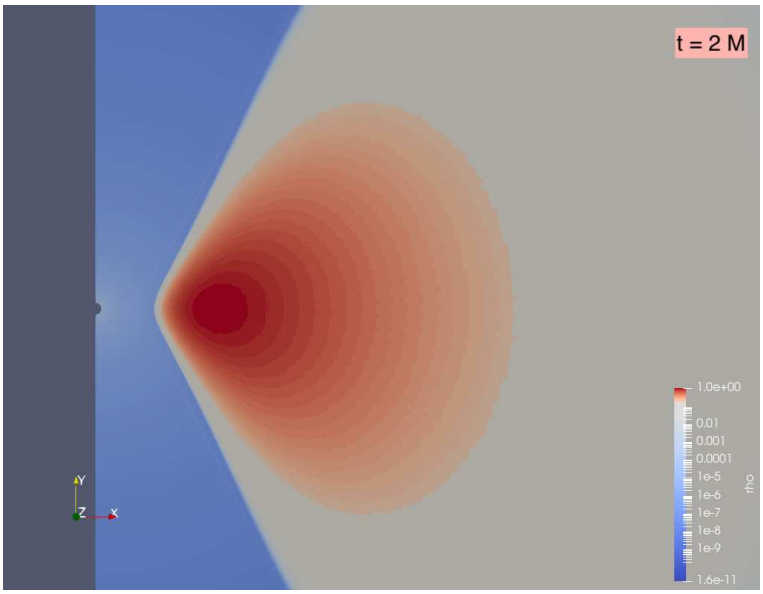

FIGURE 2.19: Initial configuration of the rest-mass density, ρ, at time $t = 2$ for the numerical black hole torus test, with a zoomed view of the inner region. The plot highlights the area containing 99% of the maximum density, showing the visible isodensity contours.

When observing the density plot of the numerical simulation on a large scale, once the instability is triggered, the jet funnel becomes apparent (see Fig. 2.20). Gradually, the sharp structure of the torus diminishes, and the jet evolves along the y-axis, aligned with the black hole's rotation axis.

As the simulation progresses, distinct regions emerge, which can be classified based on the configuration of the magnetic field and the distribution of matter [186]:

- **Torus** – characterized by a matter density that dominates over the magnetic field (high plasma beta), where the flow remains turbulent and chaotic.
- **Corona** – a region where the matter density is significantly lower than that of the torus, yet it still dominates over the turbulent magnetic field.
- **Jet funnel** – where the magnetic field becomes dominant (low plasma beta).

The numerical simulation spans a time period from $t = 0$ to $t = 200$, during which we observe the evolution of the rest-mass density, ρ, along with its primary characteristics (Fig. 2.21). Initially, the torus remains stable; however, as particles are emitted, instabilities are triggered. Clear vortex structures begin to form, with localized KHIs becoming apparent. Eventually, these instabilities grow strong enough to disrupt the torus structure. To substantiate this observation, we computed the magnitude of the fluid velocity in the plane, as depicted in Fig. 2.22. The plane velocity is defined as:

$$u_{\text{plane}} = \sqrt{u_x^2 + u_y^2}, \tag{2.121}$$

and its evolution is tracked across several key time-frames, particularly during the formation of the jets. Notably, from $t = 155$ onward, strong localized shear flows, susceptible to the KHI, are observed. These result in the formation of large-scale vortex structures, which dominate the turbulent and intermittent transport in the disk region. To further explore the onset of turbulence in these extreme environments,

the next Chapter will introduce the PIC method to simulate the particle dynamics within localized regions of the black hole surroundings.

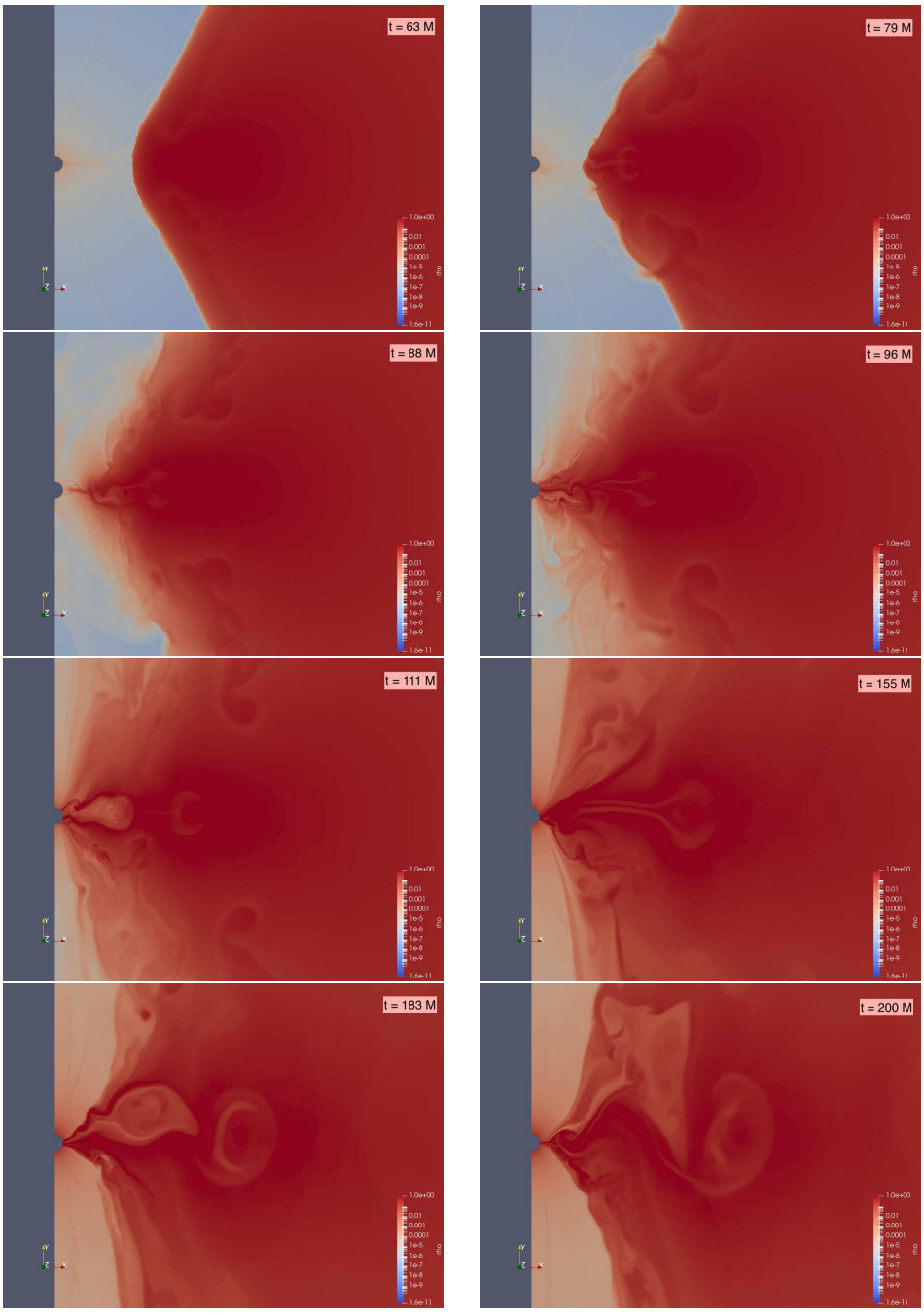

FIGURE 2.21: The evolution of the rest-mass density, ρ, in the numerical simulation. Plasma is emitted, and at $t = 63$ (first image in the top-left corner), the instability is triggered. By $t = 79$, vortex structures become visible, likely indicating the onset of local KHI. As the simulation progresses (from $t = 88$ until the final time $t = 200$), the torus structure is gradually disrupted and eventually destroyed.

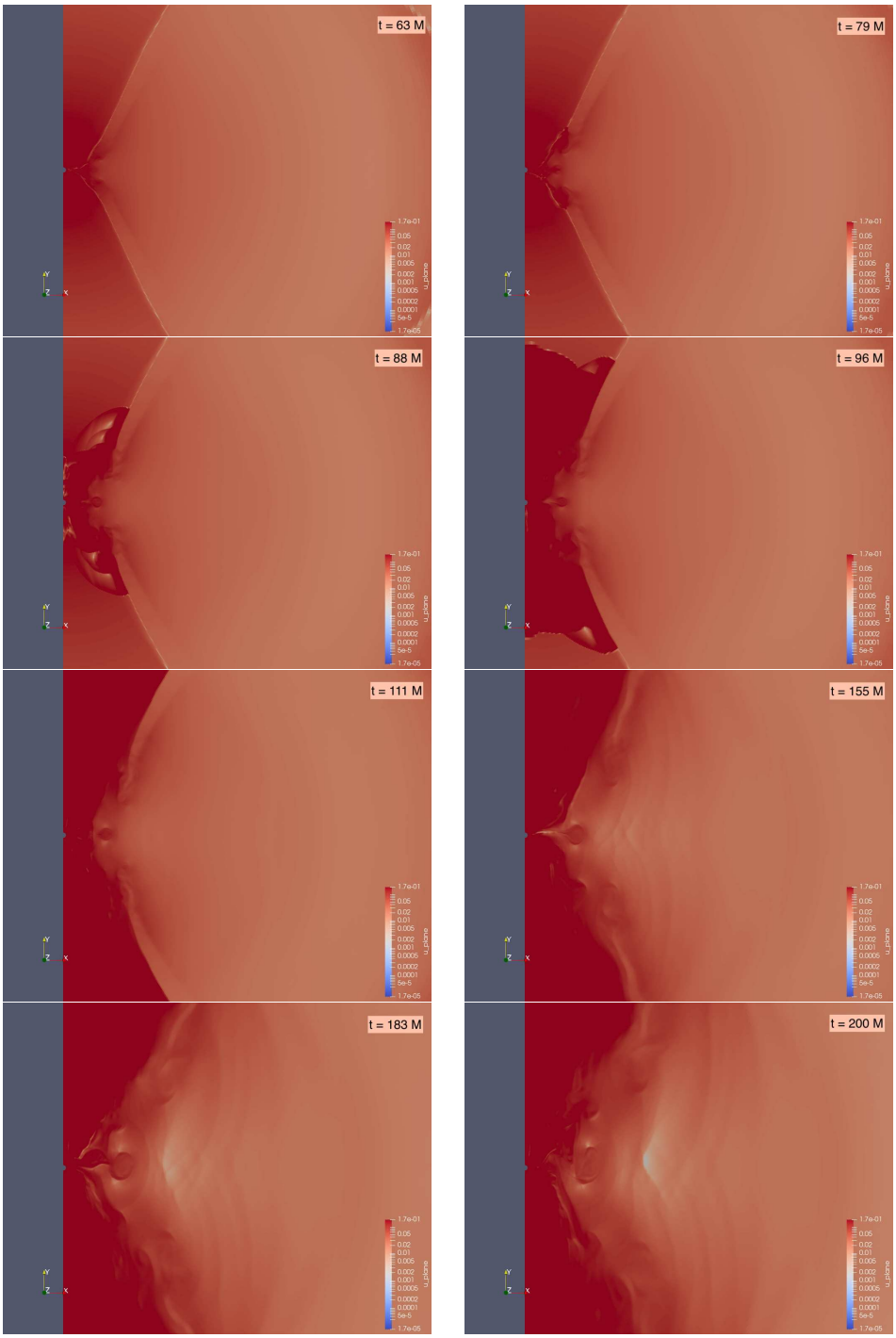

FIGURE 2.22: The evolution of the plane velocity, u_{plane}, in the numerical simulation. Notably, from $t = 155$ until the end of the simulation, strong localized shear flows, unstable to the KHI, are observed.

2.6 The Power Spectrum of Turbulence near Black Holes

The well-known black holes Sagittarius A* and Messier 87*, which represent the first directly imaged black holes (see Fig. 2.23), are classified as low-luminosity active galactic nuclei (LLAGNs) [187, 188]. In many such systems, strong collimated jets have been observed, particularly in X-ray observations, with their mechanisms commonly attributed to the theoretical models proposed by Blandford and Znajek [128] and Blandford and Payne [189].

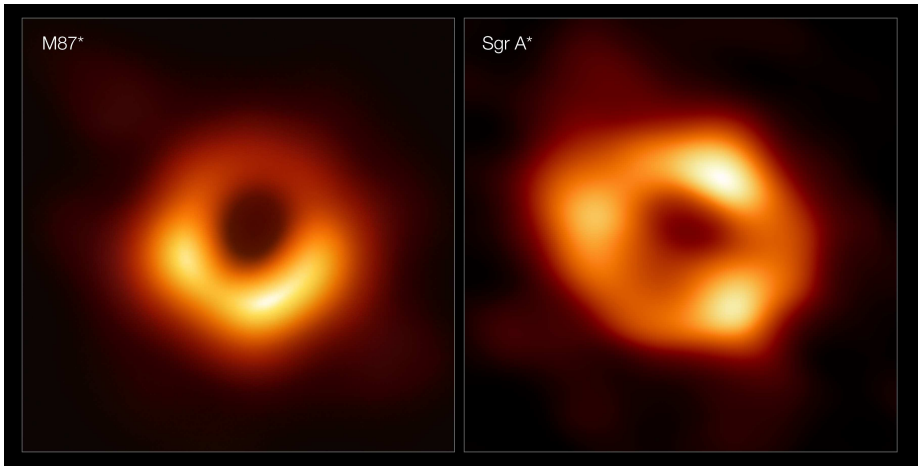

FIGURE 2.23: The supermassive black holes captured by the EHT collaboration: M87* on the left, and SgrA* on the right. Image credit: Event Horizon Telescope.

Black hole accretion disks are characterized by the accumulation of diffuse material in orbital motion. GRMHD provides a framework to describe the relativistic macroscopic plasma dynamics observed in astrophysical phenomena, such as accretion processes near compact objects. This framework reveals that turbulence is ubiquitously present in astrophysical plasmas with high Reynolds numbers, often triggered by instabilities. For instance, the Magneto-Rotational Instability (MRI) serves as a crucial mechanism for angular momentum transport in turbulent accretion disks [190], while the KHI leads to the formation of swirl-like vortices [191]. These instabilities act as perturbative channels that can initiate magnetic reconnection within the accretion disk—a rapid reconfiguration of magnetic field lines at interfaces of opposing polarity, leading to the formation of circular magnetic islands [192, 193]. The second-order structure function is a key tool for investigating density fluctuations within the disk, offering critical insights into gravitational instabilities and turbulence that significantly influence matter distribution. Specifically, identifying evidence of an inertial range and a fluid-like turbulent cascade in the plasma orbiting around compact objects is essential. The relationship between the power spectrum of a generic scalar field and the second-order structure function establishes a connection between macroscopic observations of accretion disks and the underlying microphysical processes governing their dynamics.

The structure function of a generic scalar field f (e.g., temperature, density) quantifies the statistical relationship between the field at position $\boldsymbol{x}$ and the field displaced by $\boldsymbol{x}+\boldsymbol{l}$. It is defined as

$$S_2(\boldsymbol{l}) = \langle |f(\boldsymbol{x}+\boldsymbol{l}) - f(\boldsymbol{x})|^2 \rangle = \frac{1}{V}\int |f(\boldsymbol{x}+\boldsymbol{l}) - f(\boldsymbol{x})|^2 d^3x, \tag{2.122}$$

where, in the second expression, we apply the ergodic theorem, replacing the ensemble average with the volume average. This approach is commonly employed in turbulence studies, particularly when the system volume V contains several integral scales, which is valid under the assumption of homogeneity. The structure function, representing density fluctuations, is intricately related to the autocorrelation function through the following relation:

$$S_2(\boldsymbol{l}) = 2E_0 - 2C(\boldsymbol{l}), \tag{2.123}$$

where E_0 denotes the mean square density, which corresponds to the autocorrelation function at zero separation, namely the variance ($E_0 = C(0)$).

We employ an increment-space estimation of the power spectra, utilizing the Blackman–Tukey (B-T) estimation technique [194, 195], applied to the second-order structure function in Eq. 2.122. The B-T method is a widely used approach for estimating the Power Spectral Density (PSD) of a signal [114]. It involves calculating the autocorrelation function of the signal, applying an appropriate window function, and then performing a DFT or FFT to obtain the PSD. According to this methodology, the power spectrum is ultimately determined by applying the Wiener-Khinchin theorem [196], which involves taking the Fourier transform of the autocorrelation function. This can be expressed as:

$$P(k, \theta^*) = \int \tilde{C}(r, \theta^*)\, e^{-ikr} dr, \tag{2.124}$$

where $P(k, \theta^*)$ is the power spectral density function and $\tilde{C}(r, \theta^*)$ is the windowed autocorrelation function at a fixed angle $\theta = \theta^*$ in spherical coordinates. In the B-T method, windowing is critical to mitigate spectral leakage and enhance the accuracy of the PSD estimation. Zero padding is often employed to smooth the PSD estimate and improve frequency resolution by increasing the number of data samples with additional zeros in the given data sequence [197]. Using this approach, we focus on analyzing turbulence locally in the vicinity of black holes, where flat spacetime can be assumed.

The simulation conducted to explore these complex and intriguing features in the environment of compact objects utilizes `BHAC` [2, 182]. This code is capable of solving the ideal GRMHD equations in arbitrary but fixed and stationary spacetimes, particularly in a Kerr background expressed in the modified Kerr-Schild (MKS) coordinate system [198, 1]. It employs second-order high-resolution shock-capturing finite-volume methods, using the geometrized unit system. The relevant equations are given by Eq.s (2.116). As outlined in the previous Section, the code employs AMR techniques using an efficient block-based approach, along with a constrained-transport method that ensures the divergence of the magnetic field is maintained to round-off precision [184].

For the initial configuration, we consider an axisymmetric equilibrium torus with constant angular momentum [185] orbiting a Kerr black hole with a dimensionless spin parameter $a = 0.9375$. A magnetically arrested disk (MAD) regime is imposed [199, 200], where the accretion process is heavily influenced by the magnetic field, which inhibits the inward flow of matter, creating a dynamic equilibrium where material can only accrete through magnetic instabilities or reconnection events. The system is initialized with a vector potential of the form

$$A_\phi = \max\left[\frac{\rho}{\rho_{\max}}\left(\frac{r}{r_{\rm in}}\right)^3 \sin^3\theta \exp\left(-\frac{r}{400}\right) - 0.2, 0\right], \tag{2.125}$$

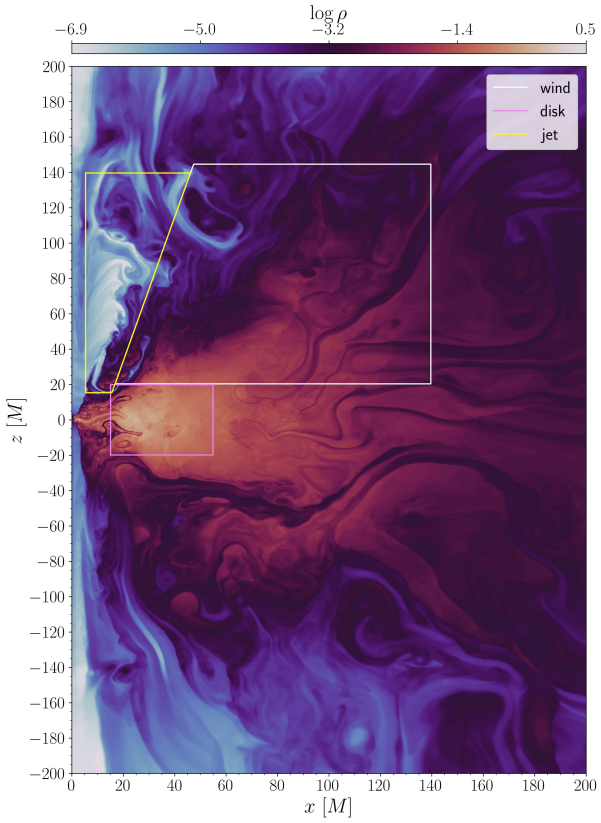

FIGURE 2.24: Logarithmic density ρ in the xz-plane, with three distinct regions highlighted: the disk (pink), the wind (white), and the jet (yellow). Lengths are expressed in units of the total mass M of the black hole.

where $\rho_{\max}$ denotes the maximum rest-mass density within the torus, and the inner radius of the torus, which determines the size and available matter, is set to $r_{\text{in}} = 12r_g$, with r_g being the Schwarzschild radius. The adiabatic index of the gas is $\Gamma = 4/3$, and the effective resolution used is $(N_r, N_\theta) = (4096, 2048)$.

Fig. 2.24 displays the logarithmic density ρ in the xz-plane of the simulation. The plot reveals intriguing spiral patterns, which suggest the potential emergence of vortices within the accretion disk. These vortices are compact, toroidal structures of magnetized plasma that form in highly dynamic environments. In addition to the large-scale vortices, the magnetized plasma within the accretion disk leads to the formation of smaller-scale structures known as plasmoids [201]. Plasmoids are highly localized, transient magnetic structures that arise from magnetic reconnection events occurring within the disk. During reconnection, magnetic field lines break and reconnect, releasing stored magnetic energy and accelerating plasma particles. This process leads to the formation of vortices near the reconnection region, which can propagate through the disk, transferring energy and influencing its overall evolution in a complex, multi-scale manner. Vortices primarily impact the global dynamics of the disk by redistributing mass and angular momentum, while also contributing to magnetic energy dissipation and particle acceleration processes at smaller scales.

Qualitatively, the simulation domain reveals three distinct regions, indicated by colored squares: the disk, the wind, and the jet. The disk is characterized by a region where the matter density dominates over the magnetic field, resulting in low magnetization and a high plasma beta, with turbulent and chaotic flow. The wind

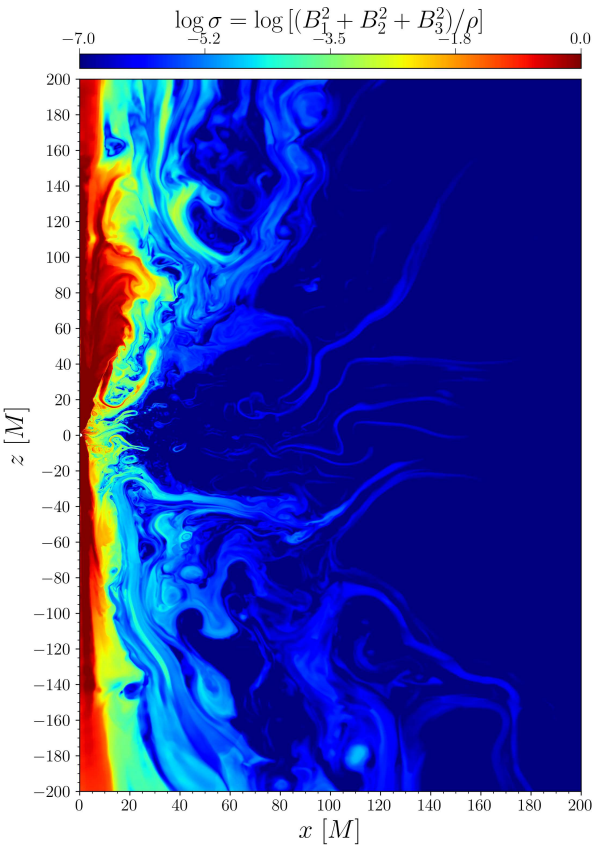

FIGURE 2.25: Logarithmic magnetization σ in the xz-plane. Lengths are expressed in units of the total mass M of the black hole.

represents a transition zone where the matter density decreases but still remains dominant over the turbulent magnetic field. In this region, current layers are also observed, with significant variations in density [202]. Lastly, the jet—a beam of particles and radiation ejected from the black hole's poles—is characterized by lower density and a dominant magnetic field, with a low plasma beta. These three zones are clearly distinguishable in Fig. 2.25, where the magnetization is plotted across the domain.

We then analyze the shell-integrated mean power spectra of the rest-mass density ρ for each of the identified regions—the disk, wind, and jet—as depicted in Fig. 2.24. This analysis is extended to explore variations in spectral characteristics as a function of the angle θ. To address challenges posed by irregular boundaries, AMR, and the curved spacetime geometry, we apply the procedure detailed in Appendix B, which includes a test on a synthetic Kolmogorov field.

Fig. 2.26 presents the spectral characteristics of the disk region. The measured data points, obtained through the B-T method, are depicted as blue markers connected by a curve. A red dashed line labeled "K41" represents the Kolmogorov law ($k^{-5/3}$). Additionally, a black dashed line illustrates the fitted power law (k^{α}), where the exponent α is determined via curve fitting. Notably, this exponent may deviate from the expected Kolmogorov exponent ($-5/3$) for various reasons. In this case, we do not observe a Kolmogorov scaling, as $\alpha \approx 2$ (instead of -1.7). This discrepancy may arise due to the turbulence being (1) two-dimensional, (2) magnetized, and (3) compressible. Vertical dashed lines labeled k_{min} and k_{max} indicate the minimum and maximum wavenumbers considered in the analysis, respectively. These limits are

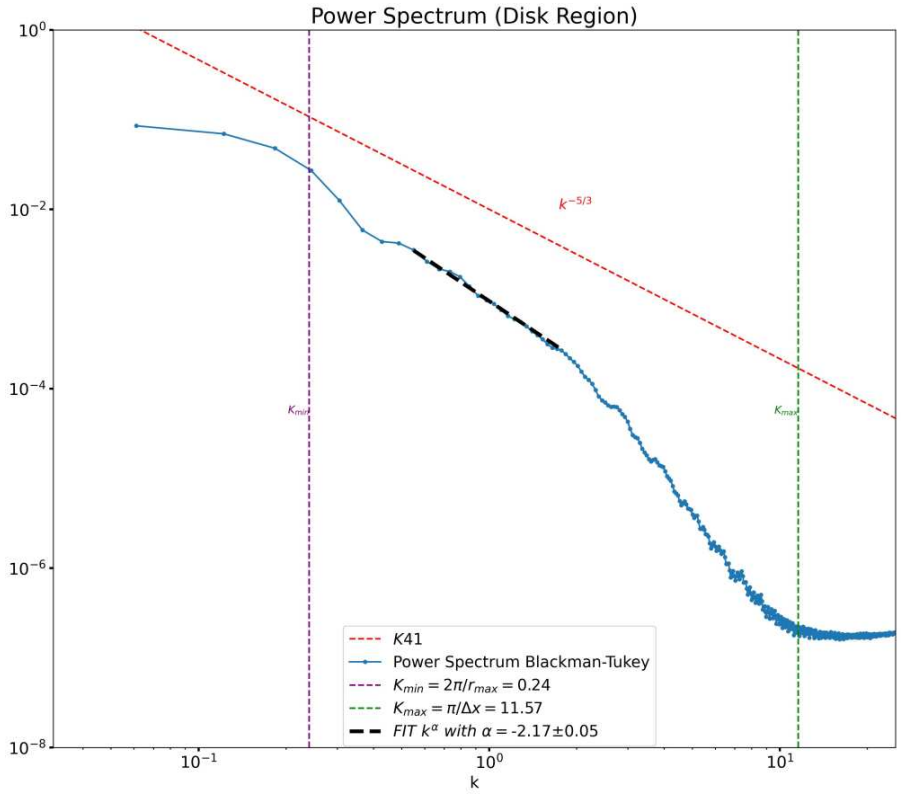

FIGURE 2.26: Average Power Spectrum for the rest-mass density in the disk region.

defined based on the system's characteristics:

$$k_{\min} = \frac{2\pi}{r_{\max}}, \tag{2.126}$$

where $r_{\max} = \Delta r\, N_r$, with Δr denoting the spatial separation between two consecutive points, and $N_r = 2N_x/3$. Conversely, $k_{\max}$, determined by the Nyquist mode, is defined as:

$$k_{\max} = \frac{2\pi}{r_{\max}} m = \frac{2\pi}{N_x \Delta x} \frac{N_x}{2} = \frac{\pi}{\Delta x}, \tag{2.127}$$

where $\Delta x = L_x/\sqrt{N_{pt}}$, and m denotes the Nyquist mode, which corresponds to the maximum frequency an analog signal can exhibit while still being accurately converted into a digital signal. Here, L_x represents the extent of the x-axis, and N_{pt} is the total number of points in the region.

The analysis of the wind spectra in Fig. 2.27 and the jet spectra in Fig. 2.28 provides interesting comparisons with the disk spectrum, highlighting distinct behaviors across these regions. The wind spectrum closely mirrors that of the disk, although it shows less developed turbulence. Additionally, it is noteworthy that the high-frequency region of the spectra reveals signs of possible aliasing and interpolation effects. This outcome was expected, as the wind spectrum was anticipated to be lower than that of the disk due to the reduced energy and activity in this zone. The similarity in spectral patterns suggests consistent turbulence characteristics between these two regions, with the primary difference being the overall lower energy levels in the wind.

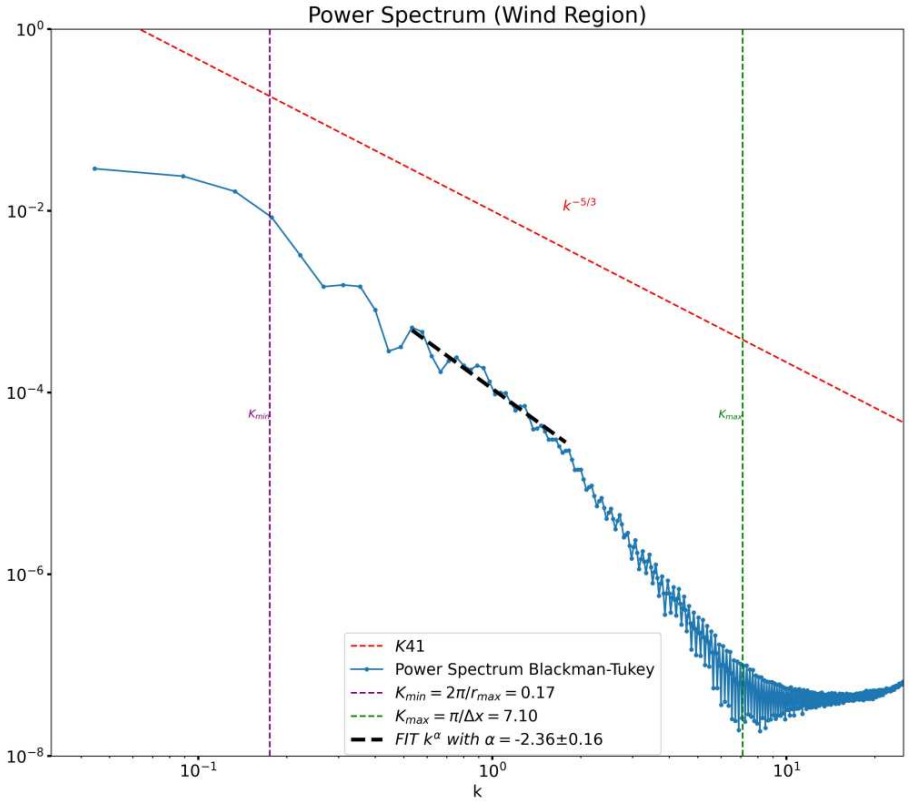

FIGURE 2.27: Average Power Spectrum for the rest-mass density in the wind region.

The jet spectrum exhibits a similar behavior to the wind and disk spectra, although the average spectrum of the jet region shows significantly lower values compared to the other two, along with a shallower slope. This observation is likely attributed to the infinitesimally small density values present in the jet region, along with the limited presence of shocks.

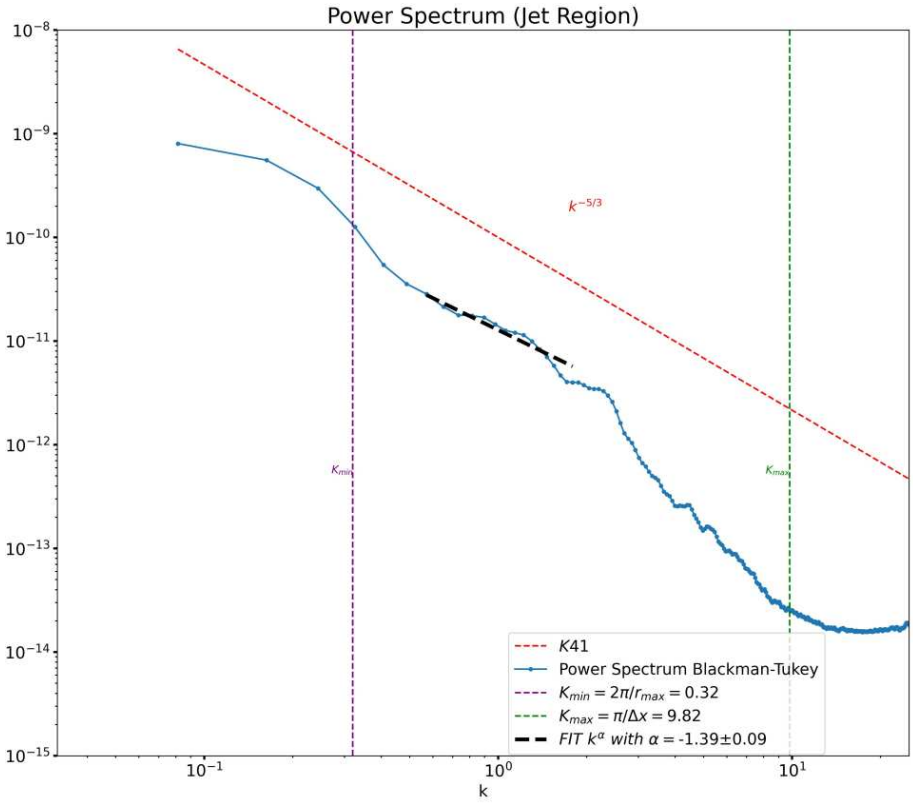

FIGURE 2.28: Average Power Spectrum for the rest-mass density in the jet region.

The power spectrum plots at different angles, θ, provide valuable insights into the system's behavior, as illustrated in Fig. 2.29. These datasets reveal a distribution of points following a descending slope as k increases. In addition to the data, several reference lines are included: a dashed black line labeled "$k^{-5/3}$," representing the Kolmogorov power law, a dashed vertical purple line indicating k_{min}, and a dashed green line marking k_{max}. The behavior of the spectrum suggests adherence to the power law with a slope of $k^{-5/3}$ within a specific range of wavenumbers, before diverging or exhibiting significant variation at higher wavenumbers. This variation with respect to the angle θ could be attributed to various physical processes occurring near the black hole, such as matter accretion or relativistic jets. The data points follow the slope implied by the $k^{-5/3}$ power law, with slight differences in distribution depending on the angle. For instance, at larger angles (e.g., $\theta = 130^{\circ}$, highlighted in red), the data spread appears broader compared to smaller angles. Furthermore, the variation in the power spectrum as a function of θ suggests the presence of anisotropic turbulence around the black hole, where turbulence properties such as energy distribution and flow characteristics exhibit directional dependence.

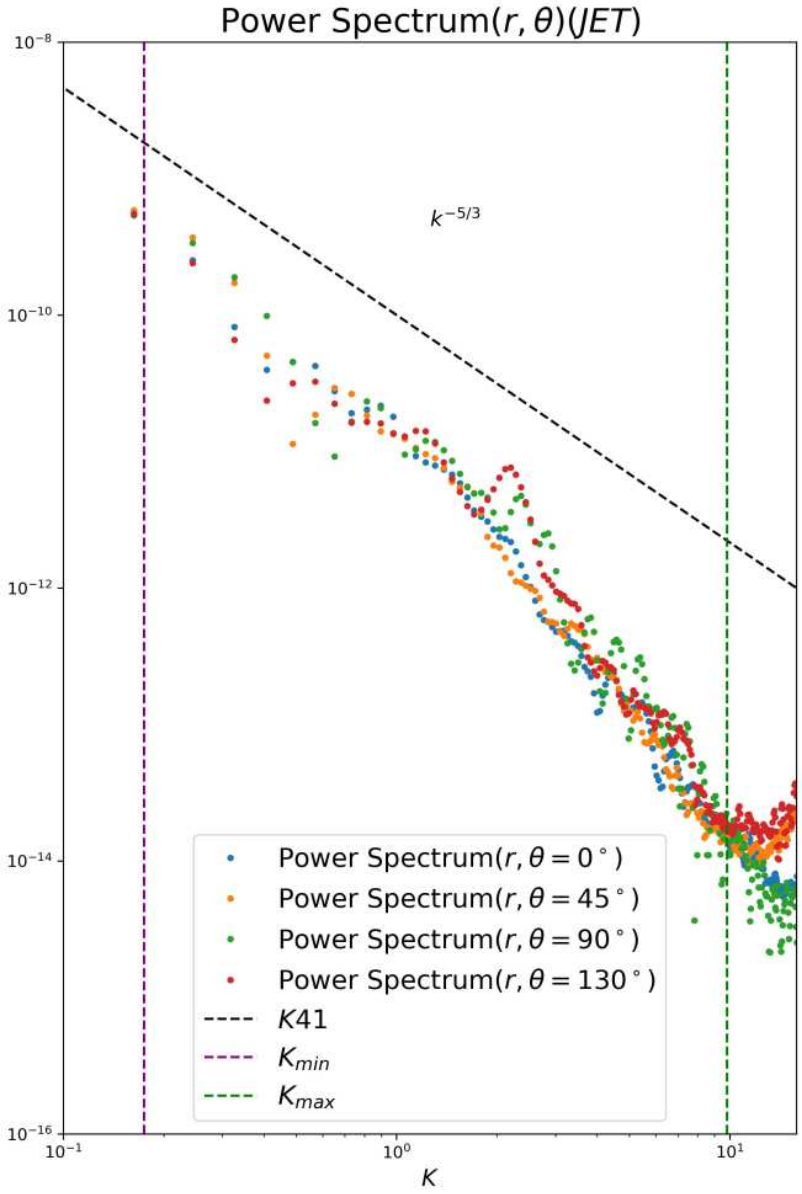

FIGURE 2.29: Average power spectrum for the rest-mass density in the jet region for different polar angles θ.

For future research, we intend to extend this analysis of turbulence in the vicinity of black holes to a general relativistic framework, accounting for the effects of curved spacetime induced by these compact objects, as well as the natural geodesic paths in a generic Riemannian manifold [203].

In this Chapter, we have focused on the macroscopic dynamics of plasmas surrounding Kerr-type black holes, particularly examining the turbulence that arises within accretion disks. These disks are characterized by strong shearing motions and intense magnetic fields, that give rise to various instabilities, notably the KHI

and the MRI. The KHI develops at fluid layer interfaces due to velocity shear, generating vortices and redistributing energy, while the MRI drives turbulence in magnetized disks, facilitating angular momentum transport and enabling accretion. Turbulence in these systems effectively transfers energy from large scales to progressively smaller scales. While at macroscopic scales, energy dissipation primarily affects the global structure and evolution of the disk, the cascading process eventually reaches plasma-specific scales, such as the Larmor radius and skin depth. At these kinetic scales, the plasma behaves as a collisionless medium, making the fluid-based GRMHD framework insufficient for capturing the intricate particle dynamics. To accurately describe plasma behavior at these scales, it becomes necessary to employ the Vlasov-Maxwell equations, which govern the kinetic interactions between particles and electromagnetic fields. This transition from a fluid to a kinetic description is essential, especially in regions dominated by magnetic reconnection and small-scale turbulence. The most suitable approach for capturing these phenomena at kinetic scales is through PIC simulations.

Up to this point, in the context of GRMHD, our focus has been on the large-scale dynamics of plasmas near black holes, examining phenomena such as accretion disks and relativistic jets. GRMHD simulations offer a powerful framework to model plasma dynamics under the influence of strong gravitational fields. However, certain regimes—particularly those involving the microphysics of plasmas—demand a kinetic approach to accurately capture local particle interactions and dynamics, especially in regions with high turbulence or intense magnetic reconnection.

While GRMHD simulations are highly effective in capturing global plasma dynamics, they are not designed to resolve the microscopic behavior of individual particles. Here, kinetic simulations, particularly those using PIC methods, become indispensable. These simulations enable us to investigate the interactions of individual electrons, protons, and other species in regions where magnetic fields dominate at small scales. The aim is not to replace GRMHD simulations but to complement them with a local, high-resolution perspective on plasma behavior. Integrating GRMHD and PIC simulations may significantly enhance our capacity to model and predict matter dynamics in extreme astrophysical environments.

In the next Chapter, we will delve into the kinetic dynamics of relativistic plasma composed of electrons and protons in a turbulent regime, using high-resolution PIC simulations. These simulations allow us to investigate the behavior of individual particles and analyze the emergence of coherent magnetic structures from the turbulent background. By capturing the detailed interactions between particles and magnetic fields at small scales, we aim to deepen our understanding of phenomena such as particle acceleration and localized instabilities, which play a crucial role in shaping the evolution of accretion disks.

Chapter 3

Kinetic Plasma Turbulence near Black Holes

The previous Chapter focused on the complex dynamics of matter surrounding black holes, emphasizing the critical roles of magnetic fields and large-scale dynamics. The matter surrounding black holes is, therefore, characterized by turbulence, which transfers energy from large to small scales. Transitioning from a GRMHD framework to a kinetic approach provides a more detailed perspective on plasma behavior at smaller spatial and temporal scales, where the dynamics of individual particles become essential for a comprehensive understanding of the underlying physical processes.

While the GRMHD approach is widely employed to describe compact astrophysical objects in various realistic scenarios, it largely leaves the microphysical properties of non-thermal plasmas undetermined. It is therefore necessary to complement global fluid simulations with local kinetic approaches to capture plasma dynamics at the microphysical level that would otherwise remain unresolved. To this end, we present results from large-scale PIC simulations using the `Zeltron` code [3]. This methodological shift allows us to explore turbulent behavior in fully kinetic plasmas through high-resolution simulations. Unlike MHD, which assumes fluid-like behavior and averages out complexities at larger scales, kinetic simulations resolve the interactions between particles, such as electrons and protons. This enables the capture of intricate dynamics across multiple scales, elucidating how turbulence drives the formation of coherent structures, including vortices, current sheets, and plasmoids. These structures play a key role in energy dissipation in various astrophysical environments. Moreover, the kinetic approach provides valuable insights into particle acceleration mechanisms, particularly in turbulent regions.

Magnetic reconnection, often triggered by turbulence, generates localized regions where particles experience significant energy gains. Such acceleration processes are relevant in many astrophysical contexts, including solar flares and the extreme environments around black holes and neutron stars (see Sironi and Spitkovsky [204]). By resolving the interactions between two particle species, electrons and protons, these advanced simulations enhance our understanding of the kinetic processes that lead to the formation of long-lived structures, such as flux ropes and magnetic vortices. These coherent patterns have been observed in both controlled laboratory experiments and space-based measurements, notably within the solar wind and Earth's magnetosphere.

Recent advancements in numerical methods and computational capabilities have enabled detailed simulations of these phenomena, unveiling the intricate interplay

between large-scale turbulence and the subtler effects of kinetic dynamics. The results from these high-resolution simulations pave the way for constructing a self-consistent kinetic model that characterizes the emergent structures in turbulent plasmas. Additionally, these advancements allow us to establish a connection between the microphysical properties of the plasma and its macroscopic (fluid-like) description using the well-established and extensively tested Gold-Hoyle solution [205, 206], achieved through a local relaxation process where magnetic helicity remains finite and plays a crucial role. By employing a cylindrical coordinate framework, we can derive solutions that converge to modified force-free equilibria. This approach provides a robust theoretical foundation for understanding the formation and evolution of these structures. Such equilibria have practical applications in various astrophysical contexts, from plasmoid formation in accretion flows around black holes to the generation of flux ropes in the solar wind.

Furthermore, we extend our plasma model to include a third species: positrons. Although the role of positrons in plasmas has been widely studied (e.g., Sironi and Spitkovsky [204] and Sironi, Petropoulou, and Giannios [134]), their concentration in different regions around black holes—such as jets, accretion disks, and winds—remains an open question. Variations in positron density can significantly influence key processes like energy transfer, particle acceleration, and emission spectra through mechanisms such as inverse Compton scattering and pair production. This is particularly relevant in turbulent environments, where these processes occur on small spatial scales and interact nonlinearly with magnetic fields. With this in mind, we intend to employ high-resolution kinetic simulations to systematically explore different positron concentrations across each of these regions. By doing so, we seek to understand how variations in positron density affect the evolution of plasma turbulence, especially over large Alfvén timescales. This approach aims to bridge the gap between global GRMHD models and the underlying kinetic processes, shedding light on the local plasma dynamics in accretion environments. These insights are crucial for advancing our understanding of matter behavior near black holes and how turbulent energy cascades impact particle energization and radiative phenomena.

3.1 A kinetic approach to plasmas

The classical or relativistic kinetic description of a physical system is based on modeling the interaction of matter elements via force fields, and PIC methods have been among the most successful approaches. In PIC simulations, plasma is treated as an ensemble of computational particles, where the system consists of charged particles (e.g., negative electrons and positive ions) interacting via the Lorentz force. The use of PIC simulations began in the 1950s, and the development of codes worldwide has been continuously expanding. With the exponential growth of computational resources, many large-scale 3D PIC simulations have now been conducted, despite the fact that such simulations typically require substantial memory.

Several PIC codes have been developed in recent years by different research groups, employing various techniques. Among the most noteworthy are `TRISTAN` (TRIdimensional STANford) [207], `VPIC` (Vector Particle-In-Cell) [208], `iPIC3D` [209], `Zeltron` [3], `PHOTON-PLASMA` [210], `PIConGPU` [211], `PICCANTE` [212], `FBPIC` [213], and others.

Hybrid models have been developed to retain key aspects of collisionless plasma physics while achieving significant improvements in resolution or simulation duration by incorporating certain fluid descriptions. For instance, in the hybrid-PIC method, electrons are treated as massless and form a perfectly conducting fluid [214, 215]. An MHD-PIC approach has been introduced to kinetically treat a specific species (e.g., cosmic rays) and to study the interaction between this collisionless plasma and a thermal plasma [216]. Relativistic fully kinetic approaches, in which both electrons and ions are treated as particles, are widely employed in the astrophysics community to simulate plasmas in turbulent regimes and to model particle acceleration processes (e.g., Duţan et al. [217], Sironi and Cerutti [218], Comisso and Sironi [219], Comisso et al. [220], and Comisso and Sironi [221]). More recently, the `GRZeltron` code has been introduced [222], representing the first PIC code that accounts for spacetime curvature in a full general relativity framework using a modified $3+1$ formulation of the equations. The authors provide a first-principles model for the magnetosphere and corona around supermassive rotating black holes [223, 224, 225].

3.1.1 The `Zeltron` code

The fundamental idea behind PIC codes is to solve the Vlasov equation indirectly:

$$\partial_t f_\alpha + \boldsymbol{v} \cdot \boldsymbol{\nabla}_{\boldsymbol{x}} f_\alpha + q_\alpha \left[\boldsymbol{E} + \frac{\boldsymbol{v}}{c} \times \boldsymbol{B} \right] \cdot \boldsymbol{\nabla}_{\boldsymbol{p}} f_\alpha = 0, \tag{3.1}$$

where $f_\alpha = f_\alpha(\boldsymbol{x}, \boldsymbol{p}, t)$ is the distribution function for the α-th species that characterizes the plasma, $\boldsymbol{p} = \gamma m_\alpha \boldsymbol{v}$ is the momentum of the particles, $\boldsymbol{v}$ is the 3-velocity of the particles, and $\gamma = 1/\sqrt{1-(v/c)^2}$ is the Lorentz factor, while q_α and m_α represent the charge and mass of the α-th species, respectively. We point out that throughout this Section, we will refer to the Lorentz factor as γ instead of W, as used in previous Chapters and Sections, following the standard convention in the literature.

In the particle approximation, each particle does not represent a single electron (or ion), but rather an ensemble of particles. For this reason, particles are often referred to as macro-particles. A macro-particle in a PIC code can be viewed as a small portion of the phase space distribution of the system. This approach is physically consistent, as it represents many particles within a constant-sized macro-particle, given that particles with the same momentum remain close to each other in phase space. It can be demonstrated that integrating the discrete particle trajectories is equivalent to solving the full kinetic, collisionless Vlasov equation along characteristic curves.

In this approach, the distribution function for N macroparticles is approximated by

$$f_\alpha(\boldsymbol{x}, \boldsymbol{p}, t) = \sum_{j=1}^{N} w_j \, \delta(\boldsymbol{r} - \boldsymbol{r}_j(t)) \, \delta(\boldsymbol{p} - \boldsymbol{p}_j(t)), \tag{3.2}$$

where $\boldsymbol{r}_j(t)$ and $\boldsymbol{p}_j(t)$ are the position and momentum of the j-th particle, and w_j is a coefficient referred to as the weight of the j-th particle. In PIC simulations, particle dynamics are driven by collective processes operating through the electromagnetic fields, rather than by individual collisions, which are not resolved by the PIC method. Plasma physics becomes relevant only at scales larger than the Debye length, defined as

$$\lambda_D = \sqrt{\frac{k_B T_e}{4\pi n e^2}}, \tag{3.3}$$

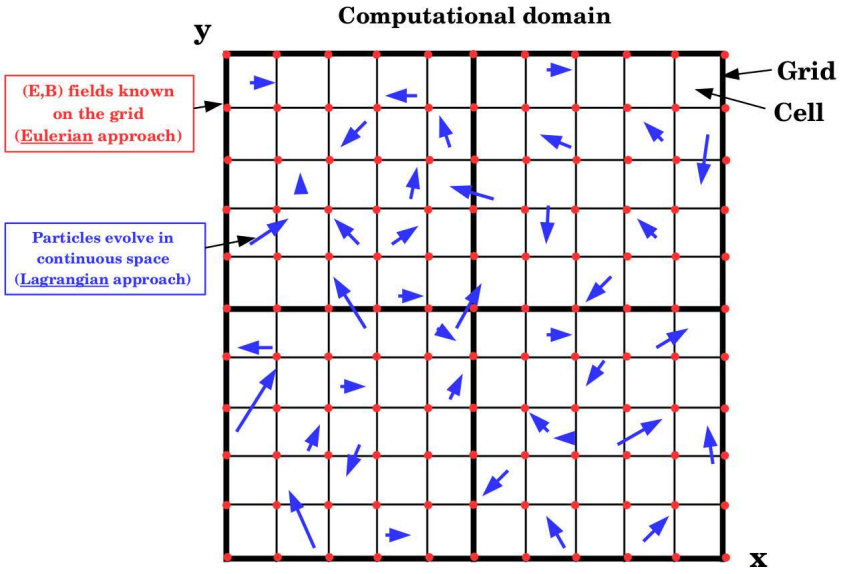

FIGURE 3.1: Schematic representation of the computational domain in PIC methods. The electromagnetic fields are defined and evolved at the grid points (red dots), while the particles evolve in continuous space (blue arrows). Each cell is delimited by four neighboring grid points. Figure from https://ipag.osug.fr/ ceruttbe/Zeltron/index.html.

where e is the electron charge. In PIC simulations, resolving microscopic kinetic scales is essential.

A PIC code must solve, in a self-consistent manner, Newton's equations for the particles and Maxwell's equations for the electric and magnetic fields. The computational macroparticles move on a grid (Lagrangian approach), where their charge and current density are weighted at every time iteration Δt. The fields are then computed from Maxwell's equations on the grid (Eulerian approach), based on the interpolated sources. Finally, the force on each particle is extrapolated from the grid, allowing for the advancement of their position and momentum in time. The force acting on the particles is calculated from the electric and magnetic fields evaluated at the particle's position, while the fields themselves are influenced by the particles in the system. A schematic representation of this approach is shown in Fig. 3.1, where the grid nodes are marked with red dots, and the blue arrows represent the positions and velocities of the particles. This sequence of operations is repeated at each time-step in a self-consistent manner, evolving both the particle and electromagnetic field states. Fig. 3.2 illustrates the procedure for a single time-step Δt.

In our relativistic kinetic simulations, we made use of the publicly available `Zeltron` code [3], an explicit relativistic electromagnetic PIC code ideally suited for modeling particle acceleration in astrophysical plasmas. Here, we briefly describe the method. In the `Zeltron` code, the equations of motion are solved at each time step Δt for each of the N particles in the simulation, with $N \gtrsim 10^9$. Therefore, when choosing the integration scheme for the particles, a compromise must be made between efficiency, accuracy, and computational storage capacity.

The `Zeltron` code employs a Leap-Frog algorithm to evolve macroparticles in time, which we describe here for a simple 1D case. In this approach, positions and velocities are staggered on the time axis by half a time step $\Delta t/2$, so that positions are defined at $t_n = n\Delta t$, while velocities are defined at $t_{n+1/2} = (n + 1/2)\Delta t$. At

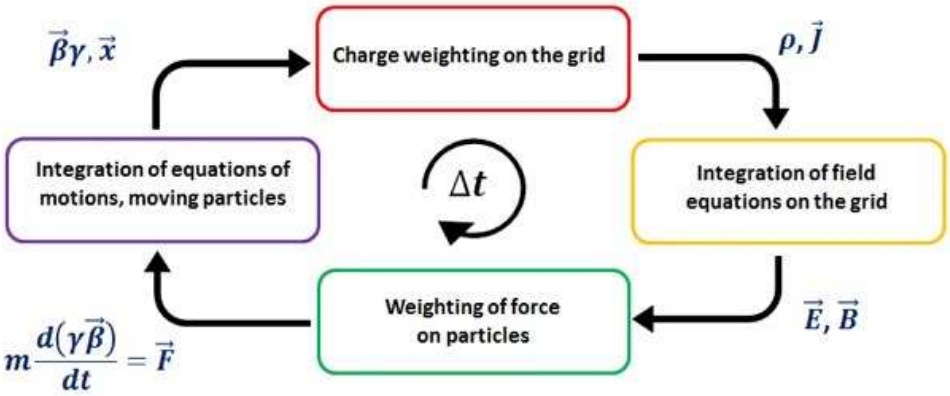

FIGURE 3.2: Typical computational procedure of the PIC algorithm per time step. Yellow box: $\vec{E}$ and $\vec{B}$ fields are evolved via Maxwell's equations. Green box: the Lorentz force acting on the particles is computed using the updated fields, evaluated at the particle positions. Purple box: the equation of motion for the particles is solved using the Lorentz force. Red box: charge and current densities are deposited on the grid points, where $\vec{E}$ and $\vec{B}$ can be updated. Figure from http://gaps.ing2.uniroma1.it/alberto/alberto/PIC.html.

time step n, the basic integration formula for the Leap-Frog algorithm is:

$$x^{n+1} = x^n + \frac{\Delta t}{m_\alpha} p^{n+1/2}, \tag{3.4}$$

$$p^{n+3/2} = p^{n+1/2} + \Delta t\, F(x^{n+1}), \tag{3.5}$$

where $F(x)$ is the velocity-independent force acting on the particles. The initialization of this scheme may appear problematic, as for a given initial position and momentum, one must compute $p^{1/2}$. This induces a first-order error, but this is inconsequential since it only needs to be done once. It can be shown through a Taylor expansion in time that this scheme is accurate to second order. Unlike the second-order Runge-Kutta method, it requires only one evaluation of the function F per time step. It is worth noting that the finite difference scheme in the equations is time-centered, making it time-reversal invariant. However, a minor inconvenience of this scheme is that positions and velocities are never known at the same time step, which may pose challenges for certain diagnostics.

The main advantage of the Leap-Frog algorithm lies in its symplecticity, which ensures the global stability of the algorithm. This property implies that no secular trends can arise, and globally conserved quantities, such as energy and angular momentum, remain bounded over time [226, 227]. In contrast, such trends can be observed over long time scales even in highly accurate non-symplectic schemes, such as the fourth-order Runge-Kutta scheme.

The equation of motion for a single macro-particle is given by the Lorentz – Abraham – Dirac equation [228]:

$$\frac{d\boldsymbol{r}}{dt} = \frac{c\boldsymbol{u}}{\gamma}, \tag{3.6}$$

$$\frac{d\boldsymbol{u}}{dt} = \frac{q_\alpha}{m_\alpha c}\left[\boldsymbol{E} + \frac{\boldsymbol{u}}{c} \times \boldsymbol{B}\right]. \tag{3.7}$$

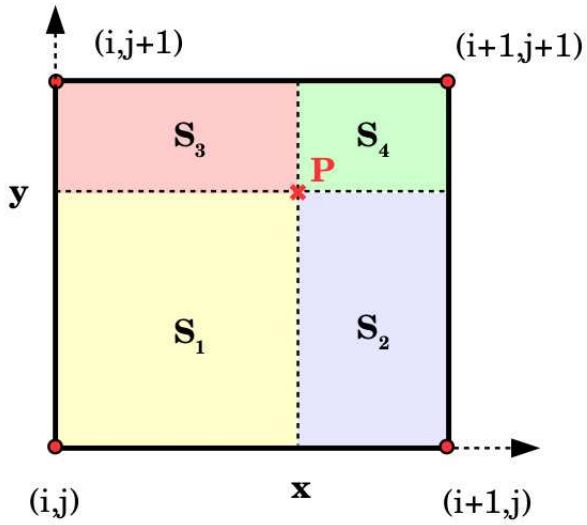

FIGURE 3.3: Area-weighting procedure on a 2D Cartesian grid. The fractional charge of a particle at point P is deposited on the four surrounding nodes in proportion to the colored shaded areas. Figure from https://ipag.osug.fr/ ceruttbe/Zeltron/index.html.

The above is the special relativistic version of Newton's equations for a macro-particle with 3-velocity $\boldsymbol{v}$ and normalized momentum $\boldsymbol{u} = \gamma \boldsymbol{v}/c = \gamma \boldsymbol{\beta}$. The `Zeltron` code also includes the radiation reaction force if synchrotron radiation is considered in the simulation, though this is not taken into account in our simulations. Moreover, the fields appearing in these equations are evaluated at the particle's position. A linear interpolation from the grid to the particle's position suffices for this purpose. A practical implementation of the particle mover is the *Boris push* [229], which separates the effects of the electric and magnetic forces and can be used to evolve the momentum under the action of the Lorentz force. This method allows us to write the discretized momentum equation as

$$\frac{\boldsymbol{u}^{+} - \boldsymbol{u}^{-}}{\Delta t} = \frac{q_\alpha}{2 m_\alpha c \gamma} \left[\boldsymbol{u}^{+} - \boldsymbol{u}^{-} \right] \times \boldsymbol{B}, \tag{3.8}$$

$$\boldsymbol{u}^{\pm} = \boldsymbol{u}^{n \pm 1/2} \mp \frac{q_\alpha \Delta t}{2 c m_\alpha} \boldsymbol{E}_n. \tag{3.9}$$

The Lorentz force is evaluated at integer time steps (see Fig. 3.4), and thus the mean velocity $\boldsymbol{u}^n \simeq \left(\boldsymbol{u}^{n+1/2} + \boldsymbol{u}^{n-1/2} \right)/2$ is employed.

In order to solve the time-dependent Maxwell's equations, the source terms must first be computed. The charge density and current density are determined by the contributions of the particles:

$$\rho(\boldsymbol{r}) = \sum_{j=1}^{N} q_j \, w_j \, \delta(\boldsymbol{r} - \boldsymbol{r}_j), \tag{3.10}$$

$$\boldsymbol{j}(\boldsymbol{r}) = \sum_{j=1}^{N} q_j \, w_j \, \boldsymbol{v}_j \, \delta(\boldsymbol{r} - \boldsymbol{r}_j). \tag{3.11}$$

The values of these source terms must be deposited onto the grid nodes, so they can be injected into the spatially discretized Maxwell equations. The `Zeltron` code

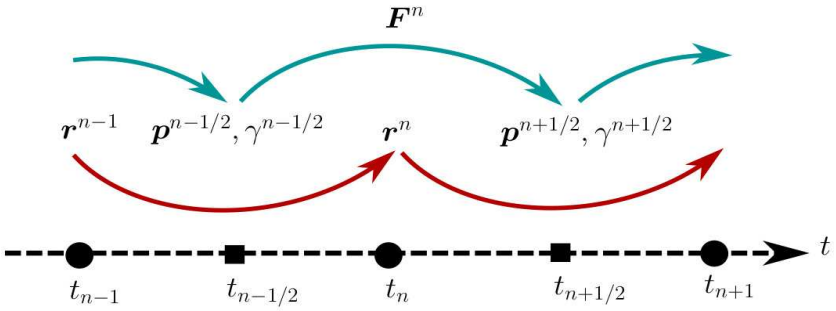

FIGURE 3.4: Representative diagram of the Leap-Frog scheme for the particles. The positions are defined at integer time steps, whereas the velocities are defined at half-integer time steps. Figure from Crinquand [223].

employs linear interpolation to deposit the charges and currents generated by each particle onto the nodes of the computational grid (see Fig. 3.3). The code also assigns variable weights to the macro-particles to model particle density gradients. Once the source terms have been updated and deposited on the grid nodes, the final step involves evolving the field equations. The code employs the Yee algorithm [230] to solve the time-dependent Maxwell equations:

$$\partial_t \boldsymbol{B} = -c\nabla \times \boldsymbol{E}, \tag{3.12}$$

$$\partial_t \boldsymbol{E} = c\nabla \times \boldsymbol{B} - 4\pi \boldsymbol{J}, \tag{3.13}$$

where $\boldsymbol{B}$ is the magnetic field, $\boldsymbol{E}$ is the electric field, and $\boldsymbol{J}$ is the current density. The key idea behind the Yee algorithm is to stagger the different components of the fields on distinct nodes of the grid. For instance, it is instructive to present Faraday's law in Eq. (3.12) in its discretized form, which reads:

$$(B_x)^{n+1/2}_{i,j+1/2} - (B_x)^{n-1/2}_{i,j+1/2} = -\frac{c\Delta t}{\Delta y}\left[(E_x)^n_{i,j+1} - (E_x)^n_{i,j}\right], \tag{3.14}$$

$$(B_y)^{n+1/2}_{i+1/2,j} - (B_y)^{n-1/2}_{i+1/2,j} = \frac{c\Delta t}{\Delta x}\left[(E_z)^n_{i+1,j} - (E_z)^n_{i,j}\right], \tag{3.15}$$

$$\begin{aligned}(B_z)^{n+1/2}_{i+1/2,j+1/2} - (B_z)^{n-1/2}_{i+1/2,j+1/2} = c\Delta t \Bigg\{ &-\frac{1}{\Delta x}\left[(E_y)^n_{i+1,j+1/2} - (E_y)^n_{i,j+1/2}\right] \\ &+\frac{1}{\Delta y}\left[(E_x)^n_{i+1/2,j+1} - (E_x)^n_{i+1/2,j}\right]\Bigg\}.\end{aligned} \tag{3.16}$$

In the above equations, the upper index denotes the time step, and the lower index denotes the spatial position on the Yee grid. A schematic representation of the electromagnetic fields staggered on a 2D Cartesian grid is shown in Fig. 3.5.

To advance the particles, the electric and magnetic fields must be known at the same time. The magnetic field is first advanced by half a time step, $\Delta t/2$, so that the particle motion can be computed. Then, the magnetic field is advanced again by $\Delta t/2$. Assuming $\boldsymbol{E}^n$ and $\boldsymbol{B}^n$ are initially known, the following five steps are taken in

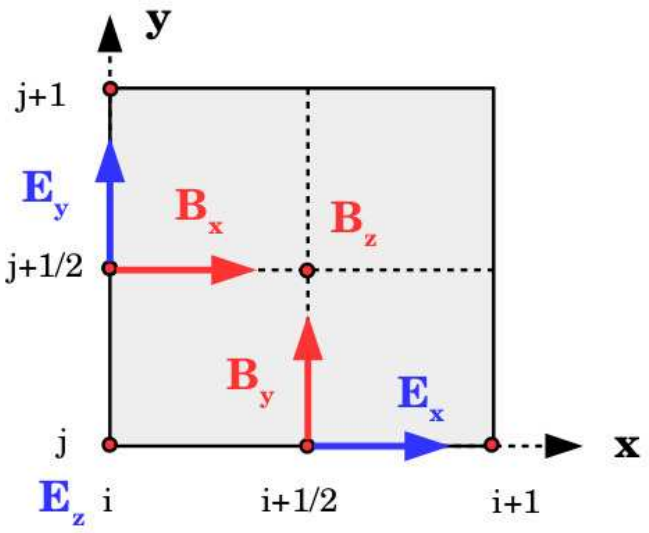

FIGURE 3.5: Graphic representation of a 2D Cartesian Yee grid. The blue arrows denote the components of the electric fields, while the red arrows denote the magnetic fields. The positions on the mesh are labeled by the indices i in the x direction and j in the y direction. Note that the two fields are staggered in space. Figure from https://ipag.osug.fr/ cerutt-be/Zeltron/index.html.

order to update the system:

$$
\begin{aligned}
&(1)\ \boldsymbol{u}^{n-1/2} \longrightarrow \boldsymbol{u}^{n+1/2};\\
&(2)\ \boldsymbol{r}^{n} \longrightarrow \boldsymbol{r}^{n+1};\\
&(3)\ \boldsymbol{B}^{n+1/2} \longrightarrow \boldsymbol{B}^{n} - \frac{c\Delta t}{2}\left[\nabla \times \boldsymbol{E}\right]^{n};\\
&(4)\ \boldsymbol{E}^{n+1} \longrightarrow \boldsymbol{E}^{n} - c\Delta t\left[\nabla \times \boldsymbol{B}\right]^{n+1/2} - 4\pi\Delta t\boldsymbol{J}^{n+1/2};\\
&(5)\ \boldsymbol{B}^{n+1} \longrightarrow \boldsymbol{B}^{n+1/2} - \frac{c\Delta t}{2}\left[\nabla \times \boldsymbol{E}\right]^{n+1};
\end{aligned}
\tag{3.17}
$$

where the current density $\boldsymbol{J}^{n+1/2}$ is computed as the average between $\boldsymbol{J}(\boldsymbol{r}^{n}, \boldsymbol{u}^{n+1/2})$ and $\boldsymbol{J}(\boldsymbol{r}^{n+1/2}, \boldsymbol{u}^{n+1/2})$. Note that in step (1), the electric field $\boldsymbol{E}^{n}$ and the magnetic field $\boldsymbol{B}^{n}$ are used to update the momentum, while in step (2), the position is updated using the momentum $\boldsymbol{u}^{n+1/2}$.

The `Zeltron` code does not exactly satisfy the Maxwell-Gauss constraint $\nabla \cdot \boldsymbol{E} = 4\pi\rho_c$, where ρ_c is the charge density, and the electric charge deposited on the grid is not perfectly conserved. If this occurs, small errors can accumulate and lead to unphysical charge densities. Therefore, the electric field must be corrected at every time step by a small amount $\delta\boldsymbol{E}$, obtained by solving the following Poisson equation:

$$
\nabla^2(\delta\phi) = \nabla \cdot \boldsymbol{E} - 4\pi\rho_c, \tag{3.18}
$$

with $\delta\boldsymbol{E} = -\nabla(\delta\phi)$, where ϕ is the electrostatic potential. This method is referred to as *divergence cleaning* [231]. `Zeltron` exhibits second-order accuracy in both space and time, while ensuring that the magnetic constraint $\nabla \cdot \boldsymbol{B} = 0$ is satisfied at every instant of the simulation. One of the major advantages of employing the Yee grid

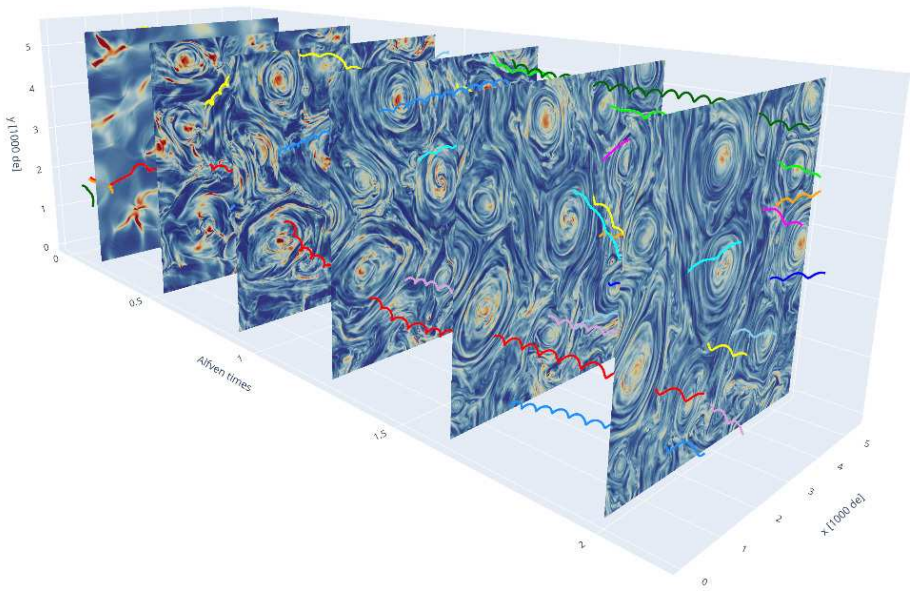

FIGURE 3.6: Evolution of the total number density n over time, progressing from left to right and expressed in Alfvén times, with selected electron trajectories traced throughout the evolution.

is that the divergence of the magnetic field is automatically maintained to machine round-off precision, provided that this constraint is satisfied at the initial time.

3.2 Turbulence and Long-lived Structures in Kinetic Plasmas

Turbulence in classical fluids is distinguished by the emergence of coherent, long-lived structures from an otherwise chaotic environment. In this Section, we explore an analogous phenomenon within the framework of fully kinetic plasma turbulence, leveraging high-resolution direct numerical simulations in two spatial dimensions. Our results reveal the development of persistent vortices exhibiting features characteristic of large-scale, magnetically dominated force-free configurations. These vortices endure over extended timescales, as shown in Fig. 3.6, mirroring the behavior typically observed in classical fluid turbulence, and thereby bridging the conceptual gap between fluid dynamics and plasma physics.

Inspired by the Harris pinch model for inhomogeneous equilibria, we construct a self-consistent kinetic model in cylindrical coordinates, centered around a representative vortex (see Imbrogno et al. [232]). This formulation begins with an explicit representation of the particle velocity distribution function for the local equilibrium regions. The resulting equilibrium can be simplified to a Gold-Hoyle solution of a modified force-free state. During this process, turbulence is mediated by these long-lived structures, which are accompanied by transient events where vortices merge and form new metastable equilibria. This dynamic is crucial for understanding a range of astrophysical phenomena, from the formation of plasmoids near compact objects to the emergence of coherent structures in the heliosphere.

Astrophysical turbulence is one of the most intricate processes, shaping diverse environments such as the heliosphere, the interstellar medium, and the surroundings of compact objects [233, 234, 235]. It spans a wide range of length and time

scales, from large eddies to sub-electron scales [236]. The cascade of energy, transferred from large-scale shear flows and boundary layers to particle-interaction scales, is central to energy conversion and dissipation [237].

While turbulence is often perceived as chaotic and unpredictable, this view oversimplifies its complexity. Persistent, long-lived structures can emerge even within turbulent states, as observed across various systems [238, 239, 240]. These coherent structures—ranging from vortices to waves and sheets—are important for understanding the underlying dynamics of turbulence [237]. Among these, Alfvén vortices [241, 239] are particularly noteworthy, as they represent large-scale structures that significantly influence plasma dynamics.

Although much research has focused on stable structures in classical (viscous) fluids [242], there remains a notable gap in understanding their counterparts in collisionless, magnetized plasmas. In such systems, stable structures can propagate undisturbed for extended periods, particularly in environments like stellar winds [243, 244] and accretion flows [202, 245]. These structures, often referred to as plasmoids or magnetic vortices, resemble hydrodynamic vortices and play a crucial role in particle energization and energy dissipation [246, 247, 248, 225]. Despite extensive research, many aspects of their internal structure remain elusive due to the intricate coupling between large-scale turbulence and plasma microphysics [206, 249].

We investigate the formation of coherent structures within fully kinetic plasma turbulence through 2.5D numerical simulations (2D in spatial dimensions with 3D field components). Our results demonstrate the emergence of long-lived, magnetically dominated force-free structures that exhibit metastability. We model these structures using a self-consistent kinetic framework in cylindrical coordinates, starting from the particle velocity distribution function. This modified force-free state provides a robust description of coherent structures in astrophysical plasmas, such as plasmoids in accretion flows and flux ropes within the solar wind.

We now provide a brief summary of the previous Sections, presenting the final set of equations addressed by `Zeltron` [3]. The code solves the motion of a distribution of charged particles (i.e., the characteristic curves of the Vlasov equation) coupled to Maxwell's equations. These equations are expressed in terms of the total magnetic field $\boldsymbol{b}$, the electric field $\boldsymbol{\epsilon}$, the current density $\boldsymbol{j} = \sum_\alpha q_\alpha n_\alpha \boldsymbol{u}_\alpha$, and the charge density $\rho_c = \sum_\alpha q_\alpha n_\alpha$, where n_α denotes the number density of each species, $\boldsymbol{u}_\alpha$ represents the bulk velocity, q_α is the charge, and α is the species index, representing either protons (p) or electrons (e). `Zeltron` solves the system of equations outlined in Subsec. 3.1.1, specifically the Lorentz–Newton and Maxwell's equations, governing the evolution of particles and fields.

Throughout this analysis, we revert to the geometrized unit system, where the speed of light c, the gravitational constant G, the elementary charge q_e, the electron mass m_e, the Boltzmann constant k_B, and the reduced Planck constant $\hbar$ are normalized to unity, while the vacuum permittivity is set to $\varepsilon_0 = 1/4\pi$ and the vacuum permeability to $\mu_0 = 4\pi$. All quantities are expressed in terms of the electron skin depth, defined as $d_e = c/\omega_{pe} = c\sqrt{m_e/4\pi n_0 q_e^2} = 1$, where the equilibrium number density is $n_0 = n_e = n_p = (4\pi)^{-1}$.

The simulation setup is described as follows. We implement periodic boundary conditions with a spatial resolution such that the grid spacing is $\Delta x = \Delta y = d_e/3$, employing 10 particles per cell (PPC), namely 5 ions and 5 electrons, with the full mass ratio. The time resolution is set to $\Delta t = 0.45\,\Delta x = 0.15\,d_e$. The magnetization, which determines the available magnetic energy per particle, is defined as $\sigma = b_{0z}^2/4\pi w_0$, where the out-of-plane mean magnetic field magnitude is $b_{0z} \approx 43$, and the enthalpy density is given by $w_0 = (n_p m_p + n_e m_e)c^2 + \Gamma_e \varrho_e + \Gamma_p \varrho_p$. Here,

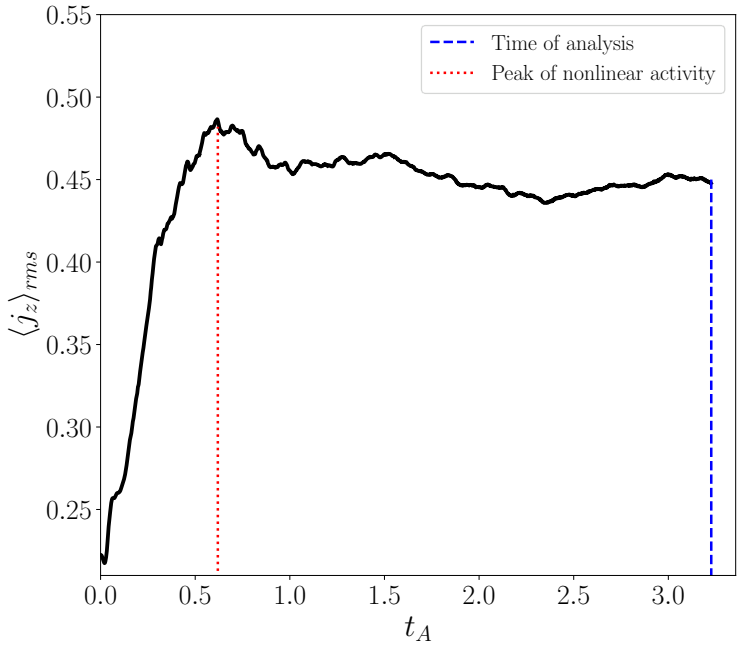

FIGURE 3.7: RMS of the vertical component of the current density (black solid line). The dotted (red) line marks the time of peak nonlinear activity, while the dashed (blue) line indicates the time of analysis.

the internal energy density is $\varrho_\alpha \approx n_\alpha k_B T_\alpha (\Gamma_\alpha - 1)^{-1}$, and the adiabatic index is $\Gamma_\alpha = 4/3$. Since we are in a weakly relativistic regime, the magnetization σ is approximately equal to $\sigma_p^{\rm cold} = b_{0z}^2/4\pi n_p m_p c^2$. The choice $\sigma \approx \sigma_p^{\rm cold} = 1$ indicates an equilibrium between magnetic and kinetic forces, a condition commonly found in astrophysical scenarios such as black hole winds near accretion disks. Additionally, the plasma beta is defined as $\beta_p = \beta_e = 8\pi n_0 k_B T_\alpha / b_{0z}^2 = 3 \times 10^{-3}$, where the temperature $T_\alpha = \theta_\alpha m_\alpha c^2/k_B$ is chosen to ensure initial thermal equilibrium between species. The selection of both σ and β is crucial in determining the plasma regime [250]. The dimensionless temperatures for each species are $\theta_p = 1.5 \times 10^{-3}$ for protons and $\theta_e \approx 2.75$ for electrons, respectively. This configuration allows us to resolve the Debye length, defined as $\lambda_D = \sqrt{(m_e\theta_e + m_p\theta_p)c^2/4\pi n_0 e^2} \approx 2.35 d_e$. As the turbulence fully develops, the electron velocity distribution becomes highly non-thermal, with their Larmor radius significantly increasing due to large accelerations, effectively enhancing our resolution. The Alfvén crossing time is defined as $t_A = L_0/v_A \approx 7748$, where the Alfvén velocity is $v_A = c\sqrt{\sigma/(1+\sigma)} \approx 0.71$.

To establish a strongly turbulent state, we initialize the simulation by imposing large-scale random conditions for the magnetic field power spectrum. This is achieved by superimposing low-wavenumber Fourier modes and setting $\delta b/b_{0z} \sim 1$, where δb denotes the RMS of the magnetic field fluctuations, and b_{0z} represents the mean magnetic field strength along the z-axis. To prevent excessive compressive activity, no initial out-of-plane magnetic field fluctuations, bulk flows, or density perturbations are introduced. The in-plane magnetic field components (b_x and b_y) are then initialized by applying a 2D Fourier spectrum of random modes to the z-component of the vector potential (whose curl generates the in-plane magnetic field),

expressed as:

$$a_z(x,y) = \sum_{k_x,k_y} \tilde{a}_z(k) e^{i(\boldsymbol{k}\cdot\boldsymbol{x}-\varphi_k)}, \qquad \tilde{a}_z(k) = \frac{1}{1+\left(\frac{k}{k_0}\right)^{15/3}}, \tag{3.19}$$

where the phases φ_k are randomly assigned. The spectrum peaks at $k_0 = 4$ and is truncated for $k > k^* = 7$, ensuring consistency with large-scale structures. The analysis focuses on a time $t \approx 3.23\, t_A$, by which the peak of nonlinear activity has subsided. As shown in Fig. 3.7, the RMS of the vertical current density component, $j_z = (\boldsymbol{\nabla} \times \boldsymbol{b}/4\pi) \cdot \hat{z}$, reaches its maximum much earlier, at $t \approx 0.62\, t_A$.

The simulation setup closely follows that described in Meringolo et al. [251], employing $N_x = N_y = 16384$ mesh points in a square domain with side length $L_0 \approx 5461\, d_e$, where d_e represents the electron skin depth. A realistic mass ratio of $m_p/m_e = 1836$ is used, with approximately 2.7×10^9 macroparticles. With a magnetization $\sigma \approx 1$, which quantifies the ratio of magnetic pressure to enthalpy density (the latter being the sum of the mass-energy density $\sum_\alpha n_\alpha m_\alpha c^2$ and the internal energy density $\sum_\alpha \varrho_\alpha \approx \sum_\alpha P_\alpha \left(\Gamma_\alpha - 1\right)^{-1}$, where Γ_α is the adiabatic index and P_α is the partial pressure of species α), and a plasma beta $\beta_p = \beta_e = 3 \times 10^{-3}$, which measures the ratio of kinetic to magnetic pressure, the resulting dynamics correspond to a weakly relativistic plasma.

The initial conditions rapidly produce a turbulent cascade, similar to fluid plasma models [192]. Our analysis focuses on the point when the peak of the averaged current density (see Fig. 3.7), which also corresponds to the time of most intense nonlinear activity [252], has long been reached. Furthermore, under these conditions, a balance between the large-scale energy flux and the collisionless energy-conversion mechanisms is established, resulting in a quasi-steady state. The power spectrum at this stage is fully developed, as shown in Fig. 3.8-(a), and is consistent with typical observations of astrophysical turbulence [253, 236, 254]. As the broadband turbulence evolves, coherent structures emerge and propagate through the turbulent background, as inferred from the out-of-plane component of the magnetic potential a_z in Fig. 3.8-(b). Similar to MHD [255, 256], kinetic turbulence tends to form localized correlations, where the current $\boldsymbol{j}$ exhibits a significant tendency to align with the total magnetic field $\boldsymbol{b}$. We estimate the strength of this alignment by computing $\cos(\boldsymbol{j},\boldsymbol{b}) = \boldsymbol{j}\cdot\boldsymbol{b}/|\boldsymbol{j}||\boldsymbol{b}|$, and, as displayed in Fig. 3.8-(b), dominant structures are evident, with morphologies reminiscent of hydrodynamic swirls and cyclones. These structures possess a distinct “eye," where the alignment is strongest, and an outer region with advecting arms, where the cosine regularly changes sign while maintaining overall circular symmetry. The characteristic size of these structures is approximately $140\, d_e (3\, d_p)$ for the eye and approximately $515\, d_e (12\, d_p)$ for the spiral arms, which are typical of inertial-range turbulence, as seen in Fig. 3.8-(a). Notably, the largest vortices (eye and arms) are on the order of a few d_p, corresponding to the correlation length, λ_C, set by the initial conditions of homogeneous turbulence. For the analyzed configuration, $\lambda_C \approx 440\, d_e \approx 10\, d_p$.

To gain further insight into the properties of these long-lived features, we focus on regions where the magnitude of the magnetic potential a_z at the center of the structure significantly exceeds its own RMS value [192]. After the time of maximum turbulence, we select four principal vortices, which are indicated by (white) circumferences in Fig. 3.8-(b). For each of these vortices, we adopt a local cylindrical coordinate system centered at the O-point of the vector potential and use it to derive locally azimuthally averaged quantities. More specifically, for any generic field h,

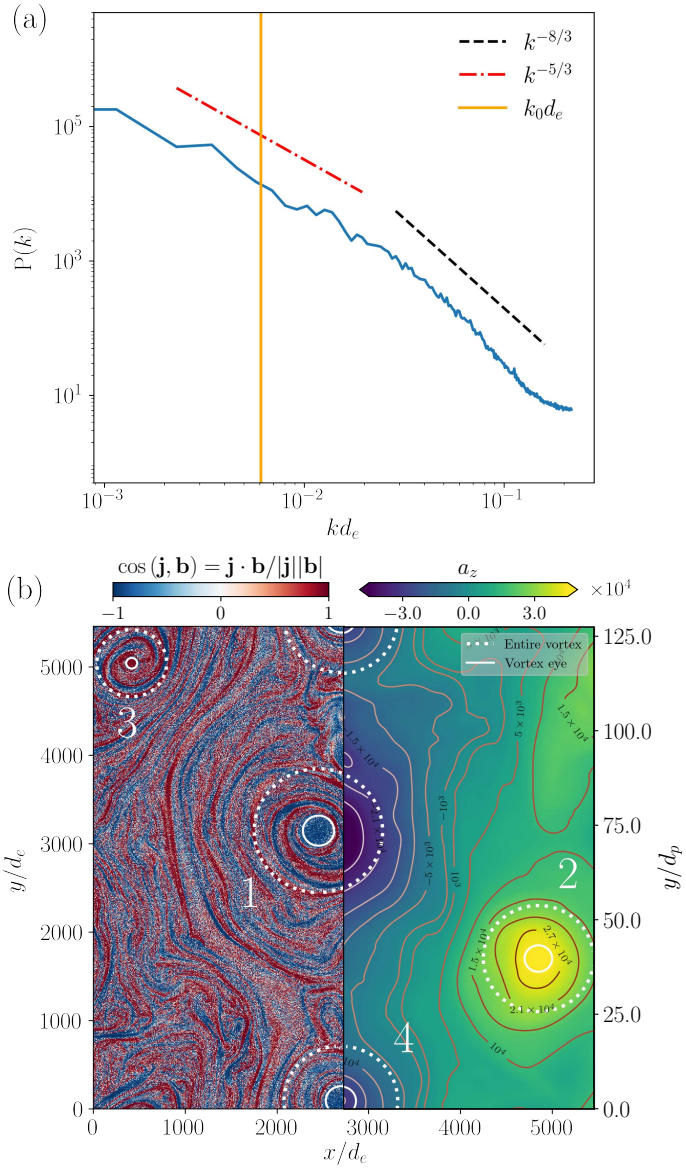

FIGURE 3.8: (a) Magnetic power spectrum at a time beyond the peak of nonlinear activity as a function of kd_e. The vertical (orange) line marks the wavenumber $k_0 d_e$, which corresponds to the typical scale of the persistent vortices. (b) 2D contour plot of the magnetic vector potential component a_z (right panel) and the cosine of the angle between the current density and the total magnetic field (left panel). The y-axis is normalized to both the electron skin depth d_e (left axis) and the proton skin depth d_p (right axis).

we first transform it into the cylindrical coordinate frame, i.e., $h(x,y) \rightarrow h(r,\phi)$, and then compute the corresponding average as

$$H(r) = \frac{1}{2\pi}\int_0^{2\pi} h(r,\phi')\, d\phi'.$$

From this point forward, capital letters are used to denote azimuthally averaged quantities.

The components of the field h at any given point on the new 2D cylindrical grid are computed through bilinear interpolation. First, we identify the corresponding

cell in the Cartesian grid that contains the point. Then, for each direction (x and y), we determine the points immediately preceding and following the interpolation point within the Cartesian grid. Subsequently, the area of each of the four subregions, into which the cylindrical grid point divides the Cartesian cell along its diagonally opposite vertices, is computed. Using the known values of the field at each vertex, we then calculate a weighted sum to interpolate the value of h at the cylindrical grid point. Hence, the interpolated field at the cylindrical grid point is expressed as:

$$h(\boldsymbol{x}_c) = \frac{1}{\Delta x \Delta y} \sum_{i=1}^{4} \Xi_i \, h(\boldsymbol{x}_i), \tag{3.20}$$

where Ξ_i denotes the areas of the subregions, which act as the weights in the summation. Next, a coordinate transformation is applied to convert the field components from the Cartesian to the cylindrical system. This is accomplished using the coordinate transformation operator Λ, allowing the transformation of both tensors and vectors. For a tensor field h_{ij} and a vector field h_i, the transformed components in cylindrical coordinates are given by:

$$\hat{h}_{\alpha\beta} = \Lambda^{iT}_{\alpha} h_{ij} \Lambda^{j}_{\beta}, \qquad \hat{h}_{\alpha} = \Lambda^{iT}_{\alpha} h_i, \tag{3.21}$$

where the superscript T indicates the transpose of the matrix, and the hat denotes the components of the field in the new coordinate system.

In Fig. 3.9-(a), we present the angle between the azimuthally averaged current density $\boldsymbol{J}$ and the magnetic field $\boldsymbol{B}$, defined as $\Theta = \cos^{-1}(\boldsymbol{J} \cdot \boldsymbol{B}/|\boldsymbol{J}||\boldsymbol{B}|)$, evaluated within the structures. The alignment is notably strong, with all vortices—varying in size and intensity—exhibiting the same behavior: they form highly aligned cores (eyes) and wall boundaries, followed by spiraling arms [257, 258, 259, 260, 261]. These spirals display alternating $\boldsymbol{J} - \boldsymbol{B}$ alignment, indicative of a characteristic radial mode. We denote r_0 as the radius of the vortex eye, defined as the distance from the center to the first spiraling arm where the scalar product $\boldsymbol{J} \cdot \boldsymbol{B}$ changes sign (see Fig. 3.9). The alignment progressively weakens, and the plasmoid eventually merges with the surrounding background on scales of approximately $\mathcal{O}(4r_0)$, which qualitatively correspond to the last closed magnetic surfaces (dotted lines in Fig. 3.8-(b)). The observed alignment suggests a tendency of the system to approach force-free states, where $\boldsymbol{J} = (4\pi)^{-1} \boldsymbol{\nabla} \times \boldsymbol{B} = \lambda \boldsymbol{B}$, similar to large-scale fluid models [262]. In this context, we present the force-free parameter $\lambda(r) = \boldsymbol{J} \cdot \boldsymbol{B}/B^2$ in Fig. 3.9-(b). Unlike classical, global (constant-λ) force-free states, our local minimization process for each vortex reveals a strong radial dependence of λ, approaching zero at the vortex boundaries. This behavior is indicative of a nonlinear force-free state with uniform twist per unit length. The radial variation of λ suggests a more complex and nuanced relaxation process.

In what follows, we discuss the interpretation of long-lived structures within the framework of kinetic plasma theory. We begin by recalling that the Vlasov equation for the distribution function of the α-th species, denoted as $f_\alpha(\boldsymbol{x}, \boldsymbol{v}, t)$, can be expressed as $\partial f_\alpha / \partial t = \{H, f_\alpha\}$, where H is the particle Hamiltonian and $\{\cdot, \cdot\}$ represents the standard Poisson bracket. A stationary equilibrium is thus characterized by $\{H, f_\alpha\} = 0$, which implies that f_α must depend on the integrals of motion. Following the approach of Harris [263], we assume an exponential dependence on the invariants (energy and momenta), neglecting relativistic corrections (as the bulk flows are nonrelativistic), and adopt a simple drifting-Maxwellian distribution in a

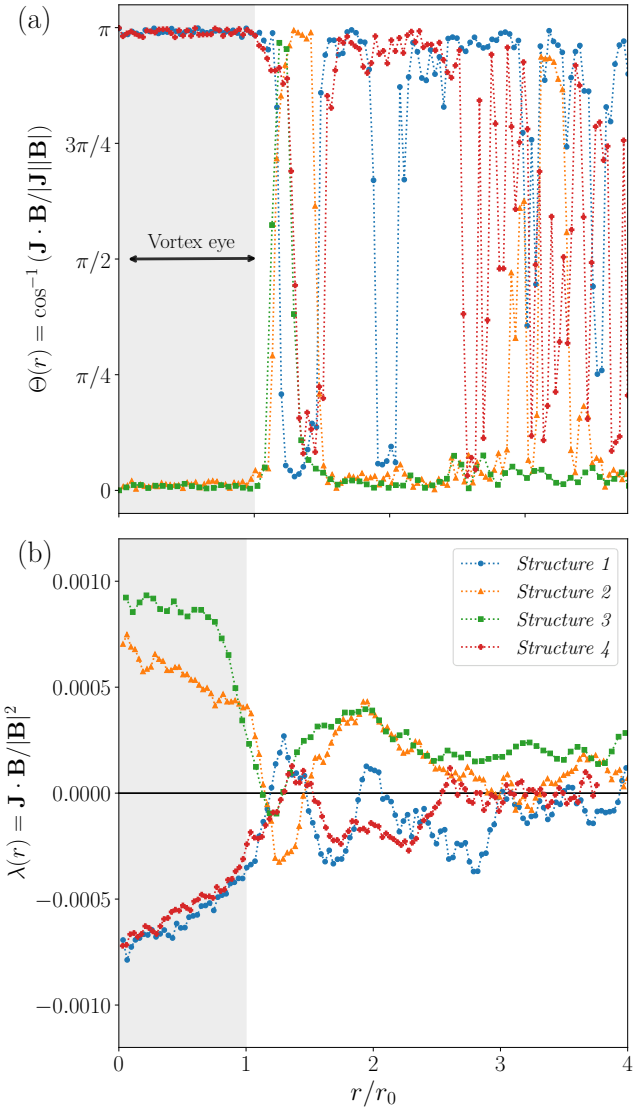

FIGURE 3.9: (a) Radial variation of the angle between the current density and the total magnetic field, shown as azimuthal averages, for each structure illustrated in Fig. 3.8-(b). (b) Force-free parameter $\lambda(r)$. The vortex eye radius, r_0, is defined as the location of the first spiraling arm.

cylindrical coordinate system:

$$f_\alpha(\boldsymbol{x}, \boldsymbol{v}) = f_{\alpha 0} \exp\left[-\frac{\mathcal{E}_\alpha - v_\alpha^* P_{z\alpha} - \Omega_\alpha^* P_{\phi\alpha}}{k_B T_\alpha}\right], \tag{3.22}$$

where $f_{\alpha 0} = N_{\alpha 0}\left(m_\alpha/2\pi k_B T_\alpha\right)^{3/2}$ is a normalization constant, with $N_{\alpha 0}$ representing the particle density at the center of the vortex, and T_α is the temperature. The particle

energy $\mathcal{E}_\alpha$ and the canonical momenta $P_{i\alpha}$ are defined as follows:

$$\mathcal{E}_\alpha = \frac{m_\alpha(v_r^2+v_\phi^2+v_z^2)}{2} + q_\alpha\psi(r), \tag{3.23}$$

$$P_{\phi\alpha} = r\left(m_\alpha v_\phi + \frac{q_\alpha A_\phi(r)}{c}\right), \tag{3.24}$$

$$P_{z\alpha} = m_\alpha v_z + \frac{q_\alpha A_z(r)}{c}, \tag{3.25}$$

where A_i are the components of the averaged vector potential in the Lorenz gauge, ψ is the electrostatic potential, and v_i denotes the components of the particle velocities. The undetermined (free) parameters in Eq. (3.22), v_α^* and Ω_α^*, correspond to the characteristic out-of-plane linear velocity and azimuthal velocity, respectively. Once these parameters are specified, an exact kinetic equilibrium can be constructed.

Considering a particle distribution function with an exponential dependence on the three invariants defined in Eqs. (3.23)–(3.25), the probability density of locating a particle at a specific point in phase space $\mathbf{\Omega}_v$ can be explicitly expressed as

$$\begin{aligned} f_\alpha\left(r,v_r,v_\phi,v_z\right) = N_{0\alpha}&\left(\frac{m_\alpha}{2\pi k_B T_\alpha}\right)^{3/2} \\ &\times\exp\left[-\frac{m_\alpha}{2k_BT_\alpha}(v_r^2+v_\phi^2+v_z^2)+\frac{m_\alpha v_\alpha^*}{k_BT_\alpha}v_z+\frac{m_\alpha\Omega_\alpha^*}{k_BT_\alpha}rv_\phi\right. \\ &\left.+\frac{q_\alpha v_\alpha^*}{c\,k_BT_\alpha}A_z(r)+\frac{q_\alpha\Omega_\alpha^*}{c\,k_BT_\alpha}rA_\phi(r)-\frac{q_\alpha}{k_BT_\alpha}\psi(r)\right], \end{aligned} \tag{3.26}$$

which must satisfy Maxwell's equations:

$$\begin{aligned} &\boldsymbol{\nabla}\cdot\boldsymbol{E} = 4\pi e\left(\int_{\mathbf{\Omega}_v} f_p(r,\boldsymbol{v})\,d^3\boldsymbol{v} - \int_{\mathbf{\Omega}_v} f_e(r,\boldsymbol{v})\,d^3\boldsymbol{v}\right), \\ &\boldsymbol{\nabla}\cdot\boldsymbol{B} = 0, \\ &\boldsymbol{\nabla}\times\boldsymbol{E} = -\frac{1}{c}\frac{\partial\boldsymbol{B}}{\partial t} = \boldsymbol{0}, \\ &\boldsymbol{\nabla}\times\boldsymbol{B} = \frac{4\pi e}{c}\left(\int_{\mathbf{\Omega}_v}\boldsymbol{v}f_p(r,\boldsymbol{v})\,d^3\boldsymbol{v} - \int_{\mathbf{\Omega}_v}\boldsymbol{v}f_e(r,\boldsymbol{v})\,d^3\boldsymbol{v}\right). \end{aligned} \tag{3.27}$$

We assume stationarity, i.e., $\partial/\partial t = 0$. Given that the fields depend only on the radial coordinate, we have $\partial/\partial\phi = \partial/\partial z = 0$. Consequently, Eqs. (3.27) reduce to three ODEs for the potentials (one for the electric potential and two for the azimuthal and vertical components of the vector potential):

$$\begin{aligned} &\frac{1}{r}\frac{d}{dr}\left(r\frac{d\psi}{dr}\right) = -4\pi e\left(\int_{\mathbf{\Omega}_v} f_p\,d^3\boldsymbol{v} - \int_{\mathbf{\Omega}_v} f_e\,d^3\boldsymbol{v}\right), \\ &\frac{d}{dr}\left(\frac{1}{r}\frac{d(rA_\phi)}{dr}\right) = -\frac{4\pi e}{c}\left(\int_{\mathbf{\Omega}_v} v_\phi f_p\,d^3\boldsymbol{v} - \int_{\mathbf{\Omega}_v} v_\phi f_e\,d^3\boldsymbol{v}\right), \\ &\frac{1}{r}\frac{d}{dr}\left(r\frac{dA_z}{dr}\right) = -\frac{4\pi e}{c}\left(\int_{\mathbf{\Omega}_v} v_z f_p\,d^3\boldsymbol{v} - \int_{\mathbf{\Omega}_v} v_z f_e\,d^3\boldsymbol{v}\right). \end{aligned} \tag{3.28}$$

By taking the moments of Eq. (3.22), after some algebra, we can compute the particle number densities as follows:

$$N_\alpha(r) = \int_{\mathbf{\Omega}_v} f_\alpha \, d^3\boldsymbol{v} = \exp\left[\gamma_\alpha(r)\right], \tag{3.29}$$

where

$$\begin{aligned}\gamma_\alpha(r) = \ln\left(N_{0\alpha}\right) + \frac{q_\alpha}{c k_B T_\alpha}\Big[v_\alpha^* A_z(r) + r\Omega_\alpha^* A_\phi(r) \\ - c\psi(r)\Big] + \frac{m_\alpha}{2k_B T_\alpha}\left(r^2\Omega_\alpha^{*^2} + v_\alpha^{*^2}\right).\end{aligned} \tag{3.30}$$

Similarly, by computing the azimuthally averaged bulk velocity, defined as $\boldsymbol{U}_\alpha(r) = N_\alpha^{-1}(r)\int_{\mathbf{\Omega}_v} \boldsymbol{v} f_\alpha \, d^3v$, we can establish its relationship with the free parameters:

$$U_{\alpha z}(r) = v_{\alpha z}^*, \quad U_{\alpha\phi}(r) = \Omega_\alpha^* r. \tag{3.31}$$

With these quantities defined, the current densities can subsequently be expressed as $J_{\phi\alpha}(r) = q_\alpha \, N_\alpha(r) \, U_{\phi\alpha}(r)$ and $J_{z\alpha}(r) = q_\alpha \, N_\alpha(r) \, U_{z\alpha}(r)$. The problem can be further simplified by assuming a negligible net constant charge separation, defined as:

$$\kappa = N_e(r) - N_i(r) = \exp\left[\gamma_e(r)\right] - \exp\left[\gamma_p(r)\right], \tag{3.32}$$

where κ is a constant. It is important to emphasize that this charge separation, although small (less than 10%), is nonetheless present, particularly in the vortex eye. Consequently, the calculation can be simplified by assuming $\boldsymbol{\nabla}\cdot\boldsymbol{E} = -\nabla^2\psi = -4\pi e\kappa$. This assumption leads directly to a straightforward expression for the electric potential of the form $\psi(r) = \psi(0) + (\pi e\kappa)\, r^2$. Due to gauge invariance, we set all potentials to zero at the vortex axis, i.e., $\psi(0) = 0$, $A_z(0) = 0$, and $A_\phi(0) = 0$. Introducing the quantity $\eta(r) = \gamma_e(r) - \gamma_p(r)$, Eq. (3.32) can be reformulated as

$$\kappa = \exp\left[\gamma_e(r)\right] - \exp\left[\gamma_e(r) - \eta(r)\right], \tag{3.33}$$

which yields $\eta(r) = -\ln\left\{1 - \kappa\exp\left[-\gamma_e(r)\right]\right\}$. The relationship between the exponents $\gamma_e(r)$ and $\gamma_p(r)$ leads to the following expression:

$$\begin{aligned}C_p + \frac{q_p\, v_p^*}{c\, k_B T_p} A_z(r) + \frac{q_p\, \Omega_p^*}{c\, k_B T_p} r A_\phi(r) - \frac{q_p}{k_B T_p}\psi(r) \\ + \frac{m_p}{2\, k_B T_p}\Omega_p^{*^2} r^2 + \frac{m_p}{2k_B T_p} v_p^{*^2} = C_e + \frac{q_e\, v_e^*}{c\, k_B T_e} A_z(r) \\ + \frac{q_e\, \Omega_e^*}{c\, k_B T_e} r A_\phi(r) - \frac{q_e}{k_B T_e}\psi(r) + \frac{m_e}{2\, k_B T_e}\Omega_e^{*^2} r^2 \\ + \frac{m_e}{2\, k_B T_e} v_e^{*^2} - \eta(r),\end{aligned} \tag{3.34}$$

where $\eta(r)$ is a small function associated with minimal net charge separation (consistent with quasi-neutrality), and $C_\alpha = \ln\left(N_{0\alpha}\right)$. By employing the correspondence between the exponents at the vortex center, where $\gamma_p(0) = \gamma_e(0) - \eta(0)$, we derive explicit expressions for C_p and C_e, which are then substituted into Eq. (3.34). Noting that $\eta(r) - \eta(0)$ is negligible, we perform algebraic manipulation to obtain the following polynomial relation:

$$\zeta_0\psi(r) + \zeta_1 A_z(r) + \zeta_2 A_\phi(r)\, r + \zeta_3 r^2 = 0. \tag{3.35}$$

A potential solution emerges by setting $\zeta_1 = 0$ and $\zeta_2 = 0$. These conditions correspond to the Harris equilibrium in the sheet pinch configuration for a non-homogeneous magnetic field in cylindrical geometry, along with an additional condition for the in-plane azimuthal flow that is not included in the Harris formulation. Under this assumption, a straightforward relation for the electric potential can be expressed as:

$$\psi(r) = -\frac{\zeta_3}{\zeta_0} r^2 = (\pi e \kappa)\, r^2 = \frac{m_p \Omega_p^{*2} T_e - m_e \Omega_e^{*2} T_p}{2e(T_p + T_e)} r^2. \tag{3.36}$$

Ultimately, the conditions for the free parameters and charge separation, derived from Eq. (3.35), are expressed as follows:

$$\begin{aligned} v_p^* &= -\frac{T_p}{T_e} v_e^*, \Omega_p^* = -\frac{T_p}{T_e} \Omega_e^*, \\ \kappa &= \frac{m_p \Omega_p^{*2} T_e - m_e \Omega_e^{*2} T_p}{2\pi e^2 (T_p + T_e)}. \end{aligned} \tag{3.37}$$

By substituting Eq. (3.26) into Maxwell's equations using the expressions for densities and currents, and assuming stationarity ($\partial/\partial t = 0$), along with the simplifications outlined in Eq. (3.37), we derive a set of ODEs that constitute our Kinetic Vortex Reconstruction (KVR) model:

$$\frac{dA_z}{dr} = -B_\phi(r)\,, \tag{3.38}$$

$$\frac{dA_\phi}{dr} = -\frac{A_\phi(r)}{r} + B_z'(r)\,, \tag{3.39}$$

$$\frac{dB_z'}{dr} = \frac{4\pi e}{c}\left(\Omega_e^* - \Omega_p^*\right) r\, e^{\gamma_e(r)} + \Omega_p^* \kappa r\,, \tag{3.40}$$

$$\frac{dB_\phi}{dr} = -\frac{B_\phi(r)}{r} + \frac{4\pi e}{c}\left(v_p^* - v_e^*\right) e^{\gamma_e(r)} - v_p^* \kappa\,. \tag{3.41}$$

Here, B_z' denotes the fluctuations in the out-of-plane magnetic field, such that $B_z = B_z' + b_{0z}$. Equations (3.38)–(3.41) can be integrated numerically after specifying the internal temperatures of the vortex eye T_α for each vortex, along with the free parameters (v_e^*, Ω_e^*).

The KVR system of equations can be solved through direct numerical integration using a second-order Runge-Kutta scheme once the typical bulk electron velocity v_e^* and angular velocity Ω_e^* are provided, along with boundary conditions applied at each vortex center. For each coherent structure, we search for this pair of free parameters by implementing a data-driven Monte Carlo numerical technique capable of selecting the optimal fit for each vortex, starting from the results of the integration over a parameter space $\boldsymbol{\mathcal{S}}$ defined by $\{v_e^*,\ \Omega_e^*\}$.

By examining the most representative vortex depicted in Fig. 3.8-(b) at a time beyond the peak of nonlinear activity ($t \approx 3.23\, t_A$), we impose the boundary conditions $B_z'(0) \approx 40.5$, $B_\phi(r)/r|_{r=0} = 0$, and $A_\phi(r)/r|_{r=0} = 0$. For the species temperatures $(T_e,\ T_p)$, we select the averaged parallel temperature profiles within the vortex eye, specifically $T_\alpha = T_{\|\alpha}$, with $T_{\|e} = 51.8$ and $T_{\|p} = 51.7$. Each long-lived structure is uniquely characterized by the selection of the star parameters v_e^* and Ω_e^*. This selection must ensure that the distribution function, when integrated over the phase space $\boldsymbol{\Omega}$, yields the various fields and momenta in optimal agreement with the data.

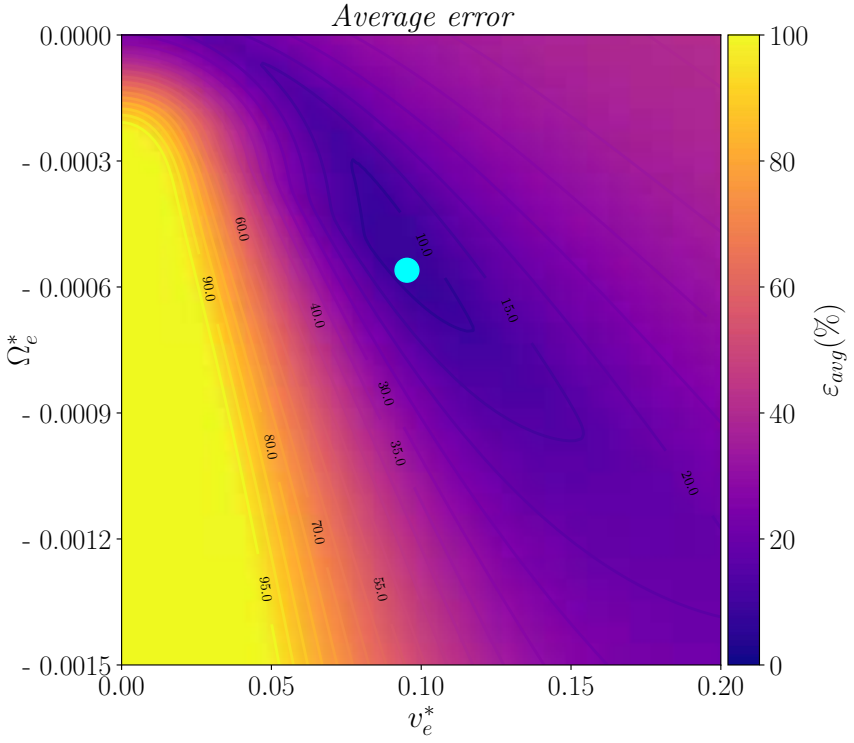

FIGURE 3.10: Average error estimated by considering all vortex profiles. The optimal selection for the free parameters is highlighted by a cyan circle. This figure illustrates the optimization process employed to identify the best fit for the free parameters v_e^* and Ω_e^*, ensuring that the KVR model closely aligns with the observed vortex profiles.

Consequently, a Monte Carlo method is employed over the parameter space $\boldsymbol{\mathcal{S}}$ to calculate the discrepancies between the KVR outputs and the observed profiles as described below.

We span the parameter space by discretizing the domain

$$\{v_e^*,\ \Omega_e^*\} \in \{[-0.2, 0.2],\ [-0.0015, 0.0015]\}, \tag{3.42}$$

performing a series of reconstructions to minimize the error defined as

$$\varepsilon_g(v_e^*,\ \Omega_e^*) = \frac{\int_0^{r_0} \left[g_{\mathrm{KVR}}(r) - g_{\mathrm{sim}}(r)\right]^2 dr}{\int_0^{r_0} g_{\mathrm{sim}}(r)^2 dr}, \tag{3.43}$$

where g_{sim} represents a generic field from the simulation, while g_{KVR} denotes the reconstructed field derived from Eqs. (3.38)–(3.41).

We minimize for $g = [A_\phi,\ A_z,\ B_\phi,\ B_z',\ J_\phi,\ J_z,\ N_e,\ N_p]$, obtaining the associated error ε_g for each field. To achieve the best possible profiles, we compute a single average over all fields, expressed as $\varepsilon_{avg}(v_e^*,\ \Omega_e^*) = \bar{\varepsilon}_g(v_e^*,\ \Omega_e^*)$. In Fig. 3.10, we present a zoomed-in view of the average error ε_{avg}, with its minimum located in the fourth quadrant of the parameter space (positive v_e^* and negative Ω_e^*). The minimum is found at $v_e^* = 0.09$ and $\Omega_e^* = -5.30 \times 10^{-4}$, as indicated by a cyan circle. The resulting parameters are closely related to the flux tube current density. For the KVR

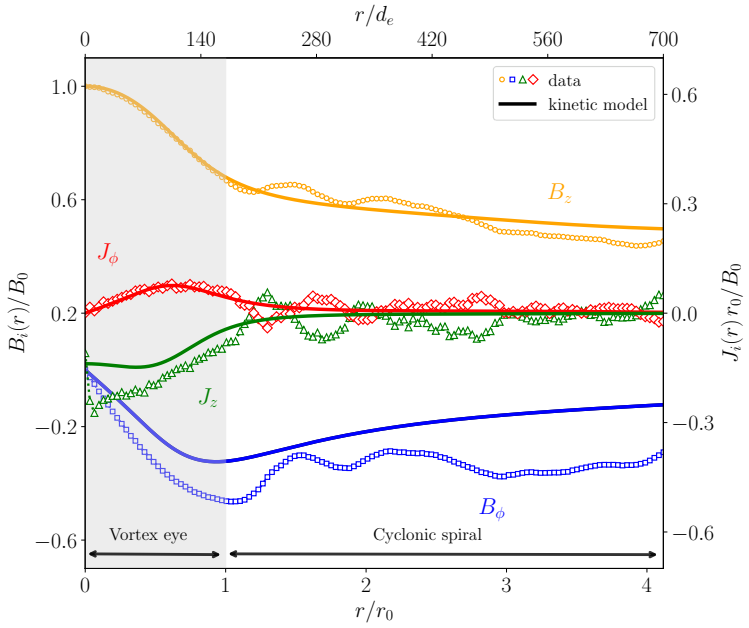

FIGURE 3.11: (a) Total magnetic field and current density components for the central vortex shown in Fig. 3.8 (open symbols) compared to the KVR model (solid lines). The data have been time-averaged in the reference frame of the vortex.

model, we obtain

$$\boldsymbol{J}^*(r) = q_e \left[0,\ \left(N_p(r)\,\Omega_p^* - N_e(r)\,\Omega_e^*\right) r,\ \left(N_p(r)\,v_p^* - N_e(r)\,v_e^*\right)\right], \tag{3.44}$$

from which we derive $\langle J_\phi^* \rangle_r \approx 1.17 \times 10^{-2}$ and $\langle J_z^* \rangle_r \approx -2.73 \times 10^{-2}$. For the observed structures in Fig. 3.8-(b), we measure $\langle J_\phi \rangle_r \approx 1.27 \times 10^{-2}$ and $\langle J_z \rangle_r \approx -4.69 \times 10^{-2}$. This estimate indicates a strong agreement between the model and the observed data.

Fig. 3.11 presents a direct comparison between the KVR model (lines) and the actual numerical data (symbols). The model effectively captures the behavior of all fields, particularly in the inner regions of the vortex ($r \lesssim r_0$) and in terms of the dependence of the magnetic field. Notably, an azimuthal current J_ϕ vanishes at both the center and asymptotically, while a non-zero vertical current J_z is present along the axis. Even outside the eye, the magnetic field components exhibit qualitative consistency with the model, despite the influence of the cyclonic arms observed in Fig.s 3.8–3.9. Similar behaviors are also exhibited by the other vortices tracked during the evolution: B_z demonstrates a peak in the eye and diminishes at larger r, whereas B_ϕ reaches its maximum at the vortex wall.

To understand the merging dynamics of existing vortices, we analyze the simulation at various time intervals, identifying and monitoring the most stable and long-lasting structures. In particular, we present in Fig. 3.13 the *"merging history"* of two individual, isolated vortices (or magnetic islands) that traverse the background until they ultimately merge with a companion. The figure illustrates, as a function of time (from top to bottom), the plasma number density, the cosine angle, and the magnetic helicity density (see later). When both structures possess high energy, their encounter can be quite explosive, resulting in a net current layer between them,

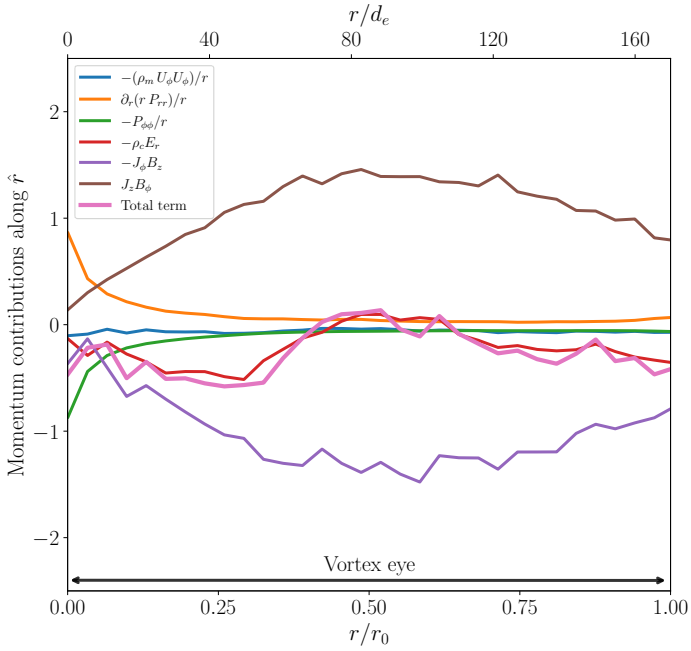

FIGURE 3.12: Components of the momentum equation for the fluid approximation within the vortex eye.

where magnetic reconnection occurs [264, 192] and non-thermal particles are generated [221]. The cosine of the angle between the current density and the magnetic field, $\cos(\boldsymbol{j},\ \boldsymbol{b})$, is notably strong within the structures and changes sign between them. The example depicted in Fig. 3.13 further illustrates that the spiral arms mentioned previously are indeed the remnants of merger events. This process is associated with the conservation of magnetic helicity, akin to the framework proposed by Alexakis, Mininni, and Pouquet [265], where the inverse cascade of magnetic helicity can occur across all scales. In our case, this results in meta-stable vortices that range from large injection scales (a few d_p) to electron scales, falling within the sub-inertial range.

We now reconcile the KVR model presented in Fig. 3.11 with the fluid-like states depicted in Fig. 3.9. By taking the moments of the Vlasov equation, a hierarchy of contributions that influence the equilibrium within the islands can be defined, leading to the conclusion that magnetic forces dominate the dynamics of long-lived equilibria. Specifically, upon computing the moments of the Vlasov-Maxwell system, one derives the momentum equation, which, in a stationary case, is expressed as

$$\boldsymbol{\nabla}\cdot(\rho_m \boldsymbol{U}\otimes\boldsymbol{U}) + \boldsymbol{\nabla}\cdot\boldsymbol{P}_{tot} - \rho_c\boldsymbol{E} - \boldsymbol{J}\times\boldsymbol{B} = \boldsymbol{0}, \tag{3.45}$$

where ρ_m denotes the total mass density, ρ_c represents the total charge density, and $\boldsymbol{P}_{tot}$ signifies the total pressure tensor. Employing the continuity equation in the expression above, while recalling the divergence of a symmetric tensor of rank two in cylindrical coordinates, and imposing the conditions $U_r = 0$, $\partial/\partial\phi = \partial/\partial z = 0$,

one can decompose Eq. (3.45) along the three cylindrical axes:

$$\hat{r}: -\frac{\rho_m U_\phi^2}{r} + \left(\frac{1}{r}\partial_r(r\,P_{rr}) - \frac{P_{\phi\phi}}{r}\right) - \rho_c E_r - \left(J_\phi B_z - J_z B_\phi\right) = 0; \tag{3.46}$$

$$\hat{\phi}: \left(\partial_r P_{r\phi} + \frac{2P_{r\phi}}{r}\right) - \rho_c E_\phi - \left(J_z B_r - J_r B_z\right) = 0; \tag{3.47}$$

$$\hat{z}: \frac{1}{r}\partial_r(r\,P_{rz}) - \rho_c E_z - \left(J_r B_\phi - J_\phi B_r\right) = 0. \tag{3.48}$$

Given that the radial components of the currents and magnetic field are negligible, the out-of-diagonal terms of the pressure can be disregarded, and the dominant electric field is radial. It is important to note that the only nontrivial equation is the radial one. Establishing a hierarchical order for all the terms appearing in the radial momentum equation is instrumental in identifying the critical constituents of these metastable states. We compute all relevant quantities from Eq. (3.46) and present a comparison in Fig. 3.12. By calculating radial averages for each of these quantities, it becomes evident that magnetic forces dominate the dynamics. In fact, a clear ordering can be inferred:

$$|J_i B_j|_{i,j\neq r} > |\rho_c E_r| \gg |\,(\boldsymbol{\nabla}\cdot\boldsymbol{P}_{\rm tot})\cdot\hat{\boldsymbol{r}}| > |\,[\boldsymbol{\nabla}\cdot(\rho_m\,\boldsymbol{U}\otimes\boldsymbol{U})]\cdot\hat{\boldsymbol{r}}|. \tag{3.49}$$

As a result, neglecting secondary effects such as charge separation, one can combine Eqs. (3.40)–(3.41) to yield

$$\boldsymbol{\nabla}\times\boldsymbol{B} = \frac{4\pi}{c}\boldsymbol{J}_0^* e^{\gamma_e(r)}, \tag{3.50}$$

where $\boldsymbol{J}_0^* = q_e\left[0,\ \left(\Omega_p^* - \Omega_e^*\right)r,\ \left(v_p^* - v_e^*\right)\right]$ represents the current density normalized to the number density, and $\gamma_e(r)$ is defined in Eq. (3.30). As $r\to 0$, all functions, including $\gamma_e(r)$ and $\psi(r)$, remain regular, smooth, and continuous. Furthermore, for all vortices, we observe that B_z peaks near the origin at a non-zero value, while the azimuthal component behaves as $B_\phi \sim \alpha r$, where α is a constant. Phenomenologically, to suppress the Lorentz force term in the momentum equation, the magnetic field $\boldsymbol{B}$ tends to align with $\boldsymbol{J} \simeq \boldsymbol{J}_0^* e^{\gamma_e(r)}$. Thus, Eq. (3.50) can be approximated as

$$\boldsymbol{\nabla}\times\boldsymbol{B} = f(r)\boldsymbol{J}_0^* \sim \lambda(r)\boldsymbol{B}(r), \tag{3.51}$$

where all rescaling constraints are incorporated in $\lambda(r)$.

A very robust solution to Eq. (3.51) is known as the Gold-Hoyle (GH) vortex [205], which describes a flux tube featuring a force-free, twisted magnetic field. This equilibrium was initially discovered for force-free coronal structures and has potential applications in astrophysical contexts [266]. The GH vortex is expressed as [206]

$$\boldsymbol{A}(\tilde{r}) = \frac{B_0}{2\xi}\left(0, \frac{1}{\tilde{r}}\ln(1+\tilde{r}^2), \mp\ln(1+\tilde{r}^2)\right), \tag{3.52}$$

$$\boldsymbol{B}(\tilde{r}) = B_0\left(0, \pm\frac{\tilde{r}}{1+\tilde{r}^2}, \frac{1}{1+\tilde{r}^2}\right), \tag{3.53}$$

$$\boldsymbol{J}(\tilde{r}) = 2\frac{\xi B_0}{\mu_0}\left(0, \frac{\tilde{r}}{(1+\tilde{r}^2)^2}, \pm\frac{1}{(1+\tilde{r}^2)^2}\right), \tag{3.54}$$

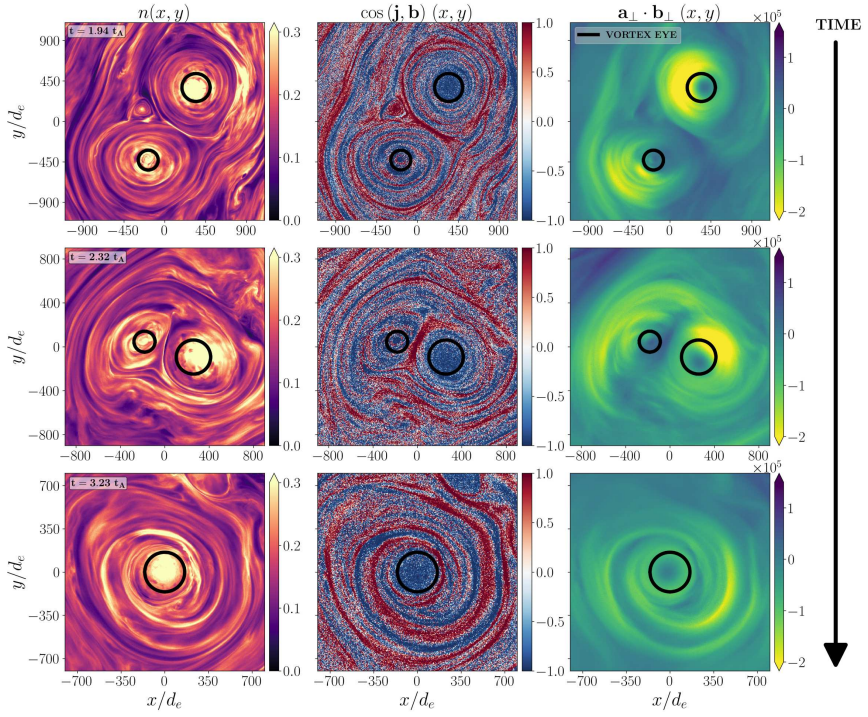

FIGURE 3.13: *Merging history* of two long-lived structures as a function of Alfvénic crossing time (from top to bottom). The plot displays the plasma density (left column), the cosine of the angle representing the force-free condition (middle column), and the magnetic helicity density (right column). The black circumferences represent the eye of each vortex.

where B_0 represents a typical magnetic field strength, $\tilde{r} = \xi r$ is a dimensionless radial coordinate, and ξ is a characteristic gradient. The solution is valid for "strong" vortices (where fluctuations are of the order of the mean field) and can be generalized for clockwise (upper sign) or counterclockwise (lower sign) rotation.

To determine whether the above model is a universal property of the turbulent cascade, we detect and analyze all ten long-lived structures appearing during the simulation, as collected in Fig. 3.14. Here, the field components are normalized to B_0 and rescaled via ξ, which is determined through a simple fitting procedure. Also reported are the corresponding GH magnetic components from Eq. (3.53) (to avoid overcrowding, we represent $-|B_\phi|$). The GH solution provides a qualitatively accurate description, suggesting that the KVR model (and its GH approximation) may characterize energetic structures in plasma turbulence. This type of solution is achieved through a local relaxation process where the magnetic helicity is finite and plays a crucial role [267, 262, 268, 265]. Such an MHD invariant measures the twisting of the field lines and, in 2.5D, is defined as the volume average $H_m = \mathcal{V}^{-1} \int_{\mathcal{V}} h_m \, d^3x$, where $h_m = \boldsymbol{a}_\perp \cdot \boldsymbol{b}_\perp$, with $\boldsymbol{a}_\perp = (a_x, a_y)$ and $\boldsymbol{b}_\perp = (b_x, b_y)$ representing the in-plane components. Contrary to the classical Bessel solutions of the linear force-free state, the numerical results are more consistent with a constant twist per unit length along the vortex axis. As shown in Fig. 3.13, the structures retain a finite amount of magnetic helicity before and after the merging. From Eqs. (3.52)–(3.53), performing a volume average over the flux tube yields:

$$|H_m| = \frac{B_0^2}{2\xi} \int_0^1 \frac{\ln(1+\tilde{r}^2)}{1+\tilde{r}^2} d\tilde{r} = \frac{B_0^2}{2\xi} \left(\frac{\pi}{2} \ln 2 - \mathcal{C} \right) \sim 10^{-1} B_0^2 \, r_0, \tag{3.55}$$

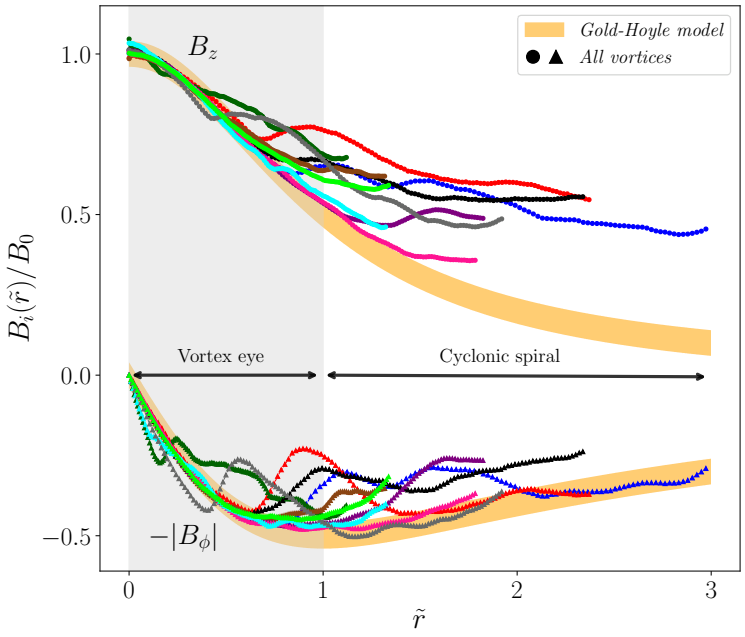

FIGURE 3.14: Radial behavior of the magnetic field components for all long-lived vortices observed during the simulation (points). The components have been rescaled to the field at the center, B_0, and normalized using their typical gradient, ξ. The GH solution (shaded) qualitatively describes the profiles near the eye.

where $\mathcal{C} \approx 0.916$ is Catalan's constant, $B_0 \approx 43$, and $r_0 \approx 170\, d_e$ for Vortex 1 in Fig. 3.8-(b). This is in accordance with the observed values in Fig. 3.13 ($H_m \sim 3 \times 10^4$). It is particularly noteworthy that all the structures described in the context of kinetic theory closely resemble those observed in the magnetosheath [269] and in the solar wind, with sizes spanning from MHD to sub-ion scales [270].

Exploiting the results of direct numerical PIC simulations, we propose a description of plasma turbulence envisioned as a mosaic of equilibrium-like patterns. In this scenario, coherent structures emerge from the turbulent background and occasionally encounter and merge with other similar metastable structures during their lifetime. This self-similar process systematically generates new equilibria that adhere to a kinetic stationary solution of the Vlasov equation. The magnetic vortices qualitatively conform to a universal form that can be simply characterized using the Gold-Hoyle equilibrium. These structures exhibit a characteristic size typical of inertial range turbulence, rendering them macroscopically relevant; they may grow through coalescence to a significant fraction of astrophysical system size, potentially producing observable signatures [225, 201].

The present discussion has focused on a 2.5D model, which considers the plane perpendicular to a mean magnetic field. While this two-dimensional approximation qualitatively differs from the more complex and computationally demanding three-dimensional case, it may still provide insights into certain relaxation processes characteristic of magnetized astrophysical plasmas. Indeed, these equilibria could also be relevant in full three-dimensional anisotropic settings, particularly in scenarios where an external field effectively reduces the dimensionality of turbulence [271, 248, 235, 272]. In such general cases, which will motivate future investigations, the KVR model may exhibit a weak dependency along the magnetic field coordinate, denoted as z, which is typical of solar flux ropes. Since the long-lived structures may

potentially grow, our results could be significantly relevant for the comprehension of astrophysical plasmas, especially in scenarios where transient and flare emissions are associated with the formation of plasmoids during the accretion process, as observed, for instance, in Sgr A*, as well as in the observation of flux tubes in the solar wind and corona (varying the magnetization σ and the plasma β parameters).

The analysis presented thus far has illuminated the intricate dynamics of turbulent plasmas composed of electrons and protons. However, understanding the full complexity of astrophysical plasmas necessitates considering additional species, such as positrons. The inclusion of positrons introduces new layers of complexity and can significantly alter the dynamics of the plasma. In the following Section, we transition to a more comprehensive kinetic model that includes positrons, allowing us to examine their influence on the formation and evolution of coherent structures within turbulent environments. This expanded approach will enable us to capture the full spectrum of interactions among these three species, offering deeper insights into the microphysical processes that govern energy dissipation, particle acceleration, and the overall behavior of astrophysical plasmas, as discussed in Imbrogno et al. [232].

3.3 Multi-species plasma turbulence

In the vicinity of black holes, plasma is not confined to electrons and protons but may also include other species, such as positrons. Positrons are produced through various mechanisms, including pair production and inverse Compton scattering, where high-energy photons interact with matter to create electron-positron pairs. Incorporating these additional species into the analysis is essential for accurately modeling the complex environments surrounding black holes, such as jets, accretion disks, and outflows. The interaction among these particles in such extreme conditions can profoundly influence the plasma's dynamics, stability, and energy distribution, especially in turbulent regions where non-linear interactions with magnetic fields and high-energy processes dominate. The interactions among these three species give rise to intricate phenomena that warrant further investigation. Notably, the presence of positrons introduces additional effects related to particle acceleration and energy dissipation mechanisms. Understanding how these dynamics manifest in the vicinity of black holes could yield new insights into the mechanisms driving jet formation and the behavior of accreting matter. This broader perspective encourages a thorough examination of multi-species plasma, paving the way for future research into the fundamental processes that govern the astrophysical environments in which these structures are observed.

The objective of this study is to investigate the kinetic behavior of plasma incorporating a third species, the positrons. Our primary focus is to perform a series of simulations, specifically in the wind region (see Fig. 3.15), by varying the species concentration ratio, as outlined in Imbrogno et al. [273] (submitted). This approach is based on the observation that limited information is available regarding this parameter in that region, suggesting that the resulting plasma dynamics could vary significantly depending on this choice. With respect to the selection of other key parameters, such as plasma beta β and magnetization σ, previous research within the framework of GRMHD provides valuable insights into the orders of magnitude for these critical features. Our simulation campaign draws inspiration from the findings of Ripperda, Bacchini, and Philippov [202]. As illustrated in Fig.s 3.16a–3.16b, it is reasonable to set the total plasma beta at $\beta \approx 0.2$ (with $\beta_e \approx 0.1$, where β_e

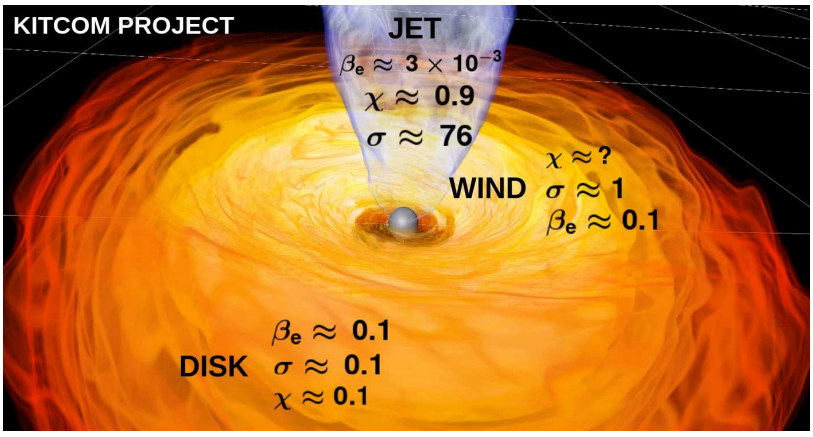

FIGURE 3.15: Schematic representation of the investigation regions for PIC simulations within the "KITCOM project", a collaboration initiated in recent months. Notably, the black hole wind region is of significant interest, as the concentration ratio between species remains uncertain.

represents the electron beta) and the magnetization at $\sigma \approx 1$. This latter choice reflects a balance between magnetic and kinetic forces, allowing the plasma to exhibit characteristic behaviors, including the formation of vortex structures and magnetic stability, while remaining susceptible to instabilities. At this stage, the focus of our investigation is to understand how the dynamics of the plasma evolve with varying the concentration ratio χ, defined below.

In our simulation, the condition of charge neutrality ensures the continuous presence of electrons. Accordingly, we define χ as the concentration ratio of positrons (e^+) to electrons (e^-):

$$\chi = \frac{n_{e^+}}{n_{e^-}}, \tag{3.56}$$

where the concentration of protons (p) can be determined from the charge neutrality condition:

$$n_{e^-} = n_p + n_{e^+} = n_0 = \frac{1}{4\pi}. \tag{3.57}$$

This formulation is advantageous because, given χ and n_{e^-}, it is straightforward to ascertain the concentrations of the other species, namely:

$$n_{e^-} = n_0, \tag{3.58}$$
$$n_p = (1-\chi)n_0, \tag{3.59}$$
$$n_{e^+} = \chi n_0. \tag{3.60}$$

An illustrative sketch that facilitates the understanding of the above notation is presented in Fig. 3.17.

Table 3.1 summarizes the settings of some simulations conducted to demonstrate the relevance of the present study. The parameters listed in the table are explained as follows. The enthalpy-weighted magnetization, commonly referred to as the "hot" magnetization, quantifies the magnetic energy available per particle and is expressed as:

$$\sigma = \frac{B_0^2}{4\pi w} = \frac{B_0^2}{4\pi(\rho_{tot}^m c^2 + \Gamma u_{tot})}, \tag{3.61}$$

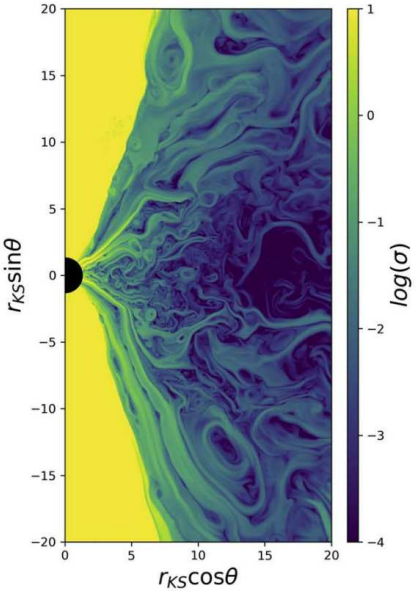

(A) Magnetization σ illustrating that the current sheets along the jet's sheath operate within the relativistic regime, while those in the disk function within the trans-relativistic regime. Image credit: Ripperda, Bacchini, and Philippov [202].

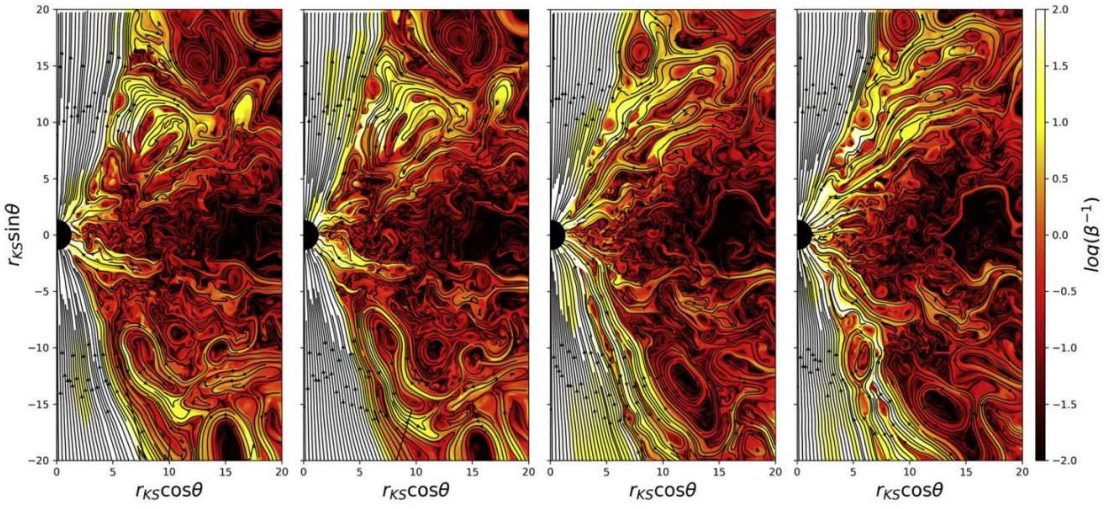

(B) Total plasma beta β during the quasi-steady-state phase of accretion. Image credit: Ripperda, Bacchini, and Philippov [202].

FIGURE 3.16: Top: magnetization σ in the jet's sheath and disk. Bottom: total plasma beta β during the accretion phase.

where ρ^m_{tot} stands for the total rest-mass density of the system, defined as:

$$\rho^m_{tot} = \sum_\alpha n_\alpha m_\alpha = n_0 \left(m_{e^-} + (1-\chi) m_p + \chi m_{e^+} \right), \tag{3.62}$$

and u_{tot} is the total internal energy density, approximated by:

$$u_{tot} \approx \sum_\alpha \frac{P_\alpha}{\Gamma - 1} = \sum_\alpha \frac{n_\alpha k_B T_\alpha}{\Gamma - 1}. \tag{3.63}$$

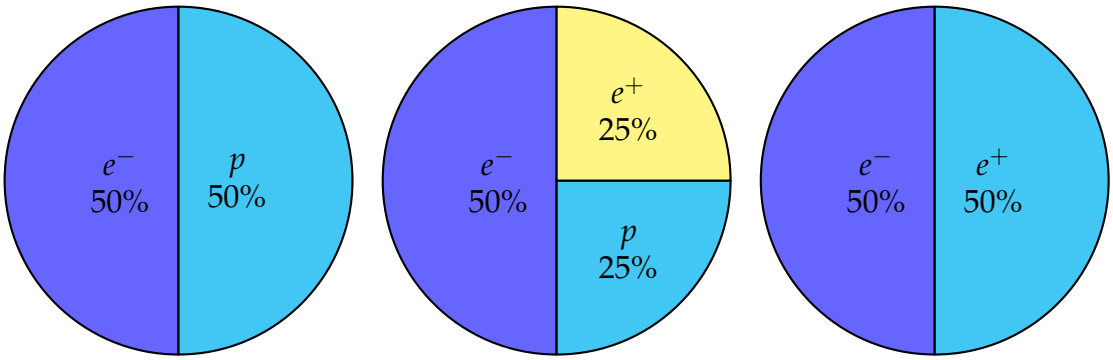

FIGURE 3.17: Pie charts for $\chi = 0.0$ (left), $\chi = 0.5$ (middle), and $\chi = 1.0$ (right).

For each species $\alpha = e^-, p, e^+$, we can also define a "cold" magnetization as:

$$\sigma_\alpha^c = \frac{B_0^2}{4\pi n_\alpha m_\alpha c^2}. \tag{3.64}$$

In the aforementioned relations, n_α, m_α, and T_α denote the number density, mass, and temperature of the α-th particle species, $\Gamma = 4/3$ is the adiabatic index, and B_0 represents the strength of the guiding magnetic field, as previously detailed in Sec. 3.2. The distinction between "hot" and "cold" magnetization is based on the contributions from both particle mass and thermal energy; "hot" magnetization reflects a scenario where thermal motion is significant, whereas "cold" magnetization accounts solely for particle mass density, disregarding thermal effects.

The effective temperature of each species T_α is determined by the dimensionless temperature θ_α through the following relationship:

$$T_\alpha = \frac{\theta_\alpha m_\alpha c^2}{k_B}. \tag{3.65}$$

The effective temperature is directly proportional to the α-th plasma beta, which quantifies the ratio of kinetic to magnetic pressure:

$$\beta_\alpha = \frac{8\pi n_\alpha k_B T_\alpha}{B_0^2}. \tag{3.66}$$

It is important to note that most constants in the equations above (i.e., m_e, k_B, and c) are set to unity in accordance with the geometrized unit system adopted throughout this thesis.

For all the simulations performed, we utilized $N_x = N_y = 4096$ mesh points within a physical box length of $L_0 = 5461.33\, d_{e^-}$, resulting in a spatial resolution of $\Delta x = 4/3\, d_{e^-}$. In general, the skin depth for species α is defined as:

$$d_\alpha = \frac{c}{\omega_{p,\alpha}} = \frac{c}{\sqrt{\dfrac{4\pi n_\alpha e^2}{m_\alpha}}}, \tag{3.67}$$

where $\omega_{p,\alpha}$ represents the plasma frequency of the α-th species. The time resolution is set as a fraction of the spatial resolution, specifically $\Delta t = 0.45\, \Delta x$, ensuring compliance with the CFL condition for the stability of the numerical evolution. In all simulations, 80 PPC are evolved, and thermal equilibrium is initially imposed

$(T_{e^-} = T_p = T_{e^+})$.

χ	σ	σ_e^c	σ_e	B_0
0.0	0.99	1836	152.8	42.85
0.5	1.95	1836	152.8	42.85
1.0	76.4	1836	152.8	42.85

χ	$(\theta_{e^-}, \theta_p, \theta_{e^+})$	$(\beta_{e^-}, \beta_p, \beta_{e^+})$	T_{mac}^{fin}
0.0	$(2.754, 1.5 \times 10^{-3}, //)$	$(3 \times 10^{-3}, 3 \times 10^{-3}, //)$	18000
0.5	$(2.754, 1.5 \times 10^{-3}, 2.754)$	$(3 \times 10^{-3}, 1.5 \times 10^{-3}, 1.5 \times 10^{-3})$	18000
1.0	$(2.754, //, 2.754)$	$(3 \times 10^{-3}, //, 3 \times 10^{-3})$	18000

TABLE 3.1: Initial parameters for the multi-species plasma simulations.

The time evolution in our simulations is measured in machine time $t_{\rm mac}$. Nevertheless, to facilitate comparisons across different configurations, it is essential to normalize this time to a characteristic timescale. In Table 3.2, we present several pertinent characteristic quantities at the moment of maximum energy, including the RMS of the electron bulk velocity $\langle \boldsymbol{v}_e \rangle_{\rm RMS}$, the fluctuations of the magnetic field $\langle \boldsymbol{b} \rangle_{\rm RMS}$ (where $\boldsymbol{b} = \boldsymbol{B} - B_0$), the correlation length λ_c, and the Taylor length λ_T associated with the magnetic field. Additionally, we report the Alfvén time and the nonlinear time, which are two distinct methodologies for normalizing time. The Alfvén time is expressed as follows:

$$t_{\rm Alf} = \frac{L_0(d_{e^-})}{\sqrt{\dfrac{\sigma}{1+\sigma}}}, \tag{3.68}$$

while the nonlinear time is defined as the ratio of the correlation length to the RMS of the electron bulk velocity:

$$t_{\rm nonlin} = \frac{\lambda_c}{\langle \boldsymbol{v}_e \rangle_{\rm RMS}}. \tag{3.69}$$

χ	t_{mac}	$\langle \boldsymbol{v}_e \rangle_{RMS}$	$\langle \boldsymbol{b} \rangle_{RMS}$	λ_c	λ_T	t_{Alf}	t_{nonlin}
0.0	10000	0.21	873.0	437.0	37.0	7748.0	2063.0
0.5	10000	0.22	875.0	420.0	42.0	6717.0	1875.0
1.0	10000	0.24	850.0	433.0	36.0	5497.0	1798.0

TABLE 3.2: Characteristic quantities at the time of maximum energy for the multi-species plasma simulations.

Since both definitions yield quantities that exhibit minimal variation across the three distinct configurations, we opt to normalize the machine time using the Alfvén time, a measure commonly employed in analogous astrophysical contexts.

Other meaningful quantities that must be considered to monitor the scales we can resolve are the Debye length and the Larmor radius (or gyroradius) associated with each species. In a classical framework, these are defined as follows:

$$\lambda_{D,\alpha} = \sqrt{\frac{m_\alpha \theta_\alpha c^2}{4\pi n_\alpha e^2}} = \sqrt{\theta_\alpha} d_\alpha \tag{3.70}$$

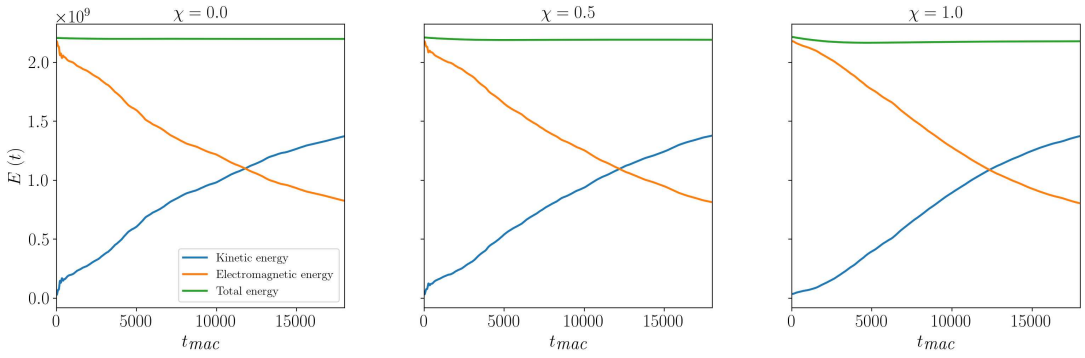

FIGURE 3.18: Variation of total energy, kinetic energy (excluding rest-mass energy), and magnetic energy (considering only fluctuations) as a function of time.

and

$$\rho_{L,\alpha} = \frac{m_\alpha c\, v_{\mathrm{th},\alpha}}{eB_0} = \sqrt{\beta_\alpha} d_\alpha, \tag{3.71}$$

respectively, where $v_{\mathrm{th},\alpha} = \sqrt{2k_B T_\alpha / m_\alpha}$ denotes the thermal velocity of the α-th species. It is crucial that, in PIC simulations, the following relationships are strictly satisfied for each species:

$$\frac{\lambda_{D,\alpha}}{\Delta x} > 1, \quad \omega_{p,\alpha}\, \Delta t < 1, \tag{3.72}$$

where, as specified previously, $\Delta t = 0.45\, \Delta x$.

Another useful parameter to consider for diagnostics is the total energy of the system E_{tot}, which is defined as the sum of the kinetic energy of the particles (excluding the rest-mass energy) $E^{\mathrm{tot}}_{\mathrm{kin}}$ and the electromagnetic energy E_{em} (considering only the fluctuations of the electric and magnetic fields):

$$E_{\mathrm{tot}} = E^{\mathrm{tot}}_{\mathrm{kin}} + E_{\mathrm{em}} = \sum_\alpha (W_\alpha - 1) m_\alpha c^2 + \frac{\langle \boldsymbol{e}^2 \rangle + \langle \boldsymbol{b}^2 \rangle}{8\pi}, \tag{3.73}$$

where W_α is the Lorentz factor associated with each species of particles. As illustrated in Fig. 3.18, the total energy remains conserved across all three test simulations. However, the kinetic and electromagnetic energies exhibit an inverse relationship: as one decreases, the other increases. This exchange occurs as magnetic energy is transferred to the kinetic energy of particles, a characteristic feature of decaying turbulence.

The initial conditions for all simulations are standardized to ensure comparable dynamics and facilitate effective analysis. We construct the initial in-plane magnetic field (b_x, b_y) from the spectrum of the vertical component of the magnetic potential $\tilde{a}_z$. The initial magnetic field, in which the particles are immersed, is derived from the curl of the vector potential, $\boldsymbol{b} = \boldsymbol{\nabla} \times \boldsymbol{a}$, where the in-plane field is expressed as $\boldsymbol{b}_\perp = \boldsymbol{\nabla}_\perp a_z \times \hat{z}$. The spectral shape is defined as follows:

$$\begin{aligned} a_z(x,y) &= \sum_{k_x, k_y} \tilde{a}_z(k) e^{i(\boldsymbol{k}\cdot\boldsymbol{x} + \varphi_k)}, \\ \tilde{a}_z(k) &= \frac{1}{1 + \left(\dfrac{k}{k_0}\right)^{15/3}}. \end{aligned} \tag{3.74}$$

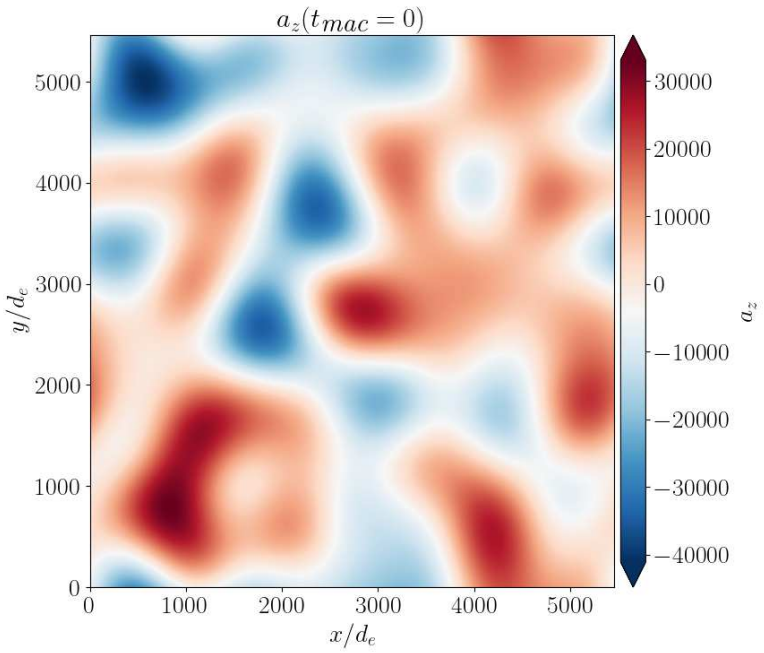

FIGURE 3.19: Initial conditions for the z-component of the vector potential.

where, as usual, a low wavenumber $k_0 = 4$ is selected to inject energy at large scales, thereby promoting the onset of turbulence, with truncation of the spectrum occurring at $k^* = 7$. Finally, the amplitude of the magnetic field fluctuations is imposed to ensure that $\langle \boldsymbol{b} \rangle \approx B_0$. The initial two-dimensional representation of the vertical component of the magnetic potential a_z is illustrated in Fig. 3.19.

The simulations, whose principal parameters are listed in Table 3.1, are evolved up to a machine time corresponding to the peak of nonlinear activity, as illustrated in Fig. 3.20, which shows the RMS of the vertical component of the current density, $\langle j_z \rangle_{\mathrm{RMS}}$. Our focus is on the time period around the point of maximum energy, which occurs at approximately $t_{\mathrm{mac}} \approx 10000$ and is indicated by (black) dashed lines.

Fig. 3.21 illustrates the two-dimensional evolution of the total number density n, normalized to the initial density n_0, for different concentration ratios ($\chi = 0$, $\chi = 0.5$, and $\chi = 1$, as depicted in Fig. 3.17), around the time of maximum nonlinear activity. The plots reveal slight variations in the evolution timescales, with coherent structures emerging, approaching each other, and merging, thereby forming current layers and plasmoids in the regions between them.

The particle spectra of electrons, protons, and positrons, along with the magnetic spectra presented in Appendix C, exhibit noticeable differences as χ is varied. The former indicates that, as χ increases, the particles become more energetic and thus experience greater acceleration. The latter reveals that when χ is higher, the spectrum broadens in the inertial range, indicating enhanced energy transport. This suggests that energy is being transferred more efficiently from large to small scales, where it is ultimately dissipated. Indeed, Fig. 3.20 indicates that dissipation is more pronounced in pair plasmas compared to plasmas composed solely of electrons and protons, or those with intermediate concentration ratios.

Due to the highly challenging nature of these simulations, we submitted a proposal to secure computing time. We were awarded a CINECA ISCRA-B project,

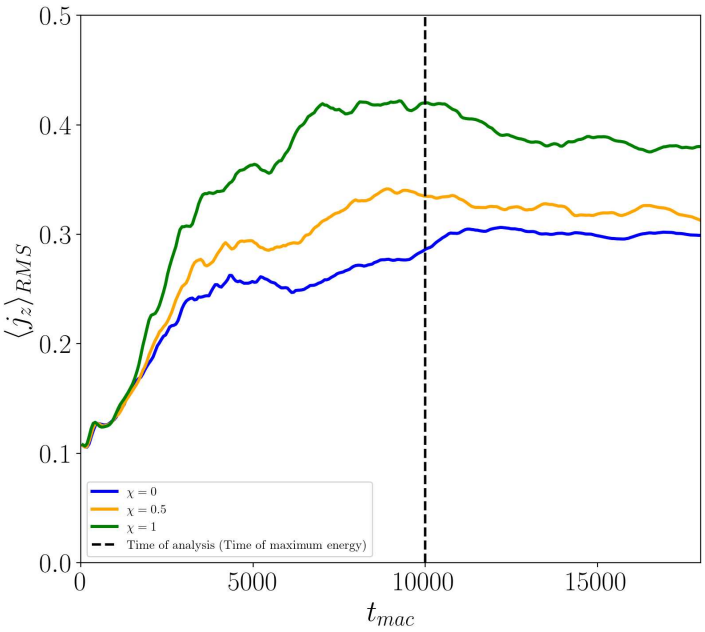

FIGURE 3.20: RMS of the vertical component of the current density for electron-proton plasma (blue solid line), electron-proton-positron plasma (orange solid line), and electron-positron plasma (green solid line). The black dashed line represents the time of maximum energy, where the analysis is focused.

named "KITCOM" (Kinetic Simulations of Turbulence near Compact Objects with Multi-species), granting us 3.5 million CPU hours. Within the framework of the "KITCOM project," we aim to replicate identical simulation parameters while achieving the same or improved spatial resolution, specifically $\Delta x = 4/3\, d_{e^-}$ or $\Delta x = 1/3\, d_{e^-}$. This will be accomplished using a squared physical box that is four times larger than previous configurations, with dimensions defined as $L_0 = 10922.66\, d_{e^-}$ and grid sizes of $N_x = N_y = 8192$ or $N_x = N_y = 32768$. Notably, the choice of particles per cell is flexible, and adjustments are allowed as long as the total number of particles within the physical box remains constant, approximately $5.4 \cdot 10^9$. This constraint is crucial for mitigating shot noise during the simulations. For instance, one may select 5 PPC with $N_x = N_y = 32768$ or 80 PPC with $N_x = N_y = 8192$. Additionally, we plan to monitor 1000 particles per species, tracking them at each timestep. To facilitate system relaxation and ensure evolution well beyond the phase of peak nonlinear activity, the final simulation time is established at $t_{\rm fin} = 4\, t_{\rm Alf}$. These simulations will be conducted on the "Leonardo HPC cluster," which is supported by CINECA.

The primary areas of interest surrounding a black hole include the disk, the jets, and the wind, as schematized in Fig. 3.15. Among these, a particularly intriguing and poorly explored region involves the current sheets within the black hole wind. Consequently, we intend to perform several local high-resolution simulations in this region, adhering to our computing budget, while maintaining a fixed magnetization of $\sigma \approx 1.0$ and a total plasma beta of $\beta \approx 0.2$ (with $\beta_e \approx 0.1$), varying the concentration ratio $\chi = \{0, 0.1, 0.4, 0.5, 0.6, 0.9, 1\}$.

Given that the magnetization σ and the total plasma beta β are fixed, the strength of the out-of-plane (guide) magnetic field B_0 and the dimensionless electron temperature $\theta = \theta_e$ are interdependent. Specifically, starting from the expression for β and

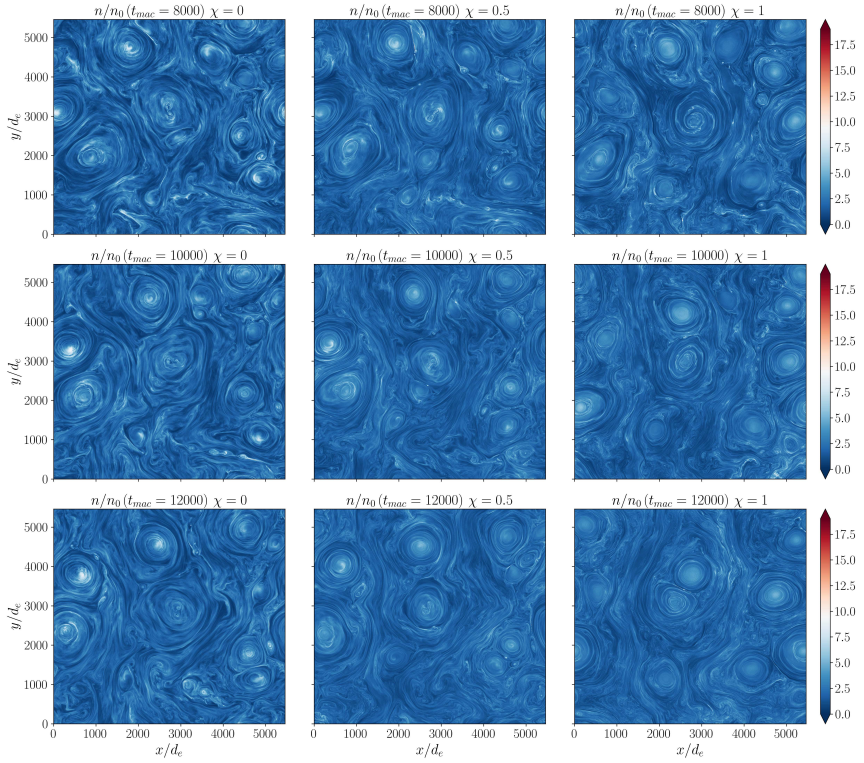

FIGURE 3.21: Total number density evolution map around the peak of nonlinear activity for electron-proton plasma (left column), electron-proton-positron plasma (middle column), and electron-positron plasma (right column).

assuming initial thermal equilibrium ($T_{e^-} = T_p = T_{e^+}$), the guide magnetic field strength is expressed as:

$$\beta = \frac{8\pi n_0 \overbrace{(\theta m_{e^-} c^2)}^{k_B T_{e^-}} f_\chi}{B_0^2} \implies B_0 = B_0(\theta) = \sqrt{\frac{8\pi n_0 \theta m_{e^-} c^2 f_\chi}{\beta}}, \tag{3.75}$$

while the dimensionless electron temperature can be obtained from the expression for σ:

$$\sigma = \frac{B_0^2}{4\pi n_0 \left[(m_{e^-} + (1-\chi) m_p + \chi m_{e^+}) c^2 + \dfrac{\Gamma}{\Gamma - 1} f_\chi (\theta m_{e^-} c^2) \right]} \tag{3.76}$$

$$\theta = \frac{\left(m_{e^-} + (1-\chi) m_p + \chi m_{e^+} \right) \sigma \beta}{m_{e^-} f_\chi \left(2 - \dfrac{\Gamma}{\Gamma - 1} \sigma \beta \right)}, \tag{3.77}$$

where f_χ is a χ-dependent function expressible as:

$$f_\chi = 1 + \chi + (1-\chi)\, T_{ratio}, \quad T_{ratio} = \frac{T_p}{T_{e^-}} = 1. \tag{3.78}$$

It is important to note that the total plasma beta β is defined as the sum of the individual plasma betas of each species β_α, which can be inferred as follows:

$$\beta_{e^-} = \frac{1}{f_\chi}\,\beta, \tag{3.79}$$

$$\beta_p = \frac{(1-\chi)\,T_{ratio}}{f_\chi}\,\beta, \tag{3.80}$$

$$\beta_{e^+} = \frac{\chi}{f_\chi}\,\beta. \tag{3.81}$$

In Appendix C, we conduct convergence tests to demonstrate that the selected resolution for the multi-species simulations remains valid, even when the electron skin depth is not fully resolved in some cases and the electron Debye length in others. Our primary objective is to achieve simulations with a high number of particles per species to mitigate shot noise, which necessitates a compromise on resolution while ensuring it remains within reasonable limits. Further methodological details are provided in Imbrogno et al. [273] (submitted).

Conclusions

This thesis has been devoted to the study of black hole dynamics, in fully nonlinear regimes. In particular, we investigated the behavior of such compact objects in complex configurations, starting from vacuum spacetimes, with multiple bodies problem, going to the study of relativistic turbulent plasmas in their surrounding regions. By employing advanced numerical simulations, we have investigated these extreme systems and uncovered intricate nonlinear behaviors.

The work began with simulations of black hole systems in vacuum, focusing on binary and multi-body interactions. Using the 3+1 formalism and the BSSN formulation, we performed stable numerical simulations of black hole mergers, allowing an accurate extraction of gravitational wave signals. After recovering the typical gravitational radiation of binary systems, this effort established the foundation for exploring more complex scenarios involving three black holes. On this regard, we started from Newtonian mechanics, where chaotic configurations led to extreme gravitational interactions (EGIs). These EGIs were used as initial data for the general relativistic case, resulting in a comprehensive set of scenarios that revealed the complexity of three-body dynamics. The analysis of three-body dynamics revealed complex gravitational waveforms that provide critical insights into the nature of multi-body interactions and offer potential signatures for detection by observatories like LIGO and Virgo. These results could contribute to the refinement of waveform templates and improve the interpretability of gravitational wave data in cases of multi-body systems, thereby advancing the strategies for future detections.

Since multi-body interactions eventually culminate in the formation of a single, spinning black hole, we subsequently shifted our attention towards understanding the behavior of relativistic plasmas in the vicinity of Kerr-type black holes. Within the framework of GRHD, we proposed a novel logarithmic formulation that might enhance numerical stability in scenarios characterized by steep gradients, such as shock fronts or stellar atmospheres. This approach has been tested under a Minkowski metric, demonstrating promising stability characteristics, with plans to extend these tests to curved spacetimes in future studies to fully assess its robustness and applicability in more realistic astrophysical settings. Additionally, we investigated both the linear and nonlinear KHI, emphasizing its role in driving turbulence and mixing within regions dominated by strong velocity shear. The outcomes of these simulations have the potential to enhance our understanding of the interplay between plasma instabilities and gravitational fields in governing energy transport and angular momentum redistribution in the vicinity of black holes, while also providing valuable insights to guide future observational efforts.

Extending this study to magnetized plasmas, we used the `BHAC` code, within the GRMHD framework. A series of simulations were carried out to model accretion disks around supermassive black holes such as Sgr A* and M87*, with the aim of capturing the complex dynamics of matter in magnetically dominated regions. By performing a spectral analysis of the surrounding matter within the accretion disks, we identified the presence of a vigorous, strong turbulent cascade characterized by

cross-scale coupling, where energy is efficiently transferred from large, inhomogeneous scales down to smaller, homogeneous lenghts. This active energy transfer was observed consistently across various regions, including the accretion disk, the wind, and the relativistic jet. The results of this comprehensive analysis revealed the crucial role of magnetic fields in shaping the behavior of turbulent plasma flows, uncovering key mechanisms that influence energy dissipation, angular momentum transport, and jet formation.

Finally, as energy is effectively transferred to smaller scales, we explored fully kinetic, relativistic plasma turbulence using PIC simulations. These simulations were designed to capture the microscopic physics of particle acceleration and magnetic reconnection processes by incorporating realistic mass ratios between different particle species. This approach provided detailed insights into the kinetic processes that drive the turbulent dynamics of relativistic plasmas. With the planned inclusion of positrons, our aim is to enable a more comprehensive investigation of multi-species plasma dynamics, offering a deeper understanding of how these additional particle species interact within turbulent magnetic fields. The analysis of these simulations revealed the emergence of long-lived coherent structures, which play a fundamental role in mediating turbulence, energy transfer, and high-energy emissions in magnetically dominated environments. To accurately characterize these structures, we developed a self-consistent kinetic model inspired by the Harris equilibrium, which finds validation in a robust, but not so popular, fluid description. This model provided a clearer framework for understanding the interplay between coherent patterns and the underlying plasma dynamics. In light of the potential presence of positrons in accretion flows around black holes, we propose the development of new numerical models to explore such multi-species, turbulent plasmas. By integrating these additional particle species into our kinetic framework, we aim to uncover the dominant mechanisms responsible for energy distribution, particle energization, and the resulting high-energy emissions.

In conclusion, this thesis has integrated multiple theoretical and computational frameworks to offer a comprehensive, cross-scale perspective on the dynamics of black holes and their interactions with surrounding relativistic plasmas. The present results might provide new theoretical background to support current and upcoming observational campaigns.

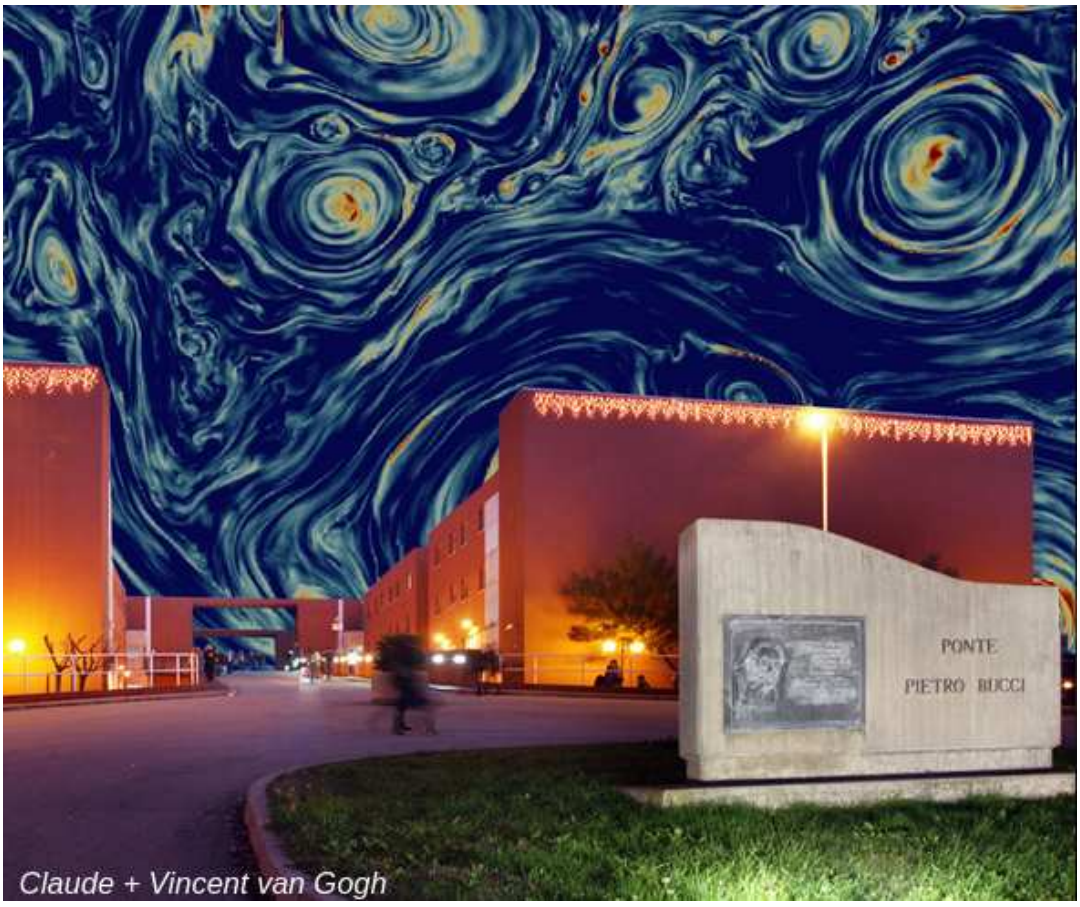

FIGURE 3.22: Turbulent starry night at University of Calabria.

Appendix A

ADM Constraint Violations

The constraints of the ADM formalism must be satisfied throughout the entire duration of the simulation. Consequently, it is essential to monitor any violations of the Hamiltonian and momentum constraints during the whole evolution of the system. In principle, one expects that the numerical solution satisfies these constraints or at least results in residuals that do not grow as the evolution of the gravitational field progresses. The violation of the constraints is evaluated through their average $\bar{L}_2$ error, defined as [274]

$$\bar{L}_2 = ||\epsilon(x,y,z)||_2 = \sqrt{\frac{\int_\Omega \epsilon^2 \sqrt{|\gamma|} d\Omega}{\int_\Omega \sqrt{|\gamma|} d\Omega}}. \tag{A.1}$$

Here, $\sqrt{|\gamma|}d\Omega$ represents the volume element calculated using the square root of the determinant of the spatial metric, and ϵ denotes the local error the Hamiltonian and momentum constraints. We emphasize that the volume integrals in equation (A.1) have been computed over the entire computational domain, including the grid regions closest to the singularities. Fig. A.1 shows the time-dependent Hamiltonian and momentum constraints for each of the analyzed configurations, indicating the violation of each constraint, which must be satisfied at every time slice. As shown, the violation remains low and fairly constant throughout the simulation, without any exponential growth.

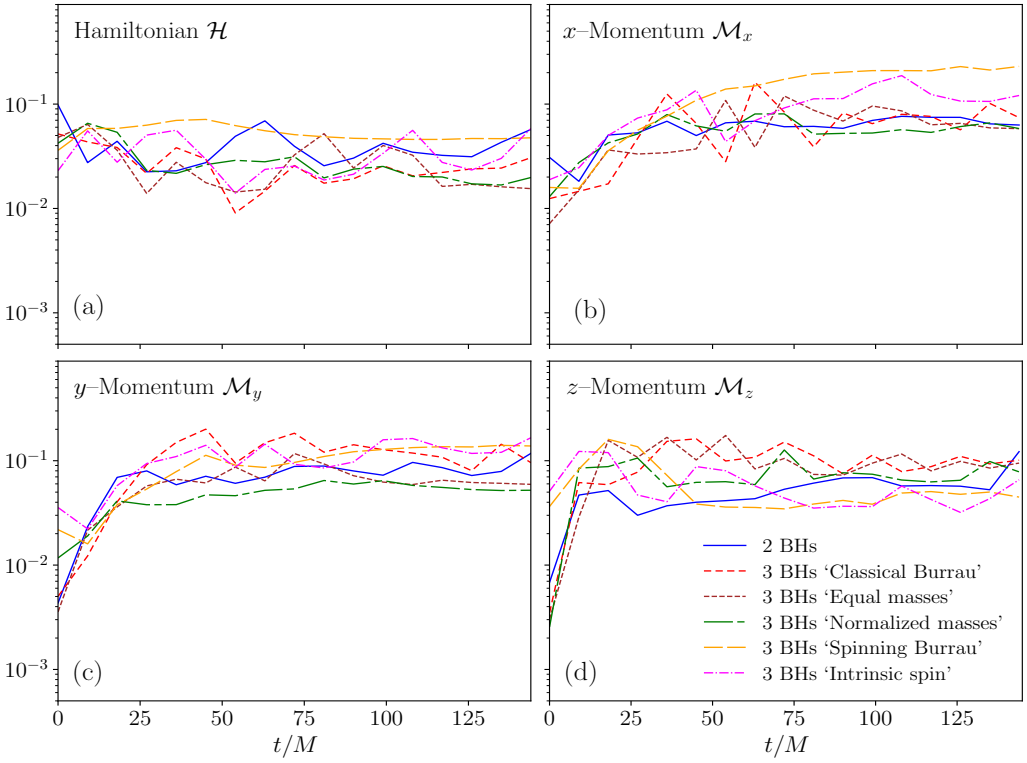

FIGURE A.1: Time evolution of the Hamiltonian constraint (a) and the momentum constraints (b)–(d). The values on the y–axis are shown in logarithmic scale.

Appendix B

Numerical Challenges in BHAC Simulations and Synthetic Field Analysis

Numerical simulations performed using the BHAC code present several challenges for subsequent analysis:

1. **Irregular boundaries:** The complex shapes of the boundaries in the simulation domain can complicate both the analysis and interpretation of results.
2. **AMR:** While AMR is advantageous for resolving fine details in specific regions, it introduces variability in grid resolution, which poses difficulties for Fourier analysis that requires a uniform grid.
3. **Curved spacetime:** The presence of a non-flat spacetime metric adds further complexity to the analysis.

To assess the effectiveness of the increment-space estimation technique for computing power spectra, as described in Sec. 2.6, we design a toy problem by defining a synthetic field with a Kolmogorov $-5/3$ power spectrum across the three regions shown in Fig. 2.24. The synthetic field is expressed in the following form:

$$F(\boldsymbol{x}) = \sum_{k_x=-\infty}^{+\infty} \sum_{k_z=-\infty}^{+\infty} A_k \, \exp[i(\boldsymbol{k}\cdot\boldsymbol{x} + \varphi_k)], \tag{B.1}$$

where $\boldsymbol{k}$ denotes the wavevector in Fourier space, φ_k are randomly assigned phases, and A_k is the amplitude, defined as:

$$A_k = \exp\left(-\alpha \left| \left(\frac{k}{k_{\max}}\right)^{\alpha} \right|\right) \frac{k^{-1/2}\,\dfrac{k}{k_0}}{\left[1 + \left(\dfrac{k}{k_0}\right)^{11/3}\right]^{1/2}}. \tag{B.2}$$

Here, α is a constant parameter that filters the field within a specified range, $k_{\max}$ is the cut-off wavenumber beyond which the filter suppresses spectral components, and k_0 represents the peak of the power spectrum. The synthetic field described by

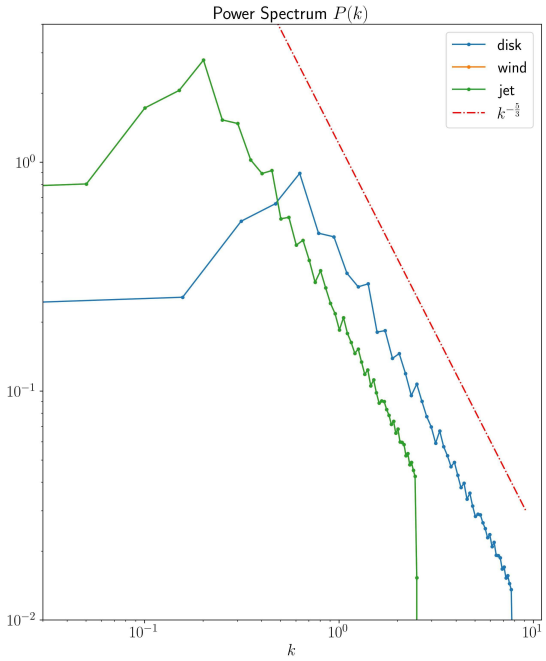

FIGURE B.1: Power spectrum of the synthetic field for the three regions: the disk (blue), the wind (orange), and the jet (green). The spectra for the wind and jet overlap. The red dash-dotted line represents the Kolmogorov $-5/3$ scaling law.

Eq. (B.1) yields the following power spectrum $P(k)$:

$$P(k) = \frac{\left(\frac{k}{k_0}\right)^2}{\left[1 + \left(\frac{k}{k_0}\right)^{11/3}\right]}. \tag{B.3}$$

In the Kolmogorov power spectrum [275], as shown in Fig. B.1, the behavior at large values of k (small scales) is dominated by the inertial range, following

$$P(k) \approx k^{-5/3}. \tag{B.4}$$

To address the analytical challenges posed by AMR, we implement a technique to construct a structured and uniform grid that facilitates both analytical and computational tasks. By interpolating the data onto this regular grid, we obtain a more coherent and uniform dataset, which improves the accuracy and efficiency of the analysis. The interpolation is performed using the `griddata` function, which estimates values at regular grid points based on the original irregular data. This process is crucial for transforming irregularly distributed data into a structured format. Specifically, we use cubic interpolation based on the Clough-Tocher method, which employs piecewise polynomial interpolants, ensuring C^1 smoothness and curvature-minimizing properties [276, 277]. For instance, Figure B.2 compares the synthetic field constructed on the irregular BHAC grid for the disk region with the same field interpolated onto a regular grid with dimensions $(N_x, N_z) = (256, 256)$. The comparison demonstrates a perfect alignment with the interpolation technique. This same procedure is applied to both the wind and jet regions.

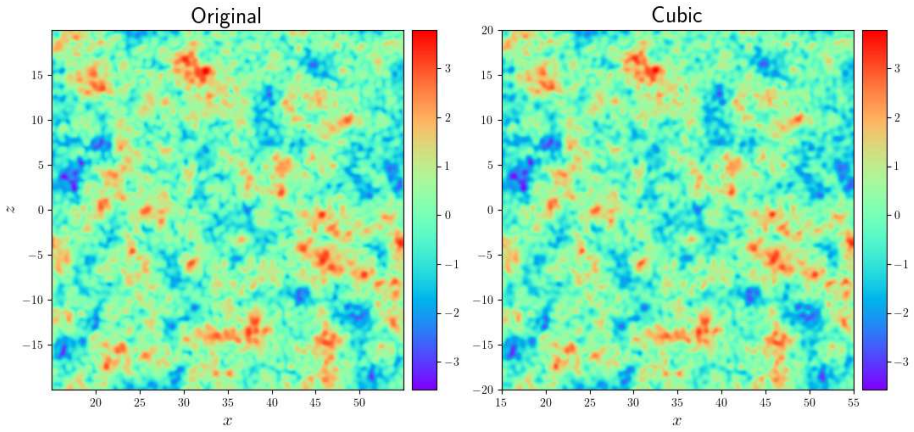

FIGURE B.2: The synthetic field with Kolmogorov $-5/3$ scaling law on the "original" unstaggered BHAC grid (left) and with cubic interpolation (right) for the disk region.

Appendix C

Convergence Analysis for Multi-Species Plasma Simulations

Simulating multi-species plasmas accurately requires selecting resolution parameters that capture key physical scales, such as the electron skin depth and Debye length, while ensuring numerical convergence. In this section, we present the key parameters for different concentration ratios χ, representing the proportion of positrons relative to electrons in the plasma. The resolution criteria and convergence studies are designed to achieve an optimal balance between computational efficiency and physical accuracy, particularly in cases where the electron skin depth or Debye length may be slightly under-resolved. Tables C.1 and C.2 summarize the parameters for each concentration ratio, followed by a discussion of convergence tests on magnetic spectra and particle distribution functions.

χ	N_x	N_y	Δx	Δt	PPC	$PPd_{e^-}^2$	$PP\lambda_{D,e^-}^2$
0.0	8192	8192	$4/3\, d_{e^-}$	$0.60\, d_{e^-}$	80	45	6889
0.1	8192	8192	$4/3\, d_{e^-}$	$0.60\, d_{e^-}$	80	45	6195
0.4	8192	8192	$4/3\, d_{e^-}$	$0.60\, d_{e^-}$	80	45	4135
0.5	8192	8192	$4/3\, d_{e^-}$	$0.60\, d_{e^-}$	80	45	3453
0.6	8192	8192	$4/3\, d_{e^-}$	$0.60\, d_{e^-}$	80	45	2756
0.9	8192	8192	$4/3\, d_{e^-}$	$0.60\, d_{e^-}$	80	45	696
1.0	32768	32768	$1/3\, d_{e^-}$	$0.15\, d_{e^-}$	5	45	7

TABLE C.1: Corresponding parameters for each concentration ratio χ, including values for mesh points, spatial and temporal resolutions, number of PPC, and the number of particles per electron skin depth squared and per electron Debye length squared.

χ	$d_{e^-}/\Delta x$	$d_p/\Delta x$	$d_{e^+}/\Delta x$	$\rho_{L,e^-}/\Delta x$	$\rho_{L,p}/\Delta x$	$\rho_{L,e^+}/\Delta x$
0.0	0.75	32.14	//	0.24	10.16	//
0.1	0.75	33.87	2.37	0.24	10.16	0.24
0.4	0.75	41.49	1.19	0.24	10.16	0.24
0.5	0.75	45.45	1.06	0.24	10.16	0.24
0.6	0.75	50.81	0.97	0.24	10.16	0.24
0.9	0.75	101.62	0.79	0.24	10.16	0.24
1.0	3.0	//	3.0	0.95	//	0.95

χ	$\lambda_{D,e^-}/\Delta x$	$\lambda_{D,p}/\Delta x$	$\lambda_{D,e^+}/\Delta x$
0.0	9.28	9.28	//
0.1	8.80	9.28	27.84
0.4	7.19	9.28	11.37
0.5	6.57	9.28	9.28
0.6	5.87	9.29	7.58
0.9	2.95	9.32	3.11
1.0	1.22	//	1.22

TABLE C.2: Corresponding parameters for each concentration ratio χ, including values for the skin depth resolution, Larmor radius resolution, and Debye length resolution of the α-th species.

As evidenced by the Tables above, selecting a resolution of $\Delta x = 4/3\, d_{e^-}$ does not adequately resolve the electron skin depth for cases with $\chi = \{0, 0.1, 0.4, 0.5, 0.6, 0.9\}$. To ensure that this choice does not compromise the results, we conduct a convergence study on magnetic spectra and particle distribution functions across different configurations with varying grid spacings, all while maintaining the same physical box length of $L_0 = 5461.33\, d_{e^-}$. Specifically, we analyzed the following resolutions: $\Delta x = d_{e^-}/3$ ($N_x = N_y = 16384$, PPC $= 5$), $\Delta x = 2/3\, d_{e^-}$ ($N_x = N_y = 8192$, PPC $= 20$), $\Delta x = 4/3\, d_{e^-}$ ($N_x = N_y = 4096$, PPC $= 80$), $\Delta x = 8/3\, d_{e^-}$ ($N_x = N_y = 2048$, PPC $= 320$), and $\Delta x = 16/3\, d_{e^-}$ ($N_x = N_y = 1024$, PPC $= 1280$). The results, focusing on a plasma composed solely of electrons and protons ($\chi = 0$), confirm that a resolution of $\Delta x = 4/3\, d_{e^-}$ is adequate for our purposes.

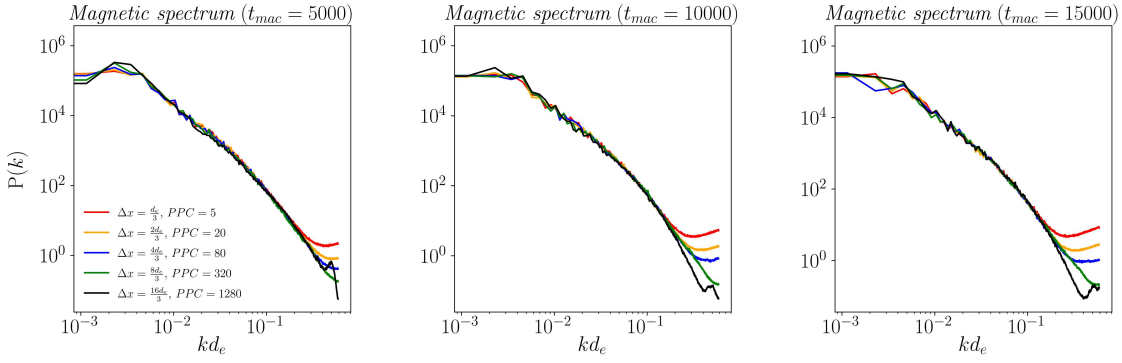

FIGURE C.1: Convergence study of magnetic spectra at various resolutions and different machine times, specifically for the case where $\chi = 0$.

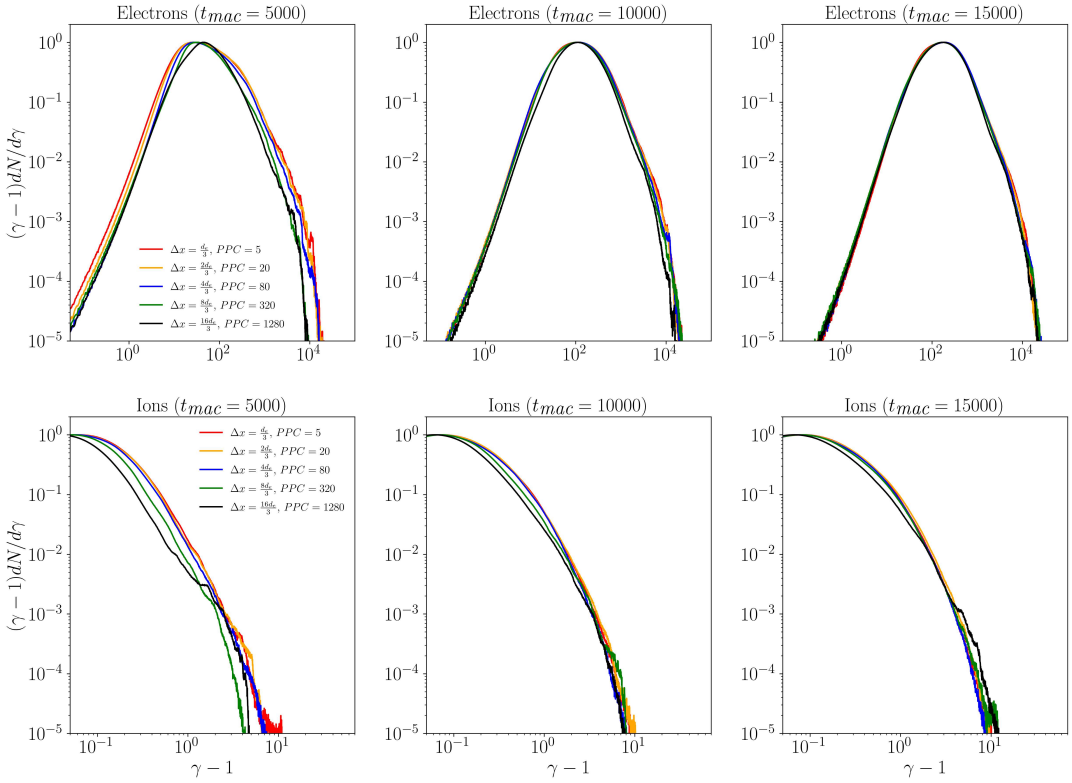

FIGURE C.2: Convergence study of the particle distribution functions for electrons (first row) and protons (second row) across different resolutions at various machine times for $\chi = 0$.

We conclude that, for $\chi = \{0, 0.1, 0.4, 0.5, 0.6, 0.9\}$, employing a resolution of $\Delta x = 4/3\, d_{e^-}$ is deemed acceptable. Consequently, it is feasible to implement 80 PPC to minimize noise in the fields and moments. Furthermore, once the turbulence is fully developed, the velocity distribution of electrons exhibits significant non-thermal characteristics, and their Larmor radius increases substantially due to considerable accelerations. This effectively enhances our resolution.

Once again, as inferred from Table C.1 and Table C.2, when the positron number density exceeds that of protons, the Debye length progressively decreases, becoming under-resolved in the case of $\chi = 1$. To address this issue, it is necessary to reduce the resolution to $\Delta x = 1/3\, d_{e^-}$. Due to computational cost constraints, which limit further resolution refinement, we verify this adjustment by conducting convergence studies on magnetic spectra and particle distribution functions across different configurations. These simulations maintain the same physical box length, though smaller, set at $L_0 = 1365.33\, d_{e^-}$, while varying the grid spacing. Specifically, we analyze the following cases: $\Delta x = 1/6\, d_{e^-}$ ($\lambda_{D,e^-}/\Delta x = 2.45$, $N_x = N_y = 8192$, PPC $= 5$), $\Delta x = 1/3\, d_{e^-}$ ($\lambda_{D,e^-}/\Delta x = 1.22$, $N_x = N_y = 4096$, PPC $= 20$), $\Delta x = 2/3\, d_{e^-}$ ($\lambda_{D,e^-}/\Delta x = 0.61$, $N_x = N_y = 2048$, PPC $= 80$), $\Delta x = 4/3\, d_{e^-}$ ($\lambda_{D,e^-}/\Delta x = 0.31$, $N_x = N_y = 1024$, PPC $= 320$), and $\Delta x = 8/3\, d_{e^-}$ ($\lambda_{D,e^-}/\Delta x = 0.15$, $N_x = N_y = 512$, PPC $= 1280$). The results, focusing on a plasma composed solely of electrons and positrons (pair plasma) with $\chi = 1$, demonstrate that a resolution slightly smaller than the Debye length can be employed effectively.

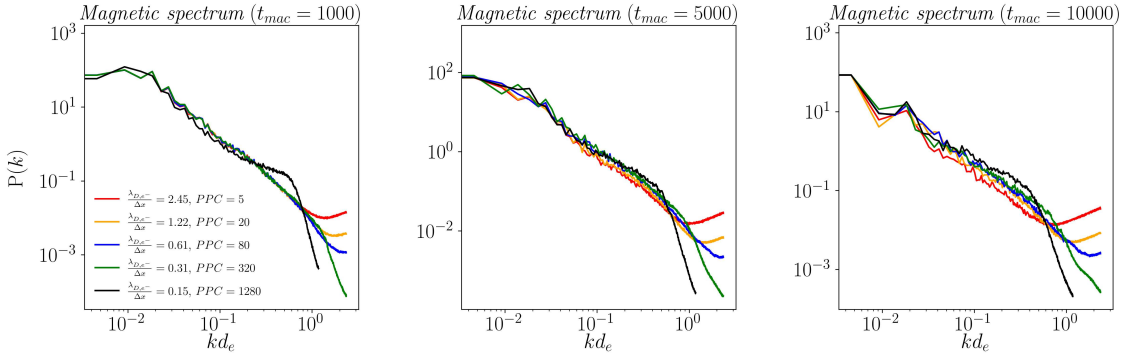

FIGURE C.3: Convergence study of magnetic spectra at various resolutions and different machine times, specifically for the case where $\chi = 1$.

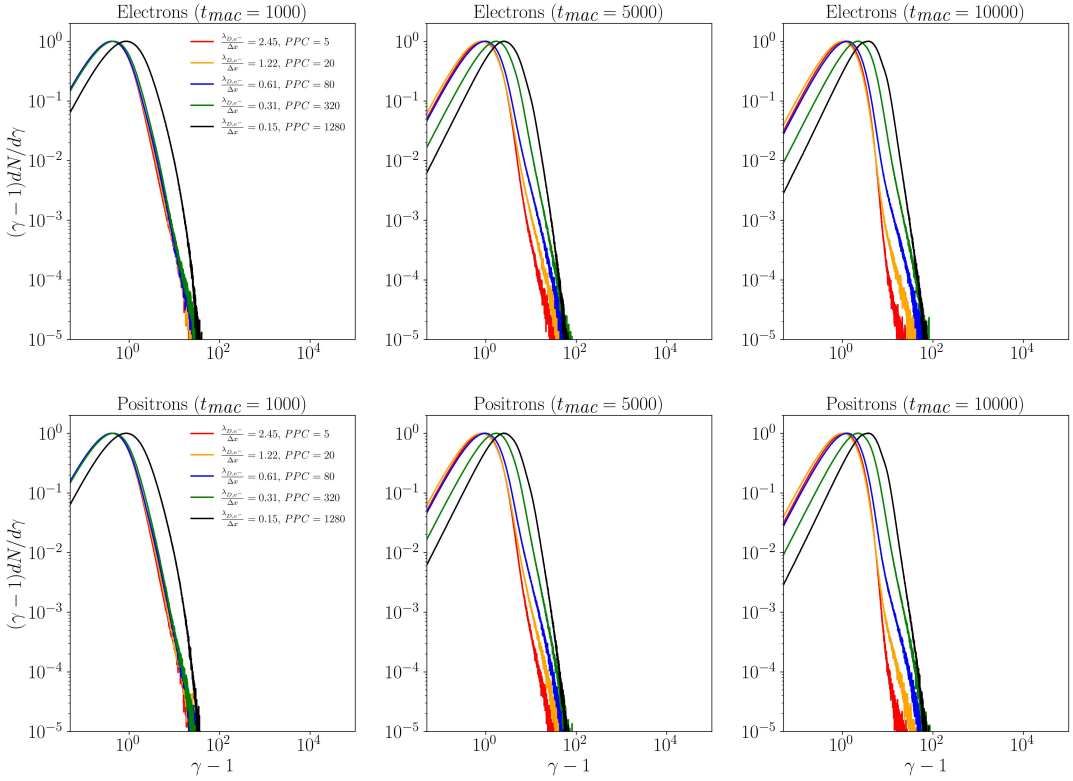

FIGURE C.4: Convergence study of the particle distribution functions for electrons (first row) and positrons (second row) across different resolutions at various machine times for $\chi = 1$.

We conclude that, for $\chi = 1$, a resolution of $\Delta x = 1/3\, d_{e^-}$ is deemed sufficient, enabling the implementation of 5 PPC to effectively reduce noise in the fields and moments.

Publications

Here, I present a list of papers developed during my Ph.D. period at the University of Calabria (UniCal), with some still in preparation. Additionally, I spent three months as a visiting researcher at the Institut de Planétologie et d'Astrophysique de Grenoble (IPAG), Université Grenoble Alpes (UGA), under the supervision of Dr. Benoît Cerutti.

Published:

- **Mario Imbrogno**, Claudio Meringolo, and Sergio Servidio, "Extreme gravitational interactions in the problem of three black holes in general relativity", *Classical and Quantum Gravity* 40.7 (2023), p. 075008, DOI: 10.1088/1361-6382/acb881
- **Mario Imbrogno**, Claudio Meringolo, Sergio Servidio, Alejandro Cruz-Osorio, Benoît Cerutti, and Francesco Pegoraro, "Long-lived Equilibria in Kinetic Astrophysical Plasma Turbulence", *The Astrophysical Journal Letters* 972.1 (2024), p. L5, DOI: 10.3847/2041-8213/ad6b9d

In Preparation:

- **Mario Imbrogno**, Rita Megale, Luca Del Zanna, and Sergio Servidio, "A Novel Logarithmic Approach to General Relativistic Hydrodynamics in Curved Spacetimes" (submitted)
- Rita Megale, **Mario Imbrogno**, Claudio Meringolo, Alejandro Cruz-Osorio, Leonardo Primavera, Luciano Rezzolla, and Sergio Servidio, "The Proper Length Spectrum of Turbulence near Black Holes"
- **Mario Imbrogno**, Claudio Meringolo, Alejandro Cruz-Osorio, Luciano Rezzolla, Benoît Cerutti, and Sergio Servidio, "Multi-species Plasma Turbulence in the Vicinity of Black Holes" (submitted)

Bibliography

[1] C. W. Misner, K. S. Thorne, and J. A. Wheeler. *Gravitation*. W. H. Freeman, 1973.

[2] O. Porth et al. "The Black Hole Accretion Code". In: *Computational Astrophysics and Cosmology* 4 (2017), p. 1.

[3] Benoit Cerutti et al. "Simulations of particle acceleration beyond the classical synchrotron burnoff limit in magnetic reconnection: an explanation of the Crab flares". In: *The Astrophysical Journal* 770.2 (2013), p. 147.

[4] Albert Einstein. "The General Theory of Relativity". In: *The Meaning of Relativity*. Berlin, Heidelberg: Springer, 1922, pp. 54–75.

[5] K. Schwarzschild. "On the gravitational field of a mass point according to Einstein's theory". In: *Sitzungsberichte der Königlich Preussischen Akademie der Wissenschaften* (1916), pp. 189–196.

[6] Miguel Alcubierre. *Introduction to 3+1 Numerical Relativity*. Oxford, UK: Oxford University Press, 2008.

[7] Hans Reissner. "Über die Eigengravitation des elektrischen Feldes nach der Einsteinschen Theorie". In: *Annalen der Physik* 355.9 (1916), pp. 106–120.

[8] R. P. Kerr. "Gravitational field of a spinning mass as an example of algebraically special metrics". In: *Physical Review Letters* 11.5 (1963), pp. 237–238.

[9] S. Teukolsky. "The Kerr metric". In: *Classical and Quantum Gravity* 32 (2014).

[10] Robert H. Boyer and Richard W. Lindquist. "Maximal analytic extension of the Kerr metric". In: *Journal of Mathematical Physics* 8.2 (1967), pp. 265–281.

[11] José A. Font, José Ma. Ibáñez, and Philippos Papadopoulos. "A "horizon-adapted" approach to the study of relativistic accretion flows onto rotating black holes". In: *The Astrophysical Journal* 507.1 (1998), pp. L67–L70.

[12] Ezra T Newman et al. "Metric of a rotating, charged mass". In: *Journal of mathematical physics* 6.6 (1965), pp. 918–919.

[13] P. C. Vaidya and P. V. Bhatt. "A generalized Kerr-Schild metric". In: *Pramana* 3 (1974), pp. 28–34.

[14] Richard Arnowitt, Stanley Deser, and Charles W Misner. "Republication of: The dynamics of general relativity". In: *General Relativity and Gravitation* 40 (2008), pp. 1997–2027.

[15] Kagra Collaboration, LIGO Scientific Collaboration, Virgo Collaboration, et al. "Prospects for observing and localizing gravitational-wave transients with Advanced LIGO, Advanced Virgo and KAGRA". In: *Living Reviews in Relativity* 21.1 (2018), p. 3.

[16] W. York. *Kinematics and Dynamics of General Relativity*. Cambridge, UK: Cambridge University Press, 1979.

[17] Eric Gourgoulhon. *3 + 1 formalism in general relativity*. Springer, 2012.

[18] Thomas W. Baumgarte and Stuart L. Shapiro. *Numerical Relativity: Solving Einstein's Equations on the Computer*. Cambridge, UK: Cambridge University Press, 2010.

[19] Thomas W. Baumgarte and Stuart L. Shapiro. "On the numerical integration of Einstein's field equations". In: *Phys. Rev. D* 59 (1999), p. 024007.

[20] T. Nakamura, K. Oohara, and Y. Kojima. "General relativistic collapse to black holes and gravitational waves from black holes". In: *Progress of Theoretical Physics Supplement* 90 (1987), pp. 1–218.

[21] M. Campanelli et al. "Accurate Evolutions of Orbiting Black-Hole Binaries Without Excision". In: *Physical Review Letters* 96 (2006), p. 111101.

[22] T W Baumgarte and S L Shapiro. "Numerical Integration of Einstein's Field Equations". In: *Physical Review D* 59 (1998), p. 024007.

[23] C Bona and J Massó. "Einstein's Evolution Equations as a System of Balance Laws". In: *Physical Review D* 40 (1989), pp. 1022–1027.

[24] C. Bona et al. "New Formalism for Numerical Relativity". In: *Physical Review Letters* 75 (1995), p. 600.

[25] M Alcubierre et al. "Towards Standard Testbeds for Numerical Relativity". In: *Classical and Quantum Gravity* 21 (2003), pp. 589–613.

[26] Y Zlochower et al. "Accurate Black Hole Evolutions by Fourth-order Numerical Relativity". In: *Physical Review D* 72 (2005), p. 024021.

[27] S. Brandt and B. Brügmann. "A Simple Construction of Initial Data for Multiple Black Holes". In: *Physical Review Letters* 78 (1997), p. 3606.

[28] Charles W Misner. "Wormhole initial conditions". In: *Physical Review* 118.4 (1960), p. 1110.

[29] G B Cook. "Initial Data for Numerical Relativity". In: *Living Reviews in Relativity* 3 (2000), pp. 1–53.

[30] Eric Gourgoulhon. "3+ 1 formalism and bases of numerical relativity". In: *arXiv preprint gr-qc/0703035* (2007).

[31] R. M. Wald. *General Relativity*. The University of Chicago Press, 2010.

[32] J. M. Bowen and J. W. York Jr. "Time-asymmetric Initial Data for Black Holes and Black-hole Collisions". In: *Physical Review D* 21 (1980), p. 2047.

[33] D. R. Brill and R. W. Lindquist. "Interaction energy in geometrostatics". In: *Phys. Rev.* 131 (1963), pp. 471–476.

[34] M. Shibata and T. Nakamura. "Evolution of three-dimensional gravitational waves: Harmonic slicing case". In: *Physical Review D* 52 (1995), pp. 5428–5444.

[35] J. M. Bowen. "General form for the longitudinal momentum of a spherically symmetric source". In: *General Relativity and Gravitation* 11.3 (1979), pp. 227–231.

[36] R. A. Matzner, M. F. Huq, and D. Shoemaker. "Initial data and coordinates for multiple black hole systems". In: *Physical Review D* 59 (1998), p. 024015.

[37] F. Albu et al. "The Gauss-Seidel Fast Affine Projection Algorithm". In: *IEEE Workshop on Signal Processing Systems*. IEEE, 2002, pp. 109–114.

[38] Z Cao, H-J Yo, and J-P Yu. "Reinvestigation of Moving Punctured Black Holes with a New Code". In: *Physical Review D* 78 (2008), p. 124011.

[39] C Meringolo, S Servidio, and P Veltri. "A spectral method algorithm for numerical simulations of gravitational fields". In: *Classical and Quantum Gravity* 38 (2021), p. 075027.

[40] J. W. Cooley and J. W. Tukey. "An Algorithm for the Machine Calculation of Complex Fourier Series". In: *Mathematics of Computation* 19 (1965), p. 297.

[41] C. Canuto et al. *Spectral Methods in Fluid Dynamics*. Berlin: Springer Science & Business Media, 2012.

[42] M Boyle et al. "Testing the Accuracy and Stability of Spectral Methods in Numerical Relativity". In: *Physical Review D* 75 (2007), p. 024006.

[43] M Hossain, W H Matthaeus, and S Ghosh. "On Computing High Order Galerkin Products". In: *Computer Physics Communications* 69 (1992), pp. 1–9.

[44] S A Orszag. "On the Elimination of Aliasing in Finite-difference Schemes by Filtering High-wavenumber Components". In: *Journal of the Atmospheric Sciences* 28 (1971), p. 1074.

[45] D. Dutykh. "A brief introduction to pseudo-spectral methods: application to diffusion problems". In: *Doctoral Dissertation, Curitiba, Brazil* (2016), p. 55.

[46] J. P. Boyd. *Chebyshev and Fourier Spectral Methods*. Berlin: Springer-Verlag, 1989.

[47] R. Courant, K. Friedrichs, and H. Lewy. "Uber die partiellen Differenzengleichungender mathematischen Physik". In: *Mathematische Annalen* 100 (1928), pp. 32–74.

[48] J. C. Butcher. *Numerical Methods for Ordinary Differential Equations*. ISBN 978-0-470-72335-7. John Wiley & Sons, 2008.

[49] John C Butcher. "Coefficients for the study of Runge-Kutta integration processes". In: *Journal of the Australian Mathematical Society* 3.2 (1963), pp. 185–201.

[50] E. T. Newman and R. Penrose. "An approach to gravitational radiation by a method of spin coefficients". In: *J. Math. Phys.* 3.3 (1962). Erratum in J. Math. Phys. 4, 998 (1963), pp. 566–578.

[51] Andrea Nerozzi et al. "Towards a novel wave-extraction method for numerical relativity". In: *AIP Conference Proceedings*. Vol. 861. 1. American Institute of Physics. 2006, pp. 702–707.

[52] Andrea Nerozzi. "A new approach to the Newman-Penrose formalism". In: *arXiv preprint arXiv:1109.4400* (2011).

[53] Andrea Nerozzi et al. "Towards a wave-extraction method for numerical relativity. II. The quasi-Kinnersley frame". In: *Physical Review D—Particles, Fields, Gravitation, and Cosmology* 72.2 (2005), p. 024014.

[54] L. Rezzolla and N. T. Bishop. "Extraction of gravitational waves in numerical relativity". In: *Living Rev. Relativ.* 19 (2016), p. 2.

[55] U. Sperhake. "Black holes on supercomputers: numerical relativity applications to astrophysics and high-energy physics". In: *Classical and Quantum Gravity* 30.4 (2013), p. 044008.

[56] C Reisswig et al. "Gravitational wave extraction in simulations of rotating stellar core collapse". In: *Physical Review D* 83 (2011), p. 064008.

[57] B Brügmann et al. "Calibration of moving puncture simulations". In: *Physical Review D* 77 (2008), p. 024027.

[58] Y. Wiaux, L. Jacques, and P. Vandergheynst. "Fast spin ±2 spherical harmonics transforms and application in cosmology". In: *J. Comput. Phys.* 226 (2007), pp. 2359–2371.

[59] D. A. Varshalovich, A. N. Moskalev, and V. K. Kersonskii. *Quantum Theory of Angular Momentum: Irreducible Tensors, Spherical Harmonics, Vector Coupling Coefficients, 3nj Symbols*. Singapore: World Scientific, 1989.

[60] Mario Imbrogno, Claudio Meringolo, and Sergio Servidio. "Extreme gravitational interactions in the problem of three black holes in general relativity". In: *Classical and Quantum Gravity* 40.7 (2023), p. 075008.

[61] B. P. Abbott et al. "Observation of Gravitational Waves from a Binary Black Hole Merger". In: *Physical Review Letters* 116.6 (2016), p. 061102.

[62] Benjamin P Abbott et al. "GW170104: observation of a 50-solar-mass binary black hole coalescence at redshift 0.2". In: *Physical review letters* 118.22 (2017), p. 221101.

[63] M. J. Valtonen, M. Valtonen, and H. Karttunen. *The Three-body Problem*. Cambridge, UK: Cambridge University Press, 2012.

[64] M J Valtonen. "Triple black hole systems formed in mergers of galaxies". In: *Monthly Notices of the Royal Astronomical Society* 278 (1996), p. 186.

[65] J Monaghan. "A Statistical Theory of the Disruption of Three-Body Systems—II: High Angular Momentum". In: *Monthly Notices of the Royal Astronomical Society* 177 (1976), p. 583.

[66] M C Miller and D P Hamilton. "Four-body effects in Globular Cluster Black Hole Coalescence". In: *The Astrophysical Journal* 576 (2002), p. 894.

[67] J Makino and P Hut. "Bottlenecks in simulations of dense stellar systems". In: *The Astrophysical Journal* 365 (1990), p. 208.

[68] S G Djorgovski et al. "Discovery of a probable physical triple quasar". In: *The Astrophysical Journal Letters* 662 (2007), p. L1.

[69] K Gültekin, M C Miller, and D P Hamilton. "Three-Body Encounters of Black Holes in Globular Clusters". In: *AIP Conference Proceedings* 686 (2003), pp. 135–140.

[70] S J Berukoff and B M Hansen. "Cluster Core Dynamics in the Galactic Center". In: *The Astrophysical Journal* 650 (2006), p. 901.

[71] A Gualandris, S P Zwart, and M S Sipior. "Three-body Encounters in the Galactic Centre: the Origin of the Hypervelocity Star SDSS J090745.0+ 024507". In: *Monthly Notices of the Royal Astronomical Society* 363 (2005), p. 223.

[72] F Antonini, N Murray, and S Mikkola. "Black Hole Triple Dynamics: a Breakdown of the Orbit Average Approximation and Implications for Gravitational Wave Detections". In: *The Astrophysical Journal* 781 (2014), p. 45.

[73] J Samsing, M MacLeod, and E Ramirez-Ruiz. "The Formation of Eccentric Compact Binary Inspirals and the Role of Gravitational Wave Emission in Binary-single Stellar Encounters". In: *The Astrophysical Journal* 784 (2014), p. 71.

[74] M C Miller and N Yunes. "The New Frontier of Gravitational Waves". In: *Nature* 568 (2019), pp. 469–476.

[75] K Gültekin, M C Miller, and D P Hamilton. "Growth of Intermediate-mass Black Holes in Globular Clusters". In: *The Astrophysical Journal* 616 (2004), pp. 221–230.

[76] P Galaviz, B Bruegmann, and Z Cao. "Numerical Evolution of Multiple Black Holes with Accurate Initial Data". In: *Physical Review D* 82 (2010), p. 024005.

[77] C. O. Lousto and Y. Zlochower. "Foundations of Multiple-black-hole Evolutions". In: *Physical Review D* 77 (2008), p. 024034.

[78] F Pretorius. "Evolution of Binary Black-hole Spacetimes". In: *Physical Review Letters* 95 (2005), p. 121101.

[79] F Pretorius. "Simulation of Binary Black Hole Spacetimes with a Harmonic Evolution Scheme". In: *Classical and Quantum Gravity* 23 (2006), S529–S552.

[80] D Ceverino et al. "Early Formation of Massive, Compact, Spheroidal Galaxies with Classical Profiles by Violent Disc Instability or Mergers". In: *Monthly Notices of the Royal Astronomical Society* 447 (2015), pp. 3291–3310.

[81] F Bournaud, P-A Duc, and E Emsellem. "High-resolution Simulations of Galaxy Mergers: Resolving Globular Cluster Formation". In: *Monthly Notices of the Royal Astronomical Society: Letters* 389 (2008), pp. L8–L12.

[82] L Lehner and F Pretorius. "Numerical Relativity and Astrophysics". In: *Annual Review of Astronomy and Astrophysics* 52 (2014), pp. 661–694.

[83] M Campanelli, C O Lousto, and Y Zlochower. "Close Encounters of Three Black Holes". In: *Physical Review D* 77 (2008), p. 101501.

[84] K Silsbee and S Tremaine. "Lidov–Kozai Cycles with Gravitational Radiation: Merging Black Holes in Isolated Triple Systems". In: *The Astrophysical Journal* 836 (2017), p. 39.

[85] K. Danzmann and LISA Study Team. "LISA: Laser Interferometer Space Antenna for Gravitational Wave Measurements". In: *Classical and Quantum Gravity* 13 (1996), A247–A250.

[86] M Armano et al. "LISA Pathfinder: the Experiment and the Route to LISA". In: *Classical and Quantum Gravity* 26 (2009), p. 094001.

[87] J Baker et al. "High Angular Resolution Gravitational Wave Astronomy". In: *Experimental Astronomy* 51 (2021), pp. 1441–1464.

[88] H Goldstein, C Poole, and J Safko. *Classical Mechanics*. Reading, MA: Addison-Wesley, 1980.

[89] R A Mardling. "Resonance, Chaos and Stability: The Three-body Problem in Astrophysics". In: *Resonances in the Solar System*. Vol. 760. Dordrecht: Springer, 2008, pp. 59–96.

[90] S Liao. "Physical Limit of Prediction for Chaotic Motion of Three-body Problem". In: *Physical Review Letters* 19 (2014), pp. 601–608.

[91] P T Boyd and S L McMillan. "Chaotic Scattering in the Gravitational Three-body Problem". In: *Chaos: An Interdisciplinary Journal of Nonlinear Science* 3 (1993), pp. 507–523.

[92] S J Aarseth et al. "Close Triple Approaches and Escape in the Three-body Problem". In: *Celestial Mechanics and Dynamical Astronomy* 60 (1994), pp. 131–144.

[93] S F P Zwart and T C N Boekholt. "Numerical Verification of the Microscopic Time Reversibility of Newton's Equations of Motion: Fighting Exponential Divergence". In: *Communications in Nonlinear Science and Numerical Simulation* 61 (2018), pp. 160–168.

[94] H J Lehto et al. "Mapping the Three-body System–decay Time and Reversibility". In: *Monthly Notices of the Royal Astronomical Society* 388 (2008), pp. 965–973.

[95] D M Hernandez, S Hadden, and J Makino. "Are long-term N-body simulations reliable?" In: *Monthly Notices of the Royal Astronomical Society* 493 (2020), pp. 1913–1926.

[96] Carl Burrau. "Numerische Berechnung eines Spezialfalles des Dreikörperproblems". In: *Astronomische Nachrichten* 195 (1913), pp. 113–119.

[97] T W Baumgarte. "Innermost Stable Circular Orbit of Binary Black Holes". In: *Physical Review D* 62 (2000), p. 024018.

[98] A Čadež. "Apparent horizons in the two-black-hole problem". In: *Annals of Physics* 83(2) (1974), pp. 449–457.

[99] G Jaramillo and C O Lousto. "Study of multi-black-hole and ring-singularity apparent horizons". In: *Physical Review D* 84(10) (2011), p. 104011.

[100] E Altas and B Tekin. "Basics of Apparent horizons in black hole physics". In: *Journal of Physics: Conference Series* 2191(1) (2022), p. 012002.

[101] D Pook-Kolb, R A Hennigar, and I Booth. "What Happens to Apparent Horizons in a Binary Black Hole Merger?" In: *Physical Review Letters* 127(18) (2021), p. 181101.

[102] L M Lin and J Novak. "A new spectral apparent horizon finder for 3D numerical relativity". In: *Classical and Quantum Gravity* 24(10) (2007), pp. 2665–2675.

[103] M F Huq, M W Choptuik, and R A Matzner. "Locating boosted Kerr and Schwarzschild apparent horizons". In: *Physical Review D* 66.8 (2002), p. 084024.

[104] J Baker et al. "Plunge waveforms from inspiralling binary black holes". In: *Physical Review Letters* 87 (2001), p. 121103.

[105] J. Baker et al. "Modeling gravitational radiation from coalescing binary black holes". In: *Physical Review D* 65 (2002), p. 124012.

[106] J G Baker et al. "Binary black hole merger dynamics and waveforms". In: *Physical Review D* 73 (2006), p. 104002.

[107] R N Lang and S A Hughes. "Measuring coalescing massive binary black holes with gravitational waves: The impact of spin-induced precession". In: *Physical Review D* 74 (2006), p. 122001.

[108] J Centrella et al. "Black-hole binaries, gravitational waves, and numerical relativity". In: *Reviews of Modern Physics* 82 (2010), pp. 3069–3110.

[109] R Cotesta et al. "Enriching the symphony of gravitational waves from binary black holes by tuning higher harmonics". In: *Physical Review D* 98 (2018), p. 084028.

[110] B Brügmann, W Tichy, and N Jansen. "Numerical simulation of orbiting black holes". In: *Physical Review Letters* 92 (2004), p. 211101.

[111] U Sperhake, E Berti, and V Cardoso. "Numerical simulations of black-hole binaries and gravitational wave emission". In: *Comptes Rendus Physique* 14 (2013), pp. 306–317.

[112] A Buonanno, G B Cook, and F Pretorius. "Inspiral, merger, and ring–down of equal–mass black–hole binaries". In: *Physical Review D* 75.12 (2007), p. 124018.

[113] P Anninos et al. "Three-dimensional numerical relativity: The evolution of black holes". In: *Physical Review D* 52 (1995), pp. 2059–2073.

[114] R B Blackman and J W Tukey. "The measurement of power spectra from the point of view of communications engineering—part I". In: *Bell System Technical Journal* 37 (1958), pp. 185–282.

[115] I Daubechies. *Ten Lectures on Wavelets*. Philadelphia, PA: Society for Industrial and Applied Mathematics (SIAM), 1992.

[116] M Unser. "Sampling—50 years after Shannon". In: *Proceedings of the IEEE* 88.4 (2000), pp. 569–587.

[117] C Cattani. "Shannon wavelets theory". In: *Mathematical Problems in Engineering* 2008 (2008), Article ID 164808.

[118] S Mallat. *A wavelet tour of signal processing*. Amsterdam: Elsevier, 1999.

[119] A J Lichtenberg and M A Lieberman. *Regular and Chaotic Dynamics*. 2nd ed. Vol. 38. Applied Mathematical Sciences. New York: Springer-Verlag, 1992.

[120] T C N Boekholt, A Moerman, and S F P Zwart. "Relativistic Pythagorean three-body problem". In: *Physical Review D* 104 (2021), p. 083020.

[121] M Campanelli, C O Lousto, and Y Zlochower. "Last orbit of binary black holes". In: *Physical Review D* 73 (2006), p. 061501.

[122] W Tichy. "Black hole evolution with the BSSN system by pseudospectral methods". In: *Physical Review D* 74 (2006), p. 084005.

[123] U Sperhake. "The numerical relativity breakthrough for binary black holes". In: *Classical and Quantum Gravity* 32 (2015), p. 124011.

[124] B Vaishnav et al. "Matched filtering of numerical relativity templates of spinning binary black holes". In: *Physical Review D* 76 (2007), p. 084020.

[125] M Campanelli, C O Lousto, and Y Zlochower. "Spinning-black-hole binaries: The orbital hang-up". In: *Physical Review D* 74 (2006), p. 041501.

[126] W Tichy. "Long term black hole evolution with the BSSN system by pseudospectral methods". In: *Physical Review D* 80 (2009), p. 104034.

[127] Mario Imbrogno et al. "A Novel Logarithmic Approach to General Relativistic Hydrodynamics in Curved Spacetimes". 2024.

[128] R. D. Blandford and R. L. Znajek. "Electromagnetic extraction of energy from Kerr black holes". In: *Monthly Notices of the Royal Astronomical Society* 179.3 (1977), 433–456.

[129] J. R. Wilson. "Numerical Study of Fluid Flow in a Curved Spacetime". In: *The Astrophysical Journal* 173 (1972), pp. 431–444.

[130] J. A. Font. "Hydrodynamics in full general relativity: Formulations, implementations, and tests". In: *Physical Review D* 62 (2000), p. 084017.

[131] M. Shibata and Y.-I. Sekiguchi. "Three-dimensional simulations of stellar core collapse in full general relativity: Nonaxisymmetric dynamical instabilities". In: *Physical Review D* 71 (2005), p. 024014.

[132] Charles F Gammie, Jonathan C McKinney, and Gábor Tóth. "HARM: a numerical scheme for general relativistic magnetohydrodynamics". In: *The Astrophysical Journal* 589.1 (2003), p. 444.

[133] SS Komissarov. "General relativistic magnetohydrodynamic simulations of monopole magnetospheres of black holes". In: *Monthly Notices of the Royal Astronomical Society* 350.4 (2004), pp. 1431–1436.

[134] Lorenzo Sironi, Maria Petropoulou, and Dimitrios Giannios. "Relativistic jets shine through shocks or magnetic reconnection?" In: *Monthly Notices of the Royal Astronomical Society* 450.1 (2015), pp. 183–191.

[135] J. M. Martí and E. Müller. "Numerical hydrodynamics in special relativity". In: *Living Reviews in Relativity* 2 (1999), p. 3.

[136] L. Del Zanna and N. Bucciantini. "An efficient shock-capturing central-type scheme for multidimensional relativistic flows". In: *Astronomy and Astrophysics* 390 (2002), pp. 1177–1186.

[137] M. Shibata. "Fully General Relativistic Simulation of Coalescing Binary Neutron Stars: Preparatory Test". In: *Physical Review D* 71 (2005), p. 104033.

[138] Andrea Mignone, T. Plewa, and G. Bodo. "The piecewise parabolic method for multidimensional relativistic fluid dynamics". In: *The Astrophysical Journal Supplement Series* 160.1 (2005), p. 199.

[139] José A Font. "Numerical hydrodynamics and magnetohydrodynamics in general relativity". In: *Living Reviews in Relativity* 11 (2008), pp. 1–131.

[140] MTP Liska et al. "H-AMR: A New GPU-accelerated GRMHD Code for Exascale Computing with 3D Adaptive Mesh Refinement and Local Adaptive Time Stepping". In: *The Astrophysical Journal Supplement Series* 263.2 (2022), p. 26.

[141] Zachariah B Etienne et al. "IllinoisGRMHD: an open-source, user-friendly GRMHD code for dynamical spacetimes". In: *Classical and Quantum Gravity* 32.17 (2015), p. 175009.

[142] Bruno Giacomazzo and Luciano Rezzolla. "WhiskyMHD: a new numerical code for general relativistic magnetohydrodynamics". In: *Classical and Quantum Gravity* 24.12 (2007), S235.

[143] Béla Szilágyi. "Key elements of robustness in binary black hole evolutions using spectral methods". In: *International Journal of Modern Physics D* 23.07 (2014), p. 1430014.

[144] Philipp Mösta et al. "GRHydro: a new open-source general-relativistic magnetohydrodynamics code for the Einstein toolkit". In: *Classical and Quantum Gravity* 31.1 (2013), p. 015005.

[145] James M Stone et al. "Athena: a new code for astrophysical MHD". In: *The Astrophysical Journal Supplement Series* 178.1 (2008), p. 137.

[146] Pasquale Londrillo and Luca Del Zanna. "High-order upwind schemes for multidimensional magnetohydrodynamics". In: *The Astrophysical Journal* 530.1 (2000), p. 508.

[147] Luciano Rezzolla and Olindo Zanotti. *Relativistic hydrodynamics*. Oxford University Press, USA, 2013.

[148] Josef Stoer et al. *Introduction to numerical analysis*. Vol. 1993. Springer, 1980.

[149] William H Press. *Numerical recipes 3rd edition: The art of scientific computing*. Cambridge university press, 2007.

[150] A. Mignone et al. "PLUTO: A Numerical Code for Computational Astrophysics". In: *The Astrophysical Journal Supplement Series* 170 (2007), pp. 228–242.

[151] L. Baiotti, B. Giacomazzo, and L. Rezzolla. "Accurate evolutions of inspiralling and magnetized neutron stars: Equal-mass binaries". In: *Physical Review D* 78 (2008), p. 084033.

[152] Filippo Galeazzi et al. "Implementation of a simplified approach to radiative transfer in general relativity". In: *Physical Review D—Particles, Fields, Gravitation, and Cosmology* 88.6 (2013), p. 064009.

[153] Luca Baiotti et al. "A new three-dimensional general-relativistic hydrodynamics code". In: *arXiv preprint arXiv:1004.3849* (2010). Published in Classical and Quantum Gravity. arXiv: 1004.3849.

[154] David Radice, Sebastiano Bernuzzi, and Christian D Ott. "One-armed spiral instability in neutron star mergers and its detectability in gravitational waves". In: *Physical Review D* 94.6 (2016), p. 064011.

[155] Carlos Palenzuela et al. "Linking electromagnetic and gravitational radiation in coalescing binary neutron stars". In: *Physical Review D—Particles, Fields, Gravitation, and Cosmology* 88.4 (2013), p. 043011.

[156] P. J. Montero, T. W. Baumgarte, and E. Müller. "General Relativistic Hydrodynamics in Curvilinear Coordinates". In: *Phys. Rev. D* 89 (2014), p. 084043.

[157] N. D. Hamlin and W. I. Newman. "Role of the Kelvin-Helmholtz instability in the evolution of magnetized relativistic sheared plasma flows". In: *Phys. Rev. E* 87 (2013), p. 043101.

[158] H. von Helmholtz. "Monatsberichte der Königlichen Preussische Akademie der Wissenschaften zu Berlin". In: 23 (1868), p. 215.

[159] L. Kelvin. In: *Philos. Mag.* 42 (1871), p. 362.

[160] S. A. Maslowe. "Barotropic instability of the Bickley jet". In: *J. Fluid Mech.* 229 (1991), p. 417.

[161] G. Swaters. "On the evolution of near-singular modes of the Bickley jet". In: *Phys. Fluids* 11 (1999), p. 2546.

[162] S. Chandrasekhar. *Hydrodynamic and Hydromagnetic Stability*. Oxford: Clarendon, 1961.

[163] K. Case. "Stability of an Idealized Atmosphere. I. Discussion of Results". In: *Phys. Fluids* 3 (1960), p. 149.

[164] F. J. Dyson. "Stability of an Idealized Atmosphere. II. Zeros of the Confluent Hypergeometric Function". In: *Phys. Fluids* 3 (1960), p. 155.

[165] P. G. Drazin. "The stability of a shear layer in an unbounded heterogeneous inviscid fluid". In: *J. Fluid Mech.* 4 (1958), p. 214.

[166] P. G. Drazin and L. N. Howard. "Hydrodynamic Stability of Parallel Flow of Inviscid Fluid". In: *Adv. Appl. Mech.* 9 (1966), p. 1.

[167] Z.-Y. Pu and M. Kivelson. "Kelvin-Helmholtz Instability at the Magnetopause: Solution for Compressible Plasmas". In: *J. Geophys. Res.* 88 (1983), p. 841.

[168] M. Kivelson and Z.-Y. Pu. "The Kelvin-Helmholtz instability on the magnetopause". In: *Planet. Space Sci.* 32 (1984), p. 1335.

[169] A. Otto and D. Fairfield. "Kelvin-Helmholtz instability at the magnetotail boundary: MHD simulation and comparison with Geotail observations". In: *J. Geophys. Res.* 105 (2000), p. 21175.

[170] F. Pegoraro M. Faganello F. Califano. "Competing Mechanisms of Plasma Transport in Inhomogeneous Configurations with Velocity Shear: The Solar-Wind Interaction with Earth's Magnetosphere". In: *Phys. Rev. Lett.* 100 (2008), p. 015001.

[171] Rayleigh. "Investigation of the character of the equilibrium of an incompressible heavy fluid of variable density". In: *Proceedings of the London mathematical society* 1.1 (1882), pp. 170–177.

[172] Geoffrey Ingram Taylor. "The instability of liquid surfaces when accelerated in a direction perpendicular to their planes. I". In: *Proceedings of the Royal Society of London. Series A. Mathematical and Physical Sciences* 201.1065 (1950), pp. 192–196.

[173] Robert D Richtmyer. *Taylor instability in shock acceleration of compressible fluids*. Tech. rep. Los Alamos Scientific Lab., N. Mex., 1954.

[174] _E E Meshkov. "Instability of the interface of two gases accelerated by a shock wave". In: *Fluid Dynamics* 4.5 (1969), pp. 101–104.

[175] R. Rosner G. Bodo A. Mignone. "Kelvin-Helmholtz Instability for Relativistic Fluids". In: *Phys. Rev. E* 70 (2004), p. 036304.

[176] S. Weinberg. *Gravitation and Cosmology. Principles and Applications of the General Theory of Relativity*. John Wiley & Sons, 1972.

[177] Kris Beckwith and James M Stone. "A second-order Godunov method for multi-dimensional relativistic magnetohydrodynamics". In: *The Astrophysical Journal Supplement Series* 193.1 (2011), p. 6.

[178] David Radice and Luciano Rezzolla. "THC: a new high-order finite-difference high-resolution shock-capturing code for special-relativistic hydrodynamics". In: *Astronomy & Astrophysics* 547 (2012), A26.

[179] Luciano Rezzolla and Alexander Zhidenko. "New parametrization for spherically symmetric black holes in metric theories of gravity". In: *Physical Review D* 90.8 (2014), p. 084009.

[180] James B Hartle and Kip S Thorne. "Slowly rotating relativistic stars. II. Models for neutron stars and supermassive stars". In: *Astrophysical Journal, vol. 153, p. 807* 153 (1968), p. 807.

[181] F. Löffler et al. "The Einstein Toolkit: A Community Computational Infrastructure for Relativistic Astrophysics". In: *Classical and Quantum Gravity* 29 (2012).

[182] H. Olivares et al. "Constrained Transport and Adaptive Mesh Refinement in the Black Hole Accretion Code". In: *Astronomy & Astrophysics* 629 (2019), A61.

[183] P. Londrillo and L. Del Zanna. "On the Divergence-Free Condition in Godunov-Type Schemes for Ideal Magnetohydrodynamics: The Upwind Constrained Transport Method". In: *J. Comput. Phys.* 195 (2004), p. 17.

[184] L. Del Zanna et al. "ECHO: A Eulerian Conservative High-Order Scheme for General Relativistic Magnetohydrodynamics and Magnetodynamics". In: *Astronomy & Astrophysics* 474, 1 (2007), pp. 11–30.

[185] L. G. Fishbone and V. Moncrief. "Relativistic Fluid Disks in Orbit Around Kerr Black Holes". In: *Astrophysical Journal* 207 (1976), pp. 962–976.

[186] M. Kolos and A. Janiuk. *Simulations of Black Hole Accretion Torus in Various Magnetic Field Configurations*. Submitted on 16 Apr 2020. 2020.

[187] L. C. Ho. "Nuclear Activity in Nearby Galaxies". In: *Annual Review of Astronomy and Astrophysics* 46 (2008), pp. 475–539.

[188] F. Yuan and R. Narayan. "Hot Accretion Flows Around Black Holes". In: *Annual Review of Astronomy and Astrophysics* 52 (2014), pp. 529–588.

[189] R. D. Blandford and D. G. Payne. "Hydromagnetic flows from accretion discs and the production of radio jets". In: *Monthly Notices of the Royal Astronomical Society* 199.4 (1982), 883–903.

[190] S. A. Balbus and J. F. Hawley. "Instability, Turbulence, and Enhanced Transport in Accretion Disks". In: *Review of Modern Physics* 70, 1 (1998).

[191] M. C. Begelman, R. D. Blandford, and M. J. Rees. "Theory of extragalactic radio sources". In: *Review of Modern Physics* 56 (1984), p. 255.

[192] S. Servidio et al. "Magnetic Reconnection in Two-Dimensional Magnetohydrodynamic Turbulence". In: *Physical Review Letters* 102.11 (2009), p. 115003.

[193] S. Servidio et al. "Statistical association of discontinuities and reconnection in magnetohydrodynamic turbulence". In: *Journal of Geophysical Research* 116 (2011), A09102.

[194] W. H. Matthaeus and M. L. Goldstein. "Measurement of the rugged invariants of magnetohydrodynamic turbulence in the solar wind". In: *Journal of Geophysical Research* 87 (1982), p. 6011.

[195] F. Pecora et al. "Multipoint Turbulence Analysis with HelioSwarm". In: *The Astrophysical Journal Letters* 945, 2 (2023), p. L20.

[196] Burkhard Buttkus. "Estimation of the power spectral density function". In: *Spectral Analysis and Filter Theory in Applied Geophysics*. Springer, 2000, pp. 179–213.

[197] Saeid Sanei and Jonathon A Chambers. *EEG signal processing*. John Wiley & Sons, 2013.

[198] J. C. McKinney and C. F. Gammie. "A Measurement of the Electromagnetic Luminosity of a Kerr Black Hole". In: *The Astrophysical Journal* 611.2 (2004).

[199] I. V. Igumenshchev, R. Narayan, and M. A. Abramowicz. "Three-Dimensional Magnetohydrodynamic Simulations of Radiatively Inefficient Accretion Flows". In: *Astrophysical Journal* 592 (2003), p. 2.

[200] R. Narayan, I. V. Igumenshchev, and M. A. Abramowicz. "Magnetically Arrested Disk: An Energetically Efficient Accretion Flow". In: *Publications of the Astronomical Society of Japan* 55 (2003), p. L69.

[201] Jesse Vos et al. "Plasmoid identification and statistics in two-dimensional Harris sheet and GRMHD simulations". In: *arXiv e-prints*, arXiv:2309.03267 (2023), arXiv:2309.03267.

[202] B. Ripperda, F. Bacchini, and A. A. Philippov. "Magnetic Reconnection and Hot Spot Formation in Black Hole Accretion Disks". In: *The Astrophysical Journal* 900.2 (2020), p. 100.

[203] Rita Megale et al. *The Proper Length Spectrum of Turbulence near Black Holes*. 2024.

[204] Lorenzo Sironi and Anatoly Spitkovsky. "Relativistic reconnection: an efficient source of non-thermal particles". In: *The Astrophysical Journal Letters* 783.1 (2014), p. L21.

[205] T Gold and F Hoyle. "On the origin of solar flares". In: *Monthly Notices of the Royal Astronomical Society* 120.2 (1960), pp. 89–105.

[206] O Allanson, Fiona Wilson, and Thomas Neukirch. "Neutral and non-neutral collisionless plasma equilibria for twisted flux tubes: The Gold-Hoyle model in a background field". In: *Physics of Plasmas* 23.9 (2016), p. 092106.

[207] Oscar Buneman. "TRISTAN: the 3-D, EM particle code". In: *Computer Space Plasma Physics: Simulation Techniques and Software* (1993).

[208] Kevin J Bowers et al. "Ultrahigh performance three-dimensional electromagnetic relativistic kinetic plasma simulation". In: *Physics of Plasmas* 15.5 (2008), p. 055703.

[209] Stefano Markidis, Giovanni Lapenta, et al. "Multi-scale simulations of plasma with iPIC3D". In: *Mathematics and Computers in Simulation* 80.7 (2010), pp. 1509–1519.

[210] Troels Haugbølle, Jacob Trier Frederiksen, and Åke Nordlund. "photon-plasma: A modern high-order particle-in-cell code". In: *Physics of Plasmas* 20.6 (2013), p. 062904.

[211] Michael Bussmann et al. "Radiative signatures of the relativistic Kelvin-Helmholtz instability". In: *Proceedings of the International Conference on High Performance Computing, Networking, Storage and Analysis*. 2013, pp. 1–12.

[212] Andrea Sgattoni et al. "Optimising piccante-an open source particle-in-cell code for advanced simulations on tier-0 systems". In: *arXiv preprint arXiv:1503.02464* (2015).

[213] Rémi Lehe et al. "A spectral, quasi-cylindrical and dispersion-free Particle-In-Cell algorithm". In: *Computer Physics Communications* 203 (2016), pp. 66–82.

[214] D. Winske and N. Omidi. *Hybrid codes: Methods and applications*. Presented at the 4th International School for Space Simulation, Nara, Japan, 1-5 Apr. 1991. Jan. 1991.

[215] John Michael Fife. "Hybrid-PIC modeling and electrostatic probe survey of Hall thrusters". PhD thesis. Massachusetts Institute of Technology, 1998.

[216] Xue-Ning Bai et al. "Magnetohydrodynamic-particle-in-cell method for coupling cosmic rays with a thermal plasma: application to non-relativistic shocks". In: *The Astrophysical Journal* 809.1 (2015), p. 55.

[217] Ioana Duţan et al. "Particle-in-cell Simulations of Global Relativistic Jets with Helical Magnetic Fields". In: *New Frontiers in Black Hole Astrophysics*. Ed. by Andreja Gomboc. Vol. 324. Jan. 2017, pp. 199–202.

[218] Lorenzo Sironi and Benoît Cerutti. "Particle acceleration in pulsar wind nebulae: PIC modelling". In: *Modelling Pulsar Wind Nebulae*. Springer, 2017, pp. 247–277.

[219] Luca Comisso and Lorenzo Sironi. "Particle acceleration in relativistic plasma turbulence". In: *Physical review letters* 121.25 (2018), p. 255101.

[220] L Comisso et al. "Magnetohydrodynamic turbulence in the plasmoid-mediated regime". In: *The Astrophysical Journal* 854.2 (2018), p. 103.

[221] Luca Comisso and Lorenzo Sironi. "The interplay of magnetically dominated turbulence and magnetic reconnection in producing nonthermal particles". In: *The Astrophysical Journal* 886.2 (2019), p. 122.

[222] Kyle Parfrey, Alexander Philippov, and Benoît Cerutti. "First-principles plasma simulations of black-hole jet launching". In: *Physical review letters* 122.3 (2019), p. 035101.

[223] Benjamin Crinquand. "Particle acceleration in Kerr black-hole magnetospheres". PhD thesis. Université Grenoble-Alpes, 2021.

[224] Benjamin Crinquand et al. "Synthetic Images of Magnetospheric Reconnection-Powered Radiation around Supermassive Black Holes". In: *Physical Review Letters* 129.20 (2022), p. 205101.

[225] I El Mellah et al. "Spinning black holes magnetically connected to a Keplerian disk–Magnetosphere, reconnection sheet, particle acceleration and coronal heating". In: *Astronomy & Astrophysics* 663 (2022), A169.

[226] Volker Springel. "High performance computing and numerical modelling". In: *Star Formation in Galaxy Evolution: Connecting Numerical Models to Reality*. Springer, 2016, pp. 251–358.

[227] Ernst Hairer et al. "Geometric numerical integration". In: *Oberwolfach Reports* 3.1 (2006), pp. 805–882.

[228] L. D. Landau and M. E. Lifshitz. *The Classical Theory of Fields. Vol. 2*. Addison-Wesley, 1951.

[229] Jay P Boris and Ramy A Shanny. *Proceedings*. Naval Research Laboratory, 1973.

[230] Kane Yee. "Numerical solution of initial boundary value problems involving Maxwell's equations in isotropic media". In: *IEEE Transactions on Antennas and Propagation* 14.3 (1966), pp. 302–307.

[231] Charles K Birdsall and A Bruce Langdon. *Plasma physics via computer simulation*. CRC press, 2018.

[232] Mario Imbrogno et al. "Long-lived Equilibria in Kinetic Astrophysical Plasma Turbulence". In: *The Astrophysical Journal Letters* 972.1 (2024), p. L5.

[233] Melvyn L. Goldstein, D. A. Roberts, and W. H. Matthaeus. "Magnetohydrodynamic turbulence in the solar wind". In: *Annual Review of Astronomy and Astrophysics* 33.1 (1995), pp. 283–325.

[234] Luca Baiotti and Luciano Rezzolla. "Binary neutron-star mergers: a review of Einstein's richest laboratory". In: *Reports on Progress in Physics* 80.9 (2017), p. 096901.

[235] Bart Ripperda et al. "Black hole flares: Ejection of accreted magnetic flux through 3D plasmoid-mediated reconnection". In: *The Astrophysical Journal Letters* 924.2 (2022), p. L32.

[236] F. Sahraoui et al. "Evidence of a Cascade and Dissipation of Solar-Wind Turbulence at the Electron Gyroscale". In: *Physical Review Letters* 102.23 (2009), p. 231102.

[237] William H. Matthaeus et al. "Intermittency, nonlinear dynamics and dissipation in the solar wind and astrophysical plasmas". In: *Philosophical Transactions of the Royal Society A: Mathematical, Physical and Engineering Sciences* 373.2041 (2015), p. 20140154.

[238] P. H. Chavanis and J. Sommeria. "Classification of robust isolated vortices in two-dimensional hydrodynamics". In: *Journal of Fluid Mechanics* 356 (1998), pp. 259–296.

[239] O. Alexandrova. "Solar wind vs magnetosheath turbulence and Alfvén vortices". In: *Nonlinear Processes in Geophysics* 15.1 (2008), pp. 95–108.

[240] H. Karimabadi et al. "Coherent structures, intermittent turbulence, and dissipation in high-temperature plasmas". In: *Physics of Plasmas* 20.1 (2013).

[241] O. A. Pokhotelov and V. I. Petviashvili. *Solitary Waves in Plasmas and in the Atmosphere*. Gordon and Breach, Reading, 1992.

[242] David Montgomery et al. "Relaxation in two dimensions and the "sinh-Poisson"equation". In: *Physics of Fluids A: Fluid Dynamics* 4.1 (1992), pp. 3–6.

[243] Joseph E. Borovsky. "Flux tube texture of the solar wind: Strands of the magnetic carpet at 1 AU?" In: *Journal of Geophysical Research: Space Physics* 113.A8 (2008).

[244] Francesco Pecora et al. "Single-spacecraft identification of flux tubes and current sheets in the solar wind". In: *The Astrophysical Journal Letters* 881.1 (2019), p. L11.

[245] Antonios Nathanail et al. "Magnetic reconnection and plasmoid formation in three-dimensional accretion flows around black holes". In: *Monthly Notices of the Royal Astronomical Society* 513.3 (2022), pp. 4267–4277.

[246] J. F. Drake et al. "A magnetic reconnection mechanism for the generation of anomalous cosmic rays". In: *The Astrophysical Journal* 709.2 (2010), pp. 963–974.

[247] Maria Petropoulou, Dimitrios Giannios, and Lorenzo Sironi. "Blazar flares powered by plasmoids in relativistic reconnection". In: *Monthly Notices of the Royal Astronomical Society* 462.3 (2016), pp. 3325–3343.

[248] O Khabarova et al. "Current Sheets, Plasmoids and Flux Ropes in the Heliosphere: Part I. 2-D or not 2-D? General and Observational Aspects". In: *Space Science Reviews* 217.3 (2021), p. 38.

[249] Alexander Lukin et al. "Two-dimensional self-similar plasma equilibria". In: *Physics of Plasmas* 25.1 (2018), p. 012906.

[250] David Ball, Lorenzo Sironi, and Feryal Özel. "Electron and proton acceleration in trans-relativistic magnetic reconnection: dependence on plasma beta and magnetization". In: *The Astrophysical Journal* 862.1 (2018), p. 80.

[251] Claudio Meringolo et al. "Microphysical plasma relations from special-relativistic turbulence". In: *The Astrophysical Journal* 944.2 (2023), p. 122.

[252] S. Servidio et al. "Local Kinetic Effects in Two-Dimensional Plasma Turbulence". In: *Physical Review Letters* 108.4 (2012), p. 045001.

[253] S. D. Bale et al. "Measurement of the Electric Fluctuation Spectrum of Magnetohydrodynamic Turbulence". In: *Physical Review Letters* 94.21 (2005), p. 215002.

[254] O. Alexandrova et al. "Universality of Solar-Wind Turbulent Spectrum from MHD to Electron Scales". In: *Physical Review Letters* 103.16 (2009), p. 165003.

[255] W. H. Matthaeus et al. "Rapid Alignment of Velocity and Magnetic Field in Magnetohydrodynamic Turbulence". In: *Physical Review Letters* 100.8 (2008), p. 085003.

[256] S. Servidio, W. H. Matthaeus, and P. Dmitruk. "Depression of Nonlinearity in Decaying Isotropic MHD Turbulence". In: *Physical Review Letters* 100.9 (2008), p. 095005.

[257] Sergio Servidio et al. "Local relaxation and maximum entropy in two-dimensional turbulence". In: *Physics of Fluids* 22.12 (2010), p. 125107.

[258] James C McWilliams. "The emergence of isolated coherent vortices in turbulent flow". In: *Journal of Fluid Mechanics* 146 (1984), pp. 21–43.

[259] Mark D Powell and Samuel H Houston. "Surface wind fields of 1995 hurricanes Erin, Opal, Luis, Marilyn, and Roxanne at landfall". In: *Monthly Weather Review* 126.5 (1998), pp. 1259–1273.

[260] George Haller. "An objective definition of a vortex". In: *Journal of Fluid Mechanics* 525 (2005), pp. 1–26.

[261] G. F. Carnevale et al. "Evolution of vortex statistics in two-dimensional turbulence". In: *Physical Review Letters* 66.21 (1991), pp. 2735–2738.

[262] J Brian Taylor. "Relaxation of toroidal plasma and generation of reverse magnetic fields". In: *Physical Review Letters* 33.19 (1974), pp. 1139–1141.

[263] E. G. Harris. "On a plasma sheath separating regions of oppositely directed magnetic field". In: *Il Nuovo Cimento* 23.1 (1962), pp. 115–121.

[264] Bart Ripperda et al. "Relativistic resistive magnetohydrodynamic reconnection and plasmoid formation in merging flux tubes". In: *Monthly Notices of the Royal Astronomical Society* 485.1 (2019), pp. 299–314.

[265] Alexandros Alexakis, Pablo D. Mininni, and Annick Pouquet. "On the inverse cascade of magnetic helicity". In: *The Astrophysical Journal* 640.1 (2006), pp. 335–343.

[266] Toshiaki Fushiki and Jun-Ichi Sakai. "3-D MHD simulation of the formation of spiral plasma flows during collision of two current loops". In: *Solar Physics* 161 (1995), pp. 317–330.

[267] L. Woltjer. "On Hydromagnetic Equilibrium". In: *Proceedings of the National Academy of Sciences* 44.9 (1958), pp. 833–841.

[268] W. H. Matthaeus, M. L. Goldstein, and C. Smith. "Evaluation of magnetic helicity in homogeneous turbulence". In: *Physical Review Letters* 48.18 (1982), pp. 1256–1259.

[269] Olga Alexandrova et al. "Alfvén vortex filaments observed in magnetosheath downstream of a quasi-perpendicular bow shock". In: *Journal of Geophysical Research: Space Physics* 111.A12 (2006).

[270] Alexander Vinogradov et al. "Embedded coherent structures from MHD to sub-ion scales in turbulent solar wind at 0.17 au". In: *arXiv preprint arXiv:2307.10478* (2023).

[271] John V. Shebalin, William H. Matthaeus, and David Montgomery. "Anisotropy in MHD turbulence due to a mean magnetic field". In: *Journal of Plasma Physics* 29.3 (1983), pp. 525–547.

[272] Alexander Chernoglazov, Bart Ripperda, and Alexander Philippov. "Dynamic alignment and plasmoid formation in relativistic magnetohydrodynamic turbulence". In: *The Astrophysical Journal Letters* 923.1 (2021), p. L13.

[273] Mario Imbrogno et al. "Multi-species Plasma Turbulence in the Vicinity of Black Holes". 2024.

[274] M Dumbser et al. "Conformal and covariant Z4 formulation of the Einstein equations: Strongly hyperbolic first-order reduction and solution with discontinuous Galerkin schemes". In: *Physical Review D* 97 (2018), p. 084053.

[275] U. Frish. *Turbulence: The Legacy of A. N. Kolmogorov*. English. Cambridge University Press, 1995, xiii, 674 p. ISBN: 0070353468.

[276] P. Alfeld. "A Trivariate Clough-Tocher Scheme for Tetrahedral Data". In: *Computer Aided Geometric Design* 1 (1984), pp. 169–181.

[277] R. J. Renka and A. K. Cline. "A Triangle-based C^1 interpolation method". In: *The Rocky Mountain Journal of Mathematics* 14.1 (1984), 223–237.